Surveying Young Substellar Objects: Formation Pathways and Atmospheres

Pengyu Liu



Doctor of Philosophy
The University of Edinburgh
August 2025

Abstract

Direct imaging of substellar companions is challenging due to their low luminosity compared to their host stars and small angular separations between them. The formation and evolution of substellar objects are still poorly understood. The free-floating planetary-mass objects and brown dwarfs share similar physical properties with directly imaged substellar companions. Characterisation of these free-floating objects can help us understand the atmospheric structures of substellar worlds. Thanks to the development of instruments and observational strategies, the population of directly imaged young substellar objects has been growing. The growing number makes it possible to conduct population studies of young planetary-mass objects and brown dwarfs.

In this thesis, I present a series of direct imaging surveys aimed at characterising the atmospheres of young planetary-mass objects and searching for substellar companions in young stellar regions. The overarching goal is to detect new exoplanets and place observational constraints on the formation and evolutionary pathways of wide-orbit planets and planetary-mass binaries. Collectively, these projects address key open questions in substellar astrophysics, from atmospheric processes to formation mechanisms.

In Chapter 2, I present a photometric near-infrared variability survey of young planetary-mass objects. This work provides the first constraint on the variability rate of young T dwarfs in the near-infrared. By combining these results with previous surveys, I conduct a statistical analysis of variability across ages and spectral types, demonstrating that surface gravity plays a critical role in shaping the atmospheric structures of brown dwarfs and planetary-mass objects from L to T types.

In Chapter 3, I report the first results of a direct imaging survey of wide-orbit companions in the Fornax-Horologium association. With its young age (~30 Myr)

and dissolving open cluster core, this association offers a unique laboratory for investigating wide-orbit planet formation. I present the discovery of a companion at the hydrogen-burning limit of HD 24121, along with updates on this ongoing survey.

In Chapter 4, I describe the detection of a planetary-mass candidate imaged in the Young Suns Exoplanet Survey. I developed a method to reduce the coronagraphic data of a tight stellar binary. Due to the tensions in the acceleration data, orbital fitting, spectral energy distribution fitting and radial velocity differences of the central stellar binary, there is likely an additional companion in the central stellar system. With the only detection in the H band of the candidate and unknown barycentre of the central stars, the nature of the candidate cannot be determined. It may represent a comoving planet, a free-floating brown dwarf, or a background object with unusually high proper motion. If confirmed as bound, it would be a 3–5 $M_{\rm J}$ planet at a separation greater than 700 au, challenging current theories of giant planet formation.

In Chapter 5, I present the preliminary results of a photometric and multiplicity survey of brown dwarfs and planetary-mass objects in the Taurus star-forming region using the Hubble Space Telescope. Using a dedicated photometric technique based on the combination of colours from multi-band photometry and the point spread function fitting technique, I search for companions and analyse multiplicity in this population. I find a low binary fraction among young planetary-mass objects in Taurus, suggesting that the formation of wide-orbit planetary-mass binaries is inefficient and the disruption of the binaries likely occurs at the early stage of their formation.

Lay Summary

Brown dwarfs bridge the gap between stars and planets. Unlike stars, they are not massive enough to fuse hydrogen in their cores. Instead, they gradually release energy as they contract under their own gravity, cooling as they age. Planetary-mass objects, including free-floating objects and comoving companions, are less massive than brown dwarfs and also cool with time. Both brown dwarfs and planetary-mass objects are substellar objects, and they are closely related to each other in terms of formation and evolution. Studying them gives us insight into the wide variety of worlds that exist beyond our Solar System.

Most exoplanets are discovered indirectly, by looking at the effect they have on stars, rather than by seeing them directly. To date, only about 40 exoplanets have been directly imaged. Imaging a planet is extremely difficult because planets are much fainter than their stars, similar to trying to spot a glowworm flying next to a lighthouse from space. Sophisticated techniques have been developed to directly image exoplanets. Young gas giant planets are bright and therefore easier to image than smaller and older planets. Free-floating planetary-mass objects are gas giant analogues as they share similarities in temperature, spectral type, and atmosphere. There is a rich population of isolated brown dwarfs and planetary-mass objects discovered from various surveys. They provide a natural alternative: because they are not outshone by nearby stars, they allow us to study planetary atmospheres in detail.

Despite 30 years having passed since the first discovery of brown dwarfs and planets, our knowledge of these substellar objects is still quite limited. A lot of questions remain about how they form and how they evolve. While each object is unique, focusing too narrowly on individual objects will make us not see the forest for the trees. Population studies, on the other hand, allow us to see the bigger picture, uncovering the key factors that shape their formation and atmospheres.

In this thesis, I present a series of imaging surveys of young planets and brown dwarfs. These studies advance our understanding of their atmospheres and how they form, helping us test theoretical models with real observations. In Chapter 2, I monitored young, low-mass objects for changes in brightness as they rotate. These variations reveal weather patterns and complex structures in their atmospheres. I find that young, low-gravity objects are more likely to show variability than older ones, suggesting that gravity strongly affects their atmospheric structure.

In Chapter 3, I report the first results of a direct imaging survey searching for wide-orbit planets in the Fornax-Horologium association. With a dissolving dense cluster at its centre, this young association can serve as a cornerstone in studying wide-orbit planet formation and evolution. I discovered an object near the boundary between stars and brown dwarfs with a high orbital eccentricity, which shows evidence of past gravitational interactions. This study sheds light on how the environments of star clusters influence the formation of wide-orbit planets.

In Chapter 4, I describe a planetary-mass candidate discovered from the Young Suns Exoplanet survey. I demonstrate the challenge of confirming an extremely wide-orbit low-mass planet candidate around a non-single star system.

In Chapter 5, I provide a photometric and multiplicity study of young brown dwarfs and planetary-mass objects in the Taurus star-forming region. I constrain a low binary fraction for planetary-mass objects in a young and low-density environment. This work finds that wide-orbit planetary-mass binaries are rare at young ages, putting constraints on the formation mechanisms of planetary-mass binaries.

Together, these projects provide new insights into the diversity of substellar objects, their atmospheric structures, and the environments in which they form. They bring us closer to understanding the origins of planets and brown dwarfs, and, more broadly, the variety of planetary systems that exist in our galaxy.

Declaration

I declare that this thesis was composed by myself, that the work contained herein is my own except where explicitly stated otherwise in the text, and that this work has not been submitted for any other degree or professional qualification except as specified.

Chapter 2 was published in Liu et al. (2024).
Chapter 3 consists of sections that have been published in Liu et al. (2025a).
Chapter 4 was published in Liu et al. (2025b).

I used ChatGPT to check grammar and spelling in this thesis.

(*Pengyu Liu, August 2025*)

Acknowledgements

Reaching this stage has been anything but easy. As the first in my family to attend university and coming from an environment where astronomy was always misunderstood as meteorology until I stepped into university, I often felt isolated and unsure of my path. This journey would not have been possible without the support and kindness of so many people along the way, to whom I owe my deepest gratitude. First of all, I would like to thank my supervisor, Beth Biller, who is always supportive and positive about my work and decisions. I really appreciate all the encouragement and freedom she gave me, enabling me to explore various ideas and to travel to Chile three times for observations during my PhD. I also want to thank Matthew Kenworthy for being my secondary supervisor and offering help when I needed. I am indebted to my collaborators, whose generosity and expertise enriched this thesis. In particular, I thank Johanna Vos, Clémence Fontanive, and Tomas Stolker for countless hours of discussion, problem-solving, and debugging together. I also want to thank Jackie for working with me on the VLA proposal and observations, even during the Christmas holidays of 2022, although the project ultimately did not appear in the thesis. It has been a pleasure working with you, Ben, from my master's to my PhD, from the Netherlands to Edinburgh.

My thanks also extend to the communities at the Royal Observatory of Edinburgh and Leiden Observatory, especially my fellow PhD students, who made the two places a brilliant and vibrant environment to work. It was a gift that I have met so many of you during my doctoral studies spent in Edinburgh and Leiden. I will miss all the time we spent together in and outside of the office. I fondly remember the days, Elise, that we spent in Kyoto while attending the Protostars and Planets VII conference. I would like to thank Althea, Kevin, Xueqing, Frey, Adam, Bohan, and many others for welcoming me every time I travelled from Leiden back to Edinburgh. Special thanks go to Lukas, whose insight inspired the title of this thesis. I enjoyed the chats we had in the office, Elina. And Timo, I bet we were the two who spent the most time in this office together.

Beyond academia, I am grateful to my friends who have been a constant source of joy and strength. I thank Dazhi, who encouraged me to pursue a PhD and has consistently been willing to lend a helping hand. I thank Xinyu for collecting humorous threads and sharing them with me. I thank Sai for reminding me to

stay physically active from time to time and helping me rediscover swimming. I have not forgotten the cat Phoenix, who accompanied me during the final sprint of writing this thesis.

Finally, I would like to express my gratitude to my family. Thank you to my Mum for her optimism, to my Dad for his humour, and to my grandma for her constant words of encouragement. Their belief in me has been the foundation on which I could build this journey.

Contents

Abstract i

Lay Summary iii

Declaration v

Acknowledgements vii

Contents ix

List of Figures xv

List of Tables xxi

1 Introduction 1

1.1 Properties of brown dwarfs and planetary-mass objects 1

1.1.1 Luminosity and evolutionary models 3

1.1.2 Spectral sequence 5

1.2 Exoplanet detection 11

1.2.1 Indirect detection 11

1.2.2 Direct imaging 16

1.3 Formation pathways 23

1.3.1 Core accretion: planet formation 23

1.3.2 Gravitational instability (GI) and disc fragmentation: giant planet and brown dwarf formation 24
1.3.3 Other brown dwarf formation mechanisms 26
1.3.4 Free-floating planetary-mass object formation 26
1.3.5 Observational constraint methods 27
1.4 Direct imaging surveys 34
1.5 Atmospheric structures 36
1.5.1 Clouds 36
1.5.2 Thermal and chemical instability 37
1.5.3 Variability observations 38
1.5.4 The impact of surface gravity 42
1.6 Young free-floating planetary-mass objects as exoplanet analogues: atmospheric characterisation 43
1.7 This thesis 45
2 A near-infrared variability survey of young planetary-mass objects 49
2.1 Abstract 49
2.2 Introduction 50
2.3 Sample 52
2.4 Observations and data reduction 53
2.4.1 Observations 53
2.4.2 Raw image reduction 56
2.4.3 Aperture photometry 57
2.4.4 Light curve analysis 57
2.5 Variability analysis 58

2.6 Sensitivity calculation 61
2.6.1 Significant detections 62
2.6.2 Variable candidates 68
2.6.3 Non-detections 71
2.7 Statistical analysis 72
2.7.1 Statistical formalism 75
2.7.2 Variability occurrence rates of field and young L and T dwarfs ... 78
2.7.3 Variability occurrence rates at and outside the L/T transition ... 79
2.8 A census of variable objects 82
2.9 Colour of young L and T objects 86
2.10 Conclusions 89

3 A direct imaging survey of wide-orbit exoplanets in the Fornax-Horologium association 91

3.1 Abstract 91
3.2 Introduction 92
3.3 Sample selection 94
3.4 Observations and data analysis 96
3.5 Results of the HD 24121 system 97
3.5.1 Astrometry 97
3.5.2 Photometry 99
3.5.3 Orbital fitting 100
3.5.4 Companion mass estimation 104
3.6 Discussions and conclusions of the system 105

3.7 Other Candidates 107

3.7.1 Very low-mass stellar companion: UCAC2 10099995B 107

3.7.2 Wide-separated candidate companions detected in Gaia DR3 108

4 A planetary-mass candidate imaged in the Young Suns Exoplanet Survey 115

4.1 Abstract 115

4.2 Introduction 116

4.3 Observations and data reduction 118

4.3.1 SPHERE observations and data reduction 118

4.3.2 MagAO-X observations and data reduction 122

4.3.3 MagAO-X/VIS-X observations and data reduction 123

4.4 Stellar properties 124

4.4.1 Acceleration 124

4.4.2 Orbital fitting 125

4.4.3 SED fitting 128

4.4.4 Radial velocity 129

4.4.5 Possibility of the third companion 131

4.4.6 Mass and age estimation 133

4.5 The planetary-mass candidate 133

4.5.1 Photometric analysis 135

4.5.2 Astrometric analysis 136

4.5.3 Colour-magnitude diagram 138

4.6 Discussion 139

4.6.1 A co-moving planet or free-floating object 139

4.6.2 Group membership 144

4.7 Summary 145

5 A photometric and multiplicity study of young brown dwarfs and planetary-mass objects in the Taurus star-forming region 147

5.1 Abstract 147

5.2 Introduction 148

5.3 Observations 150

5.3.1 Sample selection 150

5.3.2 HST observations 151

5.4 Photometric analysis 153

5.4.1 Aperture photometry 155

5.4.2 PSF fitting 155

5.4.3 Primary masses 156

5.5 Multiplicity analysis 159

5.5.1 Companion search 159

5.5.2 Artificial star tests 160

5.5.3 Survey completeness 161

5.5.4 Binary frequency 164

5.6 Discussion 167

5.6.1 Binary frequency in Taurus and Upper Scorpius 167

5.6.2 Binary frequency as a function of age 169

5.7 Conclusion 171

6 Conclusions 173

6.1 Summary 173

6.1.1 Chapter 2 173

6.1.2 Chapter 3 174

6.1.3 Chapter 4 175

6.1.4 Chapter 5 176

6.2 Outlook 177

6.2.1 Atmospheric structures 177

6.2.2 The relation between stellar environment and giant planet formation 178

6.2.3 Sub-Jupiter planets, small separations, and cold systems 179

A Appendix of Chapter 2 183

A.1 Reference stars and MAD-magnitude plots 183

A.2 Potentially variable light curves 198

A.3 Non-variable light curves 202

B Appendix of Chapter 4 225

B.1 Central star images 225

B.2 Posterior distribution of SED fitting for the central two stars 226

B.3 Radial velocity injection test 227

B.4 Relative astrometry of all sources 228

Bibliography 229

List of Figures

1.1 Luminosity versus age 4

1.2 Colour-magnitude diagram of M, L, T and Y dwarfs..... 6

1.3 NIR spectra of field brown dwarfs 8

1.4 NIR spectra of young brown dwarfs 9

1.5 ADI working schematic..... 21

1.6 SDI working schematic 22

1.7 PDS 70 system 31

1.8 Multiplicity versus primary mass..... 33

1.9 Condensation curves of various species 38

1.10 Spectral type and colour diagram of variable L and T dwarfs..... 43

2.1 β factor against the photometric error of detrended light curves 60

2.2 Image of 2M1119-1137AB..... 61

2.3 Observation and detection diagram in the J_S band 63

2.4 Light curves of J0819-0335..... 65

2.5 Variable target 2M1119-1137AB..... 66

2.6 Variable light curve of 2M1119-1147AB 67

2.7 Variable target W1147-2040..... 69

2.8 Variable target J2323-0152 70

2.9 Spectral distribution of brown dwarfs included in the statistical analysis 74

2.10 Average sensitivity maps 75

2.11 Spectral type against $(J - K_S)_{2MASS}$ colour of variable objects from the four surveys 76

2.12 Probability density function of variability rate of the field and young samples 80

2.13 Probability density function of variability rate for L and T spectral types 80

2.14 Probability density function of variability rate at the L/T transition and outside the L/T transition 82

2.15 Spectral type distribution of known young and field variables in the J band from the literature 86

2.16 Peak-to-peak amplitude in the J band versus spectral type of known young and field variables from the literature 87

2.17 Spectral type and colour plot of young objects 88

3.1 HD 24121B coronagraphic image 97

3.2 Common proper analysis of HD 24121B 99

3.3 SED fitting of HD 24121 101

3.4 SED fitting of HD 24121B 102

3.5 Orbital fitting of HD 24121B 103

3.6 Orbital velocity in epoch 2016.0 104

3.7 Evolutionary tracks of low-mass stars and brown dwarfs. 105

3.8 SED of UCAC2 1009995B 109

3.9 Orbital fitting of UCAC2 1009995B 110

3.10 Wide-separated candidate companions of FH, SHINE, and K-type stars in Sco-Cen 112

4.1 Image of 2M1006 122
4.2 Posterior distributions of orbital parameters 127
4.3 Orbits of the candidate 128
4.4 SED fitting of the central star system 129
4.5 MagAO-X/IFU data of the binary 131
4.6 Age estimation of 2M1006 135
4.7 Images of the candidate in five epochs of H, $J23$, $K12$, and K_S bands 136
4.8 Relative astrometry of the candidate 138
4.9 Colour-magnitude diagram of brown dwarfs 139
4.10 Proper motion and parallax posterior distribution of the candidate assuming free-floating 141
4.11 Proper motion of the candidate assuming free-floating 142
4.12 Probability ratio of the candidate assuming free-floating to bound 143
5.1 Taurus extinction map 151
5.2 $Q_{\rm HST}$ of primary sources 158
5.3 $Q_{\rm HST}$ of detected sources around WBIS2204+1536 159
5.4 An example of well-recovered and poorly-recovered artificial stars 161
5.5 Average completeness map of this survey 163
5.6 Average completeness maps in different physical units 165
5.7 Binary frequency of this survey 167
5.8 Binary frequency in Taurus and Upper Sco 169
5.9 Binary frequency as a function of primary mass 170
6.1 Planets detectable by Gaia DR4 180

6.2 Minimum detectable companion at a distance of 100 pc and 25 pc by Gaia DR4 180

A.1 Targets and their selected reference stars 184

A.2 Potentially variable light curves of 2M1553+1532 199

A.3 Potentially variable light curves of W1147-2040 200

A.4 Potentially variable light curve of J0226-1610 201

A.5 Non-variable light curves of a variable object 2M1119-1137AB 203

A.6 K_S-band non-variable light curves of a variable object 2M1119-1137AB 204

A.7 Non-variable light curves of variable objects 2M1119-1137AB and J0819-0335 205

A.8 Non-variable light curves of a variable object W1147-2040 206

A.9 Non-variable light curves of a variable object 2M1552+1532 207

A.10 Non-variable light curves of a variable object J2323-0152 208

A.11 Non-variable light curves of a variable candidate J0226-1610 210

A.12 Light curves of a non-variable object J0044+0228 212

A.13 Light curves of a non-variable object J0200-5105 213

A.14 Light curves of non-variable objects J0207+0000 and J2255-3118 216

A.15 Light curves of a non-variable object J0241-3653 217

A.16 Light curves of non-variable objects J0758+2225 and J0819+2103 218

A.17 Light curves of non-variable objects J1316+0312 and J0437-5509 219

A.18 Light curves of a non-variable object PSO168-27 220

A.19 Light curves of a non-variable object WISEJ1636-0743 221

A.20 Light curves of a non-variable object SDSS1521+0131 223

B.1 Images of the central stars from 2018-11-15 to 2024-03-23 225

B.2 Posterior distributions of the SED fitting parameters for the central stars 226

B.3 Injection test for radial velocity measurements in VIS-X IFU data 227

B.4 Relative astrometry all sources 228

List of Tables

2.1 Object information 54

2.2 Observation summary 55

2.3 Detected variables 62

2.4 Brown dwarfs included in the statistical analysis 74

2.5 Variability rates of field and young objects in the near-infrared and mid-infrared 83

2.6 Variable brown dwarf detections in the literature 84

3.1 Target list of the FH survey 95

3.2 Properties of HD 24121 AB system 98

4.1 Observation summary of 2M1006 119

4.2 Astrometry error budget of the central binary and the candidate 121

4.3 Astrometric and photometric measurements of the fainter star relative to the primary star 126

4.4 2M1006 stellar parameters 134

4.5 Photometric measurements of the candidate 137

4.6 Astrometric measurements of the candidate 138

5.1 Taurus target infomation 152

5.2 HST observation summary. 154

5.3 HST photometry of the targets 157

5.4 Photometry and mass of the targets 172

Chapter 1

Introduction

The starry night sky has long inspired mystery and curiosity in human beings. Across cultures, observers recorded the sky and developed various systems and myths to explain what they saw. Among the countless stars, people identified a class of celestial objects that moved noticeably against the background stars. These objects were named planets, from the ancient Greek word meaning 'wandering bodies'. They are the planets in our Solar System. Nowadays, thousands of planets outside of the solar system (exoplanets) have been discovered, along with brown dwarfs. They are substellar objects with masses smaller than stars. Understanding their formation and atmospheric properties is a fundamental goal of modern astronomy, particularly because some of these objects may host habitable worlds capable of supporting life.

1.1 Properties of brown dwarfs and planetary-mass objects

Brown dwarfs and planetary-mass objects share many similarities in terms of mass, temperature, composition, surface gravity, and even the time of their first discovery. Brown dwarfs are a type of celestial object that is too cool to ignite hydrogen fusion in its core but relies on electron degeneracy to resist gravitational contraction, whose existence was predicted as early as 1963 (Kumar, 1963; Hayashi & Nakano, 1963). Although GD 165B was the first strong brown dwarf candidate (Becklin & Zuckerman, 1988), the first unambiguous detection

of a brown dwarf is Gliese 229B in 1995 (Nakajima et al., 1995), which recently turned out to be an equal-mass brown dwarf binary (Xuan et al., 2024). Just weeks apart, the first exoplanet orbiting a sun-like star was also discovered, 51 Peg b (Mayor & Queloz, 1995). Since then, there has been an outbreak of detections of substellar objects including brown dwarfs and planets, resulting in a new and fast-developing field of astronomy. The typical mass range of brown dwarfs is from $13\,M_{\rm J}$ to $75\,M_{\rm J}$, where the lower limit is from the theoretical deuterium burning mass limit (Burrows et al., 2001), distinguishing between brown dwarfs and planets, and the upper limit is from the theoretical hydrogen burning mass limit (Chabrier & Baraffe, 2000), distinguishing between brown dwarfs and stars. While this classification by mass is straightforward, it is not practical as it has been found that the hydrogen burning limit depends on metallicity and the deuterium burning limit also depends on metallicity, helium abundance and deuterium abundance (Chabrier & Baraffe, 1997; Spiegel et al., 2011). This results in no clear division in evolutionary tracks between massive brown dwarfs and stars or low-mass brown dwarfs and planets (Burrows et al., 2001).

Burrows et al. (2001) suggested to distinguish brown dwarfs and planets by their formation as brown dwarfs were thought to be born star-like, while planets were thought to be formed in protostellar discs by that time. This dichotomy is challenged by the discovery of wide-orbit giant planets and free-floating planetary-mass objects, which are likely formed similarly to brown dwarfs. Some directly-imaged exoplanets have masses over $13\,M_{\rm J}$, but they are still referred to as 'planets', such as HIP 99770b (14–$16\,M_{\rm J}$, Currie et al., 2023). Therefore, there is no simple criterion to distinguish brown dwarfs and planets. It needs to be discussed case by case for objects that fall into the boundary between planets and brown dwarfs, and brown dwarfs and low mass stars. Instead, it has been found that brown dwarfs and planetary-mass objects share many similarities, such as spectral type, temperature, and radius. I use the term 'planetary-mass objects' in this thesis to refer to celestial objects that have masses comparable to planets in a sensible range, e.g.$<25\,M_{\rm J}$. This wide mass range considers the uncertainty of the estimated mass by photometry. The planetary-mass objects include free-floating objects and gravitationally bound companions as long as their masses are comparable to 'planets', such as brown dwarfs below $\sim25\,M_{\rm J}$ and directly imaged exoplanets. Given the overlap and similarity between brown dwarfs and planetary-mass objects, we introduce their properties together.

1.1.1 Luminosity and evolutionary models

The luminosity of low-mass stars, brown dwarfs and planets as a function of age is shown in Fig. 1.1. The evolutionary tracks are calculated from evolutionary models: BCAH15 (Baraffe et al., 2015) and ATMO (Chabrier et al., 2023). For objects with masses $<0.2\,M_{\odot}$, they initially cool and dim over time. Stars' luminosity stays stable when they begin to ignite hydrogen burning, and the hydrogen burning limit determined from BCAH15 models is about $0.07\,M_{\odot}$. For brown dwarfs, while they cool almost their whole lifetime, there is a plateau in their luminosity at early times between 1 Myr and 100 Myr, which is due to deuterium burning. Depending on the mass, the heavier the brown dwarfs, the earlier they begin and end deuterium burning. Moreover, this causes a non-monotonous region in luminosity versus mass for planetary-mass objects. Generally, at a given age, the heavier the objects, the brighter they are. However, for objects between $0.013\,M_{\odot}$ and $0.02\,M_{\odot}$ in ages between 10 Myr and 150 Myr, lighter objects undergoing deuterium burning may actually be brighter than heavier objects that have already completed their deuterium burning stage. VHS J125601.92-125723.9AB b (VHS1256-1257 b) is this kind of object whose mass is either $11\,M_{\rm J}$ or $16\,M_{\rm J}$ with an age of 140 ± 20 Myr which is well determined from the cooling of the host low-mass stellar binary (Dupuy et al., 2023; Miles et al., 2023). The deuterium burning limit determined from ATMO models is about $0.013\,M_{\odot}$. For planets smaller than $0.013\,M_{\odot}$, they cool roughly at a consistent rate throughout their whole lifetime. Therefore, to derive precise mass from luminosity, not only the luminosity but also the age of substellar objects needs to be well-constrained.

There are about a dozen evolutionary frameworks to depict brown dwarfs and planetary-mass objects. Burrows et al. (1997) developed a theory with non-gray body assumption for objects from $0.3\,M_{\rm J}$ to $70\,M_{\rm J}$, covering effective temperature $T_{\rm eff}$ between 100 K and 1300 K, one of the first attempts to predict the luminosity and atmospheres of brown dwarfs and planets. After that, more sophisticated models have emerged. For instance, Baraffe et al. (2003) developed the COND models for cool and cloud-free atmospheres, covering $T_{\rm eff}$ between 100 K and 3000 K. Chabrier et al. (2000); Baraffe et al. (2002) developed the DUSTY models to include dust opacity in the photosphere, better for objects with ages < 100 Myr and $T_{\rm eff} > 1300$ K. Allard et al. (2012, 2013) developed the BT-Settl models that include cloud formation and settling, with improved opacities and mixing, which applies to a very wide range of substellar objects. Marley et al. (2021) developed

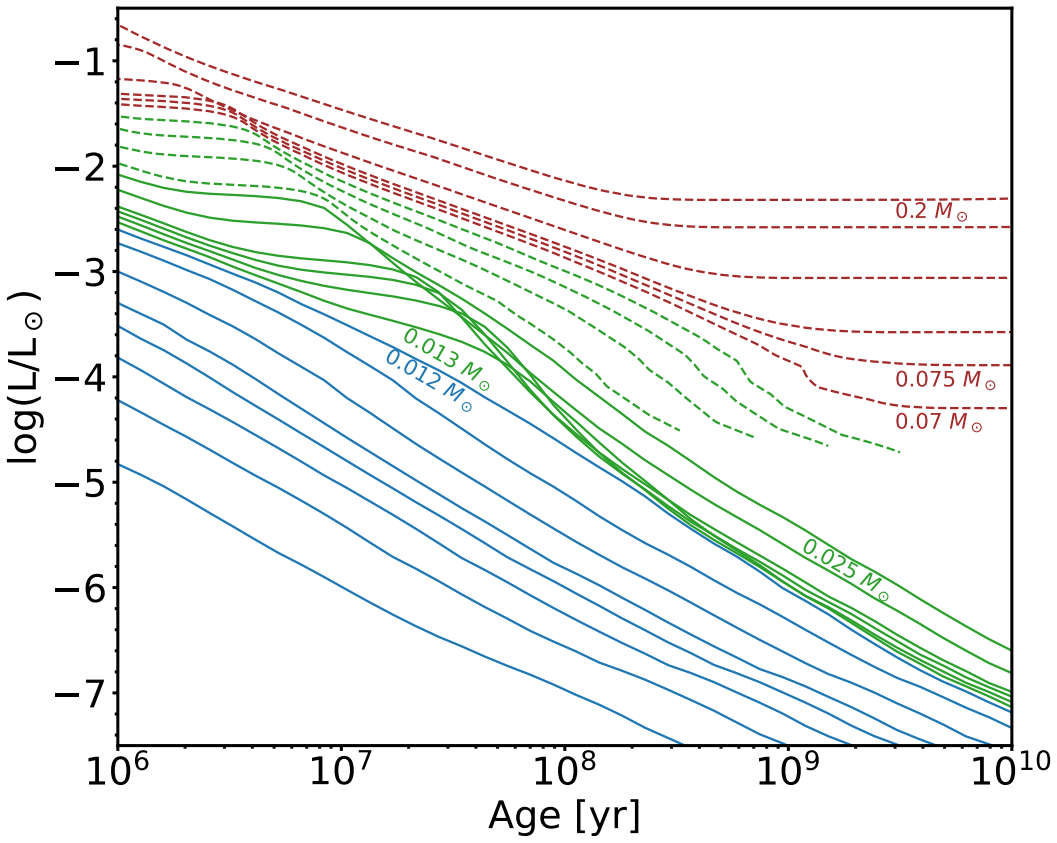


Figure 1.1: Luminosity versus age of substellar objects. The dashed lines are BCAH15 models (Baraffe et al., 2015) and the solid lines are ATMO models (Chabrier et al., 2023). The evolutionary tracks for low mass stars are the brown region, for brown dwarfs are the green region, and for planets are the blue region.

the Sonora-Bobcat models for cold planets, which are expanded to several Sonora models later for different types of objects, including Diamondback for cloudy objects between 900 and 2400 K (Morley et al., 2024) and Elf Owl for cloud-free objects between 275 and 2400 K with disequilibrium chemistry (Mukherjee et al., 2024), replacing the Cholla (Karalidi et al., 2021). Tremblin et al. (2015, 2016) utilised the radiative and convective equilibrium code ATMO to include non-equilibrium chemistry and thermal instabilities in the modelling of brown dwarfs and planets. Then Phillips et al. (2020) extended it to the cloudless ATMO2020 models for cool objects below 2000 K and Chabrier et al. (2023) updated the ATMO models with the latest equation of state for the mixture of hydrogen and helium. These models have their own applicable temperature ranges, respectively, due to the sources of opacity and atmospheric thermal gradients. Some of them include cloud formation and setting, or non-equilibrium chemistry. Therefore, while there are many evolutionary models for sub-stellar objects to choose from, they should be rationally selected based on the age, temperature, dust, cloud cover, and chemistry of the object under study. We can measure fundamental properties of exoplanets and brown dwarfs by combining observations and evolutionary models.

1.1.2 Spectral sequence

The spectral type (SpT) of a star conveys its rough temperature and luminosity. The spectral types OBAFGKM cover the full range of stellar spectral types with 'O' representing the hottest stars of $T_{\rm eff}$ over 30,000 K and 'M' representing the coolest stars of $T_{\rm eff}$ below 3700 K. A number of objects with cooler spectral classes than M were discovered from the 2-Micron All-Sky Survey (2MASS) Prototype Cameras and the Deep Near-Infrared Sky (DENIS) survey in the 1990s, leading to the establishment of a new spectral type 'L' (Kirkpatrick et al., 1999). To date, the observed brown dwarfs and planetary-mass objects have spectral types spanning between late-M, L, T and Y as shown in Fig. 1.2. As they evolve with time, their spectral types also evolve from early to late types, distinct from stars, which reach a certain spectral type on the main sequence and stay there for millions or billions of years. Figure 1.3 presents a sequence of near-infrared spectra of field brown dwarfs from M6 to T8, and Fig. 1.4 presents a sequence of near-infrared spectra of young dwarfs from M6 to T5.

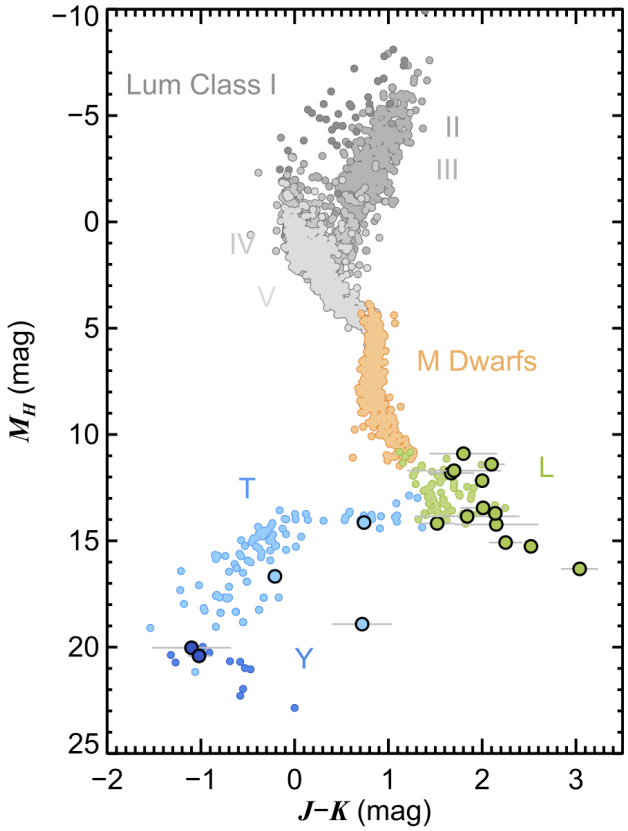


Figure 1.2: Near-infrared colour-magnitude diagram of objects from M to Y spectral types. Markers with black circles are directly imaged exoplanets. In the L/T transition, the near-infrared colour suddenly becomes bluer with roughly constant luminosity. The directly imaged planets are shown by the bold circles with redder colour than the same spectral type brown dwarfs. The figure comes from Bowler (2016a).

M dwarfs

When brown dwarfs are young, they keep high temperatures and therefore can have late-M spectral types, spanning between M6 and M9.5 with $T_{\rm eff}$ between ~2800 K and ~2300 K. Those objects are usually found in young star-forming regions, such as Taurus (Kenyon et al., 2008), Ophiuchus (Motte et al., 1998), and the Orion Nebula Cluster (Hillenbrand, 1997). Molecular absorption bands due to TiO and VO are prominent in the red optical spectra: the first one weakens toward M9 while the latter strengthens from M7 (Kirkpatrick et al., 1991). FeH absorption increases from M6 to M8 and gradually starts to fade in M9 in red optical and near-infrared, while H_2O begins to appear in the near-IR at 1.4 μm and becomes much stronger at M9.5 (Cushing et al., 2005). Neutral alkali lines such as Na I and K I are prominent in both optical and near-infrared (J band) (Allers & Liu, 2013). The $J - K_S$ colour becomes redder from M6 to M9.5.

L dwarfs

From L0 to L9.5, L dwarfs' $T_{\rm eff}$ changes from ~2500 to ~1300 K and their spectra features evolve dramatically from dwarfs, coming with the formation of condensate clouds and changing molecular chemistry. For young, low surface gravity L dwarfs, their $T_{\rm eff}$ are 200–300 K cooler than the above range, compared to the field L dwarfs (Liu et al., 2013; Bowler et al., 2013; Allers et al., 2016). In the optical band, early L dwarfs have a mix of atomic and molecular features, including neutral alkali lines, TiO and VO. As the spectral type goes to mid-L, the Na I and K I lines become very strong while the TiO and VO become weaker and disappear by L2–L3 (Kirkpatrick, 2005). In the near-infrared bands, L dwarfs present prominent molecular features. In J and H bands, FeH absorption is strong in early L and weakens by L5–L6, while H_2O absorption is very strong and strengthens to L9.5 (Cushing et al., 2005). H_2O and CO dominate the features in K band and persist across the L sequence. The $J - K_S$ colour becomes redder from L0 to L5–L6, changing from ~1 to ~2 mag. From mid-L to late-L, the $J - K_S$ colour changes the reddening trend to blueward, starting the L/T transition.

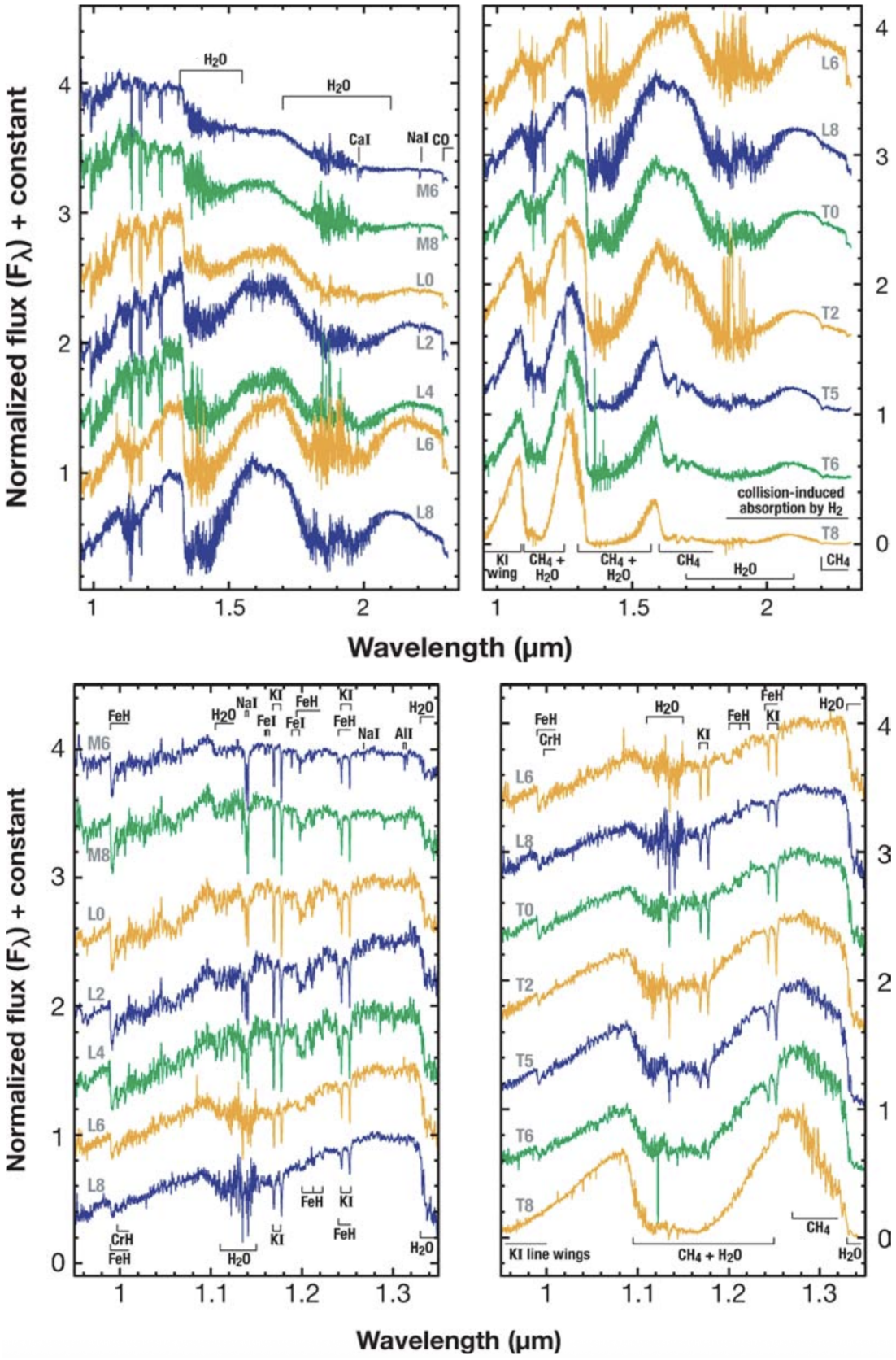


Figure 1.3: Near-infrared spectra of field dwarfs from M6 to T8. Figure adapted from Kirkpatrick (2005).

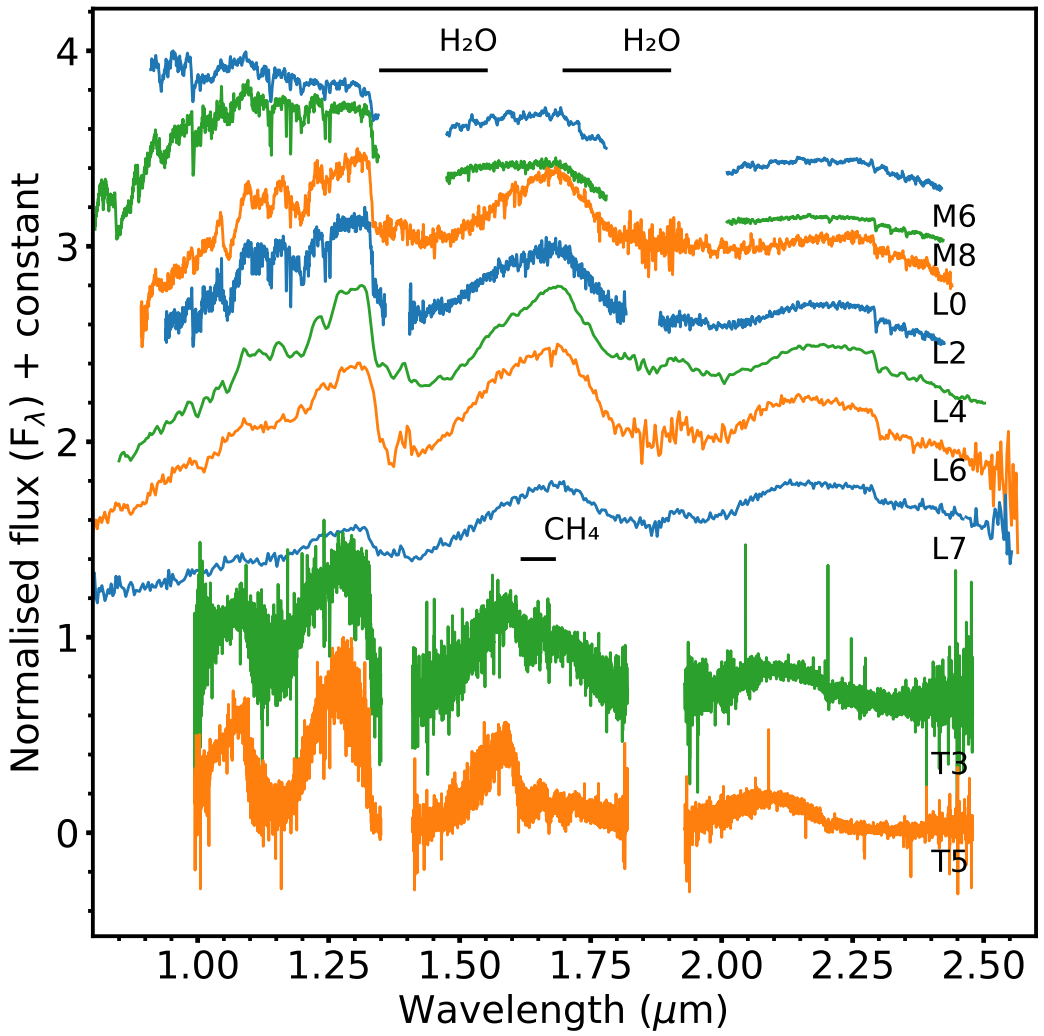


Figure 1.4: Near-infrared spectra of young dwarfs from M6 to T5. Reduced spectra come from the Montreal Spectral Library (https://jgagneastro.com/the-montreal-spectral-library/), Piscarreta et al. (2024), and Beiler et al. (2023).

L/T transition

This is a prominent feature in the near-infrared colour-magnitude diagram of L and T dwarfs that $J - K_S$ colour abruptly becomes bluer by ~2 mag while H magnitude keeps roughly the same. The Y and J magnitudes increase by ~0.7 and ~0.5 mag, respectively (Dupuy & Liu, 2012). This transition covers from mid-L to mid-T where $T_{\rm eff}$ stays roughly the same at 1400 ± 200 K (Kirkpatrick, 2005). For low surface gravity objects, L/T transition occurs at $T_{\rm eff}$ ~200 K cooler (e.g. Metchev & Hillenbrand, 2006; Dupuy et al., 2009; Zhang et al., 2020). CH_4 features begin to appear in mid-L dwarfs, marking the onset of the reaction $CO + 3\,H_2 \longrightarrow CH_4 + H_2O$ (Kirkpatrick, 2005). CH_4 absorption at 3.3 μm is detected as early as in an L5 dwarf, 2MASSW J1507476-162738 (Noll et al., 2000), while the absorption at 1.6 μm and 2.2 μm is detected in later type L dwarfs. There is no clear definition of the spectral sequence range L/T transition. It was referred as L7–T4 (Golimowski et al., 2004) or L9–T3.5 (Radigan et al., 2014) some times in practical terms.

T dwarfs

T dwarfs have $T_{\rm eff}$ from ~1300 to ~500 K with ~100 K cooler for low surface gravity objects (Gagné et al., 2018a; Zhang et al., 2020). Neutral alkali lines such as Na I and K I are still strong in the optical band across the T sequence. H_2O absorption continues strengthening in the near-infrared. A prominent feature of T dwarfs is the strong absorption of CH_4 at 1.6 μm, 2.2 μm, and 3.3 μm. NH_3 absorption in 6–12 μm begins to emerge in late-T dwarfs (Roellig et al., 2004). The $J - K_S$ colour continues to move blueward until late-T types.

Y dwarfs

Y dwarfs have $T_{\rm eff}$ below ~500 K (Cushing et al., 2011). Detailed spectral classification has only been made until Y2 with the later spectral types remaining unestablished (Beichman et al., 2013; Schneider et al., 2015). The coldest brown dwarf observed to date is WISE J085510.83-071442.5 with $T_{\rm eff}$ = ~285 K, classified as a late-Y dwarf, which is only 2 pc from the Sun (Luhman, 2014). The coolest exoplanets imaged to date have similar low temperatures: Esp Indi Ab (~275 K Matthews et al., 2024), TWA 7b (~320 K, though still a candidate Lagrange et al.,

2025), and 14 Her c (275–300 K Bardalez Gagliuffi et al., 2025b). Y dwarfs emit half of their energy in the mid-infrared beyond 4 μm. CH_4 and H_2O absorption in the near-infrared and mid-infrared are very strong. NH_3 absorption is now a prominent molecular absorption feature. Similar to L/T transition, there is also T/Y transition, marking the onset of NH_3 absorption and narrowing the flux in the near-infrared. With a spectral type of T9.5±0.5, COCONUTS-2b is a cool planetary-mass object at the T/Y transition (Zhang et al., 2025).

1.2 Exoplanet detection

Past imaging surveys in the red optical and infrared have discovered over 4,000 ultracool dwarfs within 100 pc, according to the UltracoolSheet[1]. While the detection of free-floating ultracool dwarfs is straightforward, the detection of exoplanets is tremendously more challenging due to their proximity to their host stars. Multiple methods have been developed to detect exoplanets, and they can be divided into indirect methods and direct detection.

1.2.1 Indirect detection

Indirect techniques make use of the signal change of the primary stars to infer the existence of orbiting planets. Indirect techniques include radial velocity, transit light curve, microlensing, pulsar timing variations, and astrometry. As of July 2025, nearly 6,000 exoplanets have been discovered, with the majority discovered through indirect detections, primarily radial velocity and transit methods.

Radial velocity

The principle of radial velocity is that a planet and its host star orbit around the barycentre of the system. This movement of the star results in a periodic Doppler shift in the star's spectrum, which is several orders of magnitude brighter than the planet's spectrum. By monitoring line shifts in stellar spectra, the first exoplanet orbiting a sun-like star was discovered by this method with a precision of ~13 m s^{-1}, 51 Peg b (e.g., Mayor & Queloz, 1995). About 1100 exoplanets have been detected so far by this method, according to the NASA Exoplanet

[1] https://zenodo.org/records/15802304

Archive[2]. The method can characterise the orbital period and the lower limit of the planet's mass, or even the mass once the orbital inclination is measured by other methods. Radial velocity is most sensitive to massive planets at close separations, which would cause a strong signal in stellar spectra, leading to a fruitful discovery of hot Jupiters, together with other types of planets, such as cold gas giants at long orbits. Popular facilities such as High Accuracy Radial velocity Planet Searcher (HARPS) and HARPS-N (Pepe et al., 2004; Lo Curto et al., 2015; Cosentino et al., 2014) can achieve a precision of 1 m s^{-1}, sensitive to Jupiter-like planets. The most powerful instrument to date, Echelle SPectrograph for Rocky Exoplanet and Stable Spectroscopic Observations (ESPRESSO), which can combine the four 8m unit telescopes (UT) of the Very Large Telescope (VLT), can achieve a precision of 0.2 m s^{-1} and aims to achieve 0.1 m s^{-1} in single UT mode, which is required to detect Earth-like rocky planets (Pepe et al., 2021). Stellar activity is the main limitation for this method, especially at a level below 1 m s^{-1} (Fischer et al., 2016). It also requires bright stars to obtain high signal-to-noise (SNR) spectra. Therefore, planets detected by this method are mainly around old and quiet stars.

Transit

The transit method utilises periodic dimming of the star brightness to infer if there is a planet transiting in front of the star (like a solar eclipse) (e.g., Henry et al., 2000). The transit depth is proportional to $\left(\frac{R_P}{R_S}\right)^2$, where R_P is the planet's radius and R_S is the star's radius, and therefore, it is most sensitive to giant planets at close orbits. This method can characterise the radius, orbital period, and inclination of the planet. About 4,400 planets have been discovered by transit to date (NASA Exoplanet Archive). The two primary planet searching instruments using this method are Kepler (Borucki et al., 2010) and TESS (Ricker et al., 2014), which are space telescopes and have high sensitivity: Kepler could achieve a transit depth of 20 parts per million (ppm) for stars with V = 12 mag over 6.5 hours and TESS can achieve a transit depth of 60–100 ppm for stars with V = 10 hours over 1 hour. For a Jupiter-Solar-like system, the dimming magnitude is on the order of 0.01 (10,000 ppm); for an Earth-Solar-like system, it is on the order of 10^{-4} (100 ppm). This method has detected various types of planets, such as Earth-size planets (e,g.TRAPPIST-1 planets, Gillon et al., 2017), Super-Earths, Sub-Neptunes, and gas giants (hot Jupiters, warm and cold giants). It

[2] https://exoplanetarchive.ipac.caltech.edu/

can also detect multi-planet systems with transit timing variations (TTV), which utilises the fact that the existence of another planet can cause small deviations in the periodic transit times of a known planet in the same system. When a planet transits in front of its star (the primary eclipse), a fraction of the starlight passes through the planet's atmosphere. Comparing the stellar spectrum during and outside of transit reveals wavelength-dependent absorption features from atmospheric atoms and molecules, which constitute the planet's transmission spectrum (e.g. Seager & Deming, 2010; Madhusudhan, 2019). When a planet passes behind its star (the secondary eclipse), its thermal emission and reflected light are temporarily blocked. By comparing the combined star+planet spectrum just before eclipse with the stellar spectrum alone during eclipse, one isolates the planet's emission spectrum (e.g. Seager & Deming, 2010; Madhusudhan, 2019). The transit spectroscopy technique is a major way to characterise exoplanets. About 150 planets are characterised by the transmission or emission spectroscopy technique (NASA Exoplanet Archive).

Microlensing

During a microlensing event, two stars temporarily align along our line of sight. The light of the background star is brightened for a short time due to the gravity of the foreground star (the lens). If there is a planet orbiting the foreground star, the lensing effect of this planet will cause an abrupt and transient distortion (a sharp spike or dip) on top of the brightened smooth light curve of the background star (e.g., Bond et al., 2004). With this method, we can measure the mass ratio between the planet and the host star and therefore the mass of the planet. It is sensitive to planets at 1–10 au from the host stars and can detect cold low-mass planets beyond the snow line, such as OGLE-2005-BLG-169b (Gould et al., 2006). This method can usually be used in all-sky surveys to search for planets and perform population studies. Over 200 exoplanets have been detected by microlensing (NASA Exoplanet Archive). Moreover, it can also detect free-floating planets that pass in front of background stars, which can cause very short microlensing events, typically hours to 1–2 days. This is another way to detect free-floating planets besides direct imaging, especially at large distances, contributing to the population study of free-floating planets (Sumi et al., 2011; Mróz et al., 2017).

Pulsar timing variations

This technique exploits the reflex motion of the host star induced by an orbiting planet, not through spectroscopy but via variations in the pulse arrival times. The host star is a pulsar, which emits radio beams from its polar regions. Its rotation is extremely stable, and as a result the radio pulses received on Earth exhibit an exceptionally high degree of regularity, with timing precision reaching the microsecond to nanosecond level. In the presence of a planetary companion, the host star orbits the system's barycentre. This motion induces periodic variations in the pulse arrival times, with pulses arriving earlier when the host star is moving towards the observer and later when it is moving away. Owing to the exceptional rotational stability of pulsars, even tiny changes in the pulse timing can be detected, making this technique sensitive to low-mass planets. The first exoplanets detected are two Earth-mass planets orbiting PSR1257+12 (Wolszczan & Frail, 1992). 8 exoplanets have been detected by this method so far (NASA Exoplanet Archive).

Astrometry

This method tracks the sky motion of a star to find the reflex stellar motion ('wobble') because of an orbiting planet. The host stars are sometimes referred to as accelerating stars. The technique requires very high precision astrometric measurement: the signal is ~0.5 mas for a Jupiter-like planet orbiting a Sun-like star at 1 au at 10 pc and ~0.3 μas for an Earth-like planet (Wright & Gaudi, 2013). The release of Gaia DR3 (Gaia Collaboration et al., 2021a) opens the era of companions detected by this method, though a few studies claimed planet detections with this method before Gaia (e.g. Muterspaugh et al., 2010). Combined with the Hipparcos catalogue (van Leeuwen, 2007), Brandt (2021) compiled a Hipparcos–Gaia catalogue of accelerating stars, which results in a number of detections of low-mass stellar and substellar companions confirmed by direct imaging. AF Lep b is one of them, the planet with the lowest mass detected by astrometry and confirmed by direct imaging, ~3.8 $M_{\rm J}$ (Franson et al., 2023; Mesa et al., 2023; De Rosa et al., 2023). About 5 planets are detected by astrometry, including Gaia-3b (Sozzetti et al., 2023) and Gaia-4b (Stefánsson et al., 2025), confirmed by radial velocity (NASA Exoplanet Archive). With the longer baseline of Gaia DR4, it will release a population of planets detected by astrometry. This method can constrain the 3D orbits of planets, combining with

radial velocity.

Besides the methods above, there are also several other indirect methods that have detected several exoplanets, such as pulsation time which is similar to pulsar timing but it utilises the time variations of stellar pulsation (e.g., Silvotti et al., 2007), and disk kinematics which detects exoplanets by studying dynamic interactions between planets and their embedded disk (Pinte et al., 2019). Though there is usually degeneracy for planet properties measured by a single technique, two or more techniques combined can break the degeneracy and constrain planet properties, including mass and orbital architecture.

1.2.2 Direct imaging

Challenges

About 40 exoplanets have been directly imaged so far, and all of them are gas giants[3]. Many of them are located more than 100 au or even over 1,000 au from their host stars. The small number of detections is due to the faintness of planets and small separations from their bright host stars, and therefore, direct imaging of exoplanets is very challenging. Light received from a planet includes reflected starlight and the thermal emission of the planet itself. For a Jupiter-Solar-like system, the contrast between the starlight reflected by the planet and the starlight is on the order of 10^{-9}, much below the highest precision we can achieve from ground-based observation so far, 10^{-6} (e.g., Hunziker et al., 2020). In contrast, young giant planets emit thermal flux in the infrared on the order of 10^{-5}–10^{-4} in contrast to host stars. Therefore, with current direct imaging facilities, we are only capable of detecting the thermal emission of young gas giants.

To resolve the planet light from the star light, direct imaging has to conquer two challenges. The first one is the high contrast between host stars and planets. The host stars usually have effective temperatures higher than 3,000 K and have flux peaks in optical bands. In comparison, the effective temperature of a young Jovian planet is 1,000–2,000 K and the flux is highest from near-infrared to mid-infrared. Therefore, near-infrared and mid-infrared are the optimal wavelength ranges for direct imaging of exoplanets. The contrast in a young Jupiter-Solar like system is on the order of 10^{-5}–10^{-4} at 2 μm and 10^{-4}–10^{-3} at 5 μm; for an Earth-Solar like system, the contrast is on the order of 10^{-10} at 5 μm. The above estimation is based on the idealised assumption: only consider the flux ratio between the planet and the star. But in reality, ground-based observations have to fight against the strong and fast-varying thermal background of the Earth. Besides, the telluric absorptions of H_2O, CO_2 and O_3 in Earth's atmosphere only leave Y, J, H, and K bands for near-infrared observation and L, M, and N bands for mid-infrared observation. These effects reduce the contrast sensitivity of ground-based observation in the infrared.

The second challenge is the requirement of high spatial resolving power. The angular separation between the Sun and Jupiter is 0.″5 at 10 pc and 0.″05 at 100 pc. The diffraction limit of a 10-meter telescope is 0.″05 at 2 μm and 0.″12

[3] https://exoplanet.eu/home/

at $5\,\mu$m, based on the Rayleigh criterion, $1.22\,\lambda/D$, where λ is the wavelength and D is the telescope diameter. The turbulence in the Earth's atmosphere strongly blurs the point spread function (PSF) and produces a full width at half maximum (FWHM) of λ/r_0, where r_0 is the coherence length known as the Fried parameter, a measure of the quality of seeing (Fried, 1966). Ground-based observation at optical and infrared wavelength ranges is seeing-limited. Seeing under moderately good conditions is usually 1" for large telescopes at world-class observatories and can go as low as 0.″4 under excellent conditions.

Because of the huge contrasts but small angular separations between planets and their host stars, young and wide-orbit giant planets are the primary type of exoplanets we can directly image so far. Currently, a combination of three main approaches has been developed to tackle the challenges of direct imaging: adaptive optics (AO) and coronagraphs are solving the problems from the instrument side and observation strategies combined with post-processing algorithms are solving the problems from the data side.

Adaptive optics

The wavefront is the surface over which a light wave has the same phase and is a plane for light arriving on Earth from a distant point source (e.g. a star). The distortions of the wavefront mainly come from two sources: one is from the Earth's atmosphere and the other is from the instrument. The wavefront of starlight distorted by the telluric atmosphere produces a blurred PSF and also many speckles resulting from small coherent regions of the stellar wavefront. Speckles have a size of $\sim \lambda/D$, where λ is the wavelength and D is the diameter of the telescope aperture, resembling planet signals. All these effects reduce the sharpness of the planet PSF, generate fake planet signals, and reduce the spatial resolution power. The wavefront distorted by the turbulence of the telluric atmosphere can be amended by the deformation of telescope mirrors. This technique is called adaptive optics (AO) and is necessary for ground-based observations to reach spatial resolution below the seeing-limit down to the diffraction limit (Babcock, 1953; Hardy, 1998). In an AO closed loop, the incoming light is split between a wavefront sensor and the science camera. A real-time computer calculates the wavefront distortion measured by the wavefront sensor and the compensation needed to adjust the deformable mirror (DM), and then the DM is controlled by actuators to flatten the wavefront. A metric to

measure the quality of PSF is the Strehl ratio (SR), the peak flux of the actual PSF to the peak flux of the perfect diffraction-limited PSF. With AO, SR can be improved from 0.3–0.4 to 0.6–0.9 at 1–3 μm. Because atmospheric turbulence evolves on a very fast time scale (e.g. milliseconds), the correction of AO depends on how fast and how accurately it can predict the distortion. Extreme AO (ExAO) is the second generation of AO systems that can have a high degree of wavefront correction centred around a bright star (Guyon, 2018). Currently, AO systems are popular on 6–10 m aperture telescopes, including the Keck AO at the Keck telescopes (Wizinowich et al., 2000), the Spectro-Polarimetric High-contrast Exoplanet REsearch (SPHERE) AO for eXoplanet Observation at VLT (SAXO; Fusco et al., 2006), the LBT AO at the Large Binocular Telescope (LBT; Esposito et al., 2010), the Subaru Coronagraphic Extreme Adaptive Optics (SCExAO; Jovanovic et al., 2015), the Gemini Planet Imager (GPI) at the Gemini South telescope (Macintosh et al., 2014), the Magellan AO system (MagAO) at the Magellan Clay telescope (Close et al., 2013) and its extreme AO upgraded version, MagAO-X (Males et al., 2016).

Coronagraphy

Back in 1939, inspired by solar eclipses, Bernard Lyot designed the first coronagraph to observe the solar corona by masking sunlight (Lyot, 1939). Facing the same high contrast problem as the corona versus the Sun, coronagraphs have been found to be extremely useful in the field of direct imaging of exoplanets. The basic principle of a coronagraph is that it can suppress the central star flux while keeping as much of the planet flux. Coronagraphs enhance star–planet contrast by blocking diffracted starlight and reduce noise by suppressing the diffraction structure. The field of coronagraphs has been evolving quickly in the past decades with various types of coronagraphs emerging (Guyon et al., 2006; Mawet et al., 2012; Ruane et al., 2018). Four important concepts in terms of coronagraph performance are: throughput, inner working angle (IWA), contrast and chromaticity. Throughput is defined as the residual planet light in the image compared to that in an observation without a coronagraph. Inner working angle is usually the smallest angular separation where the throughput of the planet light at that angular separation is larger than 50%. Contrast is the flux ratio or magnitude ratio between a planet and the host star that would be detectable as a function of separation from the star and is conventionally represented as the 5σ detection threshold, the noise in a given aperture divided by the peak flux of the

star and then multiplied by 5 (assuming the noise is Gaussian). The chromaticity describes the wavelength dependence of coronagraphs. For broadband imaging and integral field spectroscopy (IFS), it requires achromatic coronagraphs.

The original Lyot coronagraph design is a focal-plane coronagraph that blocks the majority of the starlight in the focal plane with a mask. There is also a Lyot stop in the pupil plane for the Lyot coronagraph that corrects for the diffraction pattern by removing the corresponding spatial frequencies. The design of the Lyot coronagraph is simple but very practical and is still in use today, e.g. on SPHERE. Other focal-plane coronagraphs have more complicated focal-plane masks and can change either the amplitude, the phase or both of the incoming light in the focal plane to suppress the on-axis star light, e.g. the vector vortex coronagraph (VVC, Mawet et al., 2010) and the Four-Quadrant Phase Mask coronagraph (FQPM, Rouan et al., 2000). Another type of coronagraph is the pupil-plane coronagraph that works in the pupil plane by either modifying the amplitude, phase or both with transmission masks. They form the so-called dark zone in PSFs where the starlight is significantly suppressed. The shape of the dark zone depends on the design of the coronagraph. An example is the apodizing Phase Plate (APP) coronagraph, a pupil-plane coronagraph that modifies the phase to form a 180-degree dark zone in the PSF (Codona et al., 2006; Kenworthy et al., 2007). The vector Apodizing Phase plate (vAPP) is an upgraded version of APP and is installed in multiple telescopes, such as the Enhanced Resolution Imaging Spectrograph (ERIS) on VLT (Davies et al., 2023).

Focal-plane coronagraphs and pupil-plane coronagraphs have their own advantages and disadvantages. Focal-plane coronagraphs have a theoretically high contrast but are sensitive to vibrations and have multiple optical modules. Pupil-plane coronagraphs are insensitive to vibrations and have a single optic which is easy to install. Some of them are achromatic by nature, but usually result in reduced peak flux. Some of them have a larger IWA and a smaller working field. There are also hybrid coronagraphs that have masks both in the focal plane and pupil plane. Building coronagraphs with small IWA, high contrast, and high planet throughput is crucial to discover more close-in planets with direct imaging.

Observation strategies and algorithms

Planet signals are so faint that they are hardly visible or not visible at all in the raw images obtained with AO and a coronagraph. Specially designed

observation strategies and advanced data reduction algorithms are necessary to further reveal the existence of planets from the residual starlight and other noise. The observation strategies are usually referred to as differential imaging, and there are corresponding algorithms to reduce the data. The principles of post-processing algorithms are the same: reconstruct stellar PSF and other noise models, and remove them to increase the signal-to-noise ratio (SNR) of the planet.

Angular Differential Imaging (ADI): ADI is a commonly used differential imaging technique for direct imaging of exoplanets. During the observation, the telescope derotator is switched off (pupil-tracking mode). Thus, when the telescope tracks the targeted star, the images on the detector rotate due to the sky's rotation (Marois et al., 2006). The on-axis star stays in the same position on the detector, but the off-axis object, such as a planet, rotates around the central star with the parallactic angles. The stellar PSF model can be built by taking the median of all the images. Subtracting the median image from the images will leave the planet signal in each image while removing stellar diffraction patterns. Derotating these images to align the planet position in each image and taking their median will suppress the noise and increase the SNR of the planet. Figure 1.5 demonstrates the workflow of ADI. The above reduction method is referred to as classical ADI. Many more sophisticated data reduction algorithms have been developed for ADI datasets. Locally Optimised Combination of Images (LOCI) (Lafrenière et al., 2007a) optimally builds the PSF model for each sub-region of the image by linear combination of images, and it has many variants (Lafrenière et al., 2007a; Pueyo et al., 2012). Principal Component Analysis (PCA) is another powerful method widely used in image processing. It builds the reference PSF by constructing a set of orthogonal basis vectors from the frame library (Amara & Quanz, 2012; Soummer et al., 2012). The ANDROMEDA algorithm uses a maximum-likelihood and forward-modelling approach to model the expected planet signal in images (Cantalloube et al., 2015). The TRAP algorithm is also a forward-modelling method but treats the ADI dataset as frames in a time series and reconstructs the planet signal and systematics together in a linear model (Samland et al., 2021).

Reference Differential Imaging (RDI): Instead of building the stellar PSF model from its own images, a PSF model can also be built from the PSFs of other stars taken with the same instrument. One common issue of ADI is self-subtraction, where part of the planet signal is also reconstructed in the stellar PSF and noise model and subtracted from the images. Because RDI builds a PSF model from

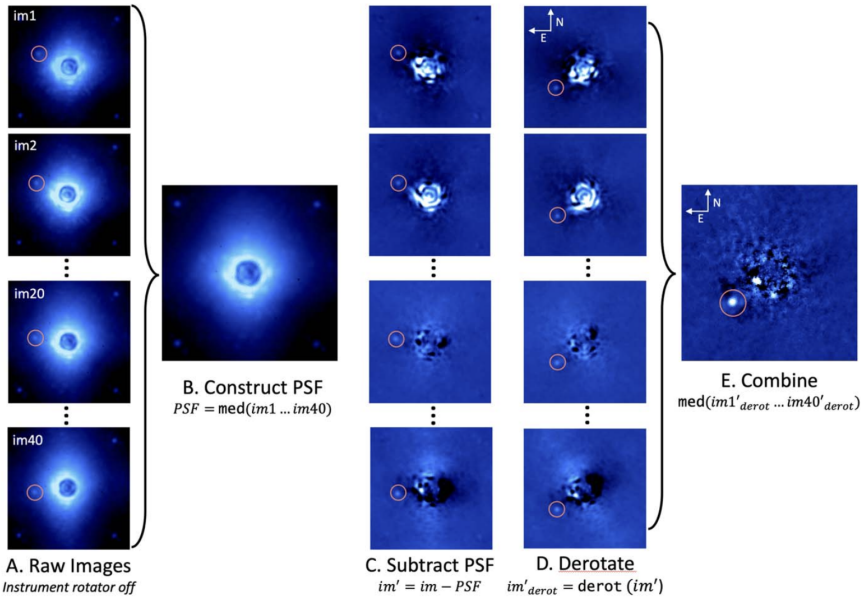


Figure 1.5: ADI working schematic. The planet is marked by the red circle. The planet moved in temporal images (A) due to the sky's rotation. Taking the median of all images in A creates a stellar PSF model in B. C shows the result of subtracting the PSF model, and D shows the results of aligning the residual images to the north. The final image in E is the median of the derotated images where the planet SNR is enhanced. Figure comes from Follette (2023): 40 GPI coronagraphic H-band images of β Pictoris b.

other stars, it can avoid self-subtraction. Ruane et al. (2019) found that RDI can improve the performance by a factor of 5 compared to ADI at small angular separations. RDI is usually applied in detecting circumstellar discs. Smith & Terrile (1984) used this method to discover the circumstellar disk around β Pictoris. PCA is usually used in RDI to build a PSF model from a reference PSF library that contains stars similar to the target star observed under comparable conditions.

Spectral/Simultaneous Differential Imaging (SDI): This technique utilises the property that the stellar PSF and speckles scale with wavelength. The diffraction structure of the central star scales as λ/D, but the planet stays in the same position in the images taken at different wavelengths simultaneously (Sparks & Ford, 2002). Hence, we can scale these images to the same wavelength and take the median or use PCA to build a PSF model. Then we can either subtract the PSF model from these scaled images and scale them back or subtract the scaled PSF model from the original images. Figure 1.6 shows the working principle of SDI. Integral field spectrograph (IFS) images are usually reduced with this technique, which can also be combined with ADI to the planet's spectra. The

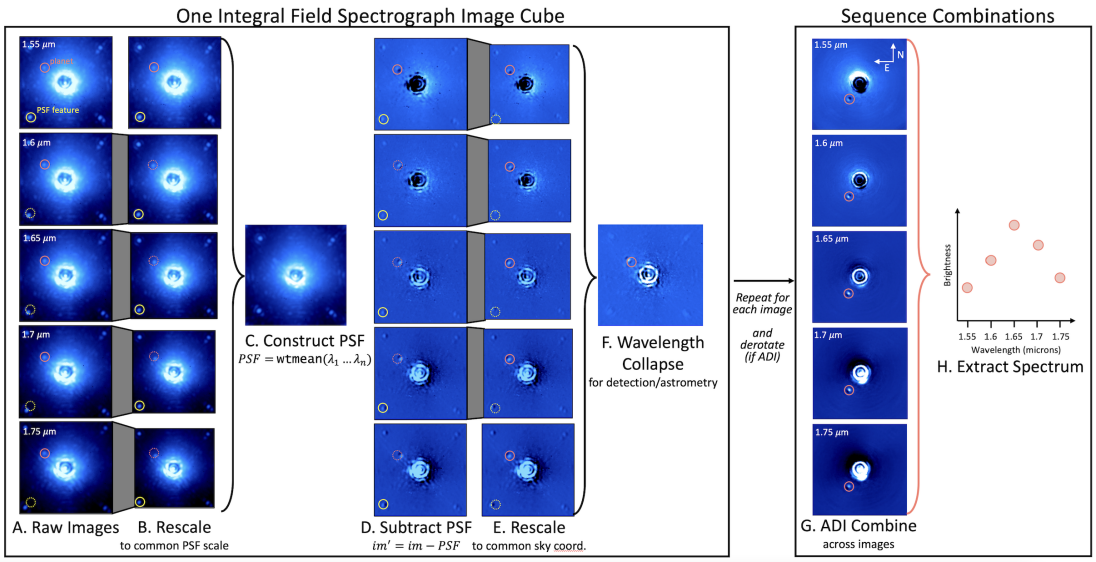


Figure 1.6: SDI working schematic. The planet is marked by the red circle. Figure comes from Follette (2023): IFS images of β Pictoris b taken by GPI in H band.

above approach does not make use of any physical spectral difference between the star and the planet. If there is a significant difference between the spectrum of a planet and its host star in the observed band, this difference can also be used in SDI to find the planet. Pioneered by Racine et al. (1999), Biller et al. (2007) conducted an SDI survey of 45 stars using the CH_4 absorption in T/Y brown dwarfs' spectra. Snellen et al. (2015) also proposed an approach to combine the high dispersion spectroscopy with SDI using cross-correlation.

Polarisation Differential Imaging (PDI): Starlight is mostly unpolarised, but the reflected starlight by planets or circumstellar discs becomes partially polarised (Stam, 2003). Then by subtracting orthogonal polarisation images, the unpolarised starlight cancels out, revealing the faint polarised signal. However, this technique is susceptible to instrumental polarisation and calibration errors. Several current high contrast imaging facilities are also able to conduct polarised observations in visible and near-infrared bands, such as SPHERE/ZIMPOL (Schmid et al., 2018), GPI (Perrin et al., 2015), and Subaru/SCExAO/CHARIS (Currie et al., 2020). This technique can be used in the future to detect the reflected light of exoplanets by direct imaging. Currently, PDI is widely used to detect circumstellar discs which scatter starlight by dust grains in their extended surface (e.g., Avenhaus et al., 2014; de Boer et al., 2016).

Besides the above techniques, there is another technique of direct imaging, which is interferometry. It combines light from multiple telescopes to detect exoplanets

using fringe patterns, such as the GRAVITY instrument on the Very Large Telescope Interferometer (VLTI) (Gravity Collaboration et al., 2017). Instead of combining light from multiple telescopes, we can use a single telescope to do interferometry, which is called Aperture masking interferometry (AMI), which uses masks inside a telescope to simulate a sparse interferometric array, improving contrast at very small separations (e.g. Tuthill et al., 2000; Sivaramakrishnan et al., 2023).

1.3 Formation pathways

The formation mechanisms of exoplanets and brown dwarfs are mainly core accretion and gravitational collapse, depending on their mass and separation from their host stars if any. Core accretion produces exoplanets at small separations, while gravitational collapse is the dominant mechanism for giant exoplanets and brown dwarfs with several sub-mechanisms operating in different environments.

1.3.1 Core accretion: planet formation

Exoplanets between a few and dozens of au around Sun-like stars are most likely formed by core accretion. In the core accretion model, micron-sized dust grains within a protoplanetary disc collide and assemble, forming larger aggregates that become kilometre-sized planetesimals. Then a rocky core is formed by the runaway accretion of solid materials. For gas giants, typically when the mass of the rocky cores reaches 5–10 $M_\oplus$, they can efficiently attract and retain a gaseous envelope from the disc via runaway gas accretion (Pollack et al., 1996). The gas accretion process should occur very early and last only a short timescale as the gas in protoplanetary discs dissipates at timescales of 1–10 Myr (Haisch et al., 2001; Fedele et al., 2010). Consequently, core accretion is more efficient in the inner and intermediate regions of the disk, where surface densities are higher. This explains the observed trend that giant planets are more commonly found around metal-rich stars, as higher metallicity enhances solid material abundance and speeds up core growth, which also supports the core accretion model (Johnson et al., 2010).

However, there is an issue for core accretion: it is challenging to grow particles beyond ~1 metre just by dust grain accretion, which is known as the metre-size barrier. This is due to two main reasons: once the solid particles grow

beyond ~1 metre, they rapidly drift inward because of the headwind they face in the discs; at 1 metre size, relative velocities between particles become high (1–10 m s^{-1}) and collisions between these solid particles lead to bounce or fragmentation instead of size growth (Blum & Wurm, 2008). To overcome this size limit, several mechanisms are proposed, such as the concentration of solids in pressure bumps (Lyra et al., 2009; Pinilla et al., 2012), which can trigger local gravitational collapse into planetesimals via the streaming instability (Youdin & Goodman, 2005). Once these larger bodies form, they can rapidly grow via pebble accretion, where gas drag-assisted capture allows for the efficient assimilation of small particles (Lambrechts & Johansen, 2012). Moreover, pebble accretion can solve the timescale issue for gas giants formed beyond ~10 au, where cm-sized pebbles are accreted rapidly by a planetesimal seed, allowing it to grow directly into a massive core while skipping the slow intermediate stage of colliding with other kilometre-sized planetesimals (Lambrechts & Johansen, 2014). Some studies reveal that pebble accretion can even form 10 $M_\oplus$ planets at ~70 au (Jiang & Ormel, 2023).

The core accretion process is highly dependent on the local disk conditions, such as mass, density, temperature, and metallicity, which influence both the core formation timescale and the availability of gas (Drążkowska et al., 2023). This mechanism can explain the formation of a variety of exoplanets, including rocky planets, super-Earths, mini-Neptunes, ice giants, and even hot Jupiters which are not formed in situ but followed by inward migration. However, the discovery of massive planets by direct imaging at wide orbits challenges the efficiency of this mechanism in the outer disk and suggests alternative or complementary processes.

1.3.2 Gravitational instability (GI) and disc fragmentation: giant planet and brown dwarf formation

Instead of the 'bottom-up' formation mechanism by core accretion, giant planets at wide separations are more likely to be directly formed by gravitational collapse in the circumstellar disc due to disc fragmentation triggered by gravitational instability. A fundamental parameter to describe the gravitational instability is the Toomre Q parameter:

$$Q = \frac{c_s \kappa}{\pi G \Sigma} \tag{1.1}$$

where c_s is the sound speed related to thermal pressure, κ is the epicyclic frequency relation to rotation, G is the gravitational constant, and Σ is the surface density. When Q $\leq$ 1–1.5, GI occurs because gravity overcomes thermal and rotational support, leading to the growth of spiral density waves (Toomre, 1964; Papaloizou & Savonije, 1991). GI can occur in any area of the disc where it is cool and has high surface density. Dense clumps formed by disc fragmentation may further become self-gravitating precursors, leading to the formation of gas giants (Durisen et al., 2007).

GI can solve the disc dispersion time versus the mass of giant planets issue, as it can form gas giants and brown dwarfs at a very short timescale. Companions formed by this mechanism are generally over 10 au away from the host stars and even at separations of hundreds of au. Hence, GI is an effective formation pathway of directly imaged exoplanets and brown dwarfs (Boss, 2011). The typical size of circumstellar discs is 50–500 au from observations (Andrews et al., 2009). For heavy companions over 1,000 au, they are most likely formed by gravitational collapse similar to binary formation. For these wide-orbit companions, there are possibilities for migrations and dynamical scattering with other objects or systems after formation by disc fragmentation.

Various sources can trigger GI in a disc. For instance, massive discs formed by protostellar cloud collapse are very likely to become gravitationally unstable when the mass ratio between the disc and the host star $\frac{M_d}{M_s} \geq 0.1$ (Kratter & Lodato, 2016), where M_d is the mass of the disc and M_s is the mass of the star. Other mechanisms include local density change due to infall of clumpy materials (Boss, 1997), slow accretion of mass (Kratter & Perets, 2012; Zhu et al., 2012), and rapid cooling of a disc (Johnson & Gammie, 2003). Moreover, dynamic interactions with other objects, such as a binary companion or encounters with another star or circumstellar disc, which occur frequently in dense clusters, can also trigger GI (Boffin et al., 1998; Durisen et al., 2007). However, some sources prevent GI and disc fragmentation. It was found that magnetic fields tend to prevent mass growth and stabilise the disc (Hennebelle & Teyssier, 2008; Chabrier et al., 2014). As rapid cooling promotes GI, inefficient cooling then hampers GI, which is the reason that it is challenging for GI to form planets at small separations (Rafikov, 2005).

1.3.3 Other brown dwarf formation mechanisms

Besides GI, there are other mechanisms that can form brown dwarfs. Brown dwarfs can be formed from an incomplete or failed stellar embryo due to photoionisation of adjacent massive OB stars or the stellar embryo ejected from the surrounding gas due to dynamical interactions with nearby protostars or fragments (Whitworth & Zinnecker, 2004; Reipurth & Clarke, 2001; Bate, 2012; Chabrier et al., 2014). These two mechanisms require the existence of nearby objects, usually in dense star clusters. However, a rich population of brown dwarfs has been discovered in loose stellar environments such as Taurus which is roughly three orders of magnitude less dense than other young star-forming regions, as well as in the field, indicating that there are other ways to form brown dwarfs. Instabilities in a molecular cloud lead to turbulent flow and fragmentation, resulting in the formation of cores of various masses, and brown dwarfs are at the tail of this mass distribution (Padoan & Nordlund, 2004; Hennebelle & Teyssier, 2008). Besides, brown dwarfs can also be formed from the fragmentation of a massive prestellar core (Bonnell et al., 2008). There are also gravitational instabilities in a massive collapsing core that can lead to the fragmentation of the core itself and form smaller cores covering a wide range of masses (Bonnell et al., 2008).

1.3.4 Free-floating planetary-mass object formation

As mentioned earlier, core accretion and disc fragmentation are the two main mechanisms to form planets orbiting stars as they accumulate materials from protostellar discs. However, the large population of free-floating objects in young clusters and the field complicates our understanding of planet formation. Several scenarios listed below have been proposed to explain their formation which can be classified into two main ways: planet-like formations followed by ejection and scale-down of brown dwarf formations.

- Wide-orbit planets liberated due to stellar encounters: those planets are formed via core-accretion or disc fragmentation in protoplanetary discs and then are ejected from their birth systems due to dynamical interactions with other stars or planetary systems (Veras & Raymond, 2012). N-body simulations found that the survivability of wide-orbit planets is low. For instance, just a single stellar encounter can significantly change their orbits,

and chances for them to migrate to outward orbits and be ejected to the field are higher than migrating inward (Carter & Stamatellos, 2023). The timescale for these planets to migrate outwards is of $\sim 10^8$–10^9 yr (Hurley & Shara, 2002).

- Turbulent gravitational collapse and fragmentation of massive prestellar cores: Just like brown dwarf formations, fragmentation of a molecular cloud due to turbulence and instabilities produces cores of planetary masses. The fragmentation of massive prestellar cores also works here (Padoan & Nordlund, 2004).

- Photoionisation: photon-erosion from nearby OB stars evaporates part of the outer layers of brown dwarfs and leaves embryos of planetary masses (Whitworth & Zinnecker, 2004).

- Embryo ejection due to dynamical interactions among cores: the smallest bodies between cores formed by fragmentation in a molecular cloud are ejected from the surrounding material due to scattering with other objects. They only grow to the planetary-mass regime before accretion termination (Reipurth & Clarke, 2001).

While all of the mechanisms are likely to contribute to the population of free-floating planets, Miret-Roig et al. (2022) found that core collapse and ejection from planetary systems are probably the two main sources of those objects with at least 10% of them coming from the latter. Moreover, most of the mechanisms can produce free-floating planets above 1 $M_{\rm J}$. For even smaller planets, they are likely formed by core accretion followed by ejection from the original systems.

1.3.5 Observational constraint methods

The actual brown dwarf and planet populations are a result of the combination of multiple mechanisms. Constraining which formation mechanism dominates the observed populations requires comparison between observations and simulations. There are several methods to probe the formation of brown dwarfs and gas giants.

Spectroscopy

Atmospheric molecular abundances are closely related to the formation history of brown dwarfs and planets. Spectroscopic observations in the infrared, where there are plenty of molecular lines, are one of the prevalent ways to put constraints on their formation by understanding their molecular features. Öberg et al. (2011) proposed that C/O ratio can be a tracer of the formation location and formation process of giant planets in the protoplanetary disk. From the outer separation to the inner separation, CO sublimates first, then CO_2 and last H_2O, due to the temperature gradient in the disk. Therefore, the C/O ratio will be altered at the CO, CO_2 and H_2O snowlines. Gravitational instabilities result in stellar C/O as the collapse process occurs so rapidly that the material consists entirely of the same matter present in the protostellar disc. Substellar C/O favours a gas accretion process with lots of icy solids, adding more O than C. Superstellar C/O indicates the formation location at the outer disc, e.g., the CO and CO_2 snowlines, by a gas accretion process with lots of carbon grains. Konopacky et al. (2013) found a superstellar C/O ratio for HR 8799 c, while Wang et al. (2020) found a substellar to stellar C/O ratio for HR 8799 c. Barman et al. (2015) found a superstellar C/O ratio for HR 8799 b and Mollière et al. (2020) found a stellar C/O ratio for HR 8799 e. Lavie et al. (2017) reported a superstellar C/O ratio for HR 8799 b, a stellar ratio for HR 8799 c, and a substellar ratio for HR 8799 d and e from their atmospheric retrieval model. Therefore, the specific formation mechanism of HR 8799 planets is still obscure due to the large range of possible C/O ratios. Moreover, it has been found that the C/O ratio is not a simple relation with CO, CO_2, and H_2O snowlines but is also subjected to other local effects, such as volatile carbon and oxygen carrier grains trapped in local regions (Bosman et al., 2021). These processes involve complicated physical and chemical reactions in different environments (Öberg & Bergin, 2021).

Isotope abundance ratio is another tracer of the formation history of brown dwarfs and giant planets, e.g., D/H and $^{12}C/^{13}C$ ratio (Mollière & Snellen, 2019; Morley et al., 2019). $^{12}C/^{13}C$ ratio can be changed by multiple processes, including partitions of ice and gas (Smith et al., 2015), ion-molecule reactions at temperatures as low as 10 K (Langer et al., 1984), and isotope-selective photodestruction (Bally & Langer, 1982) in molecular clouds. For substellar objects formed in different environments, such as protoplanetary discs or molecular clouds, they may go through different processes and thus have distinctive isotope ratios. Zhang et al. (2021a) detected a ^{13}C-rich atmosphere of

the very wide-orbit young Jovian planet, YSES 1b, indicating it accreted a lot of carbon in a ^{13}C-rich environment. Motivated by this finding, the ESO SupJup survey is currently investigating if there are distinctive formation pathways between isolated brown dwarfs and giant planet companions by comparing their $^{12}C/^{13}C$ ratio (de Regt et al., 2024). One of the recent works found that there is no significant difference between three young brown dwarfs and argues that they are likely formed by a fragmentation-related mechanism (González Picos et al., 2024).

Orbital configuration

Formation mechanisms and following evolution can leave fingerprints in the orbits of brown dwarf and planetary-mass companions. Direct imaging measures the motion of the companions in multiple epochs and therefore can constrain their orbits if they show significant motions. For instance, obvious orbital motions have been detected for several direct imaging planets. The four planets in the HR 8799 system are in low eccentricity orbits with 1:2:4:8 resonance and they are close to coplanar (Konopacky et al., 2016a; Gravity Collaboration et al., 2019). Orbital resonance usually occurs after migration and dynamical interactions between the planets (Lee & Peale, 2002). Furthermore, orbital resonance can also constrain the dynamical mass of companions, which is a fundamental parameter in studying their formation. Wang et al. (2018) combined the dynamical and luminosity constraints to estimate the mass of HR 8799 b = 5.8 ± 0.5 M_J and 6.5–7.8 M_J for HR 8799c, d and e. Eccentricity is another fundamental parameter related to the formation and evolution. Bowler et al. (2020a) found that planetary-mass companions tend to have low eccentricities, while brown dwarf companions have a broad peak of eccentricities between 0.6 and 0.9, resembling stellar binaries. This indicates that low-mass companions are more likely to form in situ and massive companions preferentially form in a star-like manner.

Planet and disc interactions

High contrast and high angular resolution imaging of protoplanetary discs in the optical and infrared has found that they have various morphological structures, such as rings, gaps, spirals, shadows and arcs (Benisty et al., 2023). These structures are possible indications of planet and disc interactions. Planet

formation may create cavities and other substructures (e.g. Kley & Nelson, 2012). Imaging planets when the disc is not dissipated yet provides the most straightforward verification of planet formation mechanisms. Thus, young stars with discs showing evidence of planet-related structures have been popular targets of searches for proto-planets. One famous system is PDS 70, a 5 Myr old T Tauri star hosting a protoplanetary disc. Two planets PDS 70b and c have been imaged (Müller et al., 2018; Chauvin, 2018; Keppler et al., 2018; Wagner et al., 2018; Haffert et al., 2019), as shown in Fig. 1.7. The large central cavity is thought to be related to planet formations (Bae et al., 2019). The two planets are still accreting materials from their surrounding gas, revealed by Hα emission detected from them (Haffert et al., 2019). HL Tau is another famous system with multiple rings and gaps observed in its protoplanetary disc (ALMA Partnership et al., 2015). Simulations show that its structures can be explained by three Saturn mass planets (Dong et al., 2015; Dipierro et al., 2015; Jin et al., 2016).

Initial mass function

The initial mass function (IMF) is generally represented as power-law forms of $\frac{dN}{dM} \propto M^{-\alpha}$ or $\frac{dN}{dM} log(M) \propto M^{-\Gamma}$, where N is the number of objects, M is the mass of the object, α and Γ are the scaling exponent and $\alpha = \Gamma + 1$. The value of α varies with stellar masses (Kroupa, 2001). If there are significant changes in IMF from stars to planetary-mass objects, this suggests that there are distinct formation channels for objects of different masses. If brown dwarfs and planetary-mass objects follow the distribution of low-mass stars, their dominant formation mechanism is likely the scale-down of star formation, e.g. at the tail of fragmentation and collapse chains in a molecular cloud. Therefore, surveying various young clusters and star-forming regions to build their IMF down to the planetary-mass regime is an essential way to understand the formation of brown dwarfs and planetary-mass objects. All sky surveys such as Wide-Field Infrared Survey Explorer (WISE) (Wright et al., 2010) and its follow-up NEOWISE survey (Marocco et al., 2021) have discovered hundreds of late-T dwarfs and Y dwarfs in the solar neighbourhood (Kirkpatrick et al., 2011; Mainzer et al., 2014; Meisner et al., 2020). They can probe isolated objects down to $\sim$5 $M_{\rm J}$ (Luhman, 2012). With JWST, we can probe fainter objects: free-floating planetary-mass objects down to 3–4 $M_{\rm J}$ have been detected in a star-forming cluster IC 348 (Luhman et al., 2024) and also candidates down to 1–2 $M_{\rm J}$ have been reported in Orion Nebula Cluster (Luhman, 2024). Usually, surveys from various datasets are

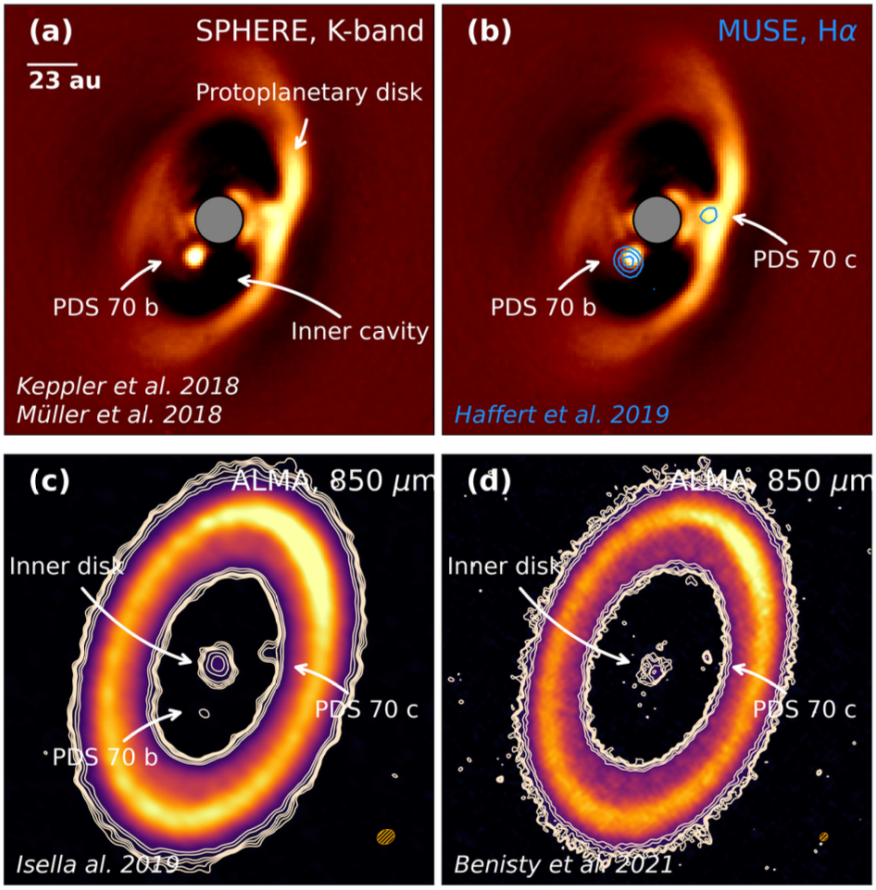


Figure 1.7: PDS 70 system imaged in SPHERE K band (a), MUSE Hα band (b), ALMA 850 μm (c and d in different angular resolution). The beam size is provided in orange in the bottom right of panels c and d. The angular solution of panels a and b is about 70 mas, a factor of three larger than the ALMA images. This system shows strong evidence of planet and disc interactions. Figure comes from Benisty et al. (2023).

combined to derive the mass and membership of ultracool objects, such as the Two Micron All-Sky Survey (2MASS, Skrutskie et al., 2006), the Deep Near-Infrared Survey of the Southern Sky (DENIS, Epchtein et al., 1999), the Sloan Digital Sky Survey (SDSS, York et al., 2000), the United Kingdom Infrared Telescope Infrared Deep Sky Survey (UKIDSS, Lawrence et al., 2007), the UKIRT Hemisphere survey (Dye et al., 2018), the Pan-STARRS1 Surveys (Chambers et al., 2016), and the Gaia (Gaia Collaboration et al., 2016, 2018, 2021a). Objects discovered from these surveys still require spectroscopic follow-up to confirm brown dwarf or planetary-mass members of young star-forming regions.

The power index of the IMF for stars and substellar objects has been found to vary with masses in the solar neighbourhood, with $\alpha = 2.35$ for stars more massive than $0.5\,M_\odot$ (e.g. Chabrier, 2001)and $\alpha = \sim 0$ for substellar objects (Luhman, 2012), demonstrating the formation difference between stars and substellar objects. In young clusters, α is measured about 0.5, suggesting a tentative difference compared to the field (Luhman, 2012). Interestingly, a dip in the IMF at 7–13 M_J was reported by Bardalez Gagliuffi et al. (2019); Gaia Collaboration et al. (2021a) in volume-limited samples in the solar neighbourhood and Miret-Roig et al. (2022) in the Upper Scorpius and Ophiuchus young stellar associations, likely evidence of the formation difference between brown dwarfs and free-floating planets. By comparing IMF in various young clusters, we can explore the relationship between stellar environment and substellar formations (e.g. Galli et al., 2021). With simulated populations from different formation mechanisms, we can determine the contribution of these mechanisms to the observed substellar IMF.

Multiplicity

Multiplicity is inherently related to formation and dynamical interactions. It is well known that the multiplicity of stars in the field decreases with primary masses as shown in Fig. 1.8. The majority of OB stars are in binary or multiple systems and half of FGK-type stars are non-single, while less than 10% M dwarfs are in binary or multiple systems (e.g. Duquennoy & Mayor, 1991; Burgasser et al., 2007; Offner et al., 2023). More detailed analyses show that both the separation distribution and the secondary-to-primary mass ratio are strongly correlated with the primary mass. When the primary mass decreases from stars to brown dwarfs, the separation between binaries decreases and the mass ratio increases (Duquennoy & Mayor, 1991; Bouy et al., 2003; Burgasser et al., 2003; Close

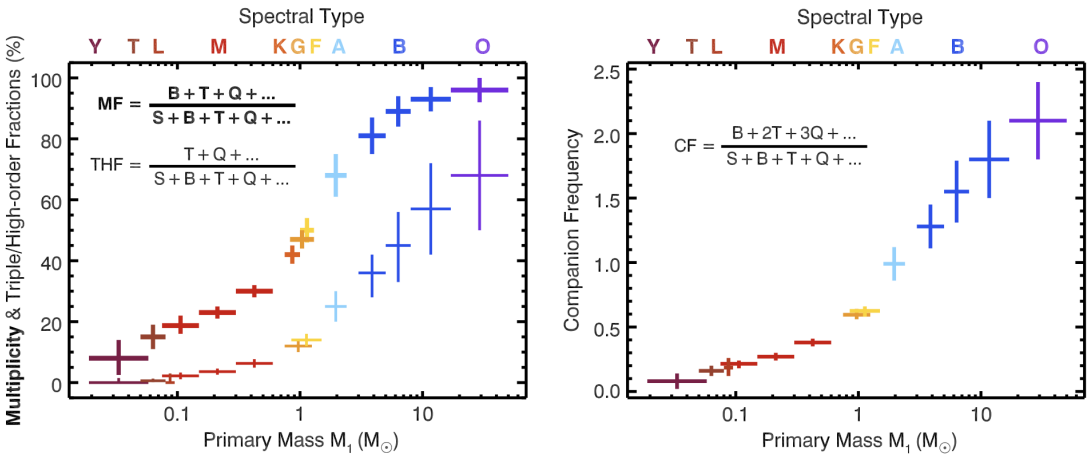


Figure 1.8: Multiplicity versus primary mass. Left panel: multiplicity fraction versus primary mass; right panel: companion frequency per object versus primary mass. Thicker markers are multiplicity fractions, and thinner markers are triple and higher-order fractions. The figure comes from Offner et al. (2023).

et al., 2003; Burgasser et al., 2007; Bergfors et al., 2010; Duchêne & Kraus, 2013). For solar-type stars, the separation follows a lognormal distribution, peaking at ~45 au and the mass ratio is a flat distribution down to 0.1 (Raghavan et al., 2010). In contrast, for very low mass stars and substellar objects, most of them have separations within 10 au and the separation peaks at 4–7 au assuming a lognormal distribution (Maxted & Jeffries, 2005; Allen et al., 2007). The majority of them have a mass ratio above 0.7 and the mass ratio is best presented as a power-law distribution (Burgasser et al., 2006; Allen et al., 2007; Duchêne & Kraus, 2013).

Multiplicity is shaped mainly during the formation stage and altered by dynamical interactions with other objects or systems, while it evolves very slowly after the objects disperse in the field. Therefore, measuring multiplicity in young star-forming regions is crucial to verify different formation scenarios of substellar objects because the multiplicity is more primordial. However, it is challenging to measure the multiplicity of planetary-mass objects because they themselves are already very faint for detection, not to mention their companions. Nevertheless, several young star-forming regions in the solar neighbourhood have been surveyed for companions of substellar objects by high contrast and high angular resolution imaging. Biller et al. (2011) surveyed 20 brown dwarfs in the Upper Scorpius association (Upper Sco) with Keck's laser guide star adaptive optics system and discovered one companion. They derived a binary fraction of <9% at 10–500 au for brown dwarfs with SpT later than M8 at the 1σ confidence level, no significant difference compared to T dwarfs of similar mass in the field. Fontanive et al.

(2018) observed 12 field brown dwarfs with HST/Wide Field Camera 3 (WFC3) and obtained a binary rate of $5.5^{+5.2}_{-3.3}$% for brown dwarfs with SpT of T5 to Y0 at separations between 1.5 and 1000 au. The follow-up work by Fontanive et al. (2023) derived a similar binary rate of <4.9% for a larger sample of 33 T8–Y1 field brown dwarfs at separations between 1 and 1000 au at the 1σ confidence level. Todorov et al. (2014) observed 47 brown dwarfs with SpT spanning in M6–L0 in Taurus and Chamaeleon I star-forming regions with HST. Combining with previous surveys, they derived a similar binary rate of 4^{+3}_{-1}% for objects with SpT later than M6 in Taurus, Upper Sco, and Chamaeleon I. From these surveys, no significant difference in the multiplicity rate has been found among the field and young star-forming regions including Taurus (145 pc, 3–5 Myr), Upper Sco (145 pc, 5 Myr), and Chamaeleon I (165 pc, 2–3 Myr). Their multiplicity rate is lower compared to the multiplicity rate of more massive objects, suggesting different formation channels. The brown dwarfs in these surveys are heavier than $10\,M_{\rm J}$. A candidate sample of Jupiter Mass Binary Objects (JUMBO) was reported in the Orion Nebula Cluster (414 pc, 0.2–3 Myr) with masses down to $0.6\,M_{\rm J}$ observed by JWST/Near Infrared Camera (NIRcam) (Pearson & McCaughrean, 2023). Although this sample is controversial with follow-up spectroscopy observations and reanalysis of the data (Luhman, 2025), it exhibits an increasing trend for the wide binary fraction after it touches the bottom at $\sim 10\,M_{\rm J}$. If it is true that objects below $10\,M_{\rm J}$ are more likely to have companions than more massive planetary-mass objects, the formation scenarios of planets would be transformed. That is also why it is essential to survey free-floating planets in various stellar regions to understand how the binary rate changes in the planetary-mass regime.

1.4 Direct imaging surveys

Numerical simulations produce a number of planets formed by various formation mechanisms, and comparison with the observed populations will constrain the contribution of different mechanisms. However, the number of directly imaged exoplanets is quite small, as is the number of planetary-mass binaries. Enlarging the sample size is the first step to probe their formation.

Several direct imaging surveys were conducted to search for exoplanets using the first-generation ground-based high contrast imaging facilities such as the Gemini Deep Planet Survey with Gemini/NIRI (Lafrenière et al., 2007b), an L-

band imaging search for giant planets with VLT/NACO(Kasper et al., 2007), the International Deep Planet Survey with VLT/NACO, Keck/NIRC2, Gemini/NIRI, Gemini/NICI (Vigan et al., 2012; Galicher et al., 2016), and the Gemini/NICI planet-finding campaign (Biller et al., 2013a; Nielsen et al., 2013; Wahhaj et al., 2013). These surveys discovered a few brown dwarf companions and the HR 8799 planetary systems after surveying hundreds of stars. The sensitivity of these surveys is generally down to 2–3 $M_{\rm J}$ at separations between 10–400 au. All of them derived a low planet occurrence rate: $0.6^{+0.7}_{-0.5}$% of young stars with masses between 0.1 and 3 $M_{\odot}$ would have 5–13 $M_{\rm J}$ companions at separations between 30–300 au (Bowler, 2016b). The occurrence rate of giant planets was not found to be significant among host stars with SpT from B to M (Bowler, 2016b). This suggests that giant planet formation over ~10 au is not efficient, especially compared to the high occurrence rate of giant planets at very short orbits discovered by radial velocity (orbital periods within 2000 days) (Cumming et al., 2008).

Second-generation high contrast imaging facilities with extreme AO emerged in recent years with improved sensitivity and wavefront correction, such as SPHERE (Beuzit et al., 2019) and GPI (Macintosh et al., 2014), and MaAO-X (Males et al., 2016). These instruments can achieve a Strehl ratio of 90% in the near-infrared and feature sophisticated coronagraph designs. Several surveys have been conducted with these instruments. SpHere INfrared survey for Exoplanets (SHINE) targeted 400 stars using VLT/SPHERE (Desidera et al., 2021) with the majority of the stars from nearby young moving groups with a median age of 45 Myr (Desidera et al., 2021; Vigan et al., 2021). It probed separations between 5 and 300 au with sensitivity down to ~1 $M_{\rm J}$ (Vigan et al., 2021). It discovered three new brown dwarfs and planets, including HIP 65426b, HIP 64892B, and HIP 74865B (Langlois et al., 2021; Chomez et al., 2025). The fraction rate of stars having at least one substellar companion is still low for the first sample of 150 stars: $23^{+13.5}_{-9.7}$% for BA stars, $5.8^{+4.7}_{-2.8}$% for FGK stars and $12.6^{+12.9}_{-7.1}$% for M dwarfs (Vigan et al., 2021). The Gemini Planet Imager Exoplanet Survey (GPIES) searched for planets within 100 au around 600 nearby stars with 152 stars from moving groups, 104 stars from Sco-Cen and 346 field stars (Nielsen et al., 2019). It discovered one new planet 51 Eridani b and one new brown dwarf HR 2562B from the initial analysis (Macintosh et al., 2015; Konopacky et al., 2016b). Its sensitivity is down to ~3 $M_{\rm J}$. Statistical analysis of this survey found that stars with masses over 1.5 $M_{\odot}$ are more likely to have planetary-mass companions than less massive stars, similar to the trend reported by SHINE (Nielsen et al., 2019; Vigan et al., 2021). Only about 1% of all the stars have

at least one brown dwarf companion, agreeing with previous surveys. Nielsen et al. (2019) also found that the mass and separation distribution of brown dwarf companions is likely distinct from that of planetary-mass companions.

Besides SHINE and GPIES, there are several other surveys targeting young stars, focusing on stars in the Scorpius–Centaurus association (Sco-Cen). Because Sco-Cen is the nearest massive star-forming region at a distance of 120 pc and with an age of 10–20 Myr (de Zeeuw et al., 1999; Pecaut & Mamajek, 2016). The Young Suns Exoplanet Survey (YSES) targets 70 K-type stars in Sco-Cen and has detected two planets at separations over 100 au in a multiple planetary system, YSES 1bc (Bohn et al., 2020a,c). The B-star Exoplanet Abundance study (BEAST) observed 85 B-type stars in Sco-Cen and detected one giant planet around a 1.9 $M_\odot$ star at a separation of 550 au, b Centauri b (Janson et al., 2021b,a). The discovery of these planets in Sco-Cen raises an interesting question about why Sco-Cen has a relatively higher detection rate of wide-orbit planets than young moving groups and the field stars that were surveyed before. The formation of these wide-orbit planets (>100 au) is particularly challenging, as the outer regions of protoplanetary discs contain less material than the inner regions. Ongoing statistical analyses of these surveys will help establish the occurrence rate of such planets and constrain possible formation pathways. Moreover, by comparing results across different stellar environments — ranging from young moving groups to star-forming associations like Sco-Cen — we can assess how factors such as stellar density, radiation fields, and dynamical histories influence the frequency and properties of wide-orbit planets. This comparative approach is crucial for disentangling the roles of local environment and intrinsic disc properties in shaping planetary systems.

1.5 Atmospheric structures

1.5.1 Clouds

Photometric and spectroscopic observations, atmospheric retrieval, and models reveal that brown dwarfs and planets have complicated atmospheres. The dramatic change of near-infrared colours from L to T spectral types is a demonstration of the remarkable change in their atmospheres. From early L to late L, temperature decreases and lots of refractory materials condense, such

as Al_2O_3, Fe, $MgSiO_3$, and Mg_2SiO_4, which can also explain the disappearance of TiO and VO in mid-L (e.g., Tsuji et al., 1996; Knapp et al., 2004; Burrows et al., 2006; Cushing et al., 2008; Marley et al., 2010). Dusty clouds form in the atmosphere, one of the main sources of the reddening of L dwarfs. Silicate absorption features have been observed in L dwarfs between 8 μm and 12 μm, verifying the existence of silicate clouds (Suárez & Metchev, 2022; Miles et al., 2023). The abrupt blueward change of $J - K_S$ colour at the L/T transition marks the start of dust condensation and cloud breakup. One scenario of what happens in L/T transition is that larger cloud grains and particles 'rain out' of the atmosphere faster, clouds suddenly break up and the atmosphere becomes clear (Knapp et al., 2004; Tsuji & Nakajima, 2003). Another scenario is the patchy clouds: high-layer clouds reduce the outgoing atmosphere radiation and thus form a dark region, while the holes in clouds allow the radiation from deeper regions to escape, resulting in J-band brightening (Ackerman & Marley, 2001; Marley et al., 2010). As the dust and clouds condense and dissipate, the atmosphere becomes clear from mid-T, suggested by the blue colours of T dwarfs. Figure 1.9 demonstrates the condensation of a variety of species, showing how the composition of clouds changes with temperature. While L dwarfs have silicate clouds, T dwarfs can also have clouds but composed of salt and sulfide such as Na_2S, KCl, ZnS, and MnS (Morley et al., 2012). From mid-Y to late-Y, even H_2O begin to form clouds and condense out from atmospheres (Morley et al., 2012) For instance, water depletion is detected in the late-Y dwarf WISE J085510.83-071442.5 (Kühnle et al., 2025).

1.5.2 Thermal and chemical instability

Besides clouds, thermal instability also presents in the atmospheres of brown dwarfs and planets. Models demonstrate that temperature fluctuations can cause spatial inhomogeneities in T-dwarfs (Robinson & Marley, 2014). The thermal instability is likely correlated with magnetospheric activities such as aurora (Hallinan et al., 2015) (e.g. the aurora on Jupiter (Cowley & Bunce, 2001)), or chemical instability (Tremblin et al., 2016). Methane emission is detected in a Y dwarf CWISEP J193518.59-154620.3, unveiling a temperature inversion layer of ~300 K at 1–10 millibar, which is possibly heated by auroral processes or other internal processes (Faherty et al., 2024). Carbon tends to exist as CO at higher temperatures and as CH_4 at lower temperatures. Likewise, nitrogen shifts from N_2 at high temperatures to NH_3 at lower temperatures. In L dwarfs, carbon has

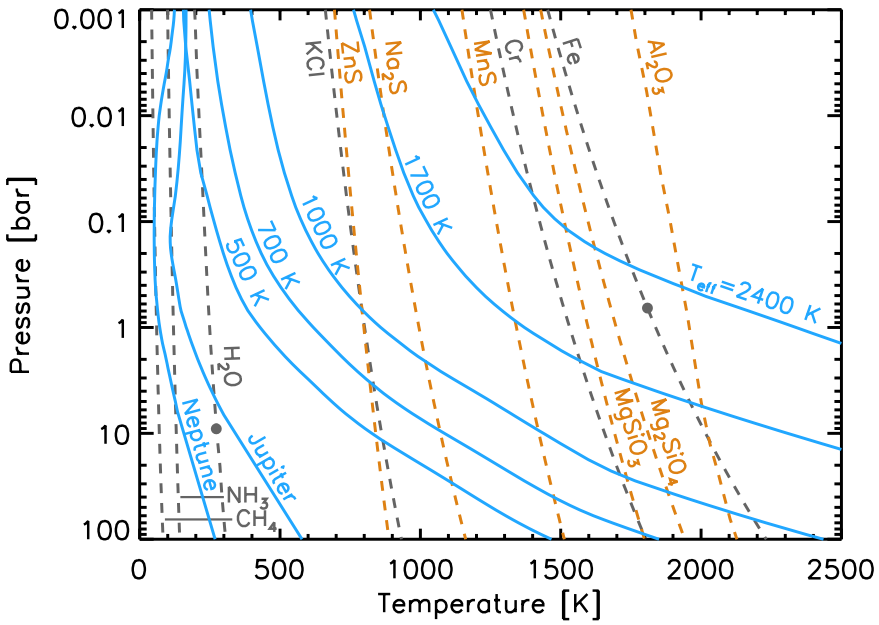


Figure 1.9: Condensation curves of various species (dashed) assuming solar abundances. Grey lines are for direct condensation and orange lines are for condensation due to chemical reactions. Filled circles mark a liquid-solid transition. Blue lines are thermal profiles from cloud-free models, including empirically derived profiles for Jupiter and Neptune. The figure comes from Marley & Robinson (2015).

this reaction: $CO + 3\,H_2 \longrightarrow CH_4 + H_2O$ and in T dwarfs, nitrogen has this reaction: $N_2 + 3\,H_2 \longrightarrow 2\,NH_3$. When there are perturbations driving $CH_4 + H_2O$ mixtures to deep layers of $CO + 3\,H_2$, the former will sink because of a higher molecular weight (Tremblin et al., 2016). It will become chemically unstable and further affect opacity and thermal profile, leading to thermal disequilibrium.

1.5.3 Variability observations

While it is impossible to resolve atmospheric structures on brown dwarfs with current direct imaging facilities, time-resolved observations can probe inhomogeneous structures in their atmospheres. The rotational speed of brown dwarfs is usually a few days to several hours as they age and contract from Myr to Gyr (Bouvier et al., 2014). High-resolution spectroscopy observations show that L/T dwarfs are fast rotators with periods of ~ 3 to ~ 20 hrs (e.g., Zapatero Osorio et al., 2006). This makes it easy to monitor the variability of brown dwarfs in a few hours or several days. Variability monitoring can also measure the rotational period of brown dwarfs and planetary-mass objects. After the discovery of large

numbers of brown dwarfs in the late 1990s, monitoring atmospheric activities such as the weather pattern, especially L and T brown dwarfs, has become a key probe of the atmospheres of these objects.

Early studies focused on variability monitoring in the red optical and very near-infrared (e.g.I band). Tinney & Tolley (1999) reported one variability detection of the M dwarf LP 944-20 with a non-detection of L dwarf, establishing the feasibility of photometric monitoring of brown dwarfs. Bailer-Jones & Mundt (1999) also reported the photometric variability of an L dwarf 2MASSW J1145572+231730 in I band monitoring. They did a larger survey 2 years later for a sample of 21 ultracool M and L dwarfs and found that L dwarfs are more likely to be variable than M dwarfs, which is due to dust formation in L dwarfs' atmosphere (Bailer-Jones & Mundt, 2001). They detected periodicity in some light curves: while some of them can be produced by rotation modulation, some of the periodic variability cannot match their rotational periods. Gelino et al. (2002) surveyed 18 L dwarfs and found that at least 7 showed significant variability. They found longer periods from the light curves of 2MASS 0746+20AB and 2MASS 1300+19 than their rotation periods from the rotation velocity, and they ascribed the variability to the rapid evolution of atmospheric structures.

After the first variability detections in the red optical and I bands, it did not take too long to perform variability monitoring of brown dwarfs in the near-infrared, where brown dwarfs reach their peak flux, although it was technically harder. Koen et al. (2004) reported the first continuous monitoring survey of 18 L and T dwarfs simultaneously observed in JHK_S bands and only reached a low-level variability <0.02 mag. Their follow-up survey of ultracool dwarfs had a similar result, with no significant variability found except for one T dwarf (Koen et al., 2005). Then after a few years of persistent exploring and with more ultracool dwarfs discovered and the improved instrument sensitivity, two large surveys (Radigan et al., 2014; Metchev et al., 2015) became a milestone in the variability monitoring of L and T dwarfs. Radigan et al. (2014) presented a J band survey of 62 L4–T9 dwarfs using the 2.5 m telescope at the Las Campanas Observatory with an advanced detrending method. In their final analysis, they found 9 out of 57 dwarfs had significant variability with >99% confidence. They also found that all the strong signals with peak-to-peak amplitude >2% were detected in the L/T transition (L9–T3.5), suggesting the strong link between variability and the L/T transition. Wilson et al. (2014) conducted another large J_S band survey of 69 L0–T8 brown dwarfs and reported an indistinguishable

occurrence frequency of variables between the L/T transition and outside of the L/T transition. However, Radigan (2014) performed an independent analysis of the data from Wilson et al. (2014) and concluded that strong variability outside the L/T transition was rare but did exist. Combining the two large surveys, they found a higher occurrence rate of strong variability at the L/T transition than outside the L/T transition, supporting that atmospheric structures change dramatically at the L/T transition, such as the emergence of patchy clouds. Metchev et al. (2015) made a variability survey of 44 L3–L8 dwarfs with the *Spitzer* space telescope at 3.5 μm and 4.5 μm and confirmed that variability is common in L and T dwarfs in the mid-infrared with 80% of L dwarfs varying more than 0.2% and 36% of T dwarfs varying more than 0.4%. They found many irregular light curves in L dwarfs, indicating that atmospheric structures of L dwarfs are more complicated than a single spot simulation. In addition, optical monitoring of brown dwarfs has not been abandoned. Heinze et al. (2015) observed 12 T dwarfs with the Kitt Peak 2.1 m telescope using an F814 filter spanning from 0.7 μm to 0.95 μm and found two strong variable T dwarfs: 17% variability of a T2.5 dwarf 2MASS 13243559+6358284 and 10% variability of a T2 dwarf 2MASS J16291840+0335371. Moreover, Vos et al. (2017) demonstrated that the viewing geometry, e.g. the inclination of the object, impacts the observed colour and variability. They found that the brown dwarfs viewed equator-on appear to be redder than those that are viewed pole-on, suggesting that clouds are thicker at the equator. And the brown dwarfs with redder colours are more likely to have higher variability amplitudes because the redder colour indicates they are more likely to be viewed equator-on.

Over the past ~20-year search, several highly variable L and T dwarfs were found, such as SIMP J013656.5+093347 (SIMP0136), 2MASS J21392676+0220226 (2M2139) and, WISEJ104915.57-531906.1AB (WISE1049AB), and VHS1256-1257b. Discovered by Artigau et al. (2006), SIMP0136 is the brightest T dwarf in the northern hemisphere. It showed a peak-to-peak variability amplitude of ~50 mmag with a periodic modulation of ~2.4 h (Artigau et al., 2009) in J band. The 2.4 h period was ascribed to the rotation period, but the long-term variations on four different nights were attributed to the evolution of surface features or differential rotation (Artigau et al., 2009). They also found that SIMP0136 had a correlated variability in the J and K_S bands with a larger amplitude in the J band, which gives more constraints on the atmospheric modelling, for example, the temperature difference between the warmer clear region (brightening in J) and the cooler dusty region in the atmosphere. 2M2139 has a similar result to

SIMP0136. It had a peak-to-peak amplitude of 26% in the J band with a periodic modulation of 7.7 h, and it showed a light curve evolution on different nights (Radigan et al., 2012). It also presented the J-band brightening while the peak-to-peak amplitude is 17% in H and 16% in K_S (Radigan et al., 2012). Located at only 2 pc from the Earth, WISE1049AB consists of two L/T transition dwarfs, an L7.5 dwarf (A) and a T0.5 dwarf (B) (Luhman, 2013; Burgasser et al., 2013). Time-resolved simultaneous photometric monitoring in $r'i'z'JHK$ bands showed that the B component had an amplitude from 5 to 15% in all the bands while A had a possible lower amplitude in $i'z'$ bands of 1 and 3%, respectively (Biller et al., 2013b). The B component presented anti-correlated light curves in the $z'HK$ in contrast to $r'i'$ (Biller et al., 2013b). Night-to-night light curve evolution was also reported by Biller et al. (2013b); Gillon et al. (2013). Spectroscopic variability monitoring was also reported by Buenzli et al. (2015a,b), who used these data to infer the possible influence of cloud height and holes on the observed variability. VHS1256-1257 is a rare triple system composed possibly entirely of substellar objects: the host is a tight binary VHSJ1256-1257AB with a total mass of 0.14 $M_\odot$ (SpT of M7) and a semimajor axis of 1.96 au, and the companion is VHS1256-1257 b at a projected separation of 178 au with a SpT of L7 (Gauza et al., 2015; Stone et al., 2016; Rich et al., 2016; Dupuy et al., 2023). VHS1256-1257 b is the known object that presents the strongest variability of 38% in the J band among brown dwarfs and planetary-mass objects (Zhou et al., 2022).

After the launch of the James Webb Space Telescope (JWST), it is feasible to conduct spectroscopic variability monitoring of brown dwarfs and planetary-mass objects from 1 to 14 microns. As different wavelengths are sensitive to different pressure layers (e.g. Yang et al., 2015), this technique can probe atmospheric structures both vertically and horizontally, which is extremely useful to pinpoint sources of variability. JWST/NIRSpec and MIRI variability monitoring from 1 to 14 microns reveal that the two brown dwarfs of WISE1049AB have complicated light curves which are possibly driven by patchy clouds and hotspots associated with thermal-chemical instability (Biller et al., 2024; Chen et al., 2025). SIMP0136 was also detected with intricate light curves between 0.8 and 11 microns, which could be explained by similar mechanisms as proposed for WISE1049AB but also aurorae (McCarthy et al., 2025).

1.5.4 The impact of surface gravity

Surface gravity has a significant impact on the atmospheres of brown dwarfs and planetary-mass objects, affecting the colour, spectra, and variability. Lower surface gravity reduces collision-induced pressure broadening in the atmosphere, which in turn diminishes the optical-to-near-infrared absorption lines and produces a triangular shape in the H band continuum (Kirkpatrick et al., 2006; Allers & Liu, 2013). Besides, lower surface gravity results in a larger cloud scale height and larger grain size (Helling et al., 2011, 2008; Ackerman & Marley, 2001). Thick clouds will absorb more outgoing flux at the shorter wavelengths and large grain size will be more efficient at scattering the outgoing flux (Helling et al., 2011; Burgasser et al., 2010). Both effects will reduce the flux from the deeper layers and lead to redder colours. Liu et al. (2016) observed 63 young ultracool dwarfs and found strong correlations between redder colours and low surface gravity.

Given the impact of surface gravity on atmospheres, surface gravity can also affect the observed variability. Metchev et al. (2015) suggested that low surface gravity is probably associated with strong variability among L3–L5.5 dwarfs from their variability survey with *Spitzer*. In fact, many of the known strongest variables turn out to be young. PSOJ318.2-22 is a young free-floating planetary-mass L7 dwarf in the field discovered by Liu et al. (2013). Biller et al. (2015) detected a strong variability of 7%–10% amplitude in the J_S band and a lower variability amplitude in the Ks band on two different nights. The previously discovered strong variable dwarfs, SIMP0136 and 2M2139 were also found to be planetary-mass objects in the ~200 Myr old Carina-Near moving group with a high membership probability by Gagné et al. (2017a) and Zhang et al. (2021c), respectively. VHS1256-1257 b is another highly variable L7 planetary-mass companion, orbiting around the ~140 Myr old binary system (Dupuy et al., 2023). HST and Spitzer spectroscopic variability monitoring from 1 to 5 μm showed that it had a strong peak-to-peak variability > 20% in the near-infrared and > 5% in the mid-infrared (Bowler et al., 2020b; Zhou et al., 2020). Vos et al. (2019) conducted the first variability survey of 30 young and low surface gravity L dwarfs in J_S band. They measured a 30% variability occurrence rate of L0-L8.5 dwarfs, higher than the 11% variability occurrence rate of the field L dwarfs. They also found a tentative trend that low surface gravity brown dwarfs are more likely to be variable in the L/T transition than outside of the L/T transition, as shown in Fig. 1.10.

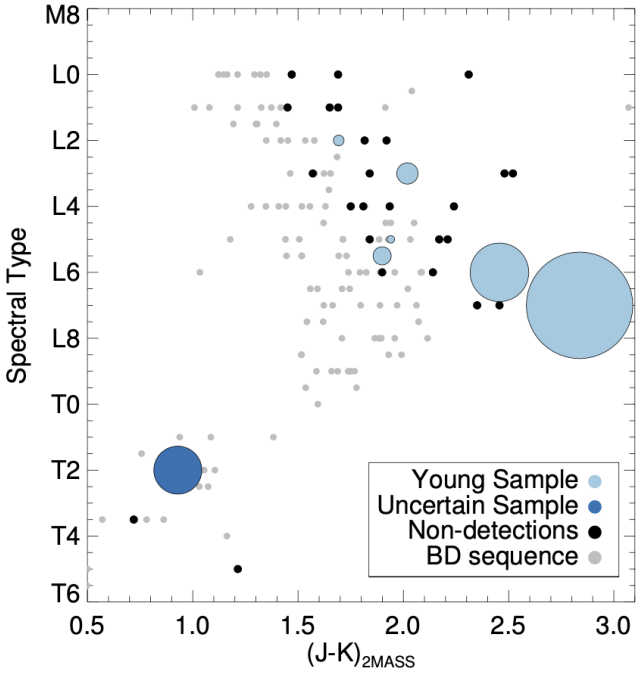


Figure 1.10: Spectral type and colour diagram of variable L and T dwarfs. Blue symbols represent young objects with radii proportional to the variability level. Young dwarfs also seem to be more variable at the L/T transition than outside of the L/T transition. The figure comes from Vos et al. (2019).

1.6 Young free-floating planetary-mass objects as exoplanet analogues: atmospheric characterisation

Directly imaged exoplanets are usually detected in young systems and their number is limited. These gas giants usually have spectral types from L to T and even Y. Because of their large separation from their host stars (e.g.>10 au), the stellar radiation can be ignored and these planets are therefore self-luminous. Meanwhile, there is an abundance of young free-floating planets in young moving groups, young stellar associations and in the field (e.g. Scholz et al., 2012; Peña Ramírez et al., 2012; Luhman et al., 2016; Miret-Roig et al., 2022). They share similar masses, SpT, and ages with directly-imaged companions and therefore can serve as exoplanet analogues. The advantages of studying these objects are that their number is large enough to perform statistical analysis and there is no contamination from adjacent stars, which is extremely helpful for atmospheric characterisation.

For instance, the atmospheric structures probed by the variability technique in Section 1.5 can be analogised to understand the atmospheres of directly-imaged exoplanets. Performing variability observations of directly-imaged exoplanets is significantly more difficult than for free-floating planets. Due to the high contrast between star and planet, AO and coronagraphy are required, which results in a very small field of view (FoV). This is a severe issue for ground-based high contrast imaging because the PSF Strehl ratio changes a lot with varying seeing and there is a lack of reliable and stable photometric calibration resources in the small FoV. HR 8799 is a young F0V star located at ~40 pc from the Earth with an age < 100 Myr (Gray & Kaye, 1999; Su et al., 2009), hosting four imaged planets bcde (Marois et al., 2008, 2010). HR 8799 b has a mass of ~7 M_J at a separation of 68 au, HR 8799 c has a mass of ~10 M_J at a separation of 38 au, HR 87999 d has a mass of ~10 M_J at a separation of 24 au, and HR 87999 e has a mass of ~10 M_J at a separation of 14 au (Marois et al., 2008, 2010; Brandt et al., 2021b). They have very red $J - K_S$ colours with bc at the L/T transition and de of late-L types (Bowler et al., 2010; Bonnefoy et al., 2016). Different atmospheric models consistently show that the four planets have thick and patchy clouds (Currie et al., 2014; Skemer et al., 2014; Mollière et al., 2020). Apai et al. (2016) tried to search for variability in these planets using VLT/SPHERE with the instrument-produced satellite spots which are artificial duplications of stellar PSFs as photometric calibration sources, and they demonstrated that it was possible to reach a photometric uncertainty of 0.1 mag and variability sensitivity of 10%. With a similar technique, Biller et al. (2021) conducted a time-revolved photometric monitoring of HR 8799 bc with VLT/SPHERE and reached a sensitivity of 5% for b and 25% for c. No significant variability was confirmed for the four planets, demonstrating the challenge of detecting variability for directly imaged exoplanets. Although space telescopes do not suffer from turbulent atmospheric conditions, their angular resolution power is worse than ground-based high angular resolution facilities, which is not friendly to planets at smaller separations. Nevertheless, with the NIRcam coronagraph, JWST has collected variability monitoring data of HR 8799 planets and another directly imaged planet, β Pictoris b, a bright L2 object with ~10 M_J at a separation of 9.93 au (Lagrange et al., 2010; Lacour et al., 2021). These data are still under analysis.

Therefore, while it is challenging to probe the atmospheric structures and clouds of directly imaged exoplanets, we can still infer the weather on them by studying free-floating planets of the same type as them, such as PSO J318.5-22 (Biller et al.,

2015, 2018), SIMP0136 (Artigau et al., 2009; McCarthy et al., 2025), 2MASS2139 (Radigan et al., 2012; Apai et al., 2013), and VHS1256-1257b (Bowler et al., 2020b; Zhou et al., 2022). Recently, the detection of silicate clouds has been reported for YSES 1c from JWST MIRI spectra Hoch et al. (2025). YSES 1c is a directly imaged planet of $6 \pm 1\,M_{\rm J}$ at the L/T transition with very red infrared colours, orbiting around 16 Myr star at a separation of 320 au (Bohn et al., 2020c). The composition of the silicate clouds resembles what was found in young free-floating planetary-mass objects, e.g. forsterite (Mg2SiO4), such as the two highly variable objects at the L/T transition SIMP0136 and 2MASS2139 (Vos et al., 2023). Directly imaged planets have similar colours or even redder colours than young L and T dwarfs shown in Fig. 1.2, indicating that they have similar cloud formation and destruction processes in their atmospheres. They also have lower surface gravity than field brown dwarfs, and hence they are expected to have atmospheric structures as complicated as young free-floating planets. Besides, molecular absorption features such as H_2O, CO, CH_4, and NH_3 have also been detected in imaged planets from low, median, and high resolution spectroscopy (Konopacky et al., 2013; Barman et al., 2015; Bonnefoy et al., 2016; Lavie et al., 2017). Two low-mass planets with mid-late T spectral types from the same young moving group β Pictoris have been discovered by direct imaging, 51 Eridani b, a $2.6\,M_{\rm J}$ planet at a separation of 13 au orbiting an F0 star (Macintosh et al., 2015), and the $3.8\,M_{\rm J}$ AF Lep b at a separation of 9 au orbiting an F8V star. Both of them have redder near-infrared colours than field mid-late T dwarfs, indicating cloudy atmospheres and disequilibrium chemistry (Macintosh et al., 2015; Samland et al., 2017; Balmer et al., 2025), similar to some young free-floating planets of the same SpT and colour.

1.7 This thesis

Just as each human is unique, every brown dwarf or planet also has its own individuality. While objects of the same spectral type share many general properties, they differ in colour and atmospheric structure due to a variety of stochastic processes. Focusing too narrowly on individual cases can therefore obscure our understanding of the broader population. By studying entire populations, we can average out individual differences and reveal the common properties that characterise the group. Surveys of brown dwarfs and planets are thus essential for probing their formation and evolution. Through statistical

analyses of these surveys, we can compare different classes of objects and explore how various parameters shape their properties.

The work presented in this thesis explores the atmospheric structures of young planetary-mass objects by variability monitoring and searches for planetary-mass companions and binaries, with a focus on understanding the atmospheres and formation of planetary-mass objects at a population level.

In Chapter 2, I present a near-infrared photometric variability survey of young planetary-mass objects with SpT between L5 and T8. I investigate how the variability rate varies with SpT and age by statistical analysis of an unprecedentedly large sample of brown dwarf variability combined with previous surveys. This work identifies the critical role of surface gravity on the atmospheric structure from L to T spectral types.

In Chapter 3, I report the initial results of a direct imaging survey of wide-orbit planets in the Fornax-Horologium association conducted with VLT/SPHERE. I present a companion at the hydrogen burning limit imaged in this survey at an eccentric orbit, indicating dynamical scattering during its formation. This survey aims to explore the possible relation between stellar environments and wide-orbit planet formation.

In Chapter 4, I investigate a planetary-mass candidate at an extremely wide orbit around a non-single star imaged in YSES. I demonstrate the challenges of confirming a faint planet candidate at a large separation, especially when the central star is not single. The formation of this candidate is difficult to explain if it is confirmed to be a planetary-mass companion.

In Chapter 5, I describe a photometric and multiplicity survey of brown dwarfs and planetary-mass objects in the Taurus with HST/WFC3. While no companion candidates are detected by the combination of colours from multi-band photometry and PSF fitting, I calculate that the sensitivity of this survey is down to $1\,M_{\rm J}$ at separations between 30 and 7000 au with artificial star injection. I include the preliminary results of the binary rate of this sample derived from statistical analysis with completeness correction.

This thesis has contributed to the main questions about the atmosphere and the formation of planetary-mass objects, providing a comprehensive understanding from surveys and statistical analysis. It advances the characterisation and detection of planetary-mass objects, producing new insights for future surveys

and individual substellar object studies.

Chapter 2

A near-infrared variability survey of young planetary-mass objects

The work presented in this chapter resulted from a collaborative effort. The initial conceptualisation of the study and primary proposal writing were led by Beth Biller. I wrote the proposal for follow-up variability confirmation and conducted observations in collaboration with Beth Biller, Johanna Vos, and Niall Whiteford. I performed the full data analysis and developed the statistical framework in consultation with Johanna Vos. I wrote the entirety of this chapter, with revisions provided by the collaborators.

2.1 Abstract

We present a photometric variability survey of young planetary-mass objects using the New Technology Telescope in the J_S and K_S band. Surface gravity plays an important role in the atmospheric structure of brown dwarfs, as young low gravity L dwarfs have a higher variability rate than field L dwarfs. In this study, we extend variability studies to young T-type planetary-mass objects and investigate the effects of surface gravity on the variability of L and T dwarfs across a large sample. We conduct continuous monitoring for 18 objects with spectral types from L5 to T8 and detect four new variables and two variable candidates. Combining with previous variability surveys of field and young L and T objects, within peak-to-peak variability amplitude ranges of 0.5%–10% and period ranges of 1.5–20 hr, we

find that young objects tend to be more variable than field objects. For the first time, we constrain the variability rate of young T dwarfs to be 56^{+20}_{-18}% compared to 25^{+8}_{-7}% for field T dwarfs. Both field and young samples have higher variability rates at the L/T transition than outside the L/T transition. The differences in the variability rates between field and young samples are about 1σ and therefore larger sample sizes are needed to confirm and refine the results. Besides the L/T transition, young L dwarfs with strong variability tend to assemble in a narrow spectral type range of L6–L7.5. This work supports the critical role of surface gravity on the atmospheric structure from L to T spectral types.

2.2 Introduction

The first direct imaging and spectroscopy observations of planetary mass objects outside of the solar system can be dated back more than 20 years ago (Oasa et al., 1999; Lucas & Roche, 2000; Zapatero Osorio et al., 2000; Lucas et al., 2001). These objects were discovered in nearby star-forming regions and are the first of a large population of free-floating exoplanets which are now discovered in young stellar associations such as Upper Scorpius and Ophiuchus (Miret-Roig et al., 2022; Bouy et al., 2022). In recent years, dozens of young brown dwarfs with planetary mass have been discovered by spectroscopy or kinematic characterisation in the field or nearby young moving groups (e.g. Liu et al., 2013; Allers & Liu, 2013; Gagné et al., 2015, 2017a, 2018a; Liu et al., 2016; Faherty et al., 2016; Schneider et al., 2016, 2017; Zhang et al., 2021c) These objects share similar properties with directly-imaged exoplanets, including mass, surface gravity, effective temperature, and spectral type. The study of these ultracool planetary-mass objects provides a unique opportunity to understand the atmospheres of giant exoplanets, as observations of giant exoplanets are often hindered by the brightness of the central stars. In contrast, young planetary-mass brown dwarfs are free-floating analogues to giant exoplanets. This makes them ideal targets for atmospheric characterization of planetary-mass objects, which opens a window to understand the atmospheres of giant exoplanets.

As brown dwarfs rotate, inhomogeneous atmospheric structures may cause variability in their light curves. Brown dwarfs are usually fast-rotators with periods varying from 1–2 hr to 1–2 d (e.g. Zapatero Osorio et al., 2004; Metchev et al., 2015; Scholz et al., 2018; Moore et al., 2019). Numerous observations have been conducted to search for atmospheric variability in field L and T

brown dwarfs. The first continuous monitoring survey, by Koen et al. (2004), detects low-level variability of less than 0.02 mag in 18 L and T dwarfs observed simultaneously in the JHK_S bands. A similar result is reported in their follow-up survey of ultracool dwarfs, with the exception of one T dwarf which shows a variability of 0.03 mag (Koen et al., 2005). A large survey of L4–T9 dwarfs in the J-band by Radigan et al. (2014) detects variability in 9 out of 57 dwarfs with over 99% confidence. The strongest signals, with peak-to-peak amplitudes over 2%, are all detected at the L/T transition (L9–T3.5), indicating that variability is most common among L/T transition brown dwarfs. Combining two large surveys by Radigan et al. (2014) and Wilson et al. (2014), Radigan (2014) report the observed frequency of strong variability is 24% at the L/T transition compared with 3.2% outside the L/T transition. These results support the theory that inhomogeneous atmospheric structures such as patchy clouds at the L/T transition are the driving sources of the observed variability.

Brown dwarfs contract as they age, and thus low surface gravity is often associated with young brown dwarfs. Surface gravity plays an important role in shaping the atmospheric structures of brown dwarfs, such as affecting dust particle size and non-equilibrium chemistry (Barman et al., 2011a,b; Marley et al., 2012). Morley et al. (2014) raise a possible link between low surface gravity and variability as planetary-mass objects tend to have thicker clouds than high-mass brown dwarfs. Metchev et al. (2015) present a variability survey of 44 L3–L8 dwarfs with the *Spitzer Space Telescope* and confirm that variability is common in L and T dwarfs with 80% of L dwarfs varying more than 0.2% and 36% of T dwarfs varying more than 0.4% in the mid-infrared. They suggest a tentative association between low surface gravity and strong variability based on six L3–L5.5 dwarfs with low gravity. Vos et al. (2019) report the first variability survey of 30 young and low-gravity L dwarfs in the J_S band and find a variability occurrence rate of 30% for low-gravity L0–L8.5 dwarfs, significantly higher than the 11% variability occurrence rate of the field L0–L8.5 dwarfs reported in Radigan et al. (2014); Radigan (2014). Vos et al. (2022) also find higher maximum variability amplitudes in young objects than field dwarfs in *Spitzer* data.

Several young low-surface gravity objects with strong variability have been discovered in recent years. For instance, PSO318.5-22 (Biller et al., 2015; Vos et al., 2019), VHS1256-1257b (Zhou et al., 2020), WISEP J004701.06+680352.1(Lew et al., 2016), and 2MASS J2244316+204343 (Vos et al., 2019) are detected with peak-to-peak amplitudes $>$ 5% in the near-infrared, which are young L6–L7.5

objects. Additionally, two strong variable T dwarfs, SIMP J013656.5+093347 (T2.5) and 2MASS J21392676+0220226 (T1.5), were initially classified as field dwarfs but were later confirmed as planetary-mass objects of the 200-Myr-old Carina-Near moving group (Gagné et al., 2017b; Zhang et al., 2021c). SIMP J013656.5+093347 is detected with a peak-to-peak amplitude of 8% in the J band with a period of 2.4 hr (Artigau et al., 2009; Radigan et al., 2014). 2MASS J21392676+0220226 has a 26% peak-to-peak amplitude in the J band with a 7.7-hour periodic modulation and night-to-night variations (Radigan et al., 2012).

Although we have a number of young L-type planetary-mass objects, there were few known young T-type objects. Only one of them has been monitored for variability in the near-infrared (Ross 458c, Manjavacas et al., 2019b) and several have been monitored for variability in the mid-infrared (Vos et al., 2022). Identifying young T-type objects is more challenging, as they do not have prominent spectral features associated with surface gravity. Zhang et al. (2021c) identify 30 new T0–T9 planetary-mass candidates of nearby young moving groups (YMG) based on their proper motions, parallaxes and available radial velocities, providing a sizeable sample of young T-type objects suited for time-resolved photometric studies. In this work, we present a first near-infrared variability survey of these T-type planetary-mass objects, which also includes several young mid-late L objects without existing variability monitoring, with the aim of estimating their variability rates, as it was performed earlier with young L dwarfs. Combining the results with previous surveys of field and young low-gravity L and T dwarfs, we make a statistical analysis of the variability of field and young objects from L0–T9 and investigate how variability properties depend on the spectral type and surface gravity.

2.3 Sample

From the new planetary-mass candidate members detected in Zhang et al. (2021c), we selected 12 objects with spectral types of T2.5–T8 that are bright enough (J <~17.5 mag) for variability monitoring with a ground-based 4-m class telescope in the southern hemisphere. We also included six young L5–L7 dwarf candidate members identified with spectral and kinematic information from Kellogg et al. (2016), Schneider et al. (2016) and Schneider et al. (2017). In total, our sample consists of 18 L5–T8 YMG candidate members with

masses $\leq$20 $M_{\rm J}$ and ages $\leq$200 Myr without previous near-infrared variability observations. They are members of the AB Doradus (149^{+51}_{-19} Myr, Bell et al., 2015), Argus (40–50 Myr, Zuckerman, 2019a), β Pictoris (22±6 Myr, Shkolnik et al., 2017), Carina-Near (200±50 Myr, Zuckerman et al., 2006) and TW Hydrae (TWA, 10±3 Myr, Bell et al., 2015) moving groups. There are two known planetary-mass binaries in our sample, 2MASS J11193254–1137466AB (Best et al., 2017b) and 2MASSI J1553022+153236AB (Dupuy & Liu, 2012), but neither are resolved in our observations. Table 2.1 lists the key information of these objects.

2.4 Observations and data reduction

2.4.1 Observations

We conducted the first epoch survey of our 18 targets for 17 nights between October 2021 and June 2022 with the infrared spectrograph and imaging camera, Son of ISAAC (SOFI) on the 3.58 m ESO New Technology Telescope (NTT) at the La Silla Observatory (Moorwood et al., 1998). Brown dwarfs tend to have strong variability in the J band (Radigan et al., 2014), so our targets were primarily monitored in the J_S band. For targets that are extremely faint in J but much brighter in K, we observed them in the K_S band. For the two TWA objects with known variability at mid-infrared wavelengths, we obtained interleaved observations in the J_S and K_S band. The J_S band has a center wavelength at 1.24 μm with a width of 0.29 μm, avoiding the water band at 1.4 μm in the J band; the K_S band is at 2.16 μm with a width of 0.28 μm, avoiding the atmospheric absorption feature at 1.9 μm and elevated thermal background beyond 2.3 μm in the K band. The field of view of SOFI is 4.′92 × 4.′92 with a pixel scale of 0.″288. Each target has continuous observations of 1.5–7.5 hr. The observations were affected by poor seeing in the October 2022 run and by clouds in the June 2022 run. We conducted a second epoch of ten nights between October 2022 and May 2023 to re-observe objects observed in poor conditions and confirm variables detected in the first epoch. Table 2.2 summarises the observing log.

Our targets were observed at airmass <2. We used an ABBA nod pattern with three exposures at each position and 12 exposures in a loop. For each exposure, the detector integration time (DIT) is 20 s and the number of DIT (NDIT) is 3

Table 2.1: Object information. Spectral type (SpT), magnitude, and membership with BANYAN II or BANYAN Σ (ref 4) probability are from the literature (Ref). The last column is the variability results in this work. Four variables are detected with two potential variable candidates.

Name	SpT	*J*	*H*	*K*	Mag	Binary	Membership	Ref	Variable
WISEA J004403.39+022810.6	L7	16.997±0.187	15.822±0.169	14.876±0.105	2MASS	N	Beta Pic (78%)	1	N
WISEA J020047.29-510521.4	L6	16.414±0.120	14.941±0.069	13.871±0.050	2MASS	N	AB Dor (98%)	1	N
WISEA J022609.16-161000.4	L6	17.334±0.266	15.750±0.142	14.581±0.093	2MASS	N	AB Dor (85%)	1	?
WISEA J114724.10-204021.3	L7	17.637±0.058	15.764±0.106	14.872±0.106	2MASS	N	TWA (96%)	2	Y
2MASS J11193254-1137466	L7	17.474±0.058	15.788±0.034	14.751±0.012	2MASS	Y	TWA (92%)	3	Y
WISE J024124.73-365328.0	T7	16.59±0.04	17.04±0.07	—	MKO	N	Argus (87.7%)	4	N
CFBDS J232304.41-015232.3	T6	17.23±0.03	17.46±0.04	17.30±0.03	MKO	N	Beta Pic (89.1%)	4	Y
WISEPCJ225540.74-311841.8	T8	17.33±0.01	17.66±0.03	17.42±0.05	MKO	N	Beta Pic (98.7%)	4	N
SDSSJ020742.48+000056.2	T4.5	16.73±0.01	16.81±0.04	16.72±0.05	MKO	N	Arg (95.6%)	4	N
WISEPAJ081958.05-033529.0	T4	14.78±0.02	14.60±0.05	14.64±0.05	MKO	N	Beta Pic (86.3%)	4	Y
ULASJ131610.13+031205.5	T3	16.75±0.02	16.13±0.02	15.43±0.02	MKO	N	Carina-Near (91.7%)	4	N
ULASJ081918.58+210310.4	T6	16.95±0.01	17.28±0.04	17.18±0.16	MKO	N	AB Dor (86.3%)	4	N
ULASJ075829.83+222526.7	T6.5	17.62±0.02	17.91±0.02	17.87±0.12	MKO	N	Arg (92.7%)	4	N
PSOJ168.1800-27.2264	T2.5	17.12±0.03	16.75±0.03	16.65±0.06	MKO	N	Arg (83.4%)	4	N
SDSSJ152103.24+013142.7	T3	16.10±0.01	15.68±0.01	15.57±0.02	MKO	N	Arg (82.3%)	4	N
WISE J163645.56-074325.1	T4.5	16.42±0.02	16.28±0.05	16.32±0.05	MKO	N	AB Dor (81.6%)	4	N
2MASSI J1553022+153236AB	T7	15.34±0.03	15.76±0.03	15.94±0.03	MKO	Y	Carina-Near (89.6%)	4	?
WISEA J043718.77-550944.0	L5	16.985±0.192	15.583±0.157	14.640±0.098	2MASS	N	Beta Pic (94%)	1	N

References: (1) Schneider et al. (2017); (2) Schneider et al. (2016); (3) Kellogg et al. (2015); (4) Zhang et al. (2021c).

in the J_S band and 10 s and 6 in the K_S band, respectively. For the interleaved observation, every 12 exposures in the J_S band were followed by 12 exposures in the K_S band. The peak intensity of the point spread function (PSF) of the target was kept below 10,000 ADU to prevent non-linearity effects.

Table 2.2: Observing log.

Date	Object	Band	DIT×NDIT (s)	FWHM[a] (arcsec)	FWHM std[b] (arcsec)	Elapsed time (hr)
2021-10-20	J0044+0228	J_S	20×3	1.45	0.18	3.75
2021-10-20	J0200-5105	J_S	20×3	1.48	0.32	4.91
2021-10-21	J0241-3653	J_S	20×3	1.59	0.11	3.27
2021-10-21	J2323-0152	J_S	20×3	1.24	0.18	5.58
2021-10-22	J0226-1610	J_S	20×3	1.36	0.15	4.35
2021-10-22	J2255-3118	J_S	20×3	1.12	0.14	4.52
2021-10-23	J0044+0228	J_S	20×3	1.54	0.20	2.04
2021-10-23	J0207+0000	J_S	20×3	1.45	0.17	3.91
2021-10-23	J0241-3653	J_S	20×3	1.30	0.16	3.20
2021-10-24	J2323-0152	J_S	20×3	0.79	0.22	4.11
2021-10-24	J0226-1610	J_S	20×3	1.02	0.13	4.73
2022-02-10	J0819-0335	J_S	20×3	0.89	0.09	4.63
2022-02-10	J1316+0312	J_S	20×3	0.92	0.11	4.37
2022-02-11	J0819+2103	J_S	20×3	1.29	0.14	3.53
2022-02-11	2M1119-1137AB	K_S	10×6	0.88	0.10	4.47
2022-02-12	J0819-0335	J_S	20×3	1.17	0.18	3.13
2022-02-12	2M1119-1137AB	J_S	20×3	1.26	0.17	5.28
2022-02-12	2M1119-1137AB	K_S	10×6	1.11	0.14	5.29
2022-02-13	J0200-5105	J_S	20×3	1.58	0.28	1.92
2022-02-13	W1147-2040	K_S	10×6	1.34	0.13	7.31
2022-02-14	J0437-5509	K_S	10×6	0.96	0.10	2.80
2022-02-14	W1147-2040	J_S	20×3	0.93	0.11	5.80
2022-02-14	W1147-2040	K_S	10×6	0.91	0.10	6.32
2022-02-17	J0758+2225	J_S	20×3	0.94	0.12	3.19
2022-02-18	PSO168-27	J_S	20×3	1.06	0.24	4.10
2022-02-19	PSO168-27	J_S	20×3	0.84	0.16	4.96
2022-06-16	SDSSJ1521+0131	J_S	20×3	1.67	0.26	5.14
2022-06-16	J2323-0152	J_S	20×3	1.41	0.09	1.62
2022-06-17	WISEJ1636-0743	J_S	20×3	0.91	0.16	5.50
2022-06-17	J2323-0152	J_S	20×3	0.90	0.06	1.81
2022-06-18	SDSSJ1521+0131	J_S	20×3	0.71	0.05	2.06
2022-06-18	2M1553+1532	J_S	20×3	0.81	0.15	4.00
2022-06-19	WISEJ1636-0743	J_S	20×3	0.92	0.12	1.90
2022-10-09	J2323-0152	J_S	20×3	1.09	0.17	5.00
2022-10-09	J0200-5105	J_S	20×3	1.36	0.17	3.94
2022-10-10	J2323-0152	J_S	20×3	1.09	0.16	4.48

Table 2.2 (Continued)

Date	Object	Band	DIT×NDIT (s)	FWHM[a] (arcsec)	FWHM std[b] (arcsec)	Elapsed time (hr)
2022-10-10	J0200-5105	J_S	20×3	0.92	0.09	2.98
2022-11-02	J0226-1610	J_S	20×3	0.72	0.10	3.01
2022-12-03	J0200-5105	J_S	20×3	0.70	0.07	3.96
2022-12-03	J0819-0335	J_S	20×3	0.68	0.09	3.99
2022-12-04	J0226-1610	J_S	20×3	0.75	0.12	3.00
2022-12-04	J0819-0335	J_S	20×3	0.91	0.11	3.25
2023-05-06	W1147-2040	K_S	10×6	1.34	0.23	3.38
2023-05-07	2M1119-1137AB	K_S	10×6	0.81	0.12	4.18
2023-05-07	2M1553+1532	J_S	20×3	1.43	0.11	1.56
2023-05-08	2M1119-1137AB	K_S	10×6	0.98	0.15	4.88
2023-05-08	SDSSJ1521+0131	J_S	20×3	0.98	0.07	1.34
2023-05-09	2M1553+1532	J_S	20×3	1.18	0.23	3.00
2023-05-09	WISEJ1636-0743	J_S	20×3	0.99	0.14	1.87
2023-05-09	W1147-2040	K_S	10×6	0.89	0.20	5.80
2023-05-09	W1147-2040	J_S	20×3	0.94	0.24	5.28
2023-05-10	2M1119-1137AB	K_S	10×6	0.84	0.11	4.92
2023-05-10	2M1553+1532	J_S	20×3	1.10	0.09	3.05
2023-05-10	WISEJ1636-0743	J_S	20×3	0.95	0.08	2.49

Notes: We measured the median full width at half maximum (FWHM) of all stars in each target's field of view.
(a) Median FWHM of all frames; (b) Standard deviation FWHM of all frames.

2.4.2 Raw image reduction

We followed the data reduction steps in the SOFI manual to reduce raw images, which is also presented in Vos et al. (2019). 1) Cross talk removal: a bright source can cause a ghost affecting the row where the source is and also the row in the other half of the detector, referred to as inter-quadrant row cross talk. These can be removed by subtracting 1.4×10^{-5} times the integrated flux of the row. 2) Flat fielding and shade pattern removal: when taking a flat, there is a difference between the shade pattern in the image with the lamp on and lamp off. Therefore, eight special dome flats were taken to do the flat-fielding including removing the residual shade pattern with the lamp on and off. 3) Illumination correction: the illumination of the dome panel is different from that of the sky, so a grid of 16 observations of a standard star was taken and we fitted a 2D surface to the photometry of the 16 positions to correct the difference in illumination between the dome panel and sky. 4) Sky subtraction and dark current correction:

we subtracted frames by frames of different nods and closest in time to remove the fast-varying thermal background and also the dark current. We scaled the frame by the median flux ratio between it and the subtracted frame before the subtraction. 5) Bad pixel flagging: bad pixels were identified in the flat frame. The median of the flat frame was obtained after three sigma clipping. Pixels with flux deviation larger than 10 sigma from the median value were identified as bad pixels. The bad pixel map provided by ESO, which was created in 2012, was also combined into the final bad pixel map.

2.4.3 Aperture photometry

We used DAOStarFinder from the photutils python package to detect sources in an image and fitted a 2D Gaussian model to the detected sources to accurately measure their positions. Then we performed aperture photometry on the detected stars with a series of aperture sizes fixed to all frames. We also took the median after three-σ clip of a concentric annulus as the local background of the star and subtracted it from the aperture measurement. The inner radius of the annulus is 18 pixels and the outer radius of the annulus is 24 pixels. The final aperture size we used is determined in the light curve analysis as described below.

2.4.4 Light curve analysis

The raw light curves contain conspicuous systematics, including the effects of seeing, airmass, atmosphere, and instrument. We selected reference stars in the field of view of the target to calibrate and remove these systematics. At first, we excluded extremely faint stars and bright stars with flux in the non-linear regime ($>$ 10,000 ADU). Second, for each star, the raw light curves of different nods were normalised by their own medians. Then the normalised light curves of different nods were corrected to the same baseline. This step scales the light curves of different stars to the same level. We then selected a set of well-behaved reference stars to build a calibration light curve for the target. We used the same iteration algorithm from Radigan et al. (2014) and Vos et al. (2019). First, stars affected by bad pixels were discarded. Then for each star, its calibration light curve was created from the median light curve of the other candidate reference stars. We divided the calibration light curve from the light curve of the star to remove the

variations caused by systematics. Good reference stars should have no intrinsic variations and have flat light curves after detrending. To exclude the effects of outliers, we calculated the robust standard deviation and robust linear slope of detrended light curves. Stars with sigma and slope <~1.2–3 times that of the target were retained for the next iteration. These steps were repeated several times until a set of well-behaved reference stars was chosen. We further removed some reference stars that showed variability after the iteration algorithm by visual inspection. We applied this iteration algorithm to light curves of different aperture sizes. For each target, the final aperture we used was the same as or close to the median full width at half maximum (FWHM) of the PSFs of all stars in all frames of the target, which results in the smallest photometric noise. The photometric noise of the detrended light curve, $\sigma_{\rm pt}$, was estimated by the robust standard deviation of the subtraction of a light curve shifted by one time bin from the original light curve, divided by $\sqrt{2}$, the same method used in Radigan et al. (2014). This method is sensitive to high-frequency noise but not sensitive to low-frequency noise such as intrinsic astrophysical variability trends in light curves. It performs better than the standard deviation in quantifying the photometric noise and uncertainty of detrended light curves, especially for variable targets.

2.5 Variability analysis

The variability of the targets was detected using a periodogram analysis of their detrended light curves. We used the Lomb-Scargle (LS) periodogram method as the primary analysis tool (Lomb, 1976; Scargle, 1982). We also used a secondary analysis, the Bayesian Generalised Lomb-Scargle (BGLS) periodogram, to independently verify the peaks in the LS periodogram (Mortier et al., 2015). Manjavacas et al. (2018) find that unlike LS, BGLS is insensitive to gaps in light curves. BGLS calculates the relative probability between peaks rather than the power spectrum calculated by the LS periodogram. The peaks detected in the BGLS periodogram agree with those detected in the LS periodogram of our light curves. We also calculated the LS periodogram of detrended reference light curves, the seeing curve over the observation and the window function of the observation cadence. If the peaks in these periodograms matched those in the target light curve, they were considered false detections due to residual systematic effects. The window function was calculated as a light curve with a flux of 1 without pre-centering or using a floating-mean model in the LS calculation (VanderPlas,

2018).

To assess the significance of the peaks in the periodogram, we calculated the 1% false-alarm probability (FAP) level using the Astropy.timeseries Python package. We used the bootstrap option in that routine to calculate the peak level of 1% FAP, which is equivalent to simulating the light curve and calculating the periodogram over 10^3 times. Radigan et al. (2014) and Vos et al. (2019) calculated the 1% FAP level also by randomly permuting reference star light curves 1000 times and the β factor of every light curve which is the peak value in its periodogram divided by the 1% FAP level. They expected to have 1% reference stars with a β factor above 1 but found that more than 1% reference stars peaked above this level. Therefore, they scaled the 1% FAP level by a factor between 1.4 and 3.4. Because we included the light curve uncertainty in the LS periodogram calculation and applied the 'standard' normalisation in that routine, the power spectra value should not be compared directly between the target and reference star light curves. We also randomly permuted the target light curve 1000 times and found that the 1% FAP level calculated automatically by the bootstrap routine in Astropy.timeseries is always higher than the 1% FAP level calculated by our version of 1000 random permutations of the target light curve. We adopted the 1% FAP level calculated with Astropy.timeseries. We also calculated the β factor by dividing the periodogram power peak of every light curve by its own 1% FAP level. Four out of 216 reference stars fall above $\beta = 1$ in Fig. 2.1, which is close to 1%. Eriksson et al. (2019) used the 0.1% FAP level with the Astropy routine for the variability detection in their light curves. We also calculated the 0.1% FAP level and found our confirmed detections remain significant when using this level.

If the peak in the target periodogram is above the 1% FAP level and the detrended light curve has a well-behaved appearance upon visual inspection, the target is identified as a variable object; if the peak in the target periodogram is above the 1% FAP level but the detrended light curve is not well-behaved, it is identified as a potential variable candidate; if no peak in the periodogram exceeds the 1% FAP level, the object is identified as non-variable in this survey. While the period of the detected variability can also be estimated from the periodogram, many targets did not have a clearly defined peak in their periodogram, indicating the presence of long-term variability that exceeds the duration of our observations. In these cases, we can only place lower limits on the period.

We also calculated the instrumental magnitude and median absolute deviation

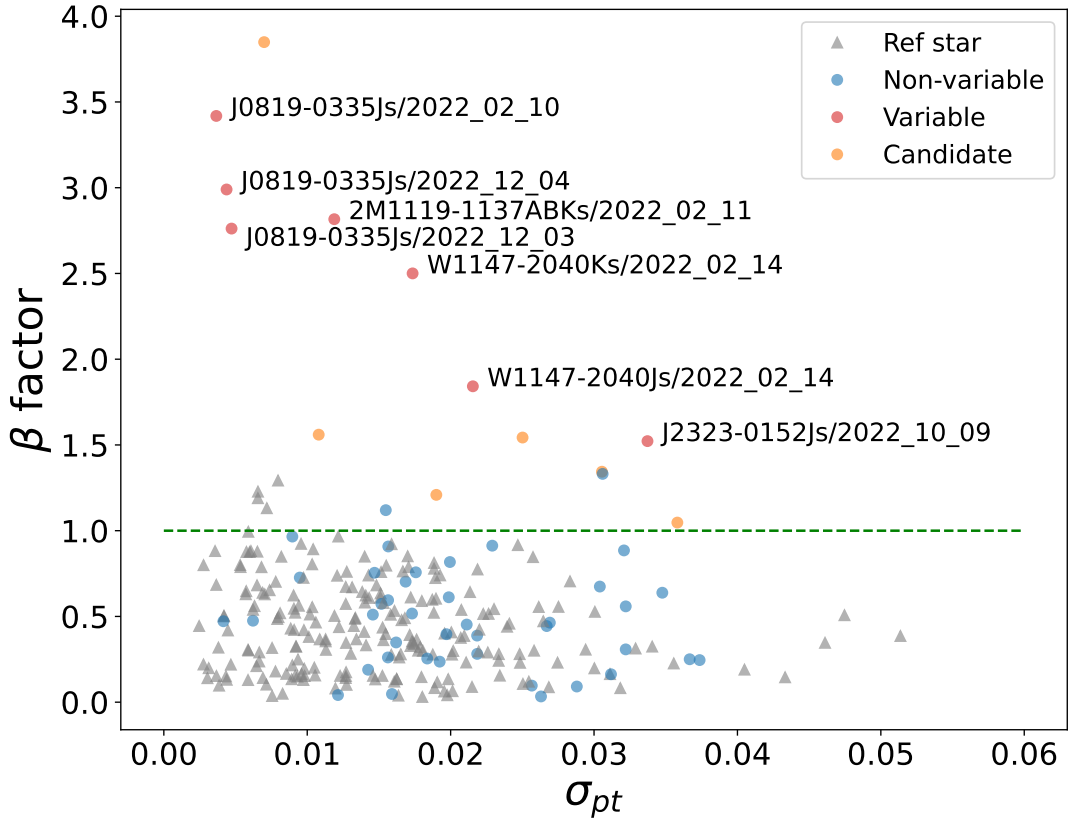


Figure 2.1: β factor against the photometric error of a detrended light curve, $\sigma_{\rm pt}$. The β factor is calculated by the periodogram power peak of every light curve divided by its own 1% FAP level. The four confirmed variable targets (red) fall above $\beta = 1$. 1.8% of reference stars fall above $\beta = 1$, which is very close to the expected value, 1%. Potential variable candidates are orange circles and non-variable targets are blue circles. The reference stars are shown by grey triangles.

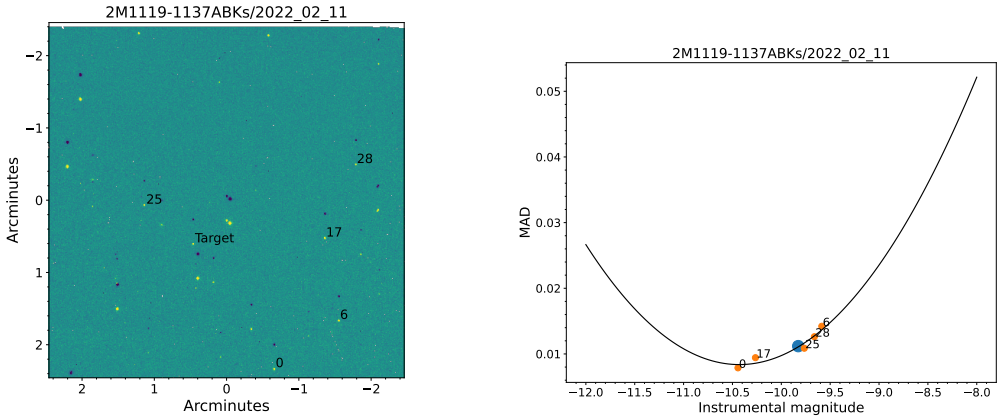


Figure 2.2: Target 2M1119-1137AB in the K_S band and the selected reference stars of the observation on 11 Feb 2022. Left panel: sky-subtracted image. It is one nod subtracted from the other nod, which results in these dark sources. The textual label of the reference stars is their original number before the reference star selection. North is left and east is down. Right panel: MAD and instrumental magnitude of the reference stars (orange) and target (blue). The black line is a second-order polynomial fitting to the reference stars. This target meets the MAD-magnitude relationship of the reference stars but it is variable.

(MAD) of the detrended light curve which is similar to the standard deviation but not sensitive to outliers. Although MAD increases generally with fainter stars, we do not find a consistent relationship between the MAD and the instrumental magnitude between different observations. For some observations, their relationship can be fitted with a second-order polynomial as the relationship presented Martín et al. (2001). For some observations, there is not a monotonous relationship between MAD and the instrumental magnitude. Figure 2.2 shows one object 2M1119-1137AB and the selected reference stars and their MAD-magnitude relationship. The same figures for all other observations can be found in Appendix A.1. Therefore, using the relationship between the standard deviation and the magnitude to do variability analysis as the method used in Martín et al. (2001) is not applicable to our datasets.

2.6 Sensitivity calculation

To estimate our detection sensitivity for each observation, we injected artificial sinusoidal curves into randomly permuted detrended target light curves. For variable light curves, we fitted a low-order polynomial fitting or a sinusoidal curve before the injection to remove its variability. The injected peak-to-peak amplitude

Table 2.3: Detected variables in this work. The amplitude is the peak-to-peak amplitude. Binaries are not resolvable with NTT.

Target	SpT	Band	Amplitude	Period (hr)	Binary
2M1119-1137AB	L7	K_S	3.2±0.8%	6.9±1.6	Y
W1147-2040	L7	J_S	4.6±1.0%	11.2±3.8	N
		K_S	4.8±0.4%	5.5±0.2	
J0819-0335	T4	J_S	1.8±0.8%	Long	N
J2323-0152	T6	J_S	~ 7.6%	Long	N

(2×amplitude of the sinusoidal curve) varies from 0.5% to 10% and the period varies from 1.5 to 20 hours. In each grid, we injected the sinusoidal curves 1000 times and calculated the detection rate. The successful retrieval criterion is that the peak of the injected curves in the periodogram is above the 1% FAP level.

2.6.1 Significant detections

WISEPAJ081958.05-033529.0: this T4 dwarf is a high-probability member of the β Pictoris young moving group identified by Zhang et al. (2021c) with trigonometric parallax, though it needs an RV measurement for confirmation. Assigning an age of ~20 Myr to it, it has an estimated mass of ~ 5.7 $M_{\rm J}$ (Zhang et al., 2021c). We observed it on four nights in the J_S band: 10 Feb 2022 and 12 Feb 2022 in the first epoch and 03 Dec 2022 and 04 Dec 2022 in the second epoch. We detected variability on three nights but not on 12 Feb 2022. The variable light curves are shown in Fig. 2.4 and the non-variable light curve is in Appendix A.3. The light curve of 10 Feb 2022 presents an obvious downward slope. We fit a line to it using the least-squares algorithm and find a peak-to-peak variability amplitude (max-min) of 1.2 ± 0.1% in the 4.63-hour observation. This variability is far above the 1% FAP level in its periodogram. If it is a periodic signal, the period is longer than the observation length. As our observation does not cover a full rotation, the fitted variability amplitude is a lower limit. We detected no variability on 12 Feb 2022. The light curve of 12 Feb 2022 has a marginal downward slope by visual inspection but it is not detected in its periodogram. The relatively poorer seeing of the second night degrades the detection sensitivity, which can be seen from its sensitivity plot. In fact, the variability of the first night would not be detectable on the second night. It is one of the reasons why there is no variability detection on the second night. Another reason could be that the object has a long rotation period and reached the peak of its light curve on 12 Feb

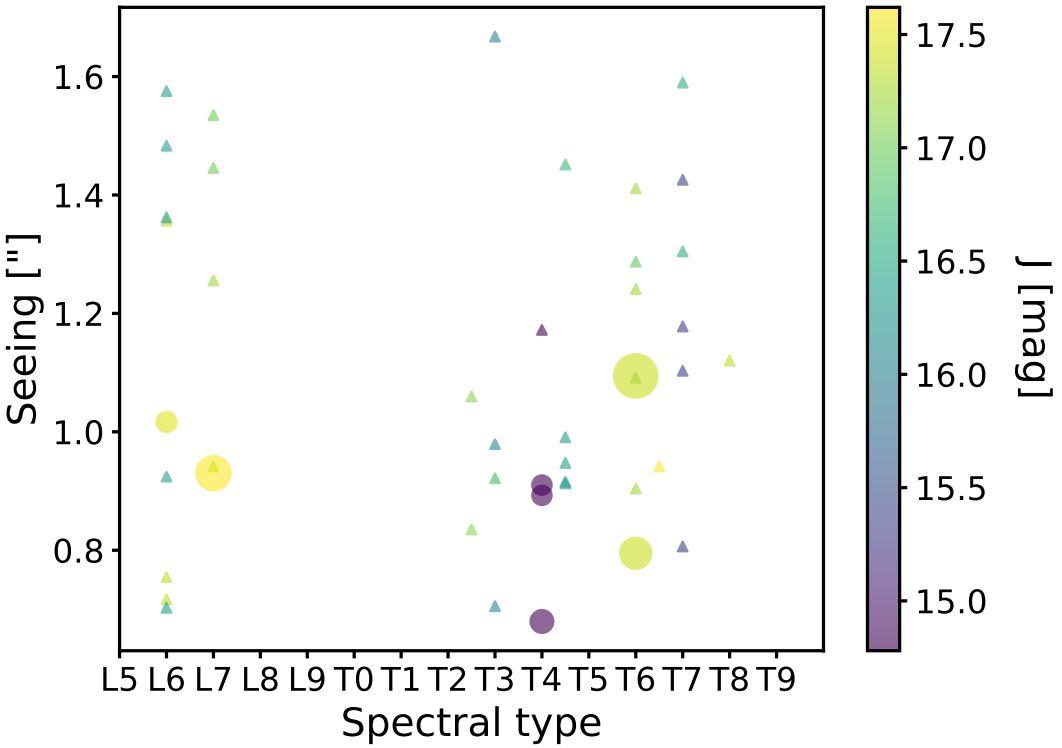


Figure 2.3: Observation and detection diagram in the J_S band. Circles represent positive detections with the radius proportional to the variability amplitude. Triangles represent non-detection observations. The colour represents the apparent magnitude of the target in the J band. All variable detections were observed under a seeing $<1\farcs1$, while they do not have a strong dependence on the magnitude.

2022 where relative variability would be lower as compared to the slope between extrema and thus it does not present an apparent relative variability during the three-hour observation.

We fit a second-order polynomial curve to the light curve of 03 Dec 2022 and measure a peak-to-peak amplitude of 1.8±0.8%. If it is a periodic signal, its period is longer than the observation length, 4 hr. Fitting a sinusoidal curve to the light curve of 04 Dec 2022, we measure a peak-to-peak amplitude of 1.2±0.1% with a period of 2.6±0.1 hr. We suspect that J0819-0335 has a period >5 hr and the light curve was transitioning from a downward to an upward trend during the observation on 04 Dec 2022. This is why a short-period sinusoidal light curve was observed. Further longer continuous observations are necessary to determine the true period of this young object.

2MASS J11193254-1137466AB: 2M1119-1137AB has extremely red optical and near-infrared colours (Kellogg et al., 2015). It was first characterised as a low-mass L7 dwarf and a high probability candidate of the TW Hydrae Association (TWA) by Kellogg et al. (2015, 2016). Best et al. (2017b) resolve it to be a binary system of two similar $\sim 3.7\,M_{\rm J}$ L7 brown dwarfs with a separation of $0\farcs14$, adopting the 10 Myr age of TWA. The orbital period of this system is about 90 years. It is a flux reversal binary as one component is slightly brighter in the J band but fainter in the K band. Schneider et al. (2018) report mid-infrared variability with a period of $3.02^{+0.04}_{-0.03}$ hr and semi-amplitudes of $0.230^{+0.036}_{-0.035}$% at 3.6 μm and 0.453±0.037% at 4.5 μm for this system in *Spitzer* observations. These light curves have also been suggested to show evidence of an exomoon (Limbach et al., 2021). SOFI was unable to resolve this system. We observed it on two continuous nights in the first epoch: 11 Feb 2022 in the K_S band and 12 Feb 2022 interleaved in the J_S and K_S band. We detected significant variability on the first night as shown in Fig. 2.5. We fit a sinusoidal curve to the light curve in the K_S band using the Levenberg-Marquardt least-squares (LM) method and find a peak-to-peak amplitude of 3.2±0.8% and a period of 6.9±1.6 hr. Our observation does not cover a complete cycle and thus this period needs further confirmation.

This period is longer than the variability period of 3.02 hr at 3.6 and 4.5 μm reported by (Schneider et al., 2018). To fit a sinusoidal curve with a fixed period of 3.02 hr, we need to add a linear term of 0.0047t to the sinusoidal curve as shown in Fig. 2.6, yielding a semi-amplitude of 0.86% for the sinusoidal curve. As 2M1119-1137AB is a binary system, the linear term and sinusoidal term could be attributed to the two components respectively. Schneider et al. (2018) suspect

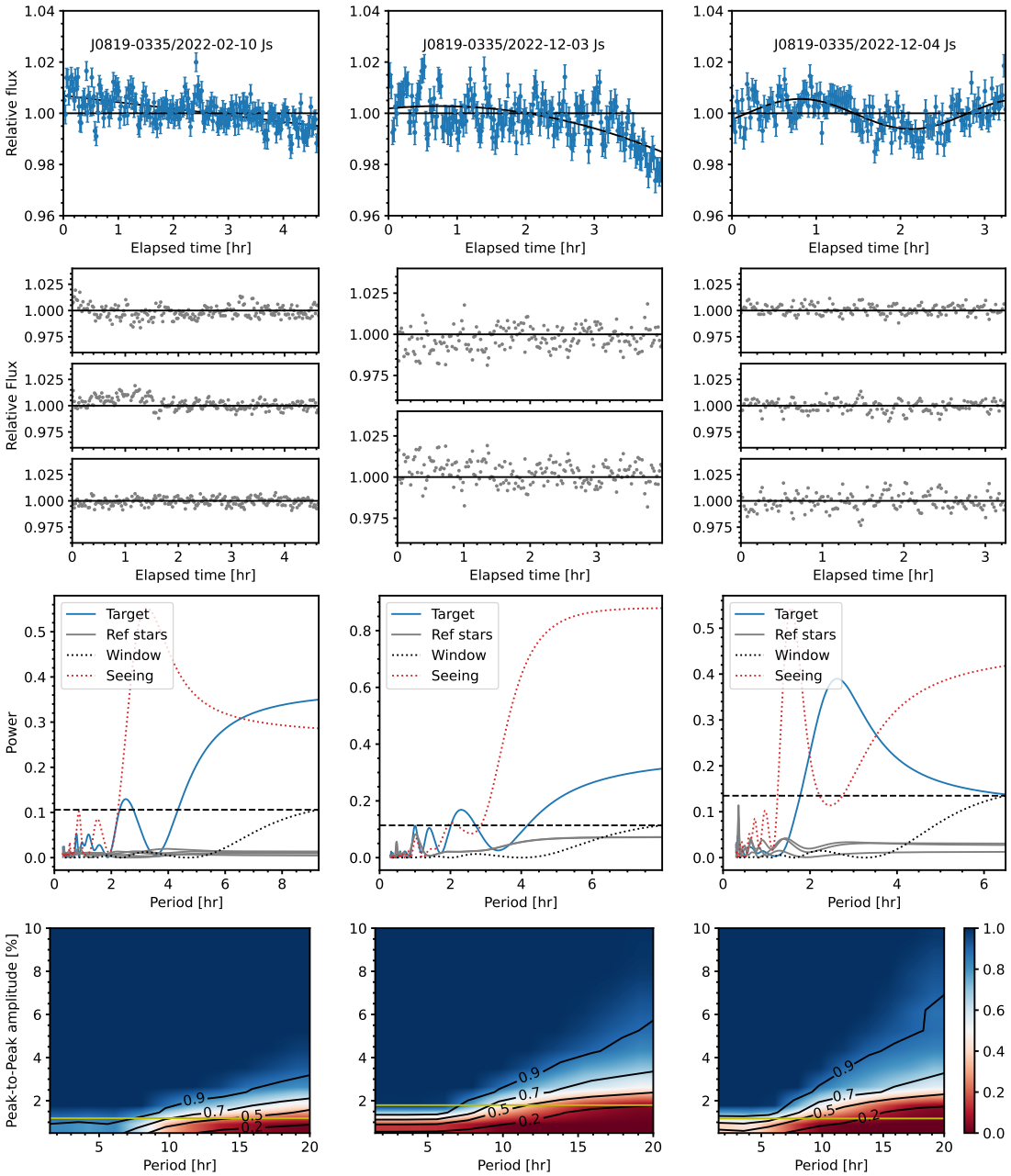


Figure 2.4: Results of a variable object, J0819-0335. Top row: detrended light curve. Second row: detrended light curve of its reference stars (show up to three stars). Third row: Lomb-Scargle periodogram of the detrended light curve of the target. We also include the periodograms of the detrended light curves of reference stars, seeing curve, and window function. They help to identify unremoved systematic variability in the detrended light curve of the target. The dashed line is the 1% FAP level of the target. Bottom row: sensitivity plot calculated from injected signals. The yellow line shows the measured amplitude. The X-axis and Y-axis are the period and peak-to-peak amplitude of the injected sinusoidal signal, respectively. The colour bar is the retrieval rate by our method, ranging from 0 to 1. The signal is injected into the variability-removed light curve of the target.

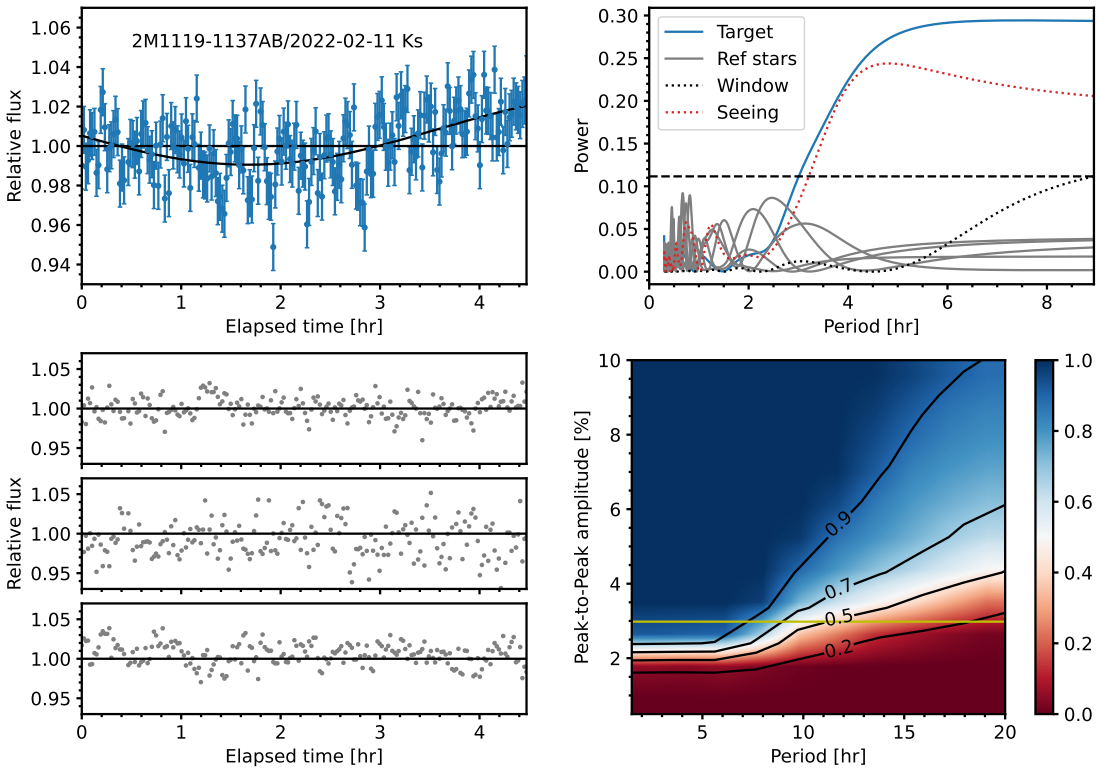


Figure 2.5: Variable light curve, periodogram and sensitivity plot of 2M1119-1137AB, including detrended light curves and periodograms of its reference stars. The variability is detected in the K_S band.

that their measured variability with the period of 3.02 hr possibly comes from one component of the binary, similar to the L7.5+T0.5 binary WISE J104915.57-531906.1AB (Burgasser et al., 2014). Further observations with larger telescopes such as the very large telescope (VLT) are necessary to resolve the variability of the two components. If confirmed, 2M1119-1137AB would be one of the few young L and T dwarfs with periods < ~3 hours. As brown dwarfs are expected to rotate faster as they age and contract because of angular momentum conservation (Schneider et al., 2018), young objects with short periods are rare.

The second night was observed under poorer seeing conditions than the previous night and we did not detect any variability. The ~3% variability of the first night could not be reliably detected under the conditions of the second night. We observed it another three times in May 2023 in the K_S band but detected no variability due to poor seeing or clouds. The non-detection results can be found in Appendix A.3.

WISEA J114724.10-204021.3: W1147-2040 is an L7 dwarf with an extremely red 2MASS $J - K_S$ colour and a mass of 5–13 M_J (Schneider et al., 2016). Its

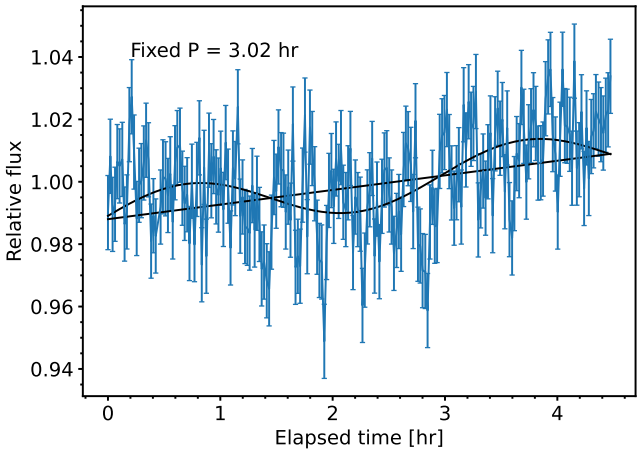


Figure 2.6: Variable light curve of 2M1119-1147AB, fitted with a linear term and a sinusoidal curve with a fixed period of 3.02 hr, which is its variability period at 3.6 and 4.5 μm. Its K_S-band light curve can be depicted by two variability terms which may come from the two components.

spectrum has obvious evidence of youth. Schneider et al. (2016) identify it as a high probability member of the TWA using its sky position and proper motion. Schneider et al. (2018) find variability with a period of $19.39^{+0.33}_{-0.28}$ hr by combining its *Spitzer* light curves at 3.6 μm and 4.5 μm. The light curves have a semi-amplitude of $0.798^{+0.081}_{-0.083}$% and $1.108^{+0.093}_{-0.094}$%, respectively. We observed it on two consecutive nights: 13 Feb 2022 and 14 Feb 2022. It was monitored in the K_S band on the first night under relatively poor seeing conditions and we did not detect significant variability. These plots are in Appendix A.3. The observations on the second night were interleaved in the J_S and K_S band with seeing about 0.″9. We detect variability in both bands with significance higher than 99% as shown in Fig. 2.7. We fit a sinusoidal curve to each light curve using the LM method. We find a peak-to-peak amplitude of 4.6±1.0% with a period of 11.2±3.8 hr in the J_S band and a peak-to-peak amplitude of 4.8±0.4% with a period of 5.5±0.2 hr in the K_S band. The K_S band light curve just covers a full period while the J_S band light curve does not. The periods in the J_S band, K_S band, and mid-infrared of this target are quite different. We are cautious about whether these differences are astrophysical since these observations are relatively short compared to their measured periods. We also fit the curves with a sinusoidal curve with the period in the mid-infrared. The fitting in the J_S band is acceptable while the K_S band is poorly-fitted. We did follow-up observations of it on 06 May 2023 in the K_S band and on 09 May 2023 interleaved in the K_S and J_S band. Only the J_S band on the second night presents variability. Its periodogram shows a peak above the 1%FAP level around 6 hr but it coincides with the seeing curve. We consider this

night as a possible detection and the light curves are presented in Appendix A.2. The light curves of 06 May can be found in Appendix A.3.

CFBDS J232304.41-015232.3: discovered by Albert et al. (2011), this T6 dwarf is identified as a high-probability member of β Pictoris with a mass of ~4.8 M_J (Zhang et al., 2021c). We observed J2323-0152 on 21 Oct 2021 and 24 Oct 2021 in the first epoch and 09 Oct 2023 and 10 Oct 2022 in the second epoch. We also observed J2323-0152 on 16 Jun 2022 and 17 Jun 2022 less than two hours per night. But these observations were taken under high humidity or cloudy conditions without any variability detection. We detected no variability on 21 Oct 2021 and 10 Oct 2022. These non-variable light curves are shown in Appendix A.3. We have positive detections on 24 Oct 2021 and 09 Oct 2022. The results are shown in Fig. 2.8. We find marginal variability just above the 1% FAP level on 24 Oct 2021. The peak around ~2 hr in the periodogram of 24 Oct 2021 is close to the peak of the seeing curve. This peak is likely related to the residual seeing effect since we were only able to pick two good reference stars. There is another long-term variability according to the periodogram. The light curve shows a variable pattern with a decreasing trend and a plateau-shaped enhancement on 09 Oct 2022, which is confirmed to be significant in the periodogram with a reported period of 3.15 hr, but this period is not evident from visual inspection of the light curve. If we assume the variability is caused by this decreasing trend with a plateau-shaped enhancement, the period is longer than the observing length of 5 hr. The max-min amplitude of the light curve of 09 Oct 2022 is ~ 7.6%. We also notice that the light curve of 24 Oct 2021 begins to rise at the end, which is likely another plateau-shaped enhancement. We also fit a linear trend with a plateau-shaped enhancement to this light curve and measure a max-min amplitude of ~ 3.7%. Therefore, J2323-0152 is classified as a variable with a long period.

2.6.2 Variable candidates

We identify two potentially variable candidates. Although they present variability above the 1% FAP level, we are cautious in our interpretation of these results due to the low quality of the data. Their light curves, periodograms, and sensitivity plots can be found in Appendix A.2.

2MASSI J1553022+153236AB: 2M1553+1532 is a T7 candidate of the Carina-Near YMG with a probability of 89.6% and an estimated mass of 12 M_J according

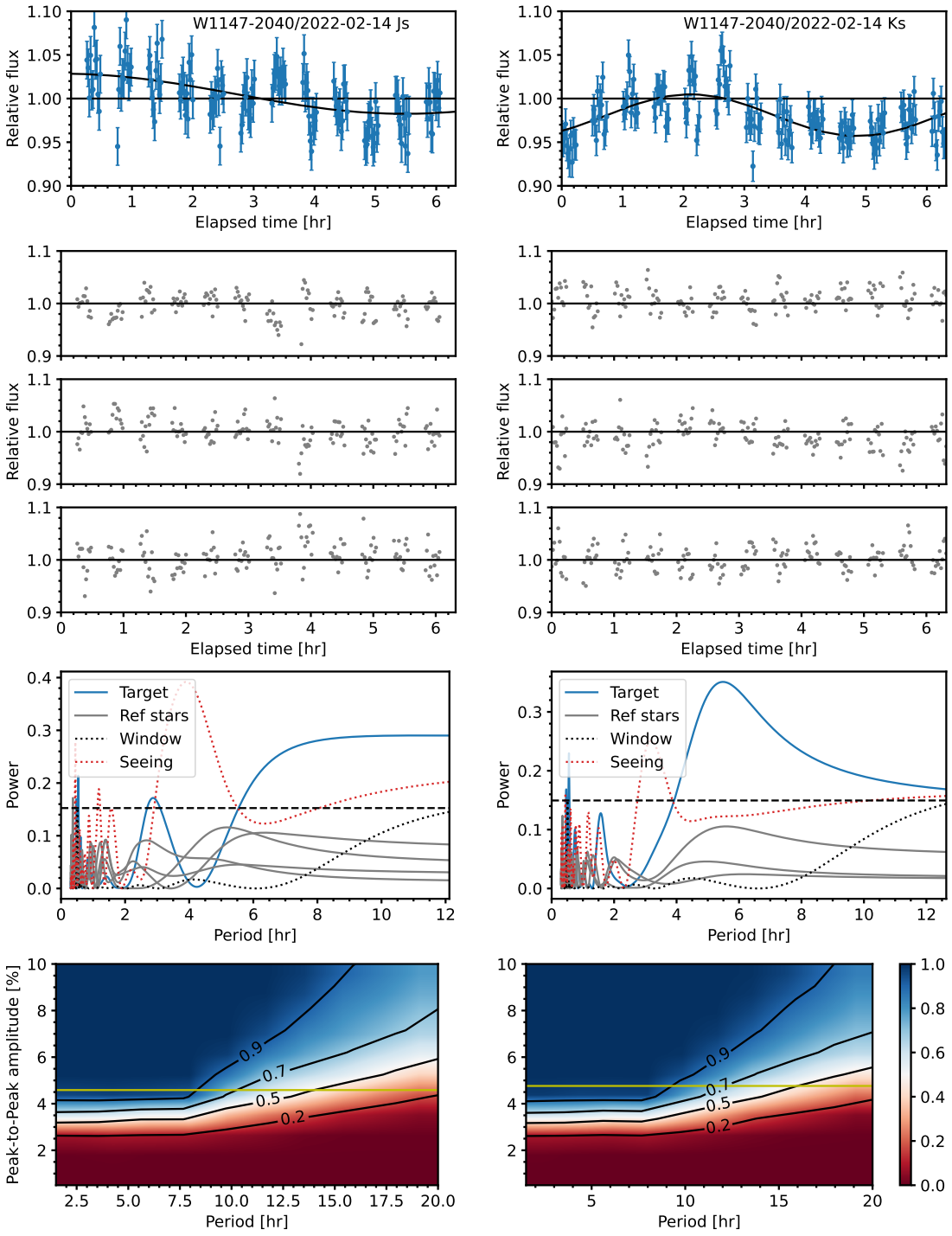


Figure 2.7: Variable light curves, periodograms, and sensitivity plots of W1147-2040, including detrended light curves and periodograms of its reference stars. The observations were interleaved in the J_S and K_S band.

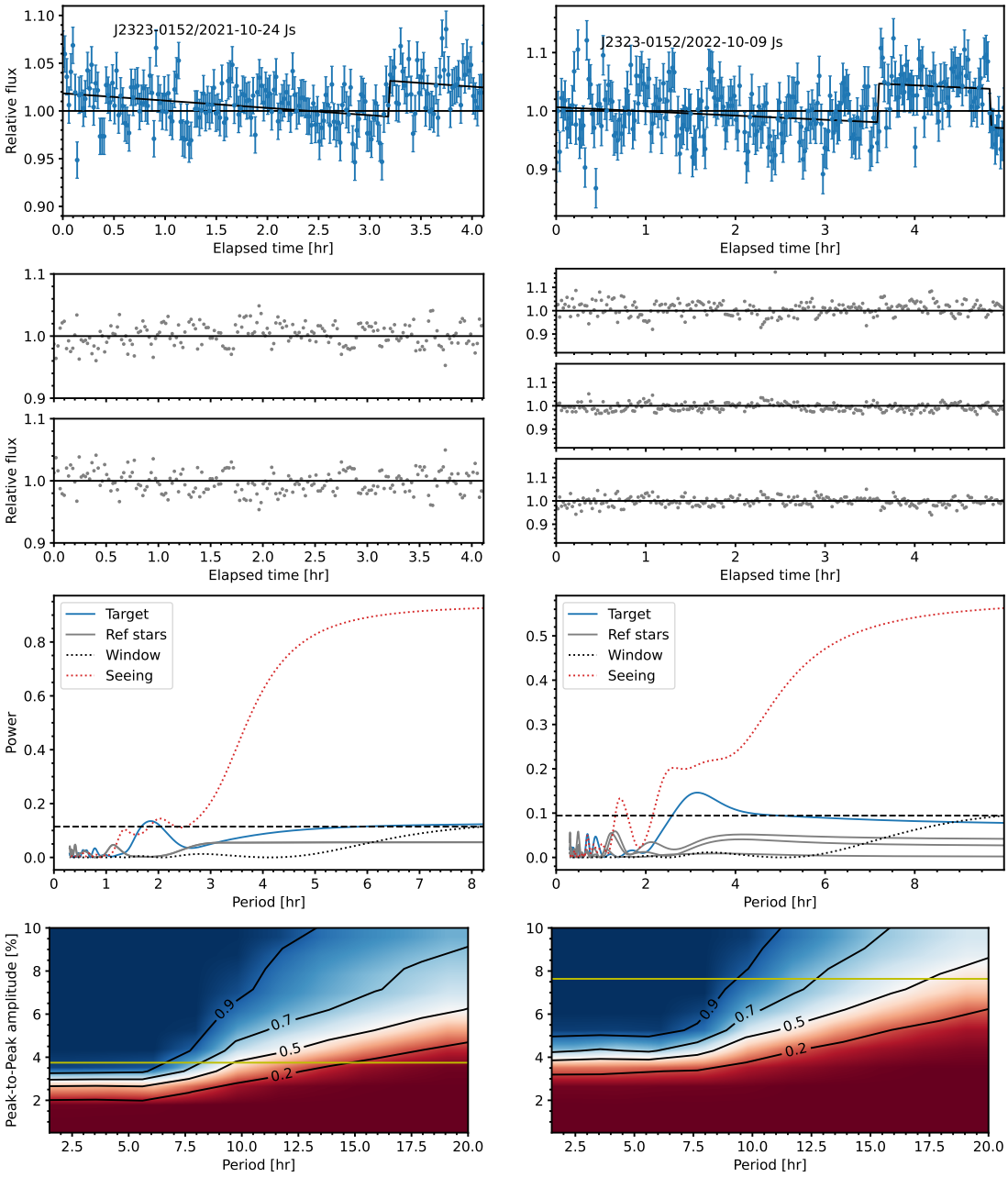


Figure 2.8: Variable light curves, periodograms, and sensitivity plots of J2323-0152 on 24 Oct 2021 and 09 Oct 2022, including detrended light curves and periodograms of its reference stars.

to Zhang et al. (2021c) using the trigonometric parallax. It was initially resolved to be a field binary system of two T6.5+T7.5 dwarfs (Burgasser et al., 2002, 2006; Dupuy & Liu, 2012). The separation is about 0.″6 in the resolved image of Dupuy & Liu (2012). It was not resolvable with SOFI. We detected long-term variability on 18 Jun 2022 and 09 May 2023. However, its periodogram shows a similar trend as the periodogram of the seeing curve on both nights and we were only able to select two good reference stars on both nights. The variability is suspicious. It might be a coincidence because the impact of the seeing variations should be removed after detrending with the reference stars as the detrended light curves of the reference stars are flat. We also observed it on 07 May 2023 for 1.56 hr and 10 May 2023 for 3.02 hr but did not detect any variability. Therefore, we consider it a potential variable.

WISEA J022609.16-161000.4: this L6 dwarf is a high-probability member of AB Doradus and has a mass range of 16–28 $M_{\rm J}$ (Schneider et al., 2017). We observed it on two nights: 22 Oct 2021 and 24 Oct 2021. On the first night, poor weather conditions resulted in the loss of two hours of data and no variability was detected. The weather conditions were much better on the second night. The periodogram detects two peaks above the 1% FAP level. The first peak around 2.3 hr coincides with the peaks of reference stars, raising suspicions of systematic variability. The second peak is actually a plateau towards long periods, showing long-term variability. However, selecting suitable reference stars for this target is challenging as there are few point sources in the field. Only three faint reference stars were chosen and their own detrended light curves are quite noisy, reducing the quality of the calibration curve created with them. We re-observed it on 02 Nov 2022 and 04 Dec 2022. There is a peak at 2.19 hr in the periodogram of 02 Nov 2022 but this variability is not evident in the visual inspection of the light curve. The light curve on 04 Dec 2022 did not show any variability. We consider J0226-1610 a potential variable.

2.6.3 Non-detections

We do not detect significant variability in eleven targets, including two L dwarfs and nine T dwarfs. Their light curves, periodograms and sensitivity plots are presented in Appendix A.3. Several noteworthy targets are discussed below.

WISEA J004403.39+022810.6: discovered by Skrzypek et al. (2016), this L7 dwarf is a high-probability member of β Pictoris with a mass of 7-11 $M_{\rm J}$ (Schneider et al.,

2017). We observed it on two nights: 3.75 hr on 20 Oct 2021 and 2.04 hr on 23 Oct 2021. We detect no variability in its light curves.

WISEA J020047.29-510521.4: J0200-5105 is a high-probability member of AB Doradus and is identified as an L6–L9 dwarf with a mass range of 16–28 M_J (Schneider et al., 2017). We observed it on 20 Oct 2021 in the first epoch and did not detect variability above the 1% FAP level. The seeing changed from 1.″0 to 2.″3 during the observation. Due to the poor seeing conditions, we re-observed it on four nights: 13 Feb 2022, 09 Oct 2022, 10 Oct 2022, and 03 Dec 2022. No variability is detected in the light curves of these observations.

ULASJ075829.83+222526.7: discovered by Burningham et al. (2013), this T6.5 dwarf is a high-probability member of Argus with a mass of approximately 4.8 M_J (Zhang et al., 2021c). With a J magnitude of 17.62, it is the faintest target in our survey. It was observed under favourable conditions on 17 Feb 2022 for 3.2 hr. While its light curve appears to exhibit a decreasing trend, this variability was below the 1% FAP level according to the periodogram. Further observations may provide evidence to confirm this variability.

PSOJ168.1800-27.2264: the T2.5 dwarf, discovered by Best et al. (2015), is a likely member of the Argus group identified with photometric parallax (Zhang et al., 2021c). It has a mass of ~8 M_J. We observed it on two consecutive nights: 4.1 hr on 18 Feb 2022 and 5.0 hr on 19 Feb 2022. No significant variability is detected in its light curves.

WISEA J043718.77-550944.0: this L5 dwarf was identified as a high-probability member of β Pictoris by Schneider et al. (2017). However, its predicted distance and surface gravity have conflicting results from different methods, making its youth and membership status uncertain. Due to a shortage of suitable observation targets in Feb 2022, we observed J0437-5509 on 14 Feb 2022 for 2.8 hours. The periodogram analysis of its light curve does not detect any variability.

2.7 Statistical analysis

Our sample provides a first investigation of the variability of young planetary-mass T dwarfs. To gain a comprehensive understanding of the variability of both young and field L and T dwarfs at near-infrared wavelengths, we combine our survey with previous studies. These include the variability survey of young L

dwarfs from Vos et al. (2019), the variability survey of field L and T dwarfs from Radigan et al. (2014), and the smaller variability survey of field objects at the L/T transition from Eriksson et al. (2019). All of these studies were conducted using ground-based photometric monitoring campaigns in the J band, similar to our own. They also employed similar variability identification criteria, with a variability significance level higher than the 1% FAP level in the LS periodogram (except for 0.1% FAP in Eriksson et al. (2019)). The sensitivity plots of samples from our survey, Vos et al. (2019) and Radigan et al. (2014) are also calculated in a similar way by injecting and detecting the simulated sinusoidal signals in the light curves. We extract the light curves from Eriksson et al. (2019) and calculate their sensitivity plots using the same method. Therefore, it is reasonable to compare them statistically.

We exclude known binary objects in the statistical analysis, as their variability may be due to one or both components or eclipsing binaries. We also exclude objects with uncertain youth, as our goal is to compare variability between young and field objects. The two variables in Radigan et al. (2014), SIMP0136+0933 and 2MASS2139+0220, were originally classified as field T dwarfs but were later found to be members of the Carina-Near YMG (Gagné et al., 2017b; Zhang et al., 2021c). We include the two variables in the sample of young objects instead of the field sample. Another variable T dwarf in Eriksson et al. (2019), 2MASS0013-1143, also turned out to be a candidate member of the Argus YMG (Zhang et al., 2021c) and is added to the young sample. One variable T2 dwarf in Vos et al. (2019), PSO071, was initially identified as a likely member of β Pictoris by Best et al. (2015), but was later classified as a field dwarf by Best et al. (2020); Marocco et al. (2021). Thus we include it in the field T sample. We consider only significant variability detections as variables in the statistical analysis. Marginal detections or potential variable candidates are considered non-variables. We also exclude two objects that were observed for less than 2 hr in Eriksson et al. (2019). Additionally, one variable from their sample, 2M2239+1617, has variability significance below the 1% FAP level in our periodogram analysis and thus we consider it non-variable. In total, we have 45 (10 variables) young objects consisting of 15 (3) from our survey, 26 (4) from Vos et al. (2019), 2 (2) from Radigan et al. (2014) and 1 (1) from Eriksson et al. (2019), and 63 (10 variables) field objects including 55 (7) from Radigan et al. (2014), 7 (2) from Eriksson et al. (2019) and 1 (1) from Vos et al. (2019). Table 2.4 lists the numbers of L and T brown dwarfs included in the statistical analysis. Figure. 2.9 shows the spectral distribution. Young objects span from

Table 2.4: Brown dwarfs included in the statistical analysis.

Type	Variable	Non-Variable	Total
Young L	5	23	28
Young T	5	12	17
Young L and T	10	35	45
Field L	1	17	18
Field T	9	36	45
Field L and T	10	53	63

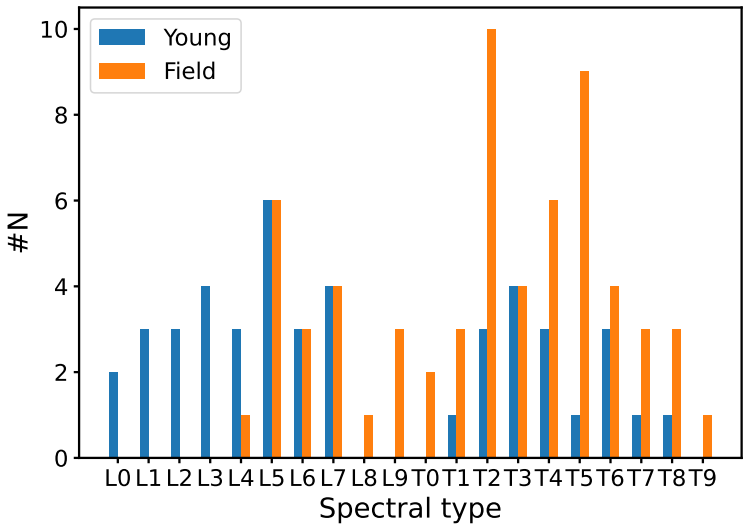


Figure 2.9: Spectral distribution of brown dwarfs included in the statistical analysis.

L0 to T8 and field objects span from L4 to T9. The averaged sensitivity maps of this survey, Vos et al. (2019), and Radigan et al. (2014) are shown in Fig. 2.10. Our objects are fainter than objects in Vos et al. (2019) and were observed under poorer conditions, while field dwarfs in Radigan et al. (2014) are much brighter than young objects. Therefore, it is easier for Radigan et al. (2014) to detect weaker variability.

Figure. 2.11 illustrates the relationship between spectral type and 2MASS $J - K_S$ colour of variable objects from the four surveys. The field sequence objects are taken from the UltracoolSheet[1] (Best et al., 2020), a catalogue of over 3,000 ultracool dwarfs and directly-imaged exoplanets. Some young T dwarfs in our sample have only MKO magnitudes and we convert their MKO $J-K$ colour to the 2MASS photometric system using the transformation equation[2]. Strong variables

[1] http://bit.ly/UltracoolSheet
[2] https://www.ipac.caltech.edu/2mass/releases/allsky/doc/sec6_4b.html

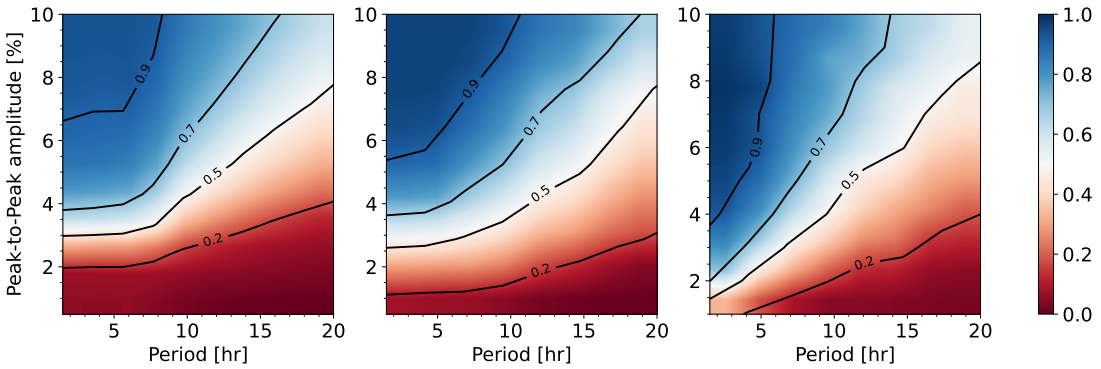


Figure 2.10: Average sensitivity maps of this survey, Vos2019, and Radigan2014a for objects included in the statistical analysis. The colour represents the retrieval rate. Our objects are fainter than objects in Vos2019 and we also have poorer seeing. Field dwarfs in Radigan2014a are bright and thus they are more sensitive to weak variability.

with peak-to-peak amplitude > 2% are concentrated within a narrow range, with strong young variables assembling in L7–T6 and strong field variables gathering from T1 to T3, a narrower distribution compared to strong young variables.

2.7.1 Statistical formalism

Although we can estimate the variability rate of brown dwarfs by the ratio of the number of variables to the total number, this is biased by the detection sensitivity which can vary significantly between different observations. To include the effect of detection sensitivity, we adopted the statistical formalism used in Vos et al. (2019) and Vos et al. (2022), which is a Bayesian method based on Lafrenière et al. (2007b) and Bonavita et al. (2013). f is the variability frequency with amplitude and rotation period in the interval $[a_{min}, a_{max}] \cap [r_{min}, r_{max}]$. If we number the observations of N objects by $j = 1...N$, p_j is the probability that such variability would be detected in observation j. In the sensitivity map calculated for each observation, $g(r, a)$ is the detection rate of the injected sinusoidal signals in each grid. p_j is the integral of $g(r, a)$ over the considered amplitude and period ranges of the injected signals normalised by the area of the map:

$$p_j = \frac{\int_{a_{min}}^{a_{max}} \int_{r_{min}}^{r_{max}} g(a, r)\, da\, dr}{\int_{a_{min}}^{a_{max}} \int_{r_{min}}^{r_{max}} 1\, da\, dr} \tag{2.1}$$

In our case, $0.005 \leq a \leq 0.1$ and $1.5 \leq r \leq 20\,hr$ as we inject these signals to

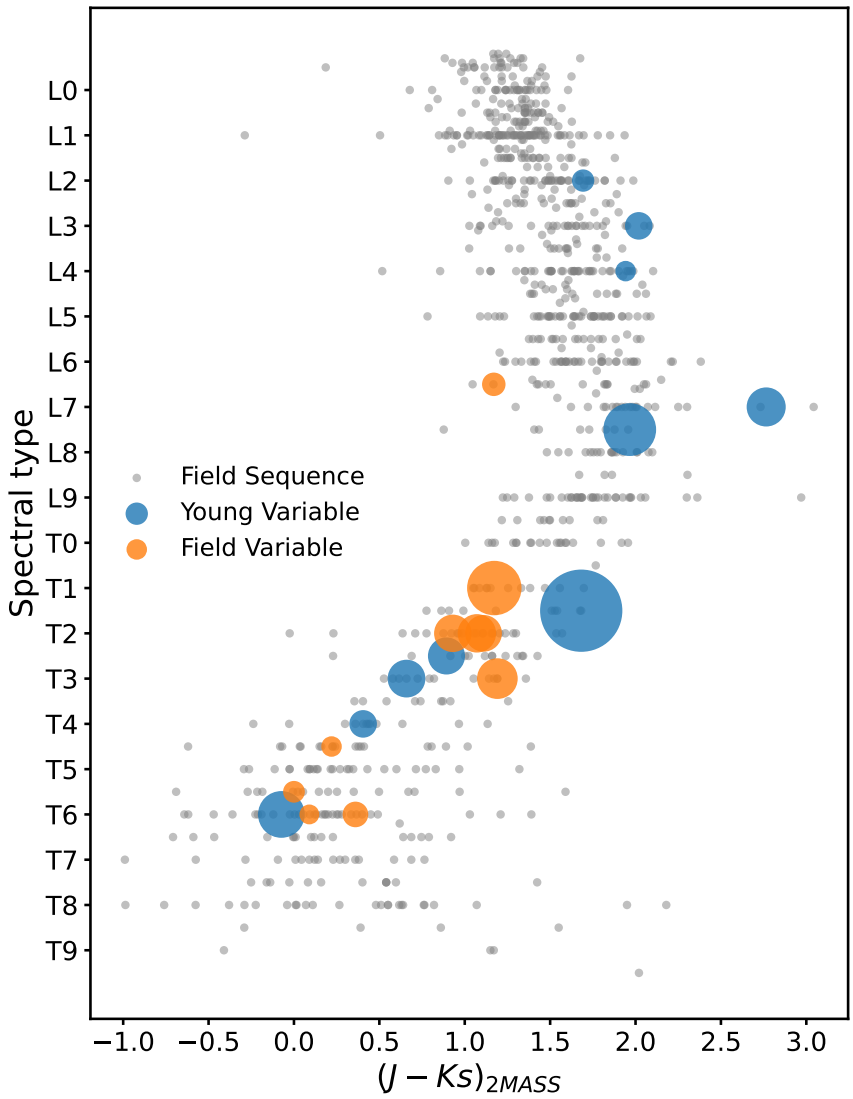


Figure 2.11: Spectral type against $(J - K_S)_{2MASS}$ colour of variable objects from the four surveys. The grey dots are the field sequence from The UltracoolSheet. The dots in blue and orange represent the variables from the four surveys, with their size proportional to the variability amplitudes.

calculate the sensitivity map. We choose the amplitude and period boundaries to keep the sensitivity map consistent with the maps of Vos et al. (2019) and Radigan et al. (2014). Though our average sensitivity rate is smaller than 0.2 when the amplitude is smaller than 2% in Fig. 2.10, we are able to detect amplitude as low as 0.5% when the observation conditions are good and the targets are bright such as the observations of J0819-0335 in Fig. 2.4. The lower boundary of the period is the shortest observation length and the upper boundary is an arbitrarily long period.

The probability of detecting one object to be variable is therefore fp_j and non-variable is $1 - fp_j$. The detection made in observation j is d_j: $d_j = 1$ for positive detection and $d_j = 0$ for non-detection. The probability of observing detections in N observations for a given f is:

$$L(d_j|f) = \prod_{j=1}^{N} (1 - fp_j)^{(1-d_j)} (fp_j)^{d_j} \tag{2.2}$$

According to Bayes's theorem, the posterior distribution (the probability density of f for a given d_j) is:

$$p(f|d_j) = \frac{L(d_j|f)p(f)}{\int_0^1 L(d_j|f)p(f)\,df} \tag{2.3}$$

The likelihood function is the previously calculated $L(d_j|f)$. Since we know little about the prior distribution of the variability occurrence rate f, we used the non-informative Jeffreys prior (Vos et al., 2022):

$$J(f) = \sqrt{\sum_j \frac{p_j}{f(1 - fp_j)}} \tag{2.4}$$

We calculate $p(f|d_j)$, the probability density function (PDF) of the variability occurrence rate of brown dwarfs using the above equations. We also calculate the 68% and 95% confidence intervals of f with the maximum likelihood following the method used in Kraft et al. (1991) and Vos et al. (2022). If both upper and lower boundaries exist, the confidence interval of credibility α in $[f_{min}, f_{max}]$ is given by:

$$\alpha = \int_{f_{min}}^{f_{max}} p(f|d_j)\,df; \qquad p(f_{min}|d_j) = p(f_{max}|d_j) \tag{2.5}$$

If only one side boundary can be calculated, the upper or lower boundary is given by:

$$\alpha = \int_{f_{min}}^{1} p(f|d_j)\, df; \qquad or\, \alpha = \int_{0}^{f_{max}} p(f|d_j)\, df \tag{2.6}$$

2.7.2 Variability occurrence rates of field and young L and T dwarfs

We calculate the sensitivity map for each observation in our survey. For objects observed multiple times, we use the most sensitive sensitivity map or the one with a positive detection. We obtained sensitivity maps of the objects from Vos et al. (2019). For field objects from Radigan et al. (2014), we are only able to obtain sensitivity maps for part of the sample via private communication. For the rest of the objects that have light curves presented in Radigan et al. (2014), we extract these curves and calculate their sensitivity maps using our routine. These give us sensitivity maps of 23 field objects with a good representation of L and T spectral types. We use the average sensitivity map for the corresponding spectral type interval when calculating f for field objects as a function of spectral type. This is a reasonable approach since Radigan et al. (2014) demonstrate that their survey sensitivity does not vary significantly with spectral type. For objects from Eriksson et al. (2019), we extract the light curves and calculate sensitivity maps for each object.

First, we calculate the total variability rates in the field and young samples with a variability amplitude between 0.5% and 10% and a period between 1.5 and 20 hours. The field sample has a variability rate of 25^{+8}_{-7}% and the young sample has a variability rate of 37^{+11}_{-9}% as shown in Fig. 2.12. Yong L and T objects tend to be more variable than field objects in ground-based near-infrared observations but the difference is not significant as the rates overlap within 1σ. We also calculate the variability rate for L (L0–L9.5) and T (T0–T9.5) spectral types separately as compared in Fig. 2.13. The field L dwarfs have a variability rate of 6^{+13}_{-5}% while the young L dwarfs have a variability rate of 27^{+13}_{-10}%, which is consistent with the previous result reported by Vos et al. (2019). But since the difference in rate is within 1σ, this trend is not significant. We find that young T dwarfs are also more variable than field T dwarfs with a variability rate of 56^{+20}_{-18}% compared with 25^{+8}_{-7}%. Though the difference is larger than 1σ, we are cautious about it as the

young T sample is small.

In both field and young samples, T dwarfs have a tendency to be more likely to be variable than L dwarfs. We suspect that this may be biased by the L/T transition, which is from L9 to T3.5 and covers more T spectral types than L types. Hence we also calculate the variability rate of field and young dwarfs with spectral types later than L9 and earlier than T3.5. Field T4–T9.5 dwarfs have a variability rate of $17^{+9}_{-7}\%$ which is higher than the rate of $7^{+15}_{-6}\%$ for field L0–L8.5 dwarfs. Young T4–T9.5 dwarfs are also still more likely to be variable than young L0–L8.5 dwarfs, with a variability rate of $44^{+18}_{-22}\%$ and $27^{+13}_{-10}\%$ separately. But these rates overlap significantly within 1σ, therefore whether T dwarfs are more likely to be variable than L dwarfs needs larger samples to refine. Nevertheless, the comparable variability rates of T dwarfs to L dwarfs suggest that clouds are also common in mid-late T spectral types. After the condensation of silicate clouds at the L/T transition, clouds composed of other species can form in the atmospheres of T dwarfs, such as sulfide clouds (Morley et al., 2012). The relatively higher rates in young samples suggest that low surface gravity is more favourable to cloud formation. Our work is from a statistical view. Characterisation of individual objects, such as time-resolved spectroscopy observations and atmospheric simulations can help study the impact of surface gravity in detail (e.g. Marley et al., 2012; Manjavacas et al., 2014; Filippazzo et al., 2015; Vos et al., 2023).

2.7.3 Variability occurrence rates at and outside the L/T transition

We also investigate how the variability occurrence rate varies at and outside the L/T transition for field and young samples with a variability amplitude between 0.5% and 10% and a period between 1.5 and 20 hours. While there is no clear definition of the spectral type range of the L/T transition, we adopted the spectral type range of L9–T3.5 used in Radigan et al. (2014) for a fair comparison with their results. This definition is also used in Vos et al. (2022) for their analysis of young object variability at mid-infrared wavelengths. As presented in Fig. 2.14, for field objects, the variability rate at the L/T transition is higher than that outside the L/T transition, with a value of $36^{+15}_{-13}\%$ and $18^{+9}_{-7}\%$, respectively. Radigan et al. (2014) also report that strong variables (peak-to-peak amplitudes > 2%) are more frequent at the L/T transition than outside of

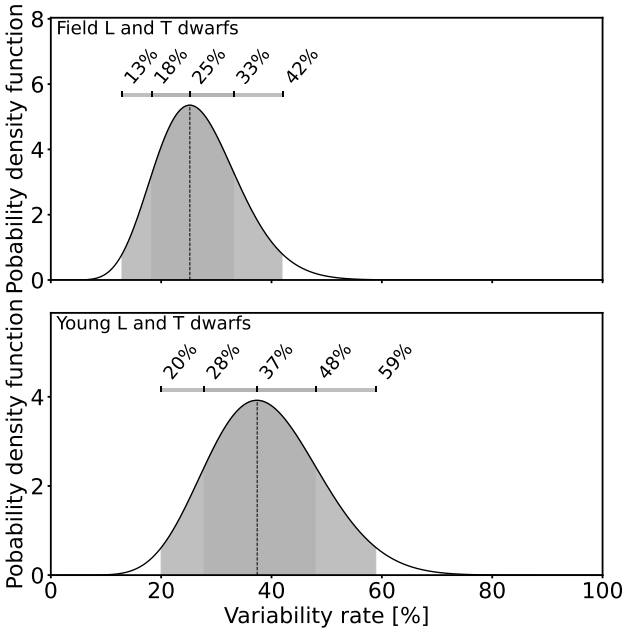


Figure 2.12: Probability density function of variability rate of the field and young samples. The dark grey area shows the 68% confidence interval and the light grey area shows the 95% confidence interval.

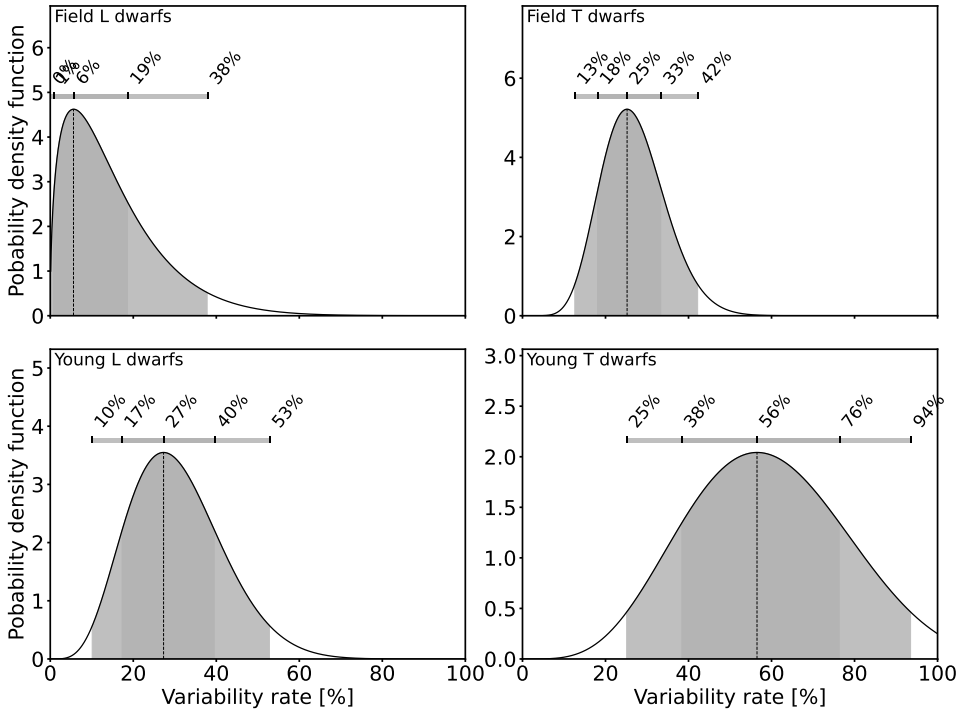


Figure 2.13: Probability density function of variability rate in the field and young samples for L and T spectral types, respectively. The dark grey area shows the 68% confidence interval and the light grey area shows the 95% confidence interval.

the L/T transition. This contradicts the variability observations at mid-infrared wavelengths by *Spitzer*. Metchev et al. (2015) report that they did not observe a variability enhancement or stronger amplitudes at the L/T transition, though their sample consists of field and young objects. Vos et al. (2022) separate field and young objects and they find a higher variability rate for field L0–L8.5 dwarfs than field dwarfs at the L/T transition. This indicates that the variability of field dwarfs in the near-infrared and mid-infrared may originate from different sources since different wavelengths probe different heights in atmospheres. *J* band detects a deeper and higher-pressure region, ~10 bar, while mid-infrared wavelengths probe lower-pressure layers, ~1 bar (Vos et al., 2022). It could also be due to the sensitivity difference between the ground-based observations which detect variability over 1% and the space observations which achieve subpercent sensitivity.

For young objects, we find that variables are also more likely to be located at the L/T transition than outside it, with a variability rate of 64^{+23}_{-22}% and 31^{+12}_{-9}% separately. The large uncertainty of the variability rate at the L/T transition is due to the small sample size. There are only three variables out of eight objects at the L/T transition compared with seven variables out of 37 outside the L/T transition in the young sample. Again, the variability rates of objects at the L/T transition and outside the L/T transitions overlap slightly within 1σ for both field and young samples. This tentative enhancement indicates that the L/T transition has an impact on the near-infrared variability properties of field brown dwarfs and planetary-mass objects.

If we compare variability rates of the three spectral ranges, L0–L8.5, L9–T3.5, and T4–T9.5, we find that the rate is the highest at the L/T transition, then T4–T9.5 and the lowest at L0–L8.5. This trend is the same for field and young objects in the near-infrared. Vos et al. (2022) find that the variability rate is high for young objects from L to T but it drops from L to T for field objects in the mid-infrared for amplitudes of 0.05%–3% and periods of 0.5–40 hr. Table 2.5 provides the statistical variability rate of field and young objects from this work and Vos et al. (2022). The variability rates of objects with spectral types later than L8.5 are consistent with each other in the near-infrared and mid-infrared for both field and young samples. For L dwarfs (L0–L8.5), there is a big discrepancy in the variability rates between the near-infrared and mid-infrared for both field and young samples. The L dwarfs have a higher variability rate in the mid-infrared but we are cautious about this discrepancy because the mid-infrared observations

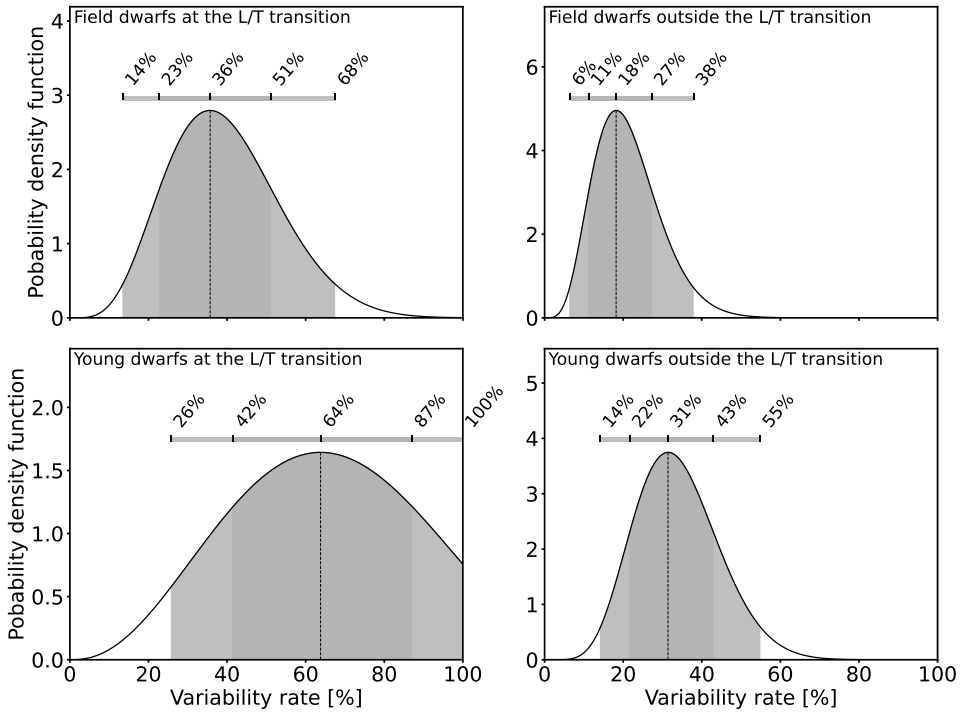


Figure 2.14: Probability density function of variability rate at the L/T transition and outside the L/T transition for field and young samples. The dark grey area shows the 68% confidence interval and the light grey area shows the 95% confidence interval.

are from *Spitzer*. These space observations have a much higher sensitivity and much longer observation time than ground-based observations. They could detect weak variables with long periods, thus resulting in higher detection rates.

2.8 A census of variable objects

Besides the four surveys discussed in the previous section, there are a few variable brown dwarfs monitored in other surveys or small sample observations (e.g. Buenzli et al., 2014; Metchev et al., 2015; Yang et al., 2015, 2016; Manjavacas et al., 2019a). To gain a comprehensive understanding of the variability in L and T objects, it is necessary to have a census of known variables. Vos et al. (2020) summarise a list of known variables from the literature and we update that list with newly discovered variables and new results from existing variables. They are presented in Table 2.6. Variability is common in L and T dwarfs from near-infrared to mid-infrared. Since our survey is conducted in the near-infrared, we focus our variability census in the J band including ground-based J band

Table 2.5: Variability rates of field and young objects in the near-infrared (NIR) and mid-infrared (MIR).

Type	L0–L8.5	L9–T3.5	T4–T9.5
Field NIR	7^{+15}_{-6}%	36^{+15}_{-13}%	17^{+9}_{-7}%
Young NIR	27^{+13}_{-10}%	64^{+23}_{-22}%	44^{+28}_{-22}%
Field MIR	83–100%	41^{+23}_{-19}%	18^{+32}_{-15}%
Young MIR	81–100%	85–100%	44–100%

Notes.
The NIR results are from this work for amplitudes of 0.5%–10% and periods of 1.5–20 hr. The MIR results are from Vos2022 for amplitudes of 0.05%–3% and periods of 0.5–40 hr.

observations and HST/WFC3/NIR observations using filters in 800–1700 nm.

The spectral type distribution of known variables in the *J* band is illustrated in Fig. 2.15. Variability is observed across a wide range of spectral types in field brown dwarfs and an even wider range in young objects. Field objects exhibit variability from L3 to T6, with a weak peak around T2–T2.5. Meanwhile, young variable objects have a range of spectral types from L2 to T8, with a peak at L6–L7.5. Figure. 2.16 shows the maximum peak-to-peak amplitudes of these objects versus their spectral types. Strong field variables with an amplitude >∼2% tend to assemble from L8 to T3, with three exceptions having spectral types L4.5, L6, and T6, respectively. The strongest field variable is a T1 object, 2MASS J2215+2110, with an amplitude of 10.7±0.4% measured by Eriksson et al. (2019). Strong young variables tend to assemble in L6–T3.5, though the latest spectral type of strong young variables can be T8. The two strongest variables in Fig. 2.16 are young objects. The L7 young object, VHS 1256-1257b, has a recorded largest variability amplitude of 38% in the *J* band measured by Zhou et al. (2022). The second-strongest young variable is a T1.5 object, 2MASS J2139+0220, with an amplitude of 26% in the *J* band measured by Radigan et al. (2012).

While young objects also show strong variability at the L/T transition as field objects, young objects have even stronger variability in the spectral range of L6–L7.5. In this narrow spectral range, there are at least five of the known strongest variables, including the one with the known maximum variability. They are VHS 1256-1257b (L7) with an amplitude of 38% (Zhou et al., 2022), PSO 318.5-22 (L7.5) with an amplitude of 10% (Vos et al., 2019), 2MASS J00470038+6803543 (L6) with an amplitude of 8% (Lew et al., 2016), 2MASS J2244316+204343 (L6) with an amplitude of 5.5% (Vos et al., 2019) and WISEA J114724.10-204021.3

Table 2.6: Variable brown dwarf detections in the literature.

Target	SpT	$A_{Jground}$ [%]	$A_{WFC3NIR}$ [%]	$A_{3.6}$ [%]	$A_{4.5}$ [%]	Period [hr]	Youth	Companion	Age [Myr]	$vsini$ [$km\,s^{-1}$]	Variability ref
2MASS J00011217+1535355	L4	-	-	0.69 ± 0.04	-	15.75 ± 0.37	1	0	120 ± 30	-	(1)
2MASS J00132229-1143006	T3 (T3.5+T4.5)	4.6 ± 0.2	-	-	-	-	1	0	45 ± 5	-	(2)
2MASSW J0030300-145033	L7	-	-	1.52 ± 0.06	-	4.22 ± 0.02	1	0	45 ± 5	-	(1)
2MASS J00310928+5749364	L9	-	-	0.35 ± 0.03	-	1.64 ± 0.01	1	0	200 ± 50	-	(1)
LSPM J0036+1821	L3.5	1.22 ± 0.04	-	0.47 ± 0.05	0.19 ± 0.04	2.7 ± 0.3	0	0	1000	36.0 ± 0.2	(3), (4)
2MASS J00452143+1634446	L2	1.0 ± 0.1	-	0.18 ± 0.04	0.16 ± 0.04	2.4 ± 0.1	1	0	45 ± 5	$31.76^{+0.22}_{-0.25}$	(5), (25)
2MASS J00470038+6803543	L6	-	8.0	1.07 ± 0.04	-	16.4 ± 0.2	1	0	130 ± 20	9.8 ± 0.3	(6), (7)
2MASS J00501994-3322402	T7	-	-	<0.59	1.07 ± 0.11	1.55 ± 0.02	0	0	1000	-	(3)
2MASSI J0103320+193536	L6	-	-	0.56 ± 0.03	0.87 ± 0.09	2.7 ± 0.1	1	0	300 ± 200	$40.0^{+3.7}_{-4.7}$	(3)
2MASS J01075242+0041563	L8	-	-	1.27 ± 0.13	1.0 ± 0.2	5.0 ± 2	0	0	1000	19.4 ± 0.8	(3)
GU PSC B	T3.5	4.0	-	-	-	-	1	0	130 ± 20	-	(8)
SIMP J013656.57+093347.3	T2.5	5.0	4.5	1.5 ± 0.2	-	2.414 ± 0.078	1	0	200 ± 50	50.9 ± 0.8	(9), (10)
2MASS J01383648-0322181	T3	5.5 ± 1.2	-	-	-	-	0	0	1000	-	(2)
2MASS J01531463-6744181	L2	-	-	0.48 ± 0.07	-	17.63 ± 1.13	1	0	45 ± 4	-	(1)
2MASSW J0310599+164816	L8	-	-	-	-	-	0	0	1000	-	(11)
2MASSI J0342162-681732	L4	-	-	0.73 ± 0.07	-	14.73 ± 0.51	1	0	45 ± 4	-	(1)
2MASS J03480772-6022270	T7	-	-	-	1.5 ± 0.1	1.08 ± 0.004	0	0	1000	-	(12)
2MASS J03492367+0635078	L5	-	-	0.53 ± 0.09	-	14.62 ± 1.08	1	0	45 ± 4	-	(1)
2MASS J03552337+1133437	L5	-	-	0.26 ± 0.02	-	9.53 ± 0.19	1	0	130 ± 20	-	(1)
2MASS J04070752+1546457	L3.5	-	-	0.36 ± 0.1	-	1.23 ± 0.01	0	0	1000	-	(12)
SDSS J042348.57-041403.5	T0	0.8 ± 0.08	-	-	-	2.0 ± 0.4	0	0	1000	68.0 ± 0.9	(13)
PSO J071.8769-12.2713	T2	4.5 ± 0.6	-	0.93	-	-	0	0	1000	-	(1), (5)
2MASS J05012406-0010452	L3	2.0 ± 1.0	-	0.36 ± 0.04	0.24 ± 0.04	15.7 ± 0.2	1	0	300 ± 200	$9.57^{+0.67}_{-0.58}$	(5), (25)
2MASS J05065012+5236338	T4.5	-	-	0.58 ± 0.1	-	13.77 ± 0.82	0	0	2000	-	(1)
2MASS J05591914-1404488	T4.5	0.7 ± 0.5	-	-	-	10.0 ± 3	0	0	1000	-	(10)
2MASS J06244595-4521548	L6.5	-	1.5	-	-	-	0	0	1000	-	(11)
2MASS J06420559+4101599	L9	-	-	2.16 ± 0.16	-	10.11 ± 0.07	1	0	42 ± 6	-	(1)
2M0718-6415	T5	-	-	2.14 ± 0.21	-	1.08 ± 0.01	1	0	23 ± 3	-	(1)
SDSS J075840.33+324723.4	T2(T0+T3.5)	4.8 ± 0.2	-	-	-	4.9 ± 0.2	0	0	1000	-	(10)
2MASS J08095903+4434216	L6	-	-	0.77 ± 0.06	-	1.365 ± 0.004	1	0	300 ± 200	-	(1)
DENIS J081730.0-615520	T6	0.6 ± 0.1	-	-	-	2.8 ± 0.2	0	0	1000	-	(10)
2MASSI J0825196+211552	L7.5	>1	-	0.81 ± 0.08	1.4 ± 0.3	7.6 ± 5	0	0	1000	-	(3)
WISE J085510.83-071442.5	Y0+	-	-	4.0 ± 1.0	4.0 ± 1.0	12.5 ± 3.5	0	0	1000	-	(14)
LP261-75B	L6	-	2.4 ± 0.14	-	-	4.78 ± 0.98	0	0	300 ± 50	-	(15)
SDSS J104335.08+121314.1	L9	-	-	1.54 ± 0.15	1.2 ± 0.2	3.8 ± 0.2	0	0	1000	-	(3)
2MASS J10475385+2124234	T6.5	-	-	-	1.04 ± 0.07	1.741 ± 0.007	0	0	1000	-	(16)
WISE 1049B	L7.5+T0.5	-	11.0	-	-	4.87 ± 0.01	0	1	1000	21.6 ± 0.2	(17), (18)
SDSS J105213.51+442255.7	T0.5	2.2 ± 0.5	-	-	-	3.0 ± 0.5	0	0	1000	-	(17)
DENIS-P J1058.7-1548	L3	0.843 ± 0.098	-	0.39 ± 0.04	<0.3	4.1 ± 0.2	0	0	1000	37.5 ± 2.5	(3)
2MASS J11193254-1137466AB	L7	-	-	0.46 ± 0.036	0.96 ± 0.037	3.02 ± 0.04	1	1	10 ± 3	-	(19), (20)
2MASS J11263991-5003550	L4.5	1.2 ± 0.1	-	0.21 ± 0.04	0.29 ± 0.15	3.2 ± 0.3	0	0	1000	$22.8^{+1.6}_{-2.4}$	(3), (10)
WISEA J114724.10-204021.3	L7	4.6±1.0	-	1.596 ± 0.08	2.216 ± 0.09	19.39 ± 0.3	1	0	10 ± 3	-	(19), (20)
2M1207b	L6	-	1.36	-	-	10.7 ±1	1	0	10 ± 3	-	(21)
2MASS J12195156+3128497	L8	-	4.8	0.55 ± 0.13	-	1.14 ± 0.03	0	0	1000	-	(11), (12)
VHS1256-1257AB b	L7	>10	38	-	5.76 ± 0.04	22.04 ± 0.05	1	0	225 ± 75	$13.5^{+3.6}_{-4.1}$	(22), (23), (24)

Table 2.6: (Continued.)

Target	SpT	$A_{Jground}$ [%]	$A_{WFC3NIR}$ [%]	$A_{3.6}$ [%]	$A_{4.5}$ [%]	Period [hr]	Youth	Companion	Age [Myr]	$vsini$ [$km\,s^{-1}$]	Variability ref
Ross 458C	T8	-	2.62 ± 0.02	<1.37	<0.72	6.75 ± 1.58	1	0	125 ± 75	-	(3)
2MASS J13243559+6358284	T2.5	-	-	3.05 ± 0.15	3.0 ± 0.3	13.0 ± 1	1	0	130 ± 20	-	(3)
WISE J140518.39+553421.3	Y0.5	-	-	3.6 ± 0.4	3.54 ± 0.09	8.2 ± 0.3	0	0	1000	-	(26)
2MASS J14252798-3650229	L4	0.7 ± 0.3	-	<0.16	<0.18	-	1	0	130 ± 20	$33.08^{+0.53}_{-0.49}$	(25)
2MASSW J1507476-162738	L5	-	0.7	0.53 ± 0.11	0.45 ± 0.09	2.5 ± 0.1	0	0	1000	19.1± 0.5	(3), (9)
SDSS J151114.66+060742.9	L5.5+T5.0	-	-	0.67 ± 0.07	<0.49	11.0 ± 2	0	1	1000	-	(3)
SDSS J151643.01+305344.4	T0.5	-	-	2.4 ± 0.2	1.3 ± 0.7	6.7 ± 5	0	0	1000	-	(3)
2MASS J16154255+4953211	L4	-	-	0.9 ± 0.2	<0.39	24.0 ± 5	1	0	300 ± 200	$9.5^{+1.3}_{-1.2}$	(3)
2MASS J16291840+0335371	T2	4.3 ± 2.4	-	-	-	6.9 ± 2.4	0	0	1000	$19.7^{+0.7}_{-0.8}$	(10)
2MASSW J1632291+190441	L8	-	-	0.42 ± 0.08	0.5 ± 0.3	3.9 ± 0.2	0	0	1000	-	(3)
2MASS J16471580+5632057	L7	-	-	0.468 ± 0.06	-	9.234 ± 0.25	1	0	300 ± 200	-	(1)
2MASSI J1721039+334415	L3	-	-	0.33 ± 0.07	<0.29	2.6 ± 0.1	0	0	1000	21.5 ± 0.3	(3)
WISEP J173835.52+273258.9	Y0	-	-	-	3.0 ± 0.1	6.0 ± 0.1	0	0	1000	-	(27)
2MASS J17410280-4642218	L7	-	-	0.35 ± 0.03	-	15.0 ± 0.71	1	0	130 ± 20	-	(1)
2MASS J17502484-0016151	L5	>1	-	-	-	-	0	0	1000	-	(11)
2MASS J17503293+1759042	T3.5	>1	-	-	-	-	0	0	1000	-	(11)
2MASS J17534518-6559559	L4	-	-	<0.25	-	-	0	0	1000	-	(3)
2MASS J18212815+1414010	L4.5	-	2.5	0.54 ± 0.05	0.71 ± 0.14	4.2 ± 0.1	0	0	1000	30.7 ± 0.2	(3), (9)
2MASS J18283572-4849046	T5.5	0.9 ± 0.1	-	-	-	5.0 ± 0.6	0	0	1000	-	(10)
2MASS J20025073-0521524	L5	1.7 ± 0.2	-	0.28	-	-	1	0	300 ± 200	-	(1)
PSO 318.5-22	L7.5	10.0 ± 1.3	-	-	3.4 ± 0.08	8.61 ± 0.06	1	0	22 ± 6	$17.5^{+2.3}_{-2.8}$	(5), (28), (29)
HD 203030B	L7.5	-	1.1 ± 0.3	-	-	7.5 ± 0.6	1	0	90 ± 60	-	(30)
2MASS J21392676+0220226	T1.5	26	27	11.0 ± 1.0	10.0 ± 1.0	7.618 ± 0.18	1	0	200 ± 50	18.7 ± 0.3	(9), (11), (31)
HN PegB	T2.5	-	1.2	0.77 ± 0.15	1.1 ± 0.5	15.4 ± 0.5	1	0	237 ± 33	-	(3)
2MASS J21481628+4003593	L6	-	-	1.33 ± 0.07	1.03 ± 0.1	19.0 ± 4	0	1	300 ± 200	$9.2^{+0.4}_{-0.3}$	(3)
2MASS J22062520+3301144	T1.5	-	-	1.2 ± 0.13	-	15.91 ± 0.62	1	0	45 ± 5	-	(1)
2MASSW J2208136+292121	L3	-	-	0.69 ± 0.07	0.54 ± 0.11	3.5 ± 0.2	1	0	22 ± 6	$40.6^{+1.3}_{-1.4}$	(3)
2MASS J22153705+2110554	T1 (T0+T2)	10.7 ± 0.4	-	-	-	5.2 ± 0.5	0	0	1000	-	(2)
2MASS J22282889-4310262	T6	1.6 ± 0.3	5.3	4.6 ± 0.2	1.51 ± 0.15	1.41 ± 0.01	0	0	1000	-	(3), (10), (32)
2MASS J2244316+204343	L6	5.5 ± 0.6	-	0.8 ± 0.2	-	11.0 ± 2	1	0	130 ± 20	$14.3^{+1.4}_{-1.5}$	(5), (7), (33)
WISEPAJ081958.05-033529.0	T4	2.0 ± 0.7	-	-	-	-	1	0	22 ± 6	-	(20)
2MASSIJ1553022+153236	T7	1.1 ± 0.2	-	-	-	-	1	1	200 ± 50	-	(20)
CFBDS J232304.41-015232.3	T6	7.6	-	-	-	-	1	0	22 ± 6	-	(20)

Notes. $A_{Jground}$: J band peak-to-peak amplitude measured from ground observations; $A_{WFC3NIR}$: peak-to-peak amplitude measured in the IR channel of HST/Wide Field Camera 3 (WFC3); $A_{3.6}$ and $A_{4.5}$: peak-to-peak amplitude measured in the 3.6 μm and 4.5 μm channels of *Spitzer*.
Varaibility references: (1) Vos et al. (2022); (2) Eriksson et al. (2019); (3) Metchev et al. (2015); (4) Croll et al. (2016); (5) Vos et al. (2019); (6) Lew et al. (2016); (7) Vos et al. (2018); (8) Naud et al. (2017) (9) Yang et al. (2016); (10) Radigan et al. (2014); (11) Buenzli et al. (2014); (12) Tannock et al. (2021); (13) Clarke et al. (2008); (14) Esplin et al. (2016); (15) Manjavacas et al. (2018); (16) Allers & Liu (2020); (17) Girardin et al. (2013); (18) Buenzli et al. (2015a); (19) Schneider et al. (2018); (20) This work; (21) Zhou et al. (2016); (22) Zhou et al. (2020); (23) Zhou et al. (2022); (24) Bowler et al. (2020a); (25) Vos et al. (2020); (26) Cushing et al. (2016); (27) Leggett et al. (2016); (28) Allers et al. (2016); (29) Biller et al. (2018); (30) Miles-Páez et al. (2019); (31) Apai et al. (2017); (32) Buenzli et al. (2012); (33) Morales-Calderón et al. (2006)

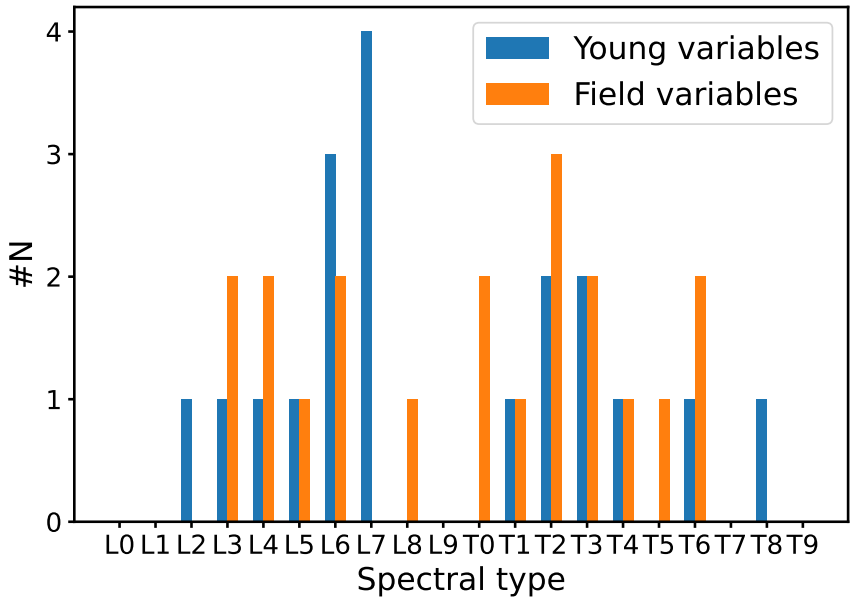


Figure 2.15: Spectral type distribution of known young and field variables in the J band from the literature.

(L7) with an amplitude of 4.6% (this work). These objects have extremely red $J-K$ colours, indicating that they have thicker clouds than field dwarfs. If we posit the patchy clouds scenario with thick and thin cloud patches (Marley et al., 2010; Apai et al., 2013), a break-up in thicker clouds could result in higher contrast and thus stronger variability in light curves. Filippazzo et al. (2015) find that low gravity L dwarfs have a cooler $T_{\rm eff}$ than field L dwarfs of the same spectral type, with a difference of up to 300 K. This implies that the start of cloud condensation in young L dwarfs may occur at an earlier spectral type than field L dwarfs if we assume that the cloud condensation occurs at a certain $T_{\rm eff}$. However, Marley et al. (2012) suggest that the L/T transition of low gravity objects occurs at a lower $T_{\rm eff}$ range than that of field dwarfs. Therefore, what drives the extreme variability of young L dwarfs in this spectral range is still unclear and needs more observations and atmospheric models to study.

2.9 Colour of young L and T objects

The sample of young L dwarfs are redder in the near-infrared compared to their field counterparts, as noted in previous studies (e.g. Liu et al., 2016; Faherty et al., 2016), while the young T dwarfs do not have this reddening trend. This agrees with the prevailing scenario that young L dwarfs tend to have thicker clouds

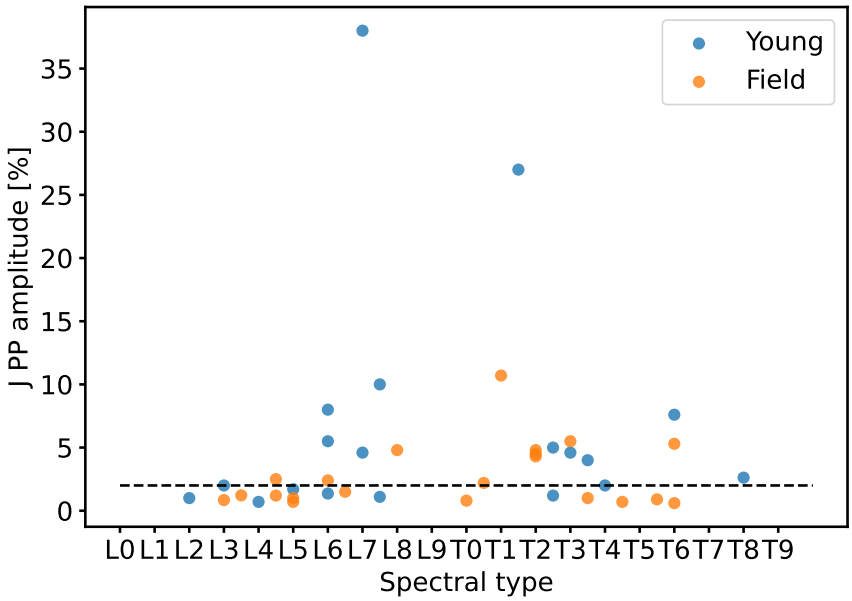


Figure 2.16: Peak-to-peak amplitude in the J band versus spectral type of known young and field variables from the literature. Variables with amplitudes >~2% are strong variables and are above the dashed line. Young strong variables span from L6 to T3.5, while field strong variables span a narrower range, from L8 to T3. Furthermore, young objects have the strongest amplitudes.

than field L dwarfs, and these silicate clouds condense below the photosphere in T dwarfs. We compare the *2MASS* $J - K_S$ colour of all the known young T dwarfs and suspect that later T types gradually become bluer than their field dwarf counterparts from T4 to T7 in Fig. 2.17. With $J - K$ MKO colours versus spectral types, Zhang et al. (2021c) also mention that earlier T are redder than their field dwarfs counterparts but this trend vanishes in later spectral types. We fit a line to young L and T dwarfs respectively and calculate the root mean square distance (rms) of the young and field samples to the fitting. Young L dwarfs have an rms of 1.40 while field L dwarfs have an rms of 3.00. Young T dwarfs have an rms of 1.11 while field T dwarfs have an rms of 2.04. Since the difference in T spectral types is not as significant as it is in L spectral types for field and young dwarfs, we are cautious about this slight bluing trend in T spectral types as it could be biased by the small number of objects known to date. Future detections of more young objects in this range are needed to confirm it. The colours of young objects from T1.5 to T4 fall within a similar range as their field counterparts. The absence of young objects between L8 and T1 hinders the understanding of how the colour of young objects changes at this critical spectral range, for example, where the young objects reach their reddest point.

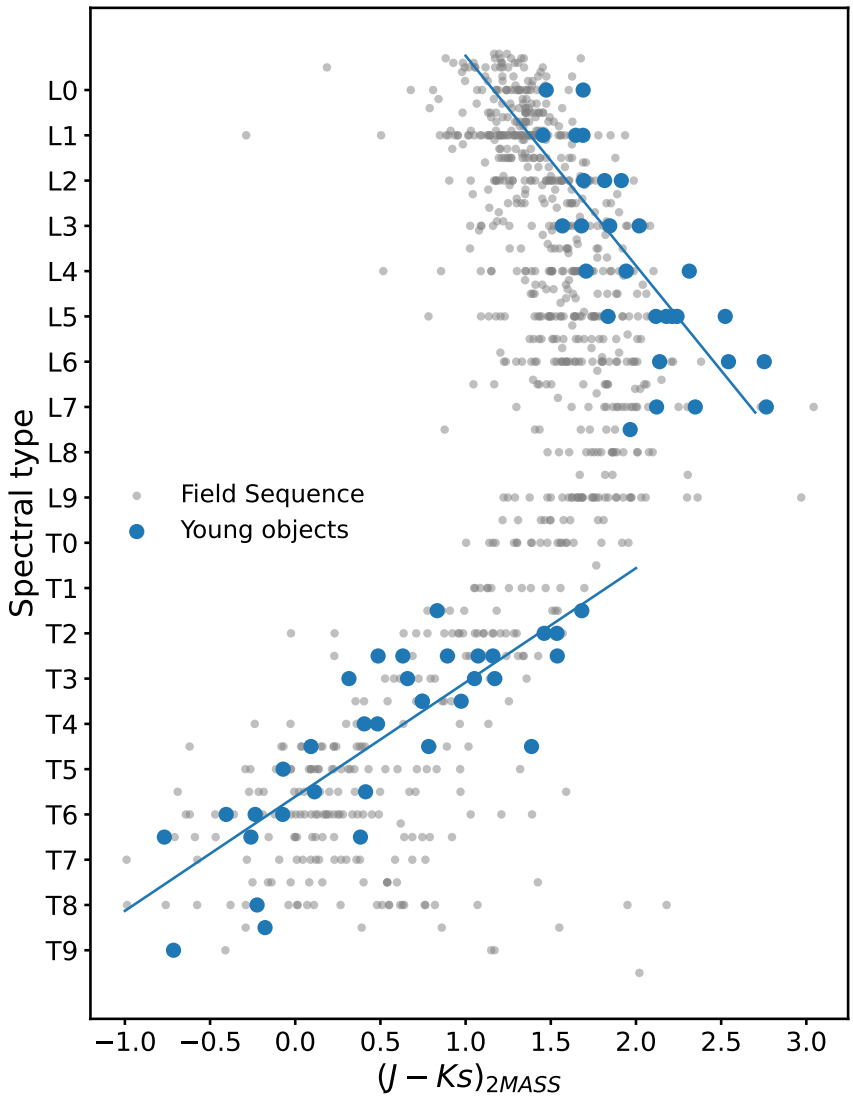


Figure 2.17: Spectral type and colour plot of young objects. The young L dwarfs have redder colour than the field dwarfs, while young T dwarfs do not have this reddening trend and even become slightly bluer from T4 to T7. Blue lines are a linear fit to young L and T dwarfs, respectively.

It is worth noticing that the colour of variable brown dwarfs is also related to their inclination angle. Vos et al. (2017) find a positive correlation between the inclination angle and the $J - K_S$ colour of variable brown dwarfs, which suggests that there are thicker or larger-grained clouds at the equator than at the poles. Suarez et al. (2023) support this by finding a positive correlation between the inclination angle and silicate absorption index. To measure the inclination angle, we need to measure the *vsini* from the high-resolution spectra of our objects. However, since our objects are mainly young T-type planetary mass objects, most of them are fainter than 16.5 magnitudes in the J band, which makes it difficult to obtain high S/N spectroscopic observations under reasonable integration time with telescopes such as VLT. Future telescopes such as the Extremely Large Telescope (ELT) can achieve *vsini* measurements of these objects with high S/N, which can also place an upper limit on the rotation period of our objects. Combined with the period from variability observations which is the lower limit for objects detected with long-term variability, the rotation period of the variable objects and their inclination angle can be constrained.

2.10 Conclusions

We report a near-infrared survey for photometric variability in young planetary-mass objects, including the largest sample of young T dwarfs monitored to date. We conduct continuous J_S- or K_S-band monitoring of 18 objects, with observation time ranging from 1.5 to 7.5 hours per object. One variable 2M1119-1137AB is an unresolved binary. We detected variability in four variables with significance higher than 99%, as well as two variable candidates. The shortest period found among the other three variables is 5.5±0.2 hours, consistent with the trend that young objects have longer rotation periods than field objects, which is due to angular momentum conservation during contraction (Schneider et al., 2018).

We combine our survey with three previous J-band photometric variability surveys of field L and T objects and young low gravity L objects, comprising a total number of 108 objects. From the statistical calculation, we find that young dwarfs have a tendency to be more variable than field dwarfs within peak-to-peak variability amplitude ranges of 0.5%–10% and period ranges of 1.5–20 hr. The variability rate of young L dwarfs is 27^{+13}_{-10}% compared to 6^{+13}_{-5}% for field L dwarfs, consistent with the previous result reported by Vos et al. (2019). We constrain the near-infrared variability rate of young T dwarfs for the first time.

Young T dwarfs have a variability rate of 56^{+20}_{-18}% compared to 25^{+8}_{-7}% for field T dwarfs. Both young L and T samples tend to be more variable than their field dwarf counterparts, with a $\sim 1\sigma$ difference. Moreover, both young and field samples also tend to be more variable at the L/T transition than objects outside the L/T transition, suggesting the strong impact of the L/T transition on atmospheric structures. The variability rate of field objects is 36^{+15}_{-13}% at the L/T transition compared to 18^{+9}_{-7}% outside the L/T transition. The variability rate of young objects is 64^{+23}_{-22}% at the L/T transition compared to 31^{+12}_{-9}% outside the L/T transition. Besides the L/T transition, our analysis of known variables in the J band in the literature finds that young low-gravity L dwarfs with high variability amplitudes tend to congregate in a narrow spectral range of L6-L7.5, while field L dwarfs do not have this trend.

This study once again demonstrates that young dwarfs and field dwarfs are likely distinct groups with differing variability properties at least in terms of strong variability ($> \sim$1%), with surface gravity playing a crucial role in the variability of brown dwarfs for both L-type and T-type dwarfs. Future multi-wavelength time-resolved observations with JWST, along with atmospheric modelling, will enable a deep understanding of how gravity impacts atmospheric structures of L and T dwarfs, and will also be critical for understanding the atmospheres of directly imaged exoplanets, which are similar to young low-gravity dwarfs.

Chapter 3

A direct imaging survey of wide-orbit exoplanets in the Fornax-Horologium association

The work presented in this chapter resulted from a collaborative effort. I led the conceptualisation of the study and the proposal writing, with advisory support from Beth Biller and Matthew Kenworthy. I was responsible for the full data analysis and the primary authorship of this chapter, incorporating suggestions from the collaborators.

3.1 Abstract

Low-mass stellar and substellar companions are indispensable objects for verifying evolutionary models of low-mass stars and planets. The formation of these companions is likely also affected by the surrounding stellar environment. The Fornax-Horologium (FH) association is a recently classified young association in the solar neighbourhood with a dissolving open cluster in its centre. It has not been searched widely for substellar companions and exoplanets with direct imaging. We search for companions of stars in the FH and investigate the formation and evolution of companions during the expansion and dissolution of a star cluster. We conduct a direct-imaging survey of 49 stars in FH with VLT/SPHERE. We present the first result of this survey: HD 24121B, a

companion at the hydrogen-burning limit imaged around HD 24121 in the core cluster of the FH. The companion is located at a projected angular separation of 2.082 ± 0.004 arcsec from the central star and has contrasts of $\Delta H2 = 5.07 \pm 0.05$ mag and $\Delta H3 = 4.98 \pm 0.05$ mag. We estimate a photometric mass of 74.9 ± 7.5 $M_{\rm J}$ for HD 24121B, which places it at the boundary of brown dwarfs and low-mass stars. It is a new benchmark object for evolutionary models at the hydrogen-burning boundary, especially at the age of 30–40 Myr. Orbital fitting with joint Gaia and SPHERE relative astrometry found a high eccentricity for HD 24121B. This suggests that it may have undergone dynamic scattering. Future chemical composition measurements such as high-resolution spectroscopic observations will provide more clues on its formation history. We update the current progress of this survey at the end of the chapter.

3.2 Introduction

The masses of brown dwarfs are intermediate between those of low-mass stars and planets. Brown dwarfs can serve as testbeds for substellar evolutionary models and formation mechanisms. Direct-imaging surveys have discovered several tens of brown dwarf companions, such as PZ Tel B (Biller et al., 2010), CD 35-2722B (Wahhaj et al., 2011), HD 1160B (Nielsen et al., 2012), HR 2562B (Konopacky et al., 2016a), and HD 4747B (Crepp et al., 2016). Unlike low-mass planets, the formation of these heavy brown dwarfs via core accretion (Pollack et al., 1996) in the protostellar and protoplanetary discs is challenging. They are more likely formed via direct collapse in the disc, such as by disc fragmentation (Boss, 1997). Moreover, 40-50% of the directly imaged substellar companions are more than 100 au from away from their host stars [1]. The stellar environment may affect the formation of wide-orbit companions via gravitational instability and dynamical interactions (e.g., Forgan et al., 2015; Zheng et al., 2015; Fujii & Hori, 2019). There are tentative findings on the frequency of stellar and brown dwarf companions that vary in different regions, but they remain limited to small samples (Gratton et al., 2024, 2025).

Past and current direct-imaging surveys mainly focus on nearby young moving groups and OB associations (e.g., Biller et al., 2013a; Nielsen et al., 2019; Desidera et al., 2021). In recent years, several new young clusters and associations have

[1] https://exoplanet.eu/catalog/.

been established. The χ^1 Fornacis cluster (XFOR) was first compiled in a catalogue of open clusters with the name of Alessi 13 by Dias et al. (2002). In this cluster, 108 member stars were identified with Gaia DR2 (Zuckerman, 2019a). After the release of Gaia-EDR3 (Gaia Collaboration et al., 2021a), its membership was extended to 164 stars, and its distance was determined to be ~108 pc (Galli et al., 2021). This region was later expanded to define the Fornax-Horologium (FH) association of 329 candidate members with XFOR as the core cluster and a halo of stars surrounding the cluster (Kerr et al., 2022). The FH is located in the Austral Complex, which is one of the nearest young stellar populations and contains other associations, including Tuc-Hor, Carina, and Columba (Kerr et al., 2022).

Open clusters are gravitationally bound, while young moving groups are not (e.g., Gagné, 2024). Initially, XFOR was identified as one of the few young open clusters in the solar neighbourhood. Hunt & Reffert (2024) reported that only 11% of the open clusters within 250 pc can be identified as bound open clusters by their Jacobi radius, and they classified XFOR as a moving group instead of an open cluster. Kerr et al. (2022) reported that XFOR is likely in the virialised state and that the FH consists of a probably dissolving cluster with a large low-density halo. Therefore, while the FH is currently not an overdense configuration, it likely formed in a much more compact configuration when we trace the motion of the stars back in time. By contrast, there are young star associations (1–5 Myr) in which stars formed in relatively loose environments. While XFOR is no longer an open cluster, it was previously in a gravitationally bound state and is now dissolving into a moving group.

The age of the FH as determined from isochrones, dynamics, and X-ray emissions, lies between 30–40 Myr, with all methods yielding consistent ages (Galli et al., 2021; Kerr et al., 2022; Mamajek, 2016). Known young associations and moving groups within 150 pc either have ages younger than 30 Myr, such as TW Hydra (~10 Myr, Bell et al., 2015), β Pictoris (~22 Myr, Shkolnik et al., 2017), Columba, and Carina (~26 Myr, Kerr et al., 2022), or older than 40 Myr, such as Tuc-Hor (~46 Myr, Kerr et al., 2022), AB Doradus (~150 Myr, Bell et al., 2015), and Argus (40–50 Myr, Zuckerman, 2019b). Therefore, the FH provides a valuable opportunity for studying planetary systems at ages between 30 and 40 Myr. The rich abundance of M dwarfs with warm debris discs in XFOR indicates that this cluster has gone through an active companion formation (Zuckerman, 2019a). Its young age and proximity make it well-suited for direct-imaging surveys of

exoplanets.

During the expansion and dissolution of the FH, there were likely frequent stellar encounters and flybys compared to those in a moving group or sparse association environment. These dynamical interactions have a significant impact on the formation and survivability of wide-orbit low-mass stellar and substellar companions. On the one hand, frequent stellar encounters in a dense environment may trigger more gravitational instability (Krumholz et al., 2012) and promote the formation of wide-orbit companions. On the other hand, they can also cause orbit instability and eject companions from their natal systems (Parker & Quanz, 2012; van Elteren et al., 2019). The FH occupies a unique parameter space in terms of age and cluster evolution. We are therefore conducting a direct imaging survey of stars in the FH.

In this chapter, we present the first companion imaged in this survey: an object at the hydrogen-burning limit orbiting HD 24121. In Sect. 3.3, we describe the sample selection for this survey. In Sect. 3.4, we describe the observations and data reduction for this survey, focusing on HD 24121. We characterise this system, including astrometry, photometry, orbit fitting and mass estimation of HD 24121B in Sect. 3.5. In Sect. 3.6, we discuss the formation of HD 24121B and conclude on what we found for this system. We also provide an update on the current status of this survey in Sect. 3.7.

3.3 Sample selection

The targets were selected from the catalogue compiled by Kerr et al. (2022). We selected stars with G brighter than 12 mag for a good AO performance by ground-based 8-m telescopes. We also ensured that every target has a renormalised unit weight error (RUWE) smaller than 1.4 in the Gaia DR3 catalogue (Gaia Collaboration et al., 2021a) to filter out targets with poor astrometry solutions due to unresolved binaries. We checked the Tycho-2 (Høg et al., 2000), Gaia DR3 and Hipparcos-Gaia (Brandt et al., 2021a) catalogues and excluded accelerating stars with possible stellar companions at small separations predicted by the COPAINS tool (Fontanive et al., 2019). After the selection, the sample contains 18 stars from the central core XFOR (Galli et al., 2021) and 31 stars from the halo (Kerr et al., 2022). They are A-K type stars with masses ranging between 0.8 and 2.4 $M_{\odot}$ (Kerr et al., 2022). Table 3.1 presents the target list of this survey.

Table 3.1: Target list

Name	RA (J2000)	Dec (J2000)
CD-42 905	02 43 21.81	-41 51 08.30
HD 17864	02 50 47.81	-39 55 56.01
HD 18184	02 53 51.82	-40 11 38.59
HD 20379	03 15 17.11	-37 02 30.10
CD-37 1224	03 16 03.07	-37 25 22.28
HD 20484	03 16 32.72	-35 41 28.24
HD 20707	03 18 52.94	-36 07 37.54
HD 20854	03 20 09.46	-40 17 40.18
CD-37 1263	03 22 20.01	-36 38 13.82
Gaia DR3 4860808694421129600	03 25 55.84	-35 55 15.19
CD-36 1309	03 28 07.44	-35 54 43.46
CD-33 1586	04 10 10.63	-32 58 12.00
HD 27120	04 15 33.16	-34 09 20.10
GUVV J033438.6-352904.2	03 34 38.68	-35 29 03.94
HD 23380	03 43 27.88	-33 30 08.16
HD 24121	03 48 51.39	-40 38 35.57
HD 23493	03 44 28.84	-30 55 02.24
CD-30 1235	03 13 18.92	-29 53 19.48
TYC 7579-1099-1	04 32 08.10	-38 17 45.11
HD 24374	03 51 18.00	-33 44 59.59
TYC 7033-1343-1	04 09 02.44	-33 21 14.67
CD-32 1029	02 49 34.75	-32 23 49.89
HD 27355	04 17 44.85	-31 06 11.17
TYC 7569-1432-1	03 45 34.41	-39 36 40.71
TYC 7027-458-1	03 35 04.44	-36 36 14.01
BD-20 638	03 26 22.05	-20 01 48.73
CD-36 1176	03 08 49.14	-36 18 44.35
UCAC4 350-003780	03 22 25.00	-20 03 51.44
TYC 5877-1308-1	03 37 06.82	-19 10 58.68
UCAC3 68-8541	04 01 10.67	-56 25 27.86
HD 18117	02 52 52.17	-48 09 11.14
HD 273371	05 03 47.87	-45 49 47.17
CD-30 1572	03 56 45.46	-30 12 23.93
CD-30 944	02 34 20.25	-30 14 39.36
HD 29843	04 40 58.59	-29 22 59.90
CD-45 1384	04 03 53.42	-44 39 31.55
TYC 7590-708-1	05 01 50.90	-41 39 07.98
UCAC2 10099995	04 38 17.77	-50 03 52.29
CD-51 993	04 02 41.23	-51 27 24.31
TYC 7006-446-1	01 58 42.31	-32 01 22.16
CPD-39 313	03 30 49.31	-38 50 36.36
TYC 7586-1115-1	04 47 31.97	-38 18 41.37
HD 28852	04 31 03.71	-39 51 40.10
TYC 6435-177-1	02 22 19.36	-27 48 51.45
CD-31 1720	04 09 48.18	-31 02 08.34
HD 17070	02 42 41.73	-49 43 45.96
HD 21341	03 25 12.81	-37 09 09.69
Gaia DR3 4861469874570139776	03 31 30.02	-33 58 14.27
TYC 6442-90-1	03 13 53.43	-26 44 49.12

3.4 Observations and data analysis

The observations are taken with the Spectro-Polarimetric High-contrast Exoplanet REsearch (SPHERE) instrument (Beuzit et al., 2019) in pupil-tracking mode. We obtained 56 h between 2023 and 2025 and 33 targets were successfully observed with a total time of 34.3 h (Programme ID 112.25SC.001 and 114.2776.001, PI.P. Liu). We used the angular differential imaging (ADI) strategy (Marois et al., 2006), observing targets in time windows of 2–4 h covering their meridian time. During the first run, each of the 11 targets was observed for 1.5 h; in the second run, following optimisation of the observation time, each of the 22 targets was observed for 45 min. They were observed in the dual-band imaging mode with SPHERE/IRDIS in the $H2$ and $H3$ filters with the N_ALC_YJH_S coronagraph.

The first-epoch observations of HD 24121 were taken on 4 Oct 2023 with a total time of 1.5 h. The science time was 1.1 h with a detector integration time (DIT) = 32 s and a number of DIT (NDIT) = 1 for each exposure. The airmass ranged from 1.04 to 1.08. The total field-of-view rotation was 42.°18. The seeing varied between 0.″46 and 0.″70. The second-epoch observations of HD 24121 were taken on 10 Nov 2024 with a total duration of 35 min. The observation mode was set to the same mode as for the first epoch. The science time was 0.16 h with DIT = 32 s and NDIT = 1. The airmass ranged from 1.063 to 1.056. The total field-of-view rotation was 5.°57. The seeing varied between 0.″63 and 0.″96. In each epoch, we also took two separate non-coronagraphic exposures of the central star of DIT = 6 s and NDIT = 1 with the neutral density filter ND_1.0 at the beginning and end of observations.

We reduced the raw images using the ESO pipeline for SPHERE wrapped in a Python script (Vigan, 2020). The companion is bright enough to be seen in each preprocessed frame. It is at a distance of ∼2 arcsec in the south-east direction of the central star, as shown in the de-rotated and stacked image of the first epoch in Fig. 3.1. We also applied classical ADI to the data cube and did not detect any other sources.

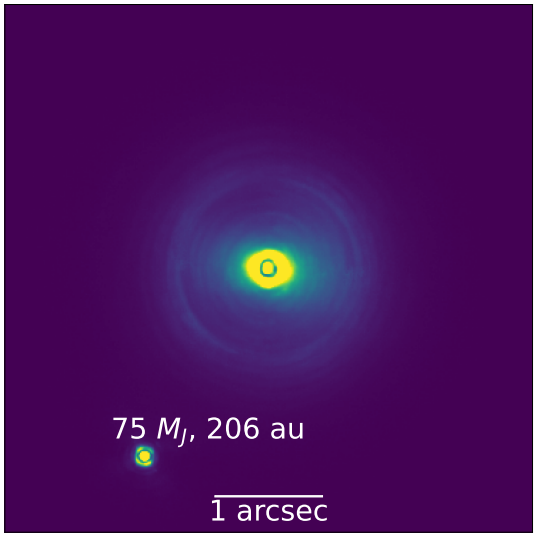


Figure 3.1: Coronagraphic image of HD 24121 at the first epoch of SPHERE observations. The brown dwarf companion is the point source in the south-east direction. North is up, and east is to the left.

3.5 Results of the HD 24121 system

This companion was also detected by Gaia with the Gaia ID of Gaia DR3 4855032616243433984 (Gaia Collaboration et al., 2021a). The Gaia ID of the primary star is Gaia DR3 4855032616243433856. They are high proper motion sources that move in similar directions in the Gaia catalogue. Their parallax agrees within 1σ, while the difference in proper motion is larger than 2σ: -0.6 ± 0.3 mas yr^{-1} in RA and -2.6 ± 0.5 mas yr^{-1} in Dec, which is likely due to the orbital motion of the companion. The primary star has a spectral type of G3 (Zuckerman, 2019a) with a mass of ~1.06 $M_\odot$(Kerr et al., 2022). Table 3.2 summarises the properties of this system, updated with our SPHERE observations.

3.5.1 Astrometry

We fitted a 2D Gaussian to each individual SPHERE frame and took the mean value as the measured position and the standard deviation as the fitting uncertainty for the companion. We also included the uncertainty from the pixel scale, centring, distortion, true north angle, and pupil offset following the astrometry calibration provided in the latest SPHERE User manual[2] and by

[2] https://www.eso.org/sci/facilities/paranal/instruments/sphere/doc.html

Table 3.2: Properties of HD 24121 AB system

Property	Primary	Secondary
Age (Myr)[a]	30 – 40	...
Parallax (mas)[b]	10.17 ± 0.01	9.67 ± 0.53
$\mu_\alpha cos(\delta)$ (mas yr^{-1})[b]	38.72 ± 0.01	38.13 ± 0.34
μ_δ (mas yr^{-1})[b]	-2.64 ± 0.01	-5.22 ± 0.48
Sep[c] (mas, 2016.0)	-	2071.2 ± 0.4
PA[c] (deg, 2016.0)	-	146.31 ± 0.01
Sep[d] (mas, 2023-10-04)	-	2082 ± 4
PA[d] (deg, 2023-10-04)	-	146.56 ± 0.15
Sep[d] (mas, 2024-11-10)	-	2082 ± 4
PA[d] (deg, 2024-11-10)	-	146.62 ± 0.15
Gaia G (mag)	9.628 ± 0.003	17.28 ± 0.01
SPHERE $\Delta H2$ (mag)[e]	-	5.07 ± 0.05
SPHERE $\Delta H3$ (mag)[e]	-	4.98 ± 0.05
2MASS J (mag)	8.656 ± 0.024	-
2MASS H (mag)	8.383 ± 0.046	-
2MASS K (mag)	8.312 ± 0.024	-
$T_{\rm eff}$ (K)[e]	5819 ± 13	2972^{+220}_{-198}
$\log(L/L_\odot)$(dex)[e]	0.012 ± 0.001	-2.48 ± 0.06
Mass	1.06 $M_\odot$[f]	74.9 ± 7.5 $M_{\rm J}$[e]

Notes. [a] There is no conclusive age for XFOR, but the latest age estimate is about 30 Myr (Galli et al., 2021; Kerr et al., 2022). We adopted a conservative age range of 30 – 40 Myr. [b] Both of them have Gaia astrometry data, and we present them here. [c] Separation and position angle in the Gaia reference epoch 2016.0. [d] Separation and position angle measured in SPHERE observations. [e] This work. [f] Kerr et al. (2022).

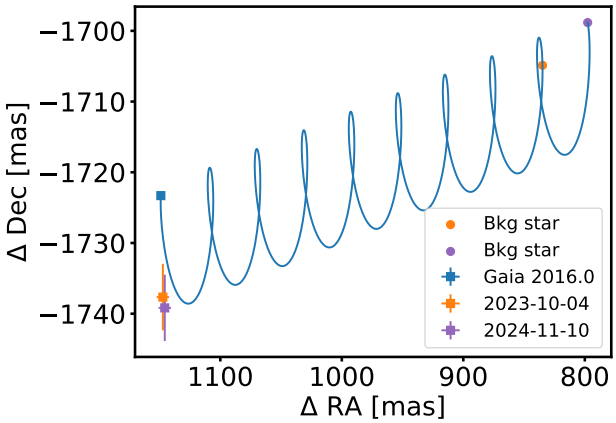


Figure 3.2: Relative positions of HD 24121B to the central star. The blue trajectory shows the relative position of a static background star over time, starting from the Gaia reference epoch 2016.0. The orange and purple dots on the track indicate the expected positions at epochs 2023-10-04 and 2024-11-10 if HD 24121B were a static background star.

Maire et al. (2021). The results are presented in Table 3.2. We present the relative astrometry measured with SPHERE in 2023 and 2024 in Fig. 3.2. We also include the relative positions of HD 24121B to HD 24121 in the Gaia reference epoch 2016.0. It is comoving with the central star between 2023 and 2024. The position difference between the Gaia and SPHERE epochs is likely due to the orbital motion of HD 24121B over 8 years. The projected separation is about 200 au given the measured angular separation of ∼2 arcsec at a distance of 98 pc.

3.5.2 Photometry

We performed aperture photometry of HD 24121B in the de-rotated and stacked image and subtracted the local sky background. We calculated the signal-to-noise ratio (S/N) of HD 24121B by performing photometry on all apertures of the same size at the same separation as the source, but at different position angles, except for the aperture on the companion. Then, we took the three σ clipped standard deviation as the noise and the average as the local sky background. We also performed aperture photometry on the non-coronagraphic image with the same aperture radius to measure the star flux. Then, we converted the flux contrast into magnitude contrast. The magnitude contrasts measured in the first epoch are $\Delta H2 = 5.09 \pm 0.11$ mag and $\Delta H3 = 4.99 \pm 0.11$ mag. The magnitude contrasts measured in the second epoch are $\Delta H2 = 5.07 \pm 0.05$ mag and $\Delta H3 = 4.98 \pm$

0.05 mag. They agree with each other within 1σ without discernible variability.

To estimate the effective temperature of HD 24121B, we fitted the spectral energy distribution (SED) using SPECIES (Stolker et al., 2020). Data are available in three photometric bands: Gaia G, and SPHERE $H2$ and $H3$. We measured the contrasts of the companion to the central star in $H2$ and $H3$. To convert the SPHERE band contrasts into the apparent magnitudes of the companion, we first performed synthetic photometry on the central star. We fitted the SED of the host star using its GALEX, Tycho, SDSS, Gaia, 2MASS, and WISE photometric data with the BT-Settl-CIFIST models (Allard et al., 2013). We fitted $T_{\rm eff}$= 5819 K, similar to 5805 K reported in Gaia. The SED fitting results of the primary star can be found in Fig. 3.3. Then, we measured the primary magnitude in $H2$ and $H3$ by applying synthetic photometry on the best-fit model spectrum. Adding the contrasts measured from direct imaging, we obtained the apparent magnitude of HD 24121B in $H2$ and $H3$.

Then, we used two evolutionary models for warm brown dwarfs to fit their SED: BT-Settl (Allard et al., 2003) and AMES-DUSTY (Allard et al., 2001; Chabrier et al., 2000). We included error inflation factors in the fitting because the uncertainty from the synthetic photometry is underestimated. We derived similar results for the two models. BT-Settl has slightly smaller residuals in the SED fitting, and therefore, we present its best-fit spectra and posterior distribution in Fig. 3.4. We fitted $T_{\rm eff}$= 2972^{+220}_{-198} K and $\log(L/L_{\odot})$= -2.48 ± 0.06 dex for the companion.

3.5.3 Orbital fitting

To find plausible orbits for this system, we used ORBITIZE (Blunt et al., 2020) to fit the relative astrometry of HD 24121B and HD 24121 by combining the Gaia reference epoch of 2016.0 and the two SPHERE epochs. We adopted a parallax of 10.17 ± 0.01 mas for the primary star from Gaia DR3, and we assumed a total mass of 1.13 ± 0.1 $M_{\odot}$. The fitted orbits and posterior distributions are shown in Fig. 3.5. We find a semi-major axis of ~205 au and a well-constrained inclination of $70.^{\circ}4^{+9.6}_{-19.1}$. The orbital period is ~2745 year. We find a high eccentricity for HD 24121B, with a median of 0.6 and a peak of 0.9, according to its posterior distribution.

We calculated the fitted orbital velocity of HD 24121B in the Gaia reference epoch

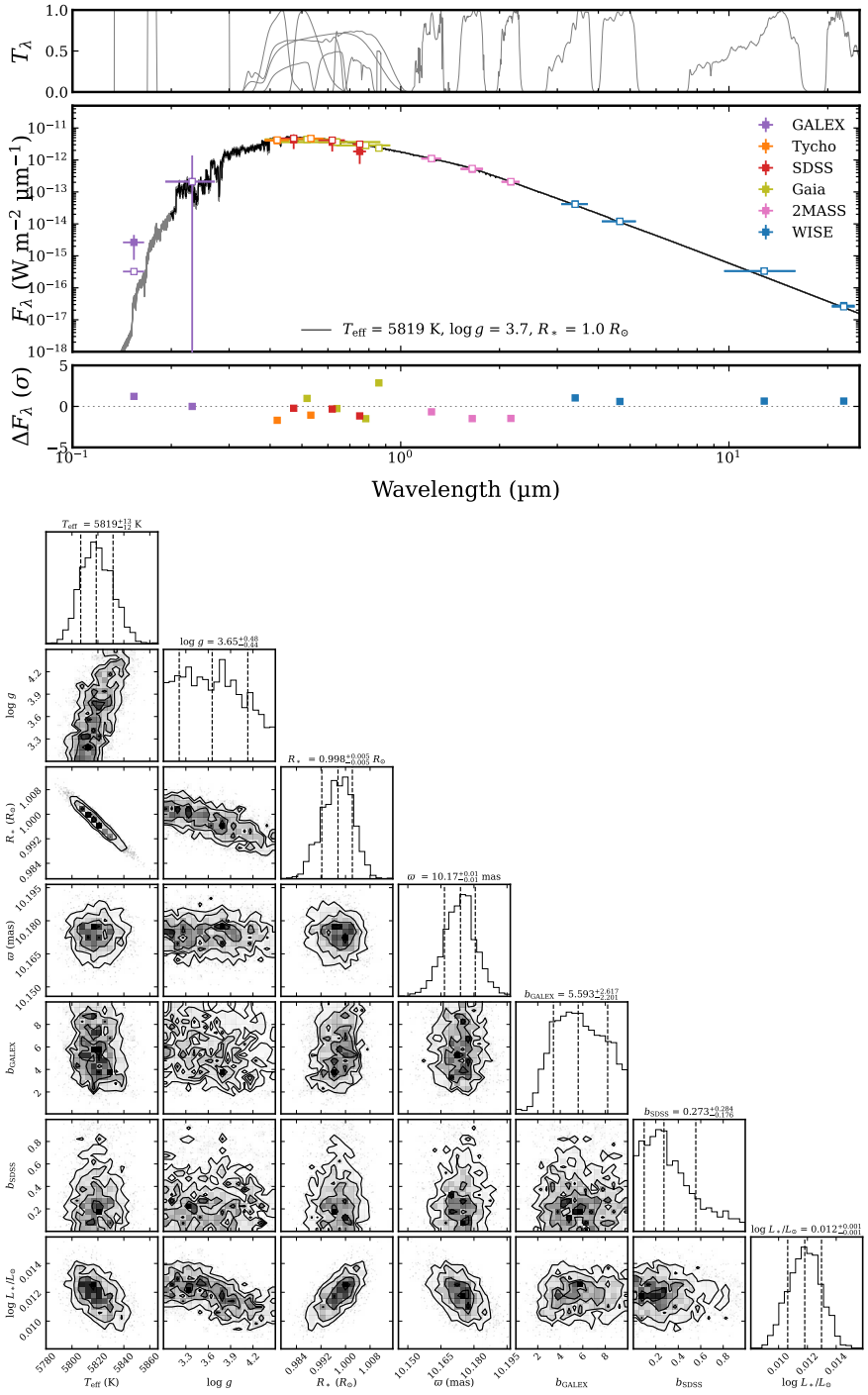


Figure 3.3: SED fitting of the central star using BT-Settl-CIFIST models. Upper panel: the filled squares with errorbars are the measured photometric data and the open squares are the modelled photometric data. The black line is the optimised model spectrum and the grey lines are 30 spectra randomly drawn from the posterior distributions. Lower panel: posterior distributions of SED fitting. b_{GALEX} and b_{SDSS} are the inflation factors of the GALEX and SDSS photometric data. We included error inflation into fitting because the uncertainty in GALEX and SDSS photometric data is likely underestimated. No infrared excess is detected.

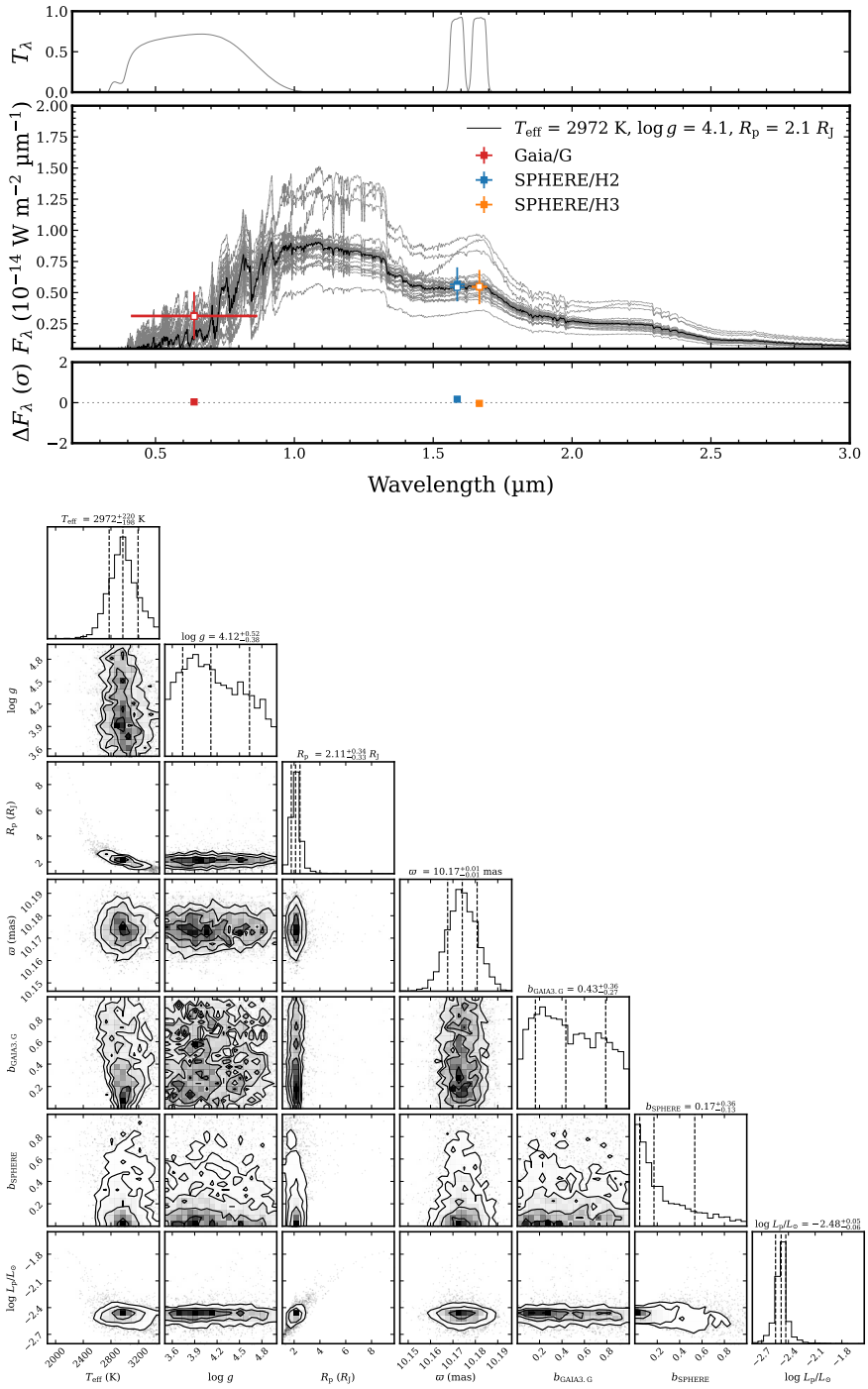


Figure 3.4: Left panel: SED fitting of the companion, combining the Gaia G, and SPHERE $H2$ and $H3$ photometric bands using BT-Settl atmospheric models. The filled squares are the measured photometric data with error bars, and the open squares are the modelled photometric data. The grey lines are 30 spectra randomly drawn from the posterior distributions. The upper panel shows the transmission of photometric bands, and the lower panel shows the residuals in σ. Right panel: Posterior distribution of the SED fitting of the companion using BT-Settl models. $b_{GAIA.G}$ and b_{SPHERE} are the inflation factors of the Gaia and SPHERE photometric data.

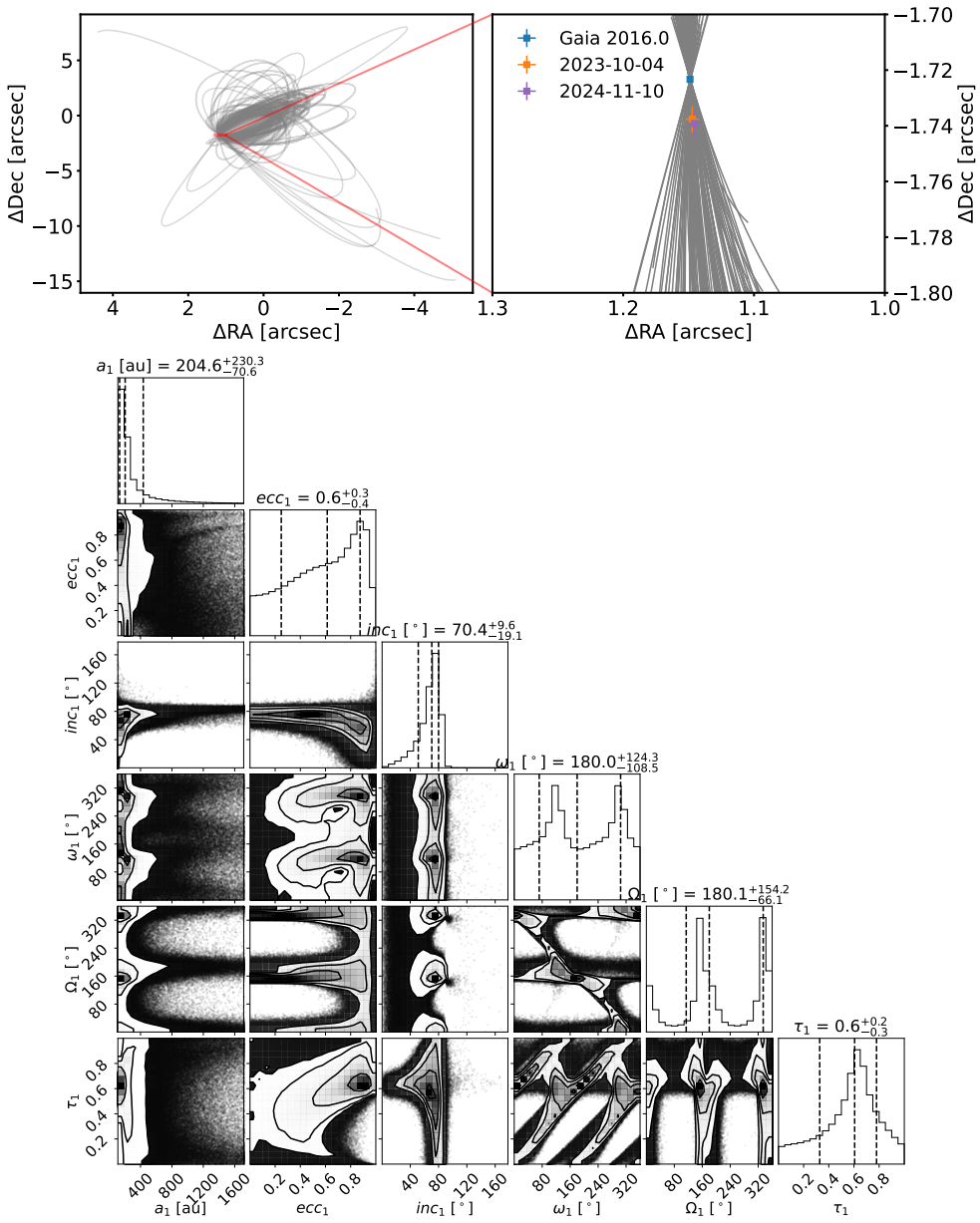


Figure 3.5: Left panel: fitted orbits of HD 24121B. We show 100 random orbits drawn from the posterior of the fit. Right panel: posterior distribution of the orbital fitting of HD 24121B.

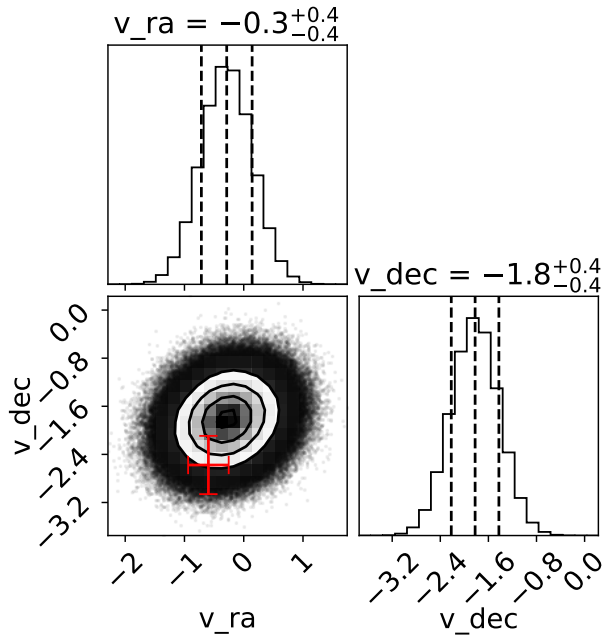


Figure 3.6: Posterior distribution of the orbital velocity of HD 24121B in the Gaia reference epoch. The units are in mas yr^{-1}. The red data point is the proper motion difference from Gaia.

and derived the velocity in RA (v_ra) = -0.3 ± 0.4 mas yr^{-1} and the velocity in Dec (v_dec) = -1.8 ± 0.4 mas yr^{-1}. The posterior distribution is presented in the right panel of Fig. 3.6. The fitted orbital velocity matches the Gaia measured proper motion difference within 1–2σ. Therefore, the two sources are very likely in a gravitationally bound system.

3.5.4 Companion mass estimation

The dynamical mass of the companion cannot be constrained in the orbital fitting due to the small orbit coverage. There is no evidence of Gaia acceleration in either source: their RUWE is smaller than 1. There is no proper motion anomaly between the Gaia and Hipparcos catalogue (Brandt et al., 2021a). Therefore, we estimated the mass from photometry using the rejection-sampling method (e.g., Dupuy & Liu, 2017). With a bolometric luminosity of -2.48 ± 0.06 dex from the SED fitting and an age of 32.4 ± 1.3 Myr (Kerr et al., 2022), the derived mass is 72.2 ± 6.4 $M_{\rm J}$ using the BT-Settl evolutionary models. With a broader uniform age distribution between 30 and 40 Myr, the derived mass is 74.9 ± 7.5 $M_{\rm J}$. We obtained consistent results with the BCAH15 model (Baraffe et al., 2015). As demonstrated in Fig. 3.7, HD 24121 straddles the region between brown dwarfs

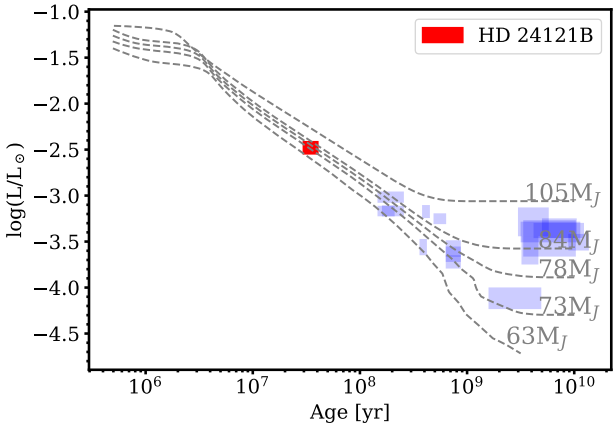


Figure 3.7: Evolutionary tracks of low-mass stars and brown dwarfs from the BCAH15 models. Hydrogen-burning stars reach stable luminosities after a certain contraction time, while brown dwarfs continue to cool. The red square indicates the luminosity (1σ) and age (30–40 Myr) range of HD 24121B. The blue squares show the companions at the hydrogen-burning limit from the Gaia ultracool dwarf companion catalogue, which includes objects within 100 pc (Baig et al., 2024). HD 24121B is located at the hydrogen-burning limit between low-mass stars and brown dwarfs, and it is much younger than the other companions.

and low-mass hydrogen-burning stars in the evolutionary tracks.

3.6 Discussions and conclusions of the system

We presented a companion of HD 24121, the object HD 24121B. With a mass of 74.9±7.5 M_J, HD 24121B can serve as a benchmark object in characterising the evolutionary models of low-mass stars and brown dwarfs at the hydrogen-burning boundary. Directly imaged low-mass stellar and substellar companions at the age of 30 Myr are rare due to the lack of moving groups or clusters of 30 Myr in the solar neighbourhood. Almost all of the benchmark brown dwarf companions at the hydrogen-burning limit were found in relatively old systems such as HD 72946B (72.4±1.6 M_J, 0.9–3 Gyr, Maire et al., 2020), HR 7672B (~68.7 M_J, 2.5 Gyr, Crepp et al., 2012), and HD 4747B (70±1.6 M_J, 2.3±1.4 Gyr, Peretti et al., 2019), and those compiled in the Gaia ultracool dwarf companion sample (Baig et al., 2024). Most of the directly imaged companions in the literature that are younger than 30 Myr have masses lower than 70 M_J, which is likely due to a selection bias of avoiding massive companions. Nevertheless,

HD 24121B provides a unique age range for studying evolutionary models at the hydrogen-burning limit. At the age of 30 Myr with a mass of 75 $M_{\rm J}$, HD 24121B is about to start lithium burning according to the BT-Settl and BCAH15 models. A future spectroscopic characterisation of HD 24121B can measure its lithium abundance.

The formation of HD 24121B is also an intriguing question. It is challenging to form such a heavy companion at 200 au by core accretion or even pebble accretion (Chambers, 2021; Savvidou & Bitsch, 2023). Disc fragmentation triggered by gravitational instability and binary-like cloud fragmentation are probably the most favourable formation mechanisms here. They can produce brown dwarfs and low-mass hydrogen-burning stellar companions around Sun-like stars (Stamatellos & Whitworth, 2009). Moreover, subsequent dynamical effects such as fragment-fragment scattering can efficiently modify the orbital parameters of companions (Hall et al., 2017; Forgan et al., 2018). Fragment-fragment scattering can populate the companions to a broader semi-major axis range such as over $10^2 - 10^3$ au (Forgan et al., 2018). Dynamical evolution including fragment-fragment scattering and multi-object scattering also results in a relatively higher eccentricity for wide-orbit companions or even planet ejection and recapturing (Forgan et al., 2015), which agrees with the high eccentricity we derived for HD 24121B. Hwang et al. (2022) reported that wide stellar binaries have a uniform eccentricity distribution for separations within 200 au. A similar trend has been found for brown dwarfs within 100 au: They have a broad peak at an eccentricity of 0.6–0.9 (Bowler et al., 2020a). Therefore, HD 24121B is likely formed by disc or cloud fragmentation, followed by a dynamical evolution, before it reached its current orbit.

The possible dynamical scattering might result from interactions with another companion in the same system. To estimate the upper mass limit of the potential additional companion, we calculated the 5σ contrast curve of the dataset of the epoch 4 Oct 2023 and reached a sensitivity of 3 $M_{\rm J}$ beyond ~1.″5. Therefore, this companion is probably smaller than 3 $M_{\rm J}$ or at a smaller separation with a higher mass if it has survived in the same system. Because HD 24121 is located in the core cluster of the FH, dynamical scattering between HD 24121 and other stars may also have been possible. The core cluster of the FH is a dissolving open cluster, and its core region is about one order of magnitude denser than the local disc stellar density (Zuckerman, 2019a). When we trace the motion of stars back, the chances of stellar encounters and flybys are probably much higher than in the

current stage.

A composition and abundance comparison of HD 24121 and HD 24121B can give more clues about the formation of HD 24121B, such as the C/O ratio, which can serve as an indicator of its formation location in the disc and evidence of gas accretion (e.g., Öberg et al., 2011). Recently, the carbon isotopologue ratio was proposed as a probe to distinguish low-mass planet and brown dwarf formation pathways (Zhang et al., 2021a,b; de Regt et al., 2024; González Picos et al., 2025). Although the central star HD 24121 may be too hot for us to measure its carbon isotopologue ratio, high-resolution spectroscopic observations of HD 24121B in the near-infrared band can constrain its isotopologue ratio, which can then be compared with that of other brown dwarfs. Spectroscopic observations can also provide the spin-rate measurement of HD 24121B from broadened spectral lines, which will provide indications about its angular momentum evolution (Bouvier et al., 2014; Schwarz et al., 2016). We therefore recommend follow-up spectroscopic observations to characterise HD 24121B. It can serve as a benchmark object for studying the evolutionary models and formation mechanisms of low-mass stellar and substellar companions.

3.7 Other Candidates

This is still an ongoing survey and we have obtained another 18.5 h to continue this survey with SPHERE in the fall of 2025. Besides HD 24121B, there are four planet candidates and a very low-mass star companion detected at the time of writing. The four planetary systems require second epoch observations for common proper motion confirmation. We estimated their masses by their H contrasts with ATMO evolutionary models (Chabrier et al., 2023). They are a $7\,M_{\rm J}$ candidate at 470 au, an $8\,M_{\rm J}$ candidate at 460 au, a $10\,M_{\rm J}$ candidate at 540 au, and an $11\,M_{\rm J}$ candidate at 310 au. Although we only have one epoch observation of the UCAC2 10099995, we confirm a very low-mass stellar companion at a separation of 243 au with Gaia DR3.

3.7.1 Very low-mass stellar companion: UCAC2 10099995B

UCAC2 10099995 was observed on 30 January 2025. The companion is 200 au away from the central star in the north-east direction, shown in the left panel of

Fig. 3.8. Its contrast to the host star is 3.12 ± 0.03 mag in $H2$ and 3.09 ± 0.03 mag in $H3$. Both the host star and the companion are in Gaia DR3 catalogue with an ID of 4787482603265516032 for the host star and 4787482607561544064 for the companion. Their parallax is consistent at the ~1σ level and proper motion only differs by several mas yr^{-1}. Given their small separation and brightness of the companion, it is very likely a comoving source of the central star. Therefore, we performed orbital fitting of the companion with two epochs of relative positions: one from our SPHERE observation and the other from Gaia observation. The results are shown in Fig. 3.9. We also found a high eccentricity with a peak at 0.9 and a 68% confidence range of 0.5–0.9 for UCAC2 10099995B. The proper motion difference observed by Gaia can also be explained by the orbital motion of the companion. Therefore, combined with one epoch observation of SPHERE and Gaia DR3, we confirm that this candidate is a comoving companion of UCAC2 10099995.

Similarly, we performed SED fitting of the companion by fitting G, $H2$, and $H3$ bands photometry with BT-Settl models. The best-fitted $T_{\rm eff}$ is 3249^{+274}_{-283} K and $\log(L/L_\odot)$ is $-2.19^{+0.05}_{-0.06}$ dex. The fitted spectra are presented in the right panel of Fig. 3.8. With this bolometric luminosity and age between 30–40 Myr, we estimated a mass of 121.6 ± 14.6 $M_{\rm J}$ for the companion using rejection sampling. The central star of 0.7 $M_\odot$ and then the mass ratio is 0.16.

3.7.2 Wide-separated candidate companions detected in Gaia DR3

As the two companions discovered in the survey are both included in Gaia DR3, this suggests that there may be more wide-orbit companions hidden in Gaia DR3. Therefore, we used selection criteria similar to Fontanive et al. (2019); Bohn et al. (2022); Bonavita et al. (2022) to match wide-separated candidate companions within a projected separation of 10,000 au of all candidate members in FH compiled in Kerr et al. (2022):

- the parallax difference is smaller than 20% of the host;
- the proper motion difference in RA and Dec is smaller than 10 km s^{-1}.

Then we estimated the masses of the candidate companions by interpolating their G magnitudes in the BHAC15 evolutionary models (Baraffe et al., 2015) assuming

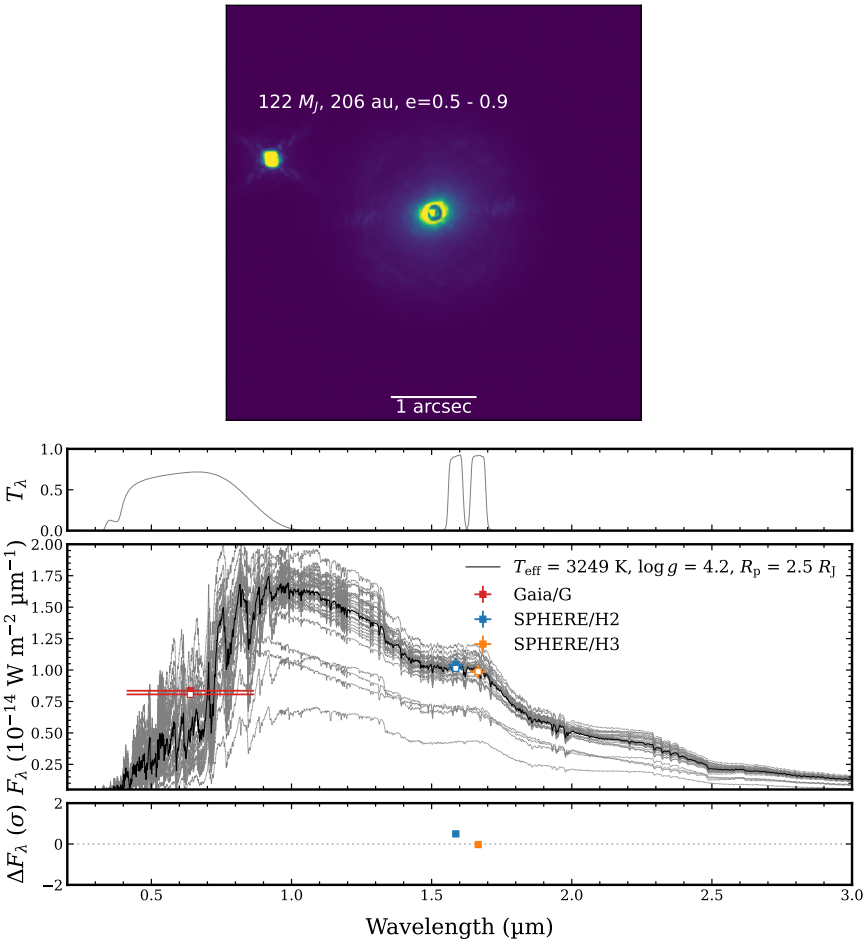


Figure 3.8: Upper panel: a coronagraphic image of UCAC2 1009995. Lower panel: SED fitting of UCAC2 1009995B.

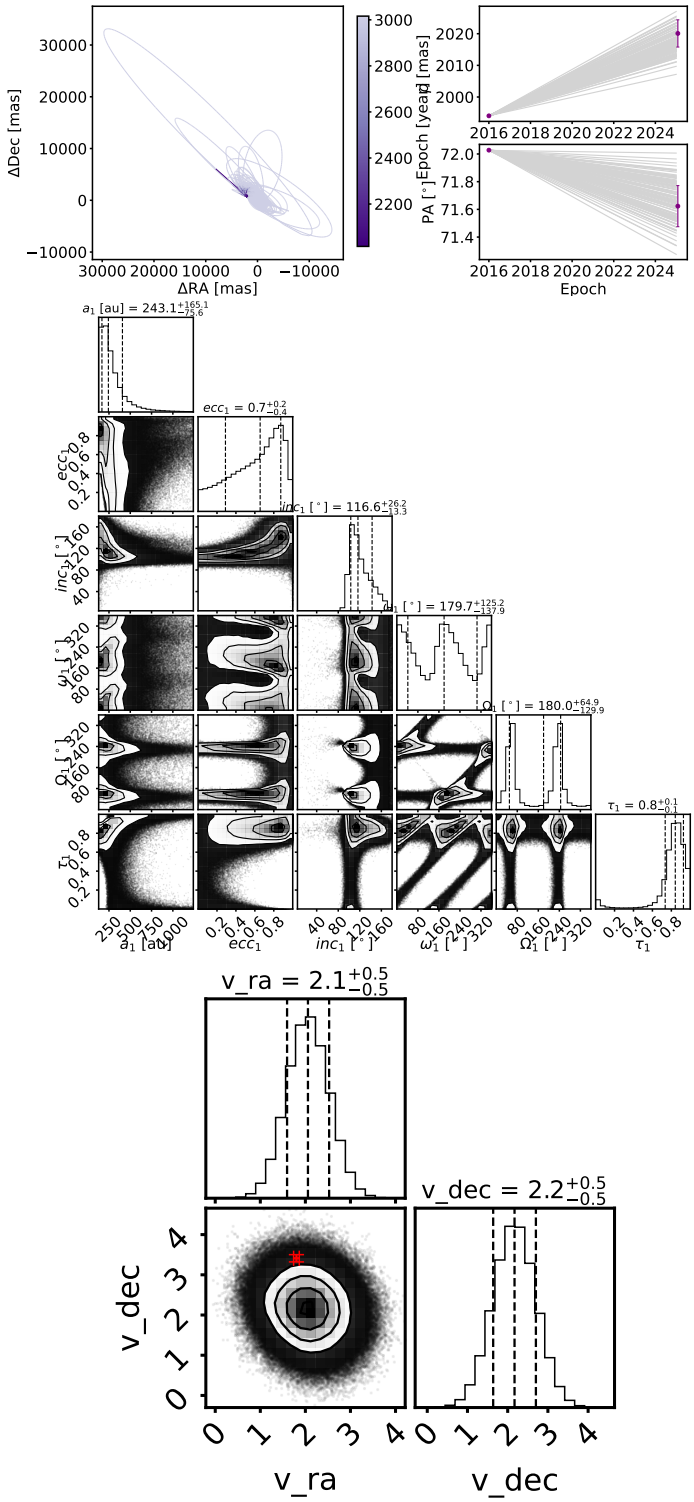


Figure 3.9: Upper panel: 100 random orbits of UCAC2 1009995B drawn from the posterior distributions of orbital fitting. Middle panel: posterior distributions of orbital parameters. Lower panel: fitted and measured orbital velocity (red marker) of UCAC2 1009995B.

an age of 30 Myr. We calculated the escape velocity according to the masses of the hosts and candidate companions. We compared the proper motion difference with the escape velocity and retained those with a proper motion difference smaller than the escape velocity, though the proper motion difference is the projected velocity, which is the lower limit of their relative velocity. This resulted in 36 candidate companions as shown in Fig. 3.10. To compare with other regions, we performed the same search for the first 150 stars (F150) in SHINE published in Desidera et al. (2021). The reason why we chose the F150 sample is that their stellar ages are well compiled, while the stellar ages of the full sample of SHINE are not publicly available yet. Bonavita et al. (2022) compiled a catalogue of 78 stellar binaries discovered in the FoV of SPHERE/IRDIS for the full sample of SHINE (463 stars). Our search supplements 19 candidate companions within 10,000 au for the F150 sample. The majority of stars in SHINE are from nearby young moving groups. Bohn et al. (2022) found 118 candidate companions of the 459 K-type stars in Sco-Cen matched in Gaia DR3. The candidate companions of SHINE and Sco-Cen are also presented in Fig. 3.10.

From our analysis of HD 24121B and UCAC2 1009995B, we found that their masses are underestimated based on just G band estimation. Therefore, the masses of these candidate companions in Fig. 3.10 are also underestimated. Nevertheless, it reveals an abundance of wide-separated stellar mass candidate companions in young moving groups, FH, and Sco-Cen. However, there is a significant difference in secondary mass for separations within 500 au. We have confirmed two wide-separated companions with masses $< \sim 120\,M_{\rm J}$ at separations of ~200 au in the FH survey, HD 24121B and UCAC2 1009995B, from just the 33 observed stars, which is a much smaller sample size compared to SHINE or the K-type stars in Sco-Cen. There is also another candidate companion with a mass in the brown dwarf regime at a separation of ~300 au. However, around stars in SHINE and K-type stars in Sco-Cen, this type of low-mass companions with separations smaller 500 au is missing, which might be related to the stellar environment. One interpretation could be that the relatively high density of FH favours low-mass stellar and massive brown dwarf companions at ~200 au–~400 au. Moreover, the high eccentricity of HD 24121B and UCAC2 1009995B indicates that they might have undergone dynamical scattering during their formation, suggesting that the dynamical interactions were frequent during the formation and expansion of the Fornax-Horologium association. With more observations scheduled, we expect to have more discoveries of this association and understand the impact of stellar density on the formation of wide-orbit substellar

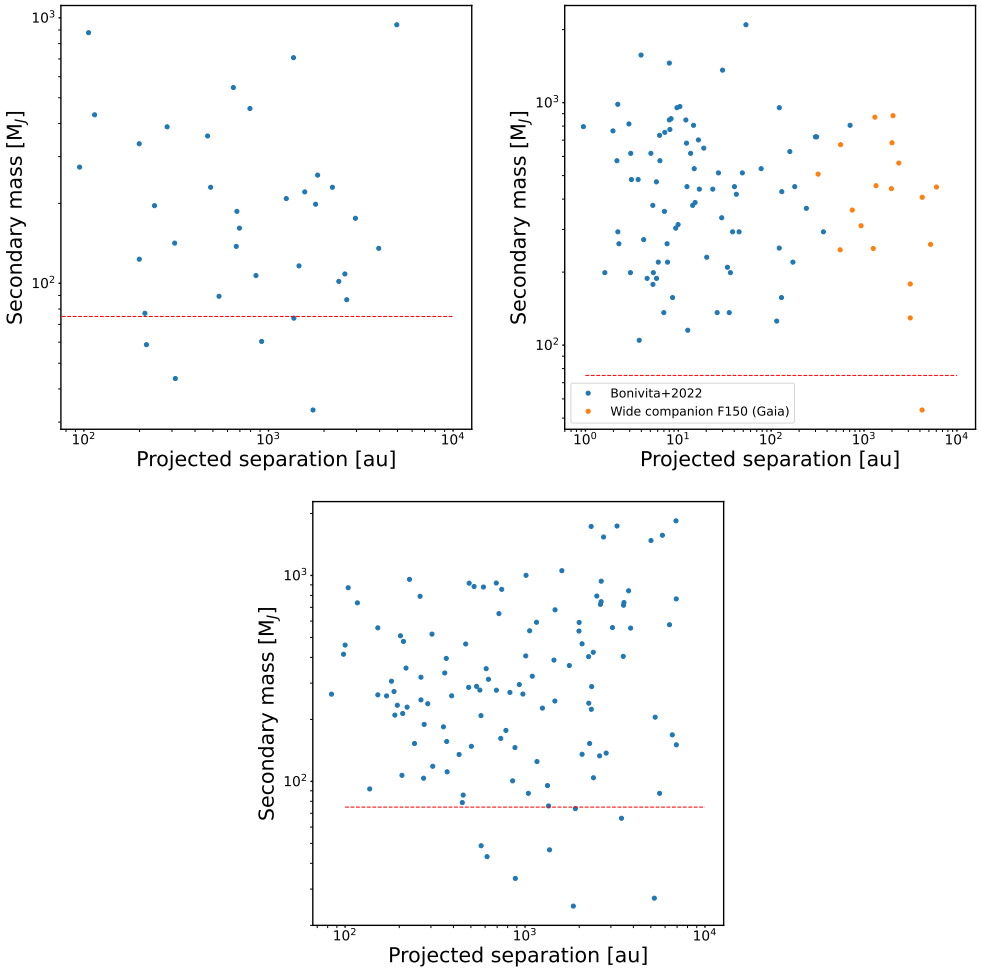


Figure 3.10: Wide-separated candidate companions of FH, SHINE, and K-type stars in Sco-Cen. Top left: candidate companions matched in Gaia DR3 of all candidate members in FH. Top right: the blue points are all stellar companions detected by SPHERE of the full sample of SHINE from Bonavita et al. (2022) and the orange points are the candidate companions matched in Gaia DR3 of the F150 sample of SHINE. Bottom: candidate companions matched in Gaia DR3 of K-type stars in Sco-Cen from Bohn et al. (2022). The red dashed lines mark the 75 M_J limit.

companions.

Chapter 4

A planetary-mass candidate imaged in the Young Suns Exoplanet Survey

The work presented in this chapter resulted from a collaborative effort. The companion candidate was initially discovered by Christian Ginski and Matthew Kenworthy as part of the YSES survey. The MagAO-X data were obtained and preprocessed by Sebastiaan Haffert. I performed the full data analysis, and Tomas Stolker assisted in updating the functionality of the SPECIES code for binary SED fitting. I wrote the chapter incorporating suggestions from the collaborators.

4.1 Abstract

Directly imaged exoplanets in wide orbits pose a challenge to current gas giant formation theories, as they need to form quickly and acquire enough material before the disc dissipates. These processes cannot be accommodated by in situ formation models based on core accretion. We searched for wide separation (> 100 au) planetary-mass companions with the Young Suns Exoplanet Survey (YSES). In this work, we present a planetary-mass candidate companion discovered as part of the survey. We conducted follow-up observations of the candidate system after the first-epoch observations and obtained six epochs of observations for the candidate system between 2018 and 2024, along with the integral field spectroscopy of the stellar component. We report the detection of a candidate companion with $H = 22.04 \pm 0.13$ mag at a projected separation of 730

± 10 au from the primary star. High-angular-resolution-imaging observations of the central star show it is a visual binary. The acceleration data, orbital fitting, spectral energy distribution fitting, and radial velocity differences all suggest that there is at least one more unresolved low-mass stellar companion in this system. The planetary-mass candidate shows a significant proper motion comparable to that of the primary star. We have estimated an age of 19–28 Myr for the primary star. We cannot confirm the companionship of the candidate due to the unknown barycentre of the stars. Long-term imaging and radial velocity monitoring of the central stars, along with spectroscopy of the candidate companion, are key to resolving the nature of this system. If confirmed, the candidate companion would be characterised by a mass of 3–5 $M_{\rm J}$ estimated with the ATMO evolutionary model. It would be another cold, low-mass planet resembling 51 Eri b and AF Lep b. Its extremely wide separation from the host star would challenge the formation theory of gas giant exoplanets.

4.2 Introduction

The number of directly imaged exoplanets has grown steadily over the past decade thanks to imaging surveys with ground-based facilities. About 40% of the imaged exoplanets are located at separations greater than 100 au from their host stars. For instance, AB Pic b is a 13.5 ± 0.5 $M_{\rm J}$ companion of a K0 star at a projected separation of 275 au (Chauvin et al., 2005); COCONUTS-2b is a 6.4 ± 2 $M_{\rm J}$ cool companion of a field M dwarf at a projected separation of 6471 au (Zhang et al., 2021d); 2MASS J1155-7919 b is a 10 $M_{\rm J}$ co-moving companion of a M3 dwarf at a projected separation of 582 au (Dickson-Vandervelde et al., 2020); HD 203030b is an 8–15 $M_{\rm J}$ companion at a projected separation of 487 au orbiting around a G8 star (Miles-Páez et al., 2017); 2M 2236+4751 b is an 11–14 $M_{\rm J}$ companion at a projected separation of 230 au orbiting around a K7 star (Bowler et al., 2017); GU Psc b is a 9–13 $M_{\rm J}$ companion at a projected separation of 2000 au orbiting around a young M3 star (Naud et al., 2014). The discovery of these exoplanets challenges known formation theories of gas giant exoplanets.

It is unclear how these planets are formed based on our current understanding of how and where gas giant exoplanets are expected to form. There are two widely accepted scenarios for the formation of gas giant exoplanets: core accretion (e.g. Pollack et al., 1996) and gravitational instability (e.g. Boss, 1997). Core accretion is based on the formation of a rocky embryo close to

the ice line within a circumstellar disc. Once the embryo reaches a critical mass, runaway accretion of gas continues until the zone around the planet is cleared. However, core accretion is problematic for wide-separation planets. It takes more than 10^7 yr for core formation by runaway planetesimal accretion beyond 5 au (Goldreich et al., 2004), which is longer than the gas dissipation time of the disc. Therefore, planet migration is required for wide-separation planets if they are formed by core accretion (Dodson-Robinson et al., 2009). Instead of core accretion by planetesimals, core growth by pebble accretion can form planets beyond 50 au much faster than via traditional core accretion (Lambrechts & Johansen, 2012). However, this process still requires ejection or scattering processes to explain the observed extremely wide-separation planets. Gravitational instability is driven by the initial fragmentation of the protostellar gas cloud. This formation mechanism has a faster timescale than that of core accretion and forms planets typically at 20 to 200 au from the star, supporting in situ planet formation. However, for planets at even wider separations, it also requires planet migration. In addition, gravitational capture of free-floating planets is another possible formation mechanism for wide-separation planetary systems (Perets & Kouwenhoven, 2012).

There are several direct imaging surveys to search for exoplanets, such as the Spectro-Polarimetric High-contrast Exoplanet REsearch (SPHERE, Beuzit et al., 2019) infrared survey for exoplanets (SHINE, Chauvin et al., 2017) and the Gemini Planet Imager (GPI) Exoplanet Survey (GPIES, Macintosh et al., 2015). Among these surveys, the Young Suns Exoplanet Survey has a relatively high planet detection yield (YSES, Bohn et al., 2019, 2020a,c, 2021). It is a direct-imaging snapshot survey of exoplanets targeting a homogeneous sample of 70 solar-mass pre-main-sequence stars in the Lower Centaurus Crux (LCC) subgroup of the Scorpius–Centaurus association (Sco-Cen, de Zeeuw et al., 1999; Pecaut & Mamajek, 2016) with SPHERE. It has detected two wide-separated exoplanets orbiting around a K3 star so far: YSES 1bc, a $14 \pm 3\ M_{\rm J}$ companion at a projected separation of 160 au and a $6 \pm 1\ M_{\rm J}$ companion at a projected separation of 320 au (Bohn et al., 2020a,c).

In this work, we present the detection of a planetary-mass candidate companion of 2MASS J10065573-6352086 (hereafter: 2M1006) as part of YSES. The primary star is referred to as star A and the fainter star is referred to as star B. The observations of the system and data reduction are detailed in Sect. 4.3. In Sect. 4.4, we present the analysis of the central stars, a stellar system consisting

of a young Sun analogue and an M dwarf. We find tension among all the data and speculate that there is at least one more stellar component in this system. The photometric and astrometric analysis of the planetary-mass candidate are presented in Sect. 4.5. We discuss the probability of the candidate being a free-floating object and co-moving planet in Sect. 4.6 and summarise our work in Sect. 4.7.

4.3 Observations and data reduction

We obtained six epochs of observations of 2M1006 between 2018 and 2024 with SPHERE and MagAO-X, including imaging and integral field unit (IFU) spectra. We summarise the imaging observation setup and conditions in Table 4.1.

4.3.1 SPHERE observations and data reduction

The SPHERE instrument is an extreme adaptive optics system and coronagraphic facility mounted on the Unit Telescope 3 of the ESO Very Large Telescope (VLT) (Beuzit et al., 2019). 2M1006 was observed with SPHERE using the infrared dual-band imager and spectrograph (IRDIS, Dohlen et al., 2008) in five epochs on 2018-11-15, 2021-12-02, 2021-12-26, 2023-01-28, and 2023-03-03. Observations in the first, second, fourth, and fifth epoch were obtained in the classical imaging mode (CI) with the broad-band H and K_S filters, while observations in the third epoch were obtained in the dual-band imaging mode (DBI, Vigan et al., 2010) using the $K12$ and $J23$ narrow-band filter combinations. Only observations in the third epoch used the field-tracking mode, while observations in other epochs used the pupil-tracking mode. All the observations used a coronagraph (N_ALC_YJH_S) to mask the central star.

The central star was resolved to be composed of two stars in the first epoch. To measure the precise location of the primary star and fainter star, we performed a point spread function (PSF) fitting to the binary in the flux image where the central star is not masked. We built a PSF template from other stars in YSES in the broad H and K_S bands. We then fit two PSFs simultaneously to the binary using the NAUTILUS package (Lange, 2023), which implements importance sampling and efficient space exploration using neural networks. The two stars were well resolved in the first epoch, marginally resolved in the second epoch,

Table 4.1: Imaging observation setup and observing conditions.

Date	MJD	Mode	Filter	DIT(s)×NDIT×N[a]	$T_{exposure}$ (min)	Field rotation (°)	Seeing (")
2018-11-15	58437.3110	CI	H	32×1×4	2.13	0.46	0.54
2018-11-15	58437.3153	CI	K_S	32×1×4	2.13	0.46	0.54
2021-12-02	59550.2894	CI	H	32×1×8	4.26	1.11	0.70
2021-12-26	59574.2406	DBI	$K12$	96×1×16	25.60	0	0.71
2021-12-26	59574.2406	DBI	$J23$	96×1×4	6.40	0	0.64
2023-01-28	59972.1385	CI	K_S	32×2×16	17.07	9.62	1.16
2023-03-03	60006.0451	CI	H	32×4×8	17.07	10.21	0.69
2024-03-23	60392.1920	MagAO-X/Sci	z'	0.25×240	1.00	0	0.59

Notes: (a).DIT: detector integration time; NDIT: number of DIT; N: number of exposures.

and moderately resolved in the fifth epoch. To better fit the location, we fixed the flux ratio obtained from the first epoch for the PSF fitting in the second and fifth epochs. For the third epoch in $J2$ and $J3$ we scaled the PSF template in the H band by the corresponding wavelength and performed the fitting. There are multiple non-coronagraphic images (flux images) of the central stars in each epoch. We fit the binary in each individual frame and took the mean and standard deviation as the fitting results and uncertainty of each epoch. The initial uncertainties of the position and the flux ratio are on the order of 10^{-2} pixels and 10^{-3}. We performed an astrometric calibration following the latest version of SPHERE User Manual[1] and Maire et al. (2021). To correct the systematic error between the PSF template and the observed images, we empirically included an additional 1 mas in RA and Dec in the final position uncertainty and the root mean square (rms) of the residuals in the final ratio uncertainty. This uncertainty agrees with the typical binary measurements in Bonavita et al. (2022), which do not use any PSF fitting. Table 4.2 lists the error budget for the binary fitting. The final uncertainty is calculated by the propagation of error.

In science images where the central star is blocked by the coronagraph, the binarity of the central source challenges image alignment between the flux images and science images. For coronagraphic observations of SPHERE/IRDIS, there are four waffle spots in the centred image, which are duplications of the PSF of the central star dispersed with wavelength (Langlois et al., 2014; Beuzit et al., 2019). They are used to determine the precise location of the central star behind the coronagraph by the intersection of the two pairs of spots. The positions of the four spots were fitted by a 2D-Gaussian model, which is effective when the central star is a single star. However, when the central star is a blend of two sources, it is problematic to use a single 2D-Gaussian fitting because the spots are dispersed images of the two sources. To measure the precise location of the brighter star in the coronagraphic images, we developed two methods to tackle this problem. The first one is to fit two 2D-Gaussian models to the spot simultaneously. The separation and flux ratio of the binary obtained from the PSF fitting of the flux image were taken as initial guesses for the two 2D-Gaussian fittings. After measuring the positions of the sources in the four waffle spots, we measured the positions of the brighter star by the intersection of the two pairs of the spots corresponding to the primary star. The second method is to perform cross-correlation between a simulated waffle image of the blended source and the observed image. We built an intensity profile of waffle spots of a single star and

[1] https://www.eso.org/sci/facilities/paranal/instruments/sphere/doc.html

Table 4.2: Astrometry error budget of the central binary and the candidate.

Object	Fitting (mas)	Pixel scale (mas)	True north (deg)	Pupil offset (deg)	Distortion (mas)	Systematics (mas)
Binary	~0.5	~0.1	0.08	0.11	~0.02	~1
Candidate	~3	~7	0.08	0.11	~2	~1

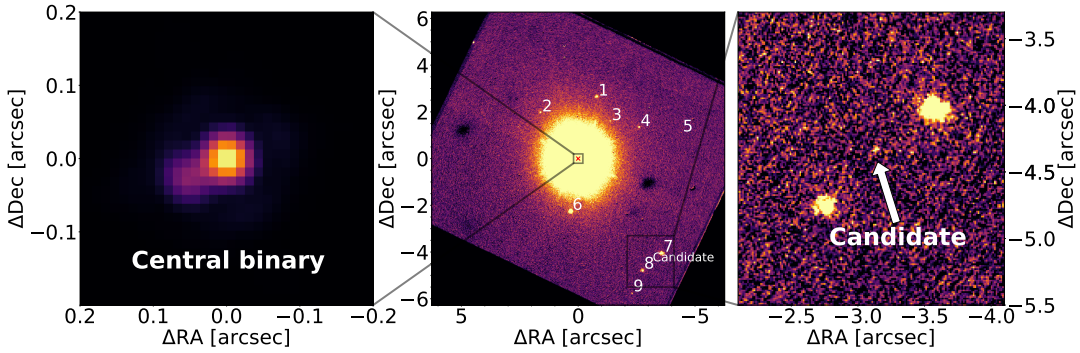


Figure 4.1: Full image of this system of the first epoch in the H band. Left panel: central stars. The fainter component is in the south-east direction of the primary star on 2018-11-15. Middle panel: stacked coronagraphic image centred on the primary star. There are ten sources in the field of view in total. The planetary-mass candidate is the faint source between the two bright background stars in the south-west. Right panel: zoomed-in image of the candidate. All images are derotated to the orientation, where north is up and east is left.

convolved it with the flux image. Then we cross-correlated the simulated waffle image with the observed waffle image. The peak position of the cross-correlation function is the offset between the two images.

The telescope was supposed to be pointed at the primary star. There are two sets of flux images taken before and in the middle of the science observations in the fifth epoch. We centred on the primary star and derotated the flux images to the orientation, where north is up and east is left. The fainter star is at the same position in the derotated flux images, verifying that the telescope was pointed at the primary star. After locating the primary star in the coronagraphic images, we derotated the coronagraphic images back to the north and centred on the primary star. Then we stacked the derotated images by averaging. We applied angular differential imaging (ADI, Marois et al., 2006) and a principal component analysis (PCA, Soummer et al., 2012; Amara & Quanz, 2012) to the de-rotated images. No objects were detected at separations smaller than 1.″6. Because the candidate is at a wide separation, we took the stacked image as the final reduced image.

4.3.2 MagAO-X observations and data reduction

The six-epoch observations were taken with the MagAO-X instrument (Males et al., 2022). MagAO-X is an extreme adaptive optics instrument for the Magellan Clay telescope at Las Campanas Observatory. MagAO-X has been specifically

designed for direct imaging at visible wavelengths (Close et al., 2018). The system was observed on 2024-03-23 in the z' filter with the EMCCD camera camsci1 on MagAO-X. The observations were made in direct imaging mode to perform follow-up astrometric measurements of the tight binary system. One minute of further observations were taken in pupil tracking mode. No significant field rotation occurred during this time and therefore the images were stacked before any processing was done. After stacking, basic detector calibration was performed by subtracting a dark frame. The data were then centred on the primary star. It was not possible to create a PSF model directly from the data due to the small separation of the two objects. YSES 2 was observed directly before the observations of this system. Those observations were used to create a reference PSF because of the targets' similarity in elevation, seeing conditions and brightness during the MagAO-X observations. The YSES 2's PSF was centred to create the reference PSF. Both components of 2M1006 were fitted with the reference PSF. A true north correction of $1\overset{\circ}{.}57 \pm 0\overset{\circ}{.}2$ (Long et al., 2025) was applied.

4.3.3 MagAO-X/VIS-X observations and data reduction

Spectroscopic data were taken with the MagAO-X system, which has an integral-field unit, the Visible Integral-field Spectrograph eXtreme (VIS-X; Haffert et al., 2022). VIS-X is a microlens-based IFU and it has been designed for high-spectral resolution ($R = 13,500, \Delta v = 20\,\mathrm{km\ s^{-1}}$) observations of the H$\alpha$ emission line. The spectral range is limited to about 5 nm around the Hα line due to the microlens design. 2M1006 was observed with VIS-X to measure the radial velocity difference between the two stars. The VIS-X observations were taken on 2024-04-02. The total on-target time is 40 minutes, consisting of eight exposures of 5 minutes each. The seeing condition varied between $0\overset{''}{.}6$ and $0\overset{''}{.}75$.

The VIS-X data reduction follows a typical IFU data reduction pipeline (Haffert et al. in prep). First, the detector calibration steps are applied by subtracting a dark frame. Internal source calibrations were used to identify the spectral trace model for each spaxel. This model can then be used to extract the 1D spectra for all the spaxels. The shifts in the wavelength solution between spaxels were calibrated using standard star observations, which was the star Sirius in this case. The IFU calibration is completed after these steps. The second part of the data reduction follows a similar approach to the imaging data. The data cubes were

derotated and a true north correction was applied. The spectra extraction is described in Sect. 4.4.4.

4.4 Stellar properties

2M1006 was identified to be a candidate member of the LCC subregion of Sco-Cen (Preibisch & Mamajek, 2008; Pecaut & Mamajek, 2016). Gaia DR3 reports a parallax of $\varpi = 7.3241 \pm 0.0689$ mas (Gaia Collaboration et al., 2021b), which translates to an estimated distance of $d = 136.15^{+1.66}_{-1.58}$ pc (Bailer-Jones et al., 2021). The first spectroscopic study of the star came from Torres et al. (2006) who reported it as a K0V(e) star with strong Li absorption (EW(Li I 6707) = 350 mÅ), EW(Hα) = 0.0 Å, fast projected rotation ($v \sin i = 77.0 \pm 7.7$ km s^{-1}), and a radial velocity of 14.0 km s^{-1}. Kiraga (2012) reported time-series photometry from the ASAS-South survey and reported variability with a period $P = 0.7271$ d. TESS observed it in Sector 10, 11, 36, 37, 38, 63, and 64. It shows a distinct rotation modulation of 0.73 d in all these sectors. Fetherolf et al. (2023) reported a detection of a rotation period of $P_{rot} = 0.725893 \pm 0.00557$ day in the *TESS* Sector 10 data in agreement with the variability period reported by the ASAS-South survey.

2M1006 was resolved as two stars in SPHERE observations in Fig. 4.1. Given their small separation, they most likely form a bound binary pair. After considering multiple lines of evidence (detailed in the following sections), there is also significant evidence for at least one more stellar companion in the system.

4.4.1 Acceleration

A companion can affect the proper motion of a star through gravitational reflex motion. Therefore, a proper motion anomaly (PMA) is the difference between the proper motion measured in the long term and the proper motion measured in the short term and is an indicative sign of a perturbing companion (Kervella et al., 2019). To search for any PMA of 2M1006, we checked the Hipparcos (Perryman et al., 1997), Tycho-2 (Høg et al., 2000), and UCAC5 catalogues (Zacharias et al., 2017). This star is not in the Hipparcos catalogue, but is in the Tycho-2 and UCAC5. The difference in proper motion between Tycho-2 and Gaia is within the large uncertainty of Tycho-2. The proper motion provided in

the UCAC5 catalogue is a long-term proper motion, calculated as the difference in position between the mean UCAC epoch and the mean Gaia DR1 epoch, divided by the difference in time between those mean epochs. The long-term proper motion can be assumed to follow the barycentre of the system and to be relatively independent of perturbations from a companion (Kervella et al., 2019). The proper motion provided in the Gaia catalogue is a short-term proper motion, over the epochs covered in the Gaia DR chosen. The difference between the short-term proper motion and the long-term proper motion is the proper motion anomaly (PMA) and is an indicator of the degree to which an unseen companion causes the measured short-term proper motion to deviate from the barycentric proper motion. Thus, we constructed the Gaia-UCAC5 PMA as

$$PMA = \mu_{Gaia} - \mu_{UCAC5-Gaia}, \tag{4.1}$$

where μ_{Gaia} is the reported short-term Gaia proper motion and $\mu_{UCAC5-Gaia}$ is the reported long-term proper motion between the UCAC and Gaia DR1 epoch.

The star's $\mu_\alpha \cos\delta$ is -21.5 ± 1.2 mas yr^{-1} and μ_δ is 8.1 ± 1.2 mas yr^{-1} between UCAC5 and Gaia DR1. Its $\mu_\alpha \cos(\delta)$ is -17.606 ± 0.086 mas yr^{-1} and μ_δ is 4.892 ± 0.079 mas yr^{-1} in Gaia DR3. The proper motion difference is larger than 1σ, suggesting that a fainter companion is perturbing its on-sky motion. Moreover, although Gaia DR3 identifies 2M1006 as a single star, its renormalised unit weight error (RUWE) is 6.012, indicating a poor astrometric fit for a single-star model, which for single stars have values close to unity. Additionally, two flare events in Tess Sector 36 were observed in 2021 with an interval of ~14 d, which could be due to the fainter star, a likely M dwarf. There was another strong flare event at the end of the Sector 36 observations, but it was only captured at the very beginning of the flare, which increased the flux by 10%.

4.4.2 Orbital fitting

Table 4.3 lists the relative astrometry and flux ratio of the fainter star to the primary star measured in our observations. The flux ratio of the fainter star to the primary star varies between 0.18 and 0.34 from z' to K_S, indicating a later spectral type for the fainter star. The images of the stars and residuals after fitted star subtraction can be found in Appendix B.1. The fainter star moves from the south-east to the northeast relative to the primary star from 2018 to 2024.

Table 4.3: Astrometric and photometric measurements of the fainter star relative to the primary star.

Epoch (jyr)	Filter	Sep (mas)	PA (deg)	Flux ratio	ΔMag (mag)
2018.8715	H	57.22±1.07	116.33±1.06	0.34±0.02	1.17 ± 0.07
2018.8715	K_S	57.52±1.21	117.54±1.21	0.33±0.02	1.19 ± 0.06
2021.9186	H	31.58±1.25	41.58±2.37	-	-
2021.9842	$J2$	31.65±1.38	35.84±2.52	0.33±0.04	1.21 ± 0.14
2021.9842	$J3$	32.23±1.42	35.80±2.54	0.32±0.04	1.24 ± 0.15
2023.1664	H	39.81±1.06	5.40±1.55	-	-
2024.2237	z'	54.20±0.62	349.51±0.65	0.18±0.02	1.88 ± 0.12

We used ORBITIZE (Blunt et al., 2020) to find any plausible orbital solutions for the two stars by fitting the positions measured from direct imaging observations. Because the observations in Ks, $K12$, and $J23$ were taken very close to the observations in the H band, we only fit the positions in the three H-band epochs and the last $z\prime$-band epoch. We set a Gaussian prior for the parallax with 7.3 mas reported in the Gaia catalogue and inflated its uncertainty to 0.5 mas. We set a broad Gaussian prior for the total mass with 1.8 ± 0.8 $M_\odot$ with an initial guess from the flux ratio. We show the posterior distributions of orbital parameters in Fig. 4.2 and 100 randomly drawn orbits in Fig. 4.3. A high inclination of 110.°4 ± 3.°1 is required to fit the orbit. The fitted total mass is 2.1 ± 0.5 $M_\odot$. The mass of the primary star is well-constrained to about 1.03 $M_\odot$ (see Sect 4.4.6). This implies that the best-fitting mass of the fainter star is 1.06 $M_\odot$, resulting in a mass ratio between the fainter star and brighter star of 1. However, a mass around 1 $M_\odot$ for the fainter star contradicts the mass expected from the measured flux ratio between the two stars. From the measured flux ratio, we expect the fainter star to be considerably less massive than the brighter star.

Furthermore, using GAIAUNLIMITED (Castro-Ginard et al., 2024) which queries Gaia scanning laws and estimates Gaia DR3 detectability of unresolved binary systems, we calculated a RUWE of 1.0 – 2.4 for the orbits fitted by ORBITIZE depending on the initial phase of the orbits observed by Gaia, much smaller than 6.012. We also tried to fit the orbit of the fainter star with STAN (Wallace et al., 2025) combining RUWE and the direct imaging observations. STAN is developed to fit the mass and orbit of a hidden companion that can cause a high RUWE of a given star by fitting Gaia absolute astrometry including proper motion, parallax and RUWE and possibly combined with image observations using Bayesian inference. However, it is not able to find plausible orbit solutions

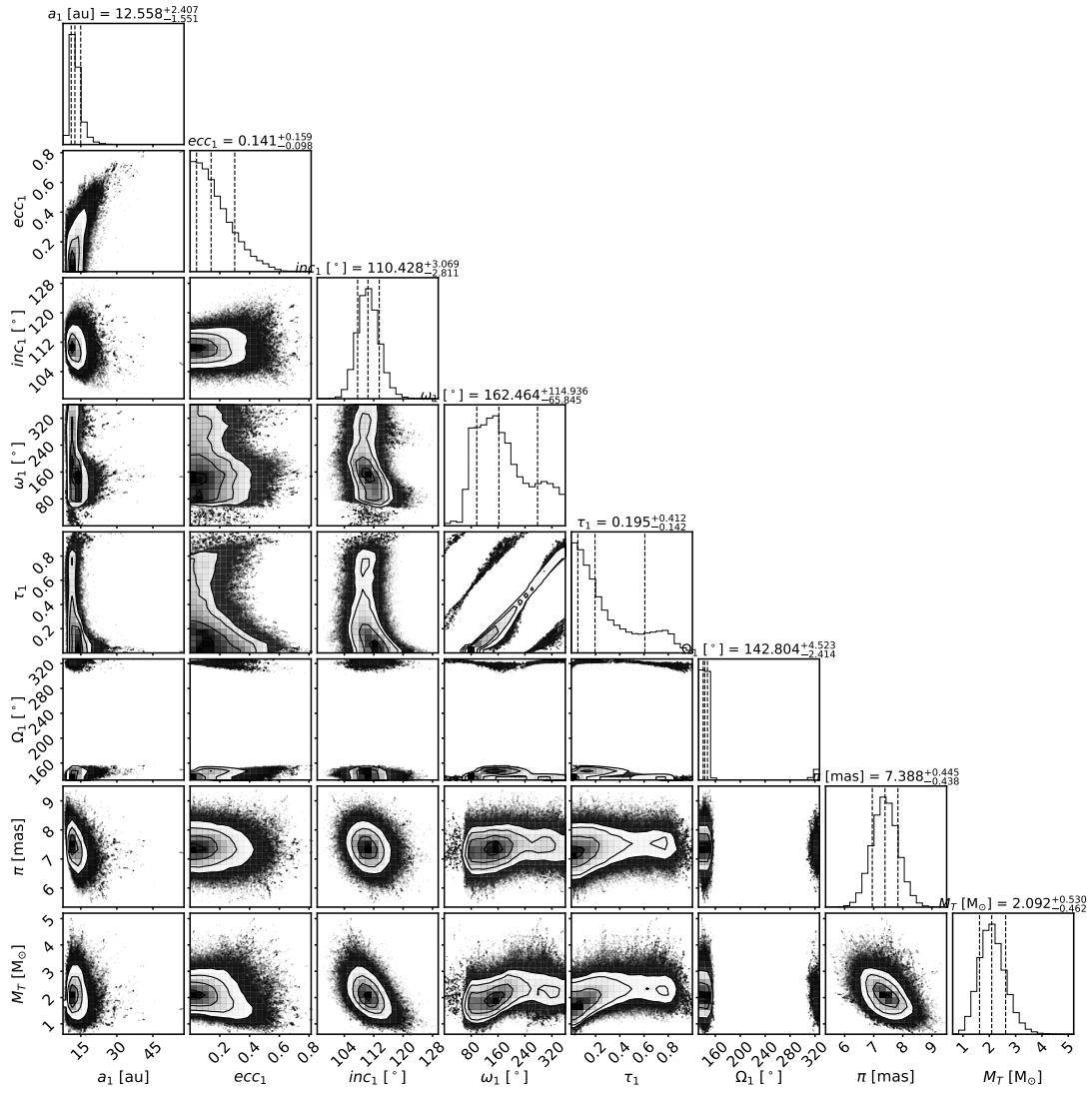


Figure 4.2: Posterior distributions of the orbital parameters by fitting the measured relative positions with ORBITIZE.

for the two stars. While we can constrain the orbit very well by including RUWE and positions only between 2018 and 2023 in the orbital fitting, the observed position in 2024 does not agree with the predicted position of 2024, which should show an arc instead of still linear motion. It is therefore also problematic to explain the high RUWE value given these orbital solutions for the two stars. We calculated the PMA from the orbital fit posteriors following the method of Biller et al. (2022), adopting masses for the fainter star of 0.1, 0.3, 0.5, 0.7, and 0.9 $M_\odot$. Only secondary masses >0.7 $M_\odot$ can produce PMA on the order of the measured PMA for this system, however, such a high mass for the secondary is in tension with the measured flux ratio between the two stars.

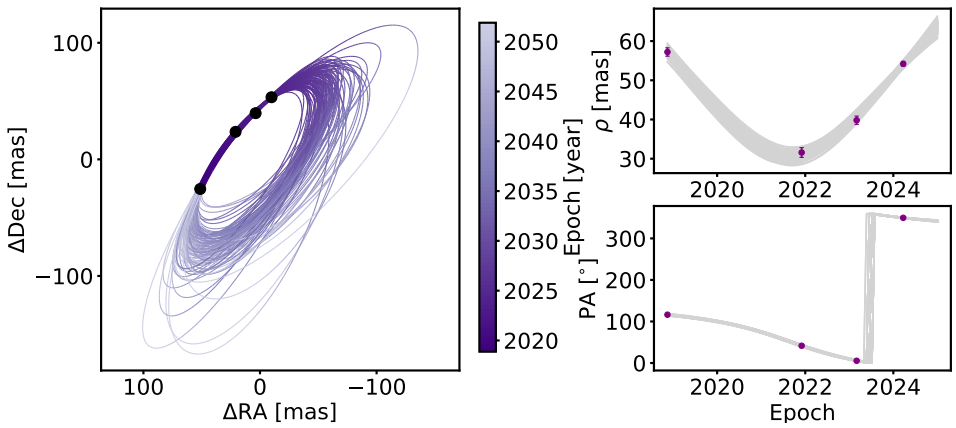


Figure 4.3: 100 orbits drawn from the posterior distributions of the binary fitted with ORBITIZE.

4.4.3 SED fitting

We performed a spectral energy distribution (SED) fitting with SPECIES (Stolker et al., 2020) to the two stars simultaneously using the multi-modal nested sampling algorithm (Feroz et al., 2009). We fit broad-band photometry (unresolved) of 2M1006 from GAIA, 2MASS, and WISE catalogues with the synthetic spectra of BT-Settl-CIFIST (Allard et al., 2013). We used the parallax from Gaia with an inflated error of 0.5 mas. We set uniform priors for the $T_{\rm eff}$, log(g), and radii of both stars: 4000 K $< T_{\rm eff\,1} <$ 7000 K, 3000 K $< T_{\rm eff\,2} <$ 4000 K, 3 dex $<$ log(g_1) $<$ 6 dex, 3 dex $<$ log(g_2) $<$ 6 dex, 0.005 $R_\odot$ $< R_1 <$ 2 $R_\odot$ and 0.005 $R_\odot$ $< R_2 <$ 2 $R_\odot$, and solar metallicity. To combine our direct image observations with broad-band photometry, we set Gaussian priors for the flux ratio of the fainter star to the primary star in SPHERE/IRDIS/B_H, SPHERE/IRDIS/B_K_S, SPHERE/IRDIS/D_J23, and MagAO-X/camsci1/z' bands. The optimised SED fitting is presented in Fig. 4.4. The posterior distributions of the fitted parameters are presented in Appendix B.2.

We derived $T_{\rm eff}$= 5196^{+162}_{-96} K, R = 1.09 ± 0.05 $R_\odot$, log(g) = $3.88^{+0.61}_{-0.50}$ dex, log(L/L_{bol}) = −0.10 ± 0.05 dex for the primary star and $T_{\rm eff}$= 3458^{+110}_{-91} K, R = 0.99 ± 0.06 $R_\odot$, log(g) = $4.48^{+0.59}_{-0.43}$ dex, and log(L/L_{bol}) = -0.90 ± 0.04 dex for the fainter star. With an estimation of $T_{\rm eff}$ for young stars from Pecaut & Mamajek (2013), the primary star should be a G8–K0 star. The radius of the primary star is constant with its $T_{\rm eff}$ for a 20 – 30 Myr 1 $M_\odot$ star from the BT-Settl evolutionary model (Baraffe et al., 2015). However, the radius of the fainter star

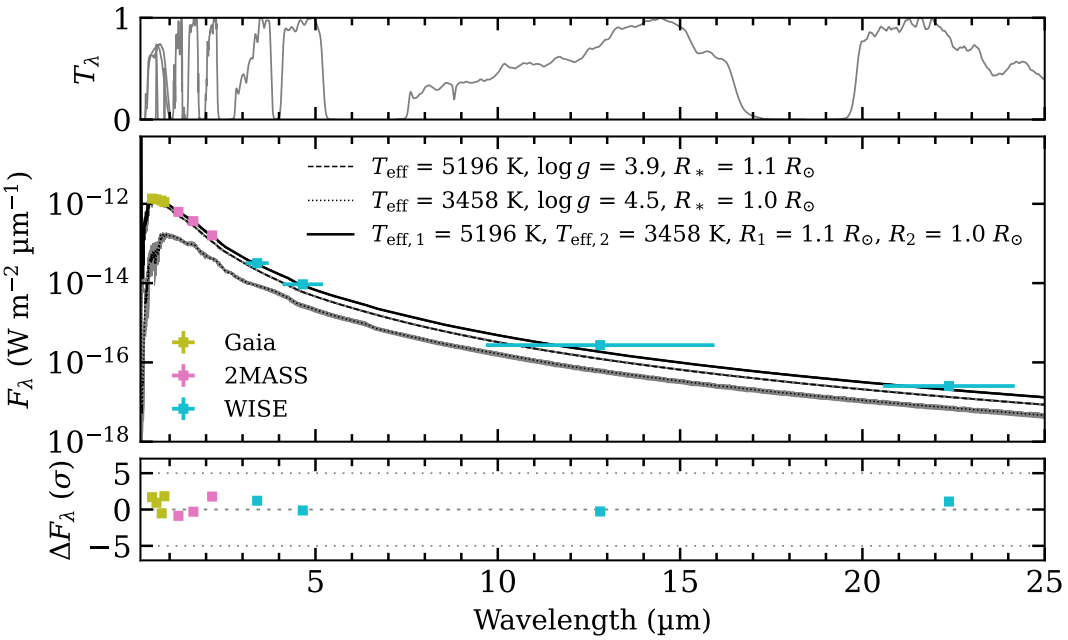


Figure 4.4: Simultaneous SED fitting of the primary star and fainter star to the unresolved broad-band photometric measurements of Gaia, 2MASS, and WISE with SPECIES. The black solid line is the combined best-fitted spectrum of the two stars. The black dashed line is the best-fitted spectrum of the primary star and the black dotted line is the best-fitted spectrum of the fainter star. Spectra drawn from 30 random samples of each star are shown in grey lines. The top panel shows the filter transmission profiles and the bottom panel shows the fitting residuals.

is too large for an M dwarf with that $T_{\rm eff}$. It has to be younger than 4 Myr to have a radius of 0.99 $R_\odot$ from the evolutionary models, but it should have a radius smaller than ~0.7 $R_\odot$ if it is in the same system as the primary star with the same age. There is likely some additional luminosity from a third unresolved object and the inflated radius of the fainter star in the SED fitting is accounting for that additional luminosity. The fitted A_V is smaller than 0.13 mag. No infrared excess was detected from the SED fitting.

4.4.4 Radial velocity

The primary star is detected at high significance while the fainter star is detected with a lower signal-to-noise ratio (S/N) in the MagAO-X/VIS-X IFU data as shown in the left panel of Fig. 4.5. The spectrum of the primary star is extracted with an aperture of a radius of 3.5 spaxels centred on the star. For the fainter star, we extracted its spectra with the same aperture but shifted the aperture

around the fainter star by 1 spaxel in either x or y direction each time. Starting from the position of the fainter star, x and y change between [-3, 3], respectively, with a total of 49 centring positions. This results in 49 spectra of the fainter star extracted from different places. This step is to include as many pixels containing the signal of the fainter star as possible while minimising the effect of possible bad pixels such as those affected by cosmic rays. Then we applied PCA to the 49 spectra to extract the spectra of the fainter star and also remove the contamination of the primary star. We compare the spectra of the primary star and the first three components of the 49 spectra in the middle panel of Fig. 4.5. We detected H_α absorption for the primary star, in agreement with the literature. We extracted the spectrum of the fainter star as the first principal component as the fainter star is the dominant source in these regions. We detected H_α emission in the first component, suggesting that the fainter star is likely a magnetically active M dwarf. The second principal component is featureless and likely originates from the background. The third principal component has the same shape as the primary star's spectrum with the same H_α absorption feature. This verifies that this method successfully distinguishes the spectra of the two stars. We also injected artificial signals of the same brightness and blue shift as the fainter star at the opposite side at the same separation to the brighter star. We successfully retrieved the injected signal using the same method, verifying the reliability of this technique. The injection test is demonstrated in Appendix. B.3.

The right panel of Fig. 4.5 presents the smoothed spectra convolved with a Gaussian kernel of a standard deviation = 0.48 Å from one exposure. The H_α absorption and emission due to the two stars are easy to identify. We have three exposures and applied the same method to them. All of them present consistent H_α absorption in the spectrum of the primary star and H_α emission in the first principal component of the fainter star's spectra. We fitted a Gaussian profile to the spectra and measured a blue shift of 2.11 ± 0.14 Å between the H_α emission line centre and the H_α absorption line centre. This corresponds to a radial velocity difference of 96.5 ± 6.6 $\mathrm{km\,s^{-1}}$. The escape velocity of the two stars is calculated by:

$$v_{esc} = \sqrt{\frac{2G(M_1 + M_2)}{r}}. \tag{4.2}$$

The total mass derived from orbital fitting is 2.1 ± 0.5 $M_\odot$ and the closest projected separation of the two stars is 32 ± 1 mas, which is 4.2 ± 0.1 au for the parallax of 7.32 ± 0.07 mas. Putting them into Eq. 4.2, the upper limit of the

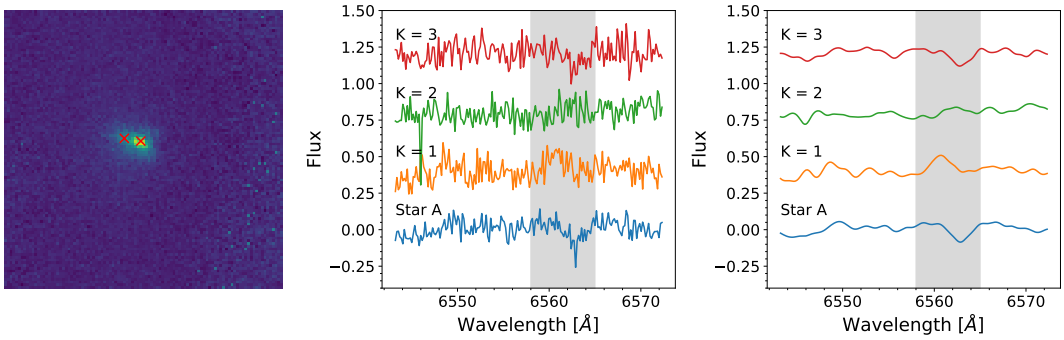


Figure 4.5: MagAO-X/IFU data of the binary. Left panel: IFU images of the binary stacked along the wavelength channel. The image is not rotated to place North up. Middle panel: Spectrum of star A and the first three principal components of star B's spectra. The grey area shows the H_α line band. Star A presents H_α absorption. The first component presents H_α emission from star B. The third component (K=3) is the contamination from star A. Right panel: Smoothed version of the middle panel by a Gaussian kernel with a standard deviation of 0.48 Å. The grey area shows the H_α line band.

escape velocity is 29.6 ± 3.6 km s^{-1}. The radial velocity difference between the two stars measured in the H_α line is much larger than their escape velocity.

We are cautious about this comparison because H_α emission profiles of M dwarfs can vary due to chromospheric activity, although it is rare to produce such a large blue shift by chromospheric activity. An analysis of H_α emission lines of 72 M dwarfs finds that 94% of the stars have blue shifts smaller than 50 km s^{-1} at H_α emission lines (Flasseur et al., 2018). We measured a full width at half maximum (FWHM) of 105 km s^{-1} of the H_α emission line for the fainter star. However, all stars that have such large FWHM in Flasseur et al. (2018) have a shift of < -50 km s^{-1} and more than half of them show redshifts. Therefore, while we could not ascertain that the two stars are not gravitationally bound from radial velocity measurements, it makes this two-body system more debatable.

4.4.5 Possibility of the third companion

There are tensions in the data treating the two stars as a binary system:

1. The dynamical mass measured for the fainter star is too high to match the observed flux ratio between the two stars.

2. The fitted orbit from direct imaging does not agree with the acceleration

measurement for this system.

3. The radius of the primary star from the SED fitting is too large if it has the same age as the primary star.

4. The radial velocity difference between the two stars is too large for them to remain gravitationally bound.

We used the equation from Brandner et al. (2000) to estimate the probability that the fainter star is a randomly aligned foreground or background star:

$$P(\Theta, m) = 1 - e^{-\pi\rho(m)\Theta^2}, \tag{4.3}$$

where Θ is the angular separation of the object to the central star and $\rho(m)$ is the cumulative surface density of background sources of limiting magnitude, m. We queried all sources within 10 arcmin of the primary star from the 2MASS catalogue (Skrutskie et al., 2006) and counted stars with magnitude down to 1 mag fainter than the faint star, which is 67 stars. Then we estimated the probability of the two stars being unrelated is 5.22×10^{-7}.

Given that the probability of the two stars being unrelated is extremely low, we hypothesise that there is at least one additional unseen companion in the system that may explain the disagreements in our current analysis. Either the primary star or the fainter star can have an additional unresolved stellar component. If it is related to the brighter star, this could explain the PMA, RUWE, and SED and also bias the measured ΔRV. If it is related to the fainter star, this can increase the total mass of the fainter star. For example, if B is an equal mass binary, then all other SED parameters remain the same but the radius of each object decreases from $1.0\,R_\odot$ to $0.7\,R_\odot$ and the individual masses are $\sim 0.4\,M_\odot$. Then the total mass of the fainter component is $0.8\,M_\odot$. The mass ratio is 0.8 and meets the required total mass of orbital fitting. While the PMA and ΔRV may also be explained by the multiplicity of the fainter star, the RUWE of A cannot be explained by the derived acceleration: with a mass ratio of 1, the derived highest RUWE is only 2.4.

Besides the astrometric perturbations caused by a companion, there are other means of producing a RUWE excess, such as variability (Belokurov et al., 2020). In TESS light curves of the system, the primary is variable at a level of $\sim 2\%$ with a period of 0.73 d. There are two flare events and one of them increases the total brightness by 4% and another very strong eruption event at the end of

the light curve, which increases the total brightness by 10%. These flare events are irregular in period and intensity and are consistent with flaring events seen from low mass stars, which we attribute as coming from B. A few percentages of variability can lead to a photocentre shift of several mas, which can cause a large RUWE excess. Therefore, this additional component can either be related to the brighter star or the fainter star.

4.4.6 Mass and age estimation

The unresolved star is variable with a V-band amplitude of ~0.07 mag and rotation period, P_{rot} = 0.7271 d (Kiraga, 2012). Adopting the colour conversions from Riello et al. (2021) and the Gaia DR3 G and $BP - RP$ colour, we estimated V = 11.015 mag, which is in the middle of the previously published estimates. We used two methods to estimate the age of the star. The first one is to estimate the age by lithium depletion. We fit the equivalent width of lithium absorption (EW(Li)) using Bayesian Ages for Field Lower-Mass Stars (BAFFLES, Stanford-Moore et al., 2020). With EW(Li) = 350 mÅ (Torres et al., 2006) and $B - V$ = 0.797 mag, BAFFLES estimates a median age of 54.5 Myr with a 95% confidence range of 2.95–396 Myr, shown in the left panel of Fig. 4.6. The second method is to place the primary star in the luminosity and $T_{\rm eff}$ diagram with isochrones and tracks from the BT-Settl evolutionary model (Baraffe et al., 2015). With $\log(L/L_{\odot})$,= -0.10 ± 0.05 dex and $\log T_{\rm eff}$ = 5196^{+162}_{-96} K, we estimated a mass of 1.03 $M_{\odot}$ with a 68% confidence range of 0.99–1.08 $M_{\odot}$ and an age of 25 Myr with a 68% confidence range of 19–28 Myr, shown in the middle panel of Fig. 4.6. All the results suggest that the primary star is a young star. We adopted the age results from the second method. The unresolved photometric observations of the system from the literature and adopted parameters of the primary and fainter stars are presented in Table 4.4.

4.5 The planetary-mass candidate

Figure 4.1 shows all the sources and the central binary in the H band. The deepest images are in the H band, with ten sources in the field of view (FoV). Several sources are not detected in the other bands, including the candidate. We detected the candidate in the H band as shown in Fig. 4.7 with marginal detection

Table 4.4: 2M1006 stellar parameters

Parameter	Value	Reference
Unresolved stellar binary		
RA(J2000)	10:06:55.72	Simbad
Dec(J2000)	-63:52:08.61	Simbad
B	11.812 ± 0.014	APASS/DR9
V	11.015	this work
g'	11.368 ± 0.054	APASS/DR9
r'	10.690 ± 0.060	APASS/DR9
i'	10.385 ± 0.033	APASS/DR9
G_{Bp}	11.227 ± 0.008	GaiaEDR3
G	10.744 ± 0.004	GaiaEDR3
G_{Rp}	10.085 ± 0.006	GaiaEDR3
G_{Bp} - G	0.482880	GaiaEDR3
G_{Bp} - G_{Rp}	1.141988	GaiaEDR3
G - G_{Rp}	0.659108	GaiaEDR3
J	9.262 ± 0.028	2MASS
H	8.744 ± 0.061	2MASS
K_s	8.580 ± 0.024	2MASS
$W1$	8.530 ± 0.023	allWISE
$W2$	8.541 ± 0.020	allWISE
$W3$	8.455 ± 0.018	allWISE
$W4$	8.236 ± 0.149	allWISE
EW(Li I λ6707) (mÅ)	350 ± 10	Torres et al. (2006)
EW(Hα) (Å)	0.00 ± 0.01	Torres et al. (2006)
$v\sin i$ (km s^{-1})	77.0 ± 7.7	Torres et al. (2006)
A_V (mag)	< 0.13	this work
Primary (A)		
SpT	G8V – K0V	Torres et al. (2006) and this work
$T_{\rm eff}$ (K)	5196^{+162}_{-96}	this work
$\log(L/L_\odot)$ (dex)	-0.1 ± 0.05	this work
Age (Myr)	25^{+3}_{-6}	this work
Mass ($M_\odot$)	1.03 ± 0.05	this work
G	10.82 ± 0.01	this work
$MagAO-X/z'$	9.94 ± 0.01	this work
$SPHERE/J2$	9.56 ± 0.01	this work
$SPHERE/J3$	9.40 ± 0.01	this work
$SPHERE/H$	9.05 ± 0.01	this work
$SPHERE/K_S$	8.96 ± 0.02	this work
Fainter star (B)		
$T_{\rm eff}$ (K)	3458^{+110}_{-91}	this work
$\log(L/L_\odot)$ (dex)	-0.90 ± 0.04	this work
G	13.67 ± 0.13	this work
$MagAO-X/z'$	11.80 ± 0.06	this work
$SPHERE/J2$	11.04 ± 0.05	this work
$SPHERE/J3$	10.83 ± 0.04	this work
$SPHERE/H$	10.30 ± 0.04	this work
$SPHERE/K_S$	10.04 ± 0.03	this work

Notes: The magnitudes of the primary star and fainter star between G and $SPHERE/K_S$ are calculated by synthetic photometry on the fitted spectra with SPECIES. Their uncertainties are likely underestimated.

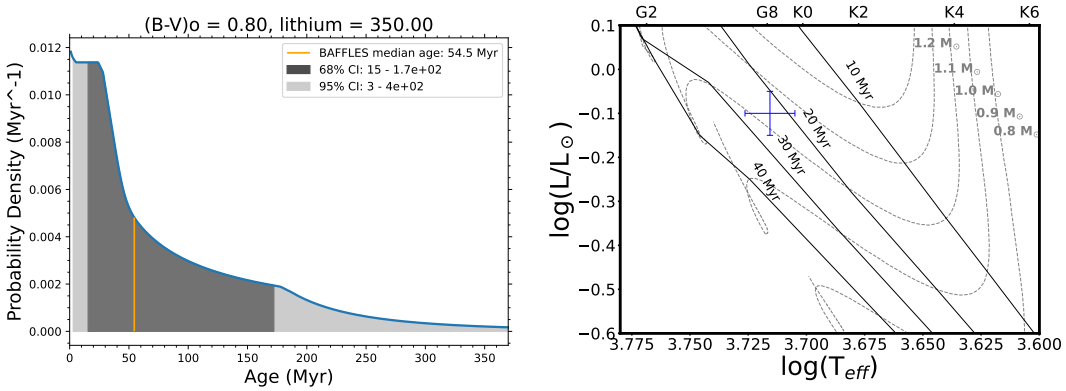


Figure 4.6: Age estimation of 2M1006. Left panel: age estimation by Li depletion using BAFFLES (Stanford-Moore et al., 2020). Right panel: age estimation by combining the luminosity and $T_{\rm eff}$ of the primary star from SED fitting with the isochrones and tracks of BT-Settl evolutionary model (Baraffe et al., 2015).

in $J23$ bands.

4.5.1 Photometric analysis

We performed aperture photometry to measure the flux of the sources in the FoV and PSF fitting to measure the flux of the central two stars. We used the same aperture with a radius equal to the mean FWHM of all sources. For each source, we took the three σ clipped median of an annulus centred on the source, with radii ranging from 10 to 15 pixels as the background level per pixel, and subtracted it from the aperture photometry.

To measure S/N, we chose 14 random apertures of the same size as the aperture on the source adjacent to the source and took their standard deviation as the noise level. Table 4.5 summarises the contrast of the candidate to the primary star and S/N. We consistently detected the candidate in the H band with S/N > 5 but with only upper detection limits in $K12$ and K_S bands and marginal detection in $J23$ bands. We achieved the highest detection significance on 2023-03-03 with S/N = 8.8. Averaging the magnitude of the candidate in three measurements, its apparent magnitude in the H band is 22.04 ± 0.13 mag.

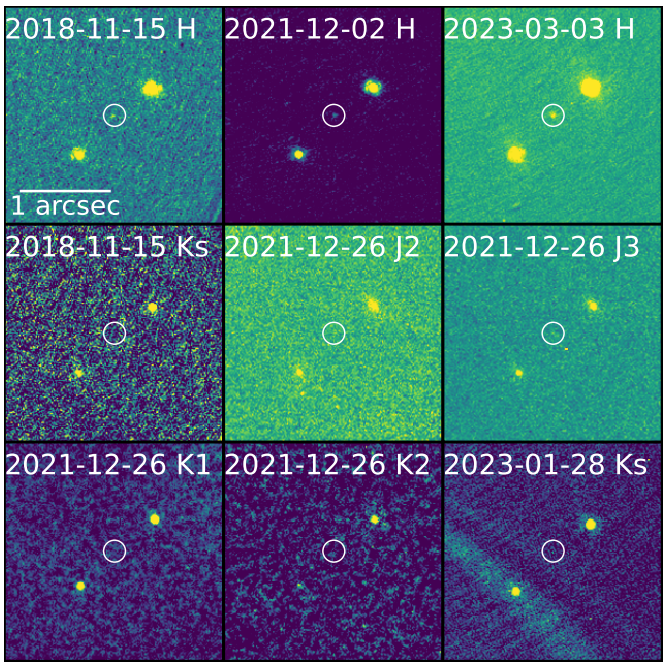


Figure 4.7: Images of the candidate in five epochs of H, $J23$, $K12$, and K_S bands. The candidate is the faint source between the two bright background stars, highlighted by the white circles. It is only visible in the H band with marginal detection in the $J23$ bands.

4.5.2 Astrometric analysis

We fitted a 2D Gaussian model to the candidate to measure its position. At first, we fit a 2D Gaussian model to the candidate with Astropy (Astropy Collaboration et al., 2013, 2018) to obtain the initial guess of the position. Then we cut out a sub-image of 31 pixels × 31 pixels at the position of the candidate. We took three σ clipped median and standard deviation of an annulus with an inner radius of 4 pixels and an outer radius of 12 pixels from the central position of the candidate as the local sky background and uncertainty of each pixel in the sub-image, respectively. We subtracted the fitted model from the sub-image and minimise residuals by minimising the chi-square $\chi^2 = \Sigma_{i=1}^{N} \frac{(Data-Model)^2}{Data\ error^2}$ (N is the number of pixels) using the emcee package (Foreman-Mackey et al., 2013).

The uncertainty from the posterior distribution is tiny, and therefore we injected artificial stars using the PSF template and retrieved positions using the above algorithm. We injected 50 stars at the same separation of the object but at the opposite side of the image with one star per injection. We took three σ clipped mean of the deviations between the injected and retrieved positions of the 50 injections as the uncertainty of our position measurement algorithm.

Table 4.5: Photometric measurements of the candidate.

Date	Band	ΔMag (mag)	Detection S/N
2018-11-15	H	12.89 ± 0.21	5.2
2021-12-02	H	12.93 ± 0.19	5.6
2023-03-03	H	13.15 ± 0.12	8.8
2018-11-15	K_S	> 11.24	-1.3
2021-12-26	$J2$	13.52 ± 0.44	2.5
2021-12-26	$J3$	12.50 ± 0.25	4.4
2021-12-26	$K1$	> 12.55	1.0
2021-12-26	$K2$	> 11.34	-0.5
2023-01-28	K_S	> 12.68	-0.7

Notes: We only detected the candidate in the H band with a marginal detection in $J23$. The contrast is relative to the flux of the primary star and is the 5σ contrast for bands of no detection. The detection S/N is calculated via aperture photometry.

We also included uncertainties from the pixel scale (12.25 ± 0.021 mas per pixel), true north angle correction (-1.75 ± 0.08 deg), pupil offset (135.99 ± 0.11 deg), distortion (0.4 mas per 1 arcsec separation), and systematics such as the coronagraph centring uncertainty (we added an arbitrary 1 mas in RA and Dec) in the propagation of the error when calculating the separation between the primary star and the candidate. The error budget is demonstrated in Table 4.2.

Table 4.6 presents the separations and position angles of the candidate relative to the primary star from 2018 to 2023. The positions of the candidate relative to the primary star between 2018 and 2023 are shown in the left panel in Fig. 4.8. They match within 1σ, suggesting that this candidate's proper motion is comparable to the proper motion of the primary star. Evolving from the position on 2018-11-15, it is more than 3σ away from the position of a static background source on 2023-03-03. The candidate is at a separation of 730 ± 10 au to the primary star assuming they are at the same distance. However, as noted in Section 4.4.5, the primary star is very likely a triple system; thus, the true barycentre of the system is unknown. Due to the unknown barycentre of the central stars, it is not possible to confirm this candidate as a co-moving source by common proper motion analysis. We discuss the plausible characterisation of this source in Sect.4.6.

Table 4.6: Relative position of the planet candidate to the primary star.

Epoch (Julian years)	Sep (arcsec)	PA (deg)
2018.8715	5.3471 ± 0.0099	215.89 ± 0.14
2021.9186	5.3458 ± 0.0097	215.90 ± 0.14
2023.1664	5.3268 ± 0.0095	215.86 ± 0.14

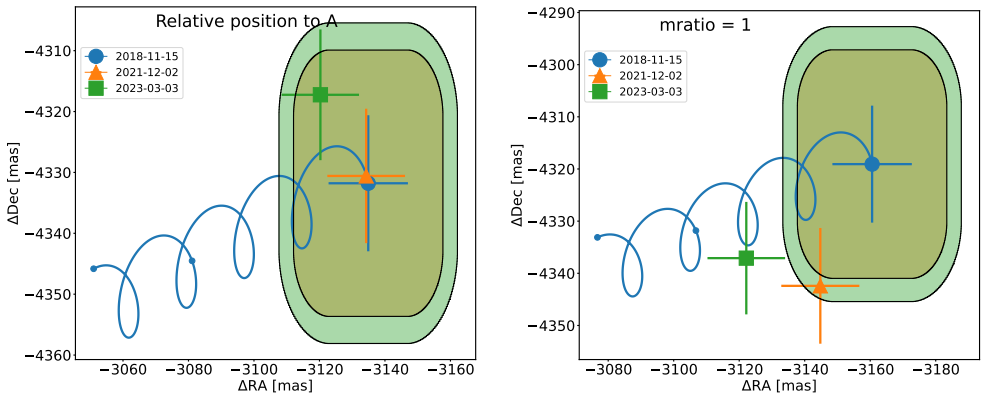


Figure 4.8: Relative astrometry of the candidate in RA and Dec offsets. Left panel: relative astrometry of the candidate to the primary star (mass ratio = 0). Right panel: relative astrometry of the candidate to the barycentre if the fainter star and primary star are an equal mass binary (mass ratio = 1) The yellow and green regions are the candidate companion positions allowed by the escape velocity within 1σ on 2021-12-02 and 2023-03-03, respectively. The blue line is the trajectory of a static background star evolving from 2018-11-15 calculated with the proper motion and parallax reported in Gaia and the two points on the track are the positions on 2021-12-02 and 2023-03-03.

4.5.3 Colour-magnitude diagram

Assuming the contrast is the same between H_{2MASS} and H_{SPHERE}, we converted the candidate's apparent magnitude to absolute magnitude with the primary star's parallax. We placed the candidate in the colour-magnitude diagram (CMD) in Fig. 4.9. Assuming the same distance of the primary star (136 pc), the candidate has an absolute magnitude of 16.38 ± 0.13 mag. Due to the unknown magnitude in the J band, we could only derive a blue limit of its 2MASS $J - H$ colour of 0.22, which is redder than most T-type objects of the same assumed H magnitude. We also present the colour of M dwarfs. Based on the current colour range, we cannot determine whether the candidate is a planetary-mass object, brown dwarf, or background M dwarf. If it is a planet, it would be one of the coolest directly imaged planets that reveals a similarity to 51 Eri b (Macintosh

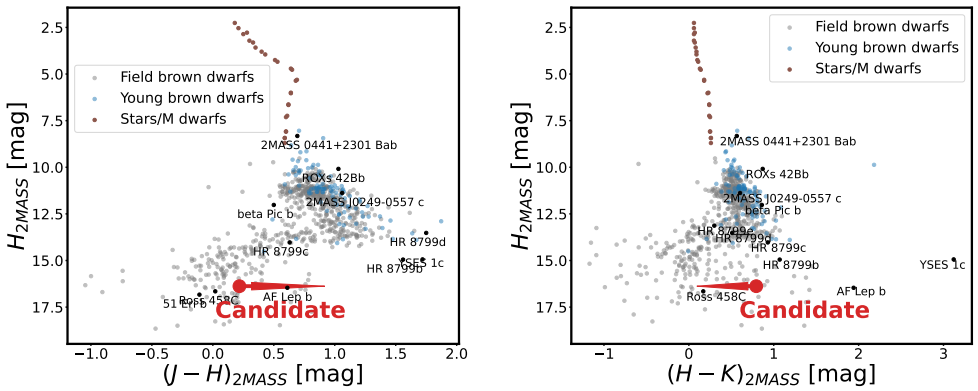


Figure 4.9: Colour-magnitude diagram of brown dwarfs. The grey points are field brown dwarfs with high surface gravity. The blue points are young or low surface gravity objects. The brown points are low-mass stars. Several directly imaged exoplanets are labelled with black text. The red arrow shows the possible positions of the candidate assuming it is at the same distance as the central stars. If confirmed, it would be one of the coolest directly imaged exoplanets.

et al., 2015; Samland et al., 2017) and AF Lep b (De Rosa et al., 2023; Franson et al., 2023; Mesa et al., 2023). Its $J-H$ colour is between these two confirmed planets. We derived a red limit to its $H-K$ colour of 0.79, redder than most objects of the same H magnitude. Using the ATMO2020 evolutionary model (Phillips et al., 2020), we estimated a mass of 3–5 $M_{\rm J}$ under the assumption of chemical equilibrium.

4.6 Discussion

4.6.1 A co-moving planet or free-floating object

The discrepancies between the orbital fitting to the central two stars with their RUWE value, SED fitting, and radial velocity measurements suggest that there might be an additional low-mass stellar companion in the system. The uncertainty in the resulting barycentre of the system makes it challenging to confirm if the candidate is a co-moving companion by conventional common proper motion analysis. This candidate may be a co-moving planet, a free-floating planetary-mass object, a brown dwarf, or a background star. We followed the method used in Nielsen et al. (2017) to quantify the probability ratio of the candidate being a background star to a bound planet of the barycentre of the central stars as a

function of the mass ratio between the fainter star and the brighter star. Nielsen et al. (2017) defined three likelihood components of each scenario: the overall likelihood of the object being a background star $P(\mathrm{bg})$ or planetary companion $P(\mathrm{pl})$, the relative likelihood as a function of separation from the star $P(\rho|\mathrm{bg})$ or $P(\rho|\mathrm{pl})$, and the relative probability as a function of projected velocity $P(v|\rho_{\mathrm{bg}})$ or $P(v|\rho_{\mathrm{pl}})$:

$$\frac{P_{\mathrm{bg}}}{P_{\mathrm{pl}}} = \frac{P(\mathrm{bg})P(\rho|\mathrm{bg})P(v|\rho_{\mathrm{bg}})}{P(\mathrm{pl})P(\rho|\mathrm{pl})P(v|\rho_{\mathrm{pl}})}, \tag{4.4}$$

where P is the probability, ρ is the projected separation, and v is the projected velocity. Below, we describe the calculation taking the mass ratio of 0 as an example, which is an extreme case assuming the barycentre is on the brighter star. We note that the positions of the candidate to the barycentre vary with the mass ratio and affect the corresponding terms.

Based on the hypothesis that the candidate is a background star, we used the Besançon galaxy model [2] (Czekaj et al., 2014) to simulate stellar populations in the direction of the stellar system. We simulated stars with distances from 0 to 50 kpc within a solid angle of one square degree. We selected stars with *2MASS* H magnitudes within 2σ of the candidate's magnitude, 21.79 – 22.30 mag, which contains 4373 stars. The SPHERE image covers regions with separations from the bright central star from $0\farcs15$ to $5\farcs5$; thus, the first term is $P_{\mathrm{b}} = 4373 \times \frac{\pi(5\farcs5)^2 - \pi(0\farcs15)^2}{(3600'')^2} = 3.2\%$. Then, $P(\rho|\mathrm{b})$ is the ratio of the area of the 2σ separation to the whole image, which is $\frac{(5\farcs367)^2 - (5\farcs327)^2}{(5\farcs5)^2 - (0\farcs15)^2} = 1.4\%$. For the third term $P(v|\rho_{\mathrm{bg}})$, we assumed the candidate was free-floating and fitted its proper motion and parallax using EMCEE. We derived its values as $\mu_\alpha \cos\delta$ = -13.86 ± 4.02 mas yr^{-1} and μ_δ = 8.70 ± 3.94 mas yr^{-1}, as presented in Fig. 4.10. The parallax is not well constrained because two of the three astrometric measurements are almost exactly one year apart. We compare its proper motion with the primary star and simulated background stars in Fig. 4.11. The primary star is within the 2σ range of the candidate. Both of them deviate from the majority of the simulated background stars. Then $P(v|\rho_{\mathrm{bg}})$ is the probability that a background star has a proper motion comparable to the measured proper motion of the candidate. This is calculated by the ratio of the number of background stars that have proper

[2] https://model.obs-besancon.fr/

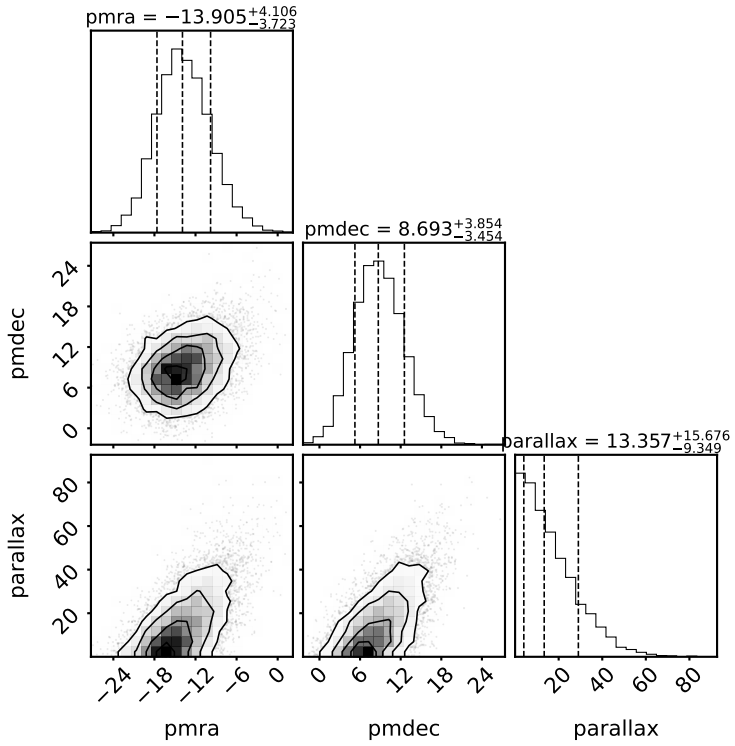


Figure 4.10: Proper motion and parallax posterior distribution of the candidate, assuming it is a free-floating object when the mass ratio of B to A is 0. The proper motion is in the unit of mas yr^{-1} and the parallax is in the unit of mas.

motions within the 2σ contour of the candidate to the total number, which is 7.6%.

In the hypothesis that the candidate is a co-moving planet bound to the central stellar system, we started with the companion occurrence rate in the SHINE survey. Vigan et al. (2021) estimated that 5.7% of FGK stars have companions of 1–75 M_J with a separation range of 5–300 au. Due to a lack of observed statistics for planets beyond 300 au, we used this rate as the lower limit of companion occurrence rate between 5 and 760 au. With an age range of 19–28 Myr and 21.79–22.30 mag, we estimated a mass range of 2.7–4.5 M_J and used the power-law distribution of planetary mass, $dN/dM \propto M^{-1.31}$ (Cumming et al., 2008) to calculate $P(\mathrm{p}) = 5.7\% \times 0.15 = 0.8\%$. We used the power-law distribution of separation, $dN/da \propto a^{-0.61}$ (Nielsen et al., 2017), and the 2σ range of the separation measured at the first epoch to calculate $P(\rho|\mathrm{p}) = \frac{(5\farcs367)^{0.39}-(5\farcs327)^{0.39}}{(5\farcs5)^{0.39}-(0\farcs15)^{0.39}} = 0.4\%$. The relative measured projected velocity between the candidate and star A (from 2018 to 2023) is 4.8 ± 3.8 mas yr^{-1} (3.4 ± 3.9 mas yr^{-1} in RA and 3.4 ± 3.6 mas yr^{-1} in Dec). The escape velocity for a companion at a similar projected distance is 3.5 ± 0.5 mas yr^{-1}, where the uncertainty is due

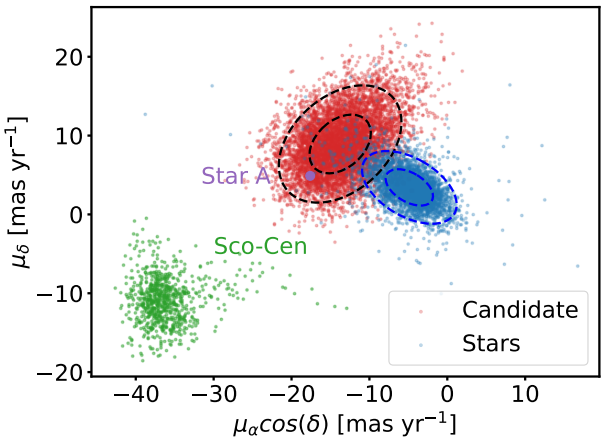


Figure 4.11: Proper motion of the candidate assuming it is free-floating when the barycentre is on the primary star. The blue populations are the stars from 0 to 50 kpc within 2σ magnitude of the candidate generated by the Besançon galaxy model. The 1 and 2σ contours are shown by the dashed blue circles. The red populations are the posterior distribution of the candidate's proper motion with black circles showing the 1 and 2σ range. The purple point is the proper motion of the primary star reported in Gaia and the errorbar is smaller than the marker size. The green points are Sco-Cen candidate members within 20 angular degrees of the primary star on the sky.

to the uncertainty in the total stellar mass. This velocity is the upper limit of the projected escape velocity due to the unknown orbital inclination and phase. We therefore calculated $P(v|\rho_{\rm pl})$ by generating 10^7 points, assuming Gaussian distributions for the measured projected velocity $\sim \mathcal{N}(4.8, 3.8^2)$ and escape velocity $\sim \mathcal{N}(3.5, 0.5^2)$. Here, the upper limit of the fraction of the points with measured projected velocity smaller than the escape velocity is 36.3%. Then, we have

$$\frac{P_{\rm b}}{P_{\rm p}} \sim \frac{3.2\% \times 1.4\% \times 7.6\%}{0.8\% \times 0.4\% \times 36.3\%} = 2.8. \tag{4.5}$$

The candidate is three times as likely to be an unbound object than a bound planet assuming that the mass ratio of B to A is zero. We then repeated this calculation increasing the mass ratio to unity and show the probability ratio in Fig. 4.12. The reason for this change is mainly due to two factors: the fitted proper motion of the candidate assuming it is free floating and the measured projected velocity of this candidate, assuming it is bound. It is 3–240 times more likely being a background star than a bound planet, with the central star mass ratio varying between 0 and 1.

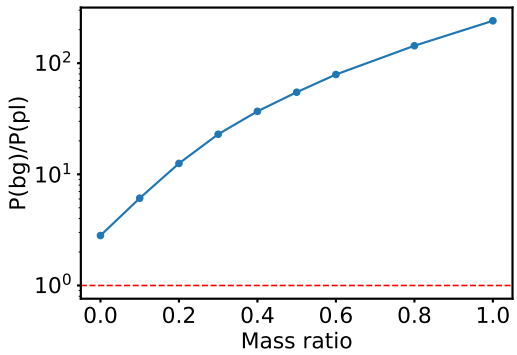


Figure 4.12: Probability ratio of the candidate being a free-floating object to a bound planet of the central stars as a function of the mass ratio of the fainter star to the brighter star. The red horizontal line is where the probability ratio = 1.

Although the probability of the candidate being a bound planet is lower compared to that of being an unbound object, we note that there are several confirmed planets beyond 300 au, such as YSES 1c (Bohn et al., 2020c), b Cen b (Janson et al., 2021a), and COCONUTS-2b (Zhang et al., 2021d). Therefore we cannot definitely rule out the possibility of this candidate being a planet by statistical analysis. A spectroscopic confirmation is therefore crucial to determine if a source is a planetary-mass object, brown dwarf, or a background star.

In addition, the statistical analysis is based on the following set of assumptions:

1. Our knowledge of the wide-orbit planet occurrence rate is incomplete: there are no statistical results on the planet occurrence rate beyond 300 au. We used two approximations: a) the planet occurrence rate is based on separations within 300 au of 150 stars from multiple stellar regions (Vigan et al., 2021) while the planet frequency statistics may vary with regions; and b) the number of planets as a function of mass is taken from Cumming et al. (2008), which was calculated for the radial velocity (RV) detected planets with periods smaller than 2000 days (within 3 au for solar mass stars). These RV planets are likely formed by core accretion, while wide-orbit planets are likely formed by different mechanisms; therefore, the planet distribution may not follow this distribution.

2. The proper motion calculation of the candidate (assuming it is a free-floating object) relies on the proper motion of the barycentre, which is approximated by the proper motion of the primary star measured by Gaia.

However, the proper motion of the primary star is likely affected by the fainter star and the potential hidden companion. The same is true for the proper motion of the barycentre.

3. Due to the unknown orbit of the planet, we adopted the escape velocity as the projected escape velocity, which is the upper limit of the projected escape velocity.

4. We used a galaxy population model to simulate the background star model in the direction of the central star, which is a good representative of the background star density on a large scale. However, there is some uncertainty regarding the local background density that has not been taken into account. This star is likely located in a crowded field given that there are a total of ten sources in the FoV besides the central stars.

Given these uncertainties, the probability ratio should not be taken as the deciding factor on the nature of this source. Regardless, the motion of the candidate is the most significant among the other nine sources in the images and is also significantly distinct from the other sources. We show the relative motion of all sources in two cases in Fig. B.4 in Appendix B.4. If it is a free-floating object, it might be a planetary-mass object, a brown dwarf, or a distant background star. We also show the positions of low-mass stars in Fig. 4.9 using the colour calculated in the evolutionary model of Baraffe et al. (2015), with an age of 1 and 5 Gyr. Their colour also falls into the colour range of the candidate. The colours of the candidate are compatible with a wide range of background M dwarfs. For instance, if the candidate were to be an M dwarf of 0.15 $M_\odot$, its absolute magnitude would be 8.7 mag in H. To match the apparent magnitude of the candidate, it would have to be 4.8 kpc away and have a very high proper motion within the Galaxy.

4.6.2 Group membership

The unresolved central star was classified as a member of LCC by Pecaut & Mamajek (2016). The age we estimated for the primary star is more than 19–28 Myr, older than the typical age of LCC members. LCC is a subregion in Sco-Cen and is revealed to be composed of several substructures of different ages, ranging from 6 to 15 Myr (Ratzenböck et al., 2023; Žerjal et al., 2023). This leads to a question about the membership of the star. Using the online association

membership analysis tool BANYAN Σ (Gagné et al., 2018a), the star is classified as a field star by 99.9% with Gaia proper motion and parallax. Furthermore, we selected Sco-Cen candidate members within 20 angular degrees of the star on the sky from Luhman (2022) and show them in Fig. 4.11. The primary star is located outside of the scattering region of these stars and we find that the closest Sco-Cen star to the primary star is at a separation of 8°.9. So the primary star is likely not a member of Sco-Cen. Detailed analysis is required to classify the star's membership, such as including the resolved absolute radial velocity measurements, instead of the unresolved radial velocity from Gaia. However, this kind of analysis is beyond the scope of this work.

4.7 Summary

We report the detection of a planetary-mass candidate companion imaged around 2M1006. We consistently detected it in the H band with marginal detection in $J23$ bands and non-detection in $K12$ and K_S bands from 2018 to 2023. The central star is resolved to consist of a G8–K0 young Sun analogue with $T_{\rm eff} = 5196^{+162}_{-96}$ K and an M dwarf for the first time. We estimated an age of 19–28 Myr for the primary star. We find tension among the acceleration data, orbital fitting, SED fitting, and radial velocity difference for the two stars if they are indeed part of a binary system. Therefore, we speculated that there is at least one additional low-mass companion in the central stellar system: either the primary star is not a single star or the fainter star is not a single star. Due to the unknown barycentre of the central stellar system, we are unable to confirm if the candidate is a co-moving planet of this system. Nevertheless, the candidate shows the most significant proper motion compared to other sources in the FoV and shares a common proper motion with the primary star. Multi-band colours and spectroscopic observations are necessary to identify the properties of this candidate. A narrow-band colour of $H2$ - $H3$ may enable us to distinguish a low-mass planet with a clear atmosphere from a dusty planet, sub-stellar, and low-mass star as the latter three types of objects would have $H2$ - $H3$ >0 mag; meanwhile a clear-sky low-mass planet would have a very blue $H2$ - $H3$ colour. A narrow-band colour $J2$ - $J3$ can also help identify a clear-sky low-mass planet, as it would have $J2$ - $J3$ >1.5 mag when the mass is smaller than 10 $M_{\rm J}$. From the marginal detection in 2021, its $J2$ - $J3$ is 1.02 ± 0.51 mag, which cannot distinguish it between a low-mass planet, brown dwarf, and M dwarf due to the large uncertainty. Future high S/N detections in

$H23$ and $J23$ may help verify whether it is indeed a clear-sky low-mass planet. Spectroscopic observations will fully confirm its nature. Due to its faintness, only JWST is capable of obtaining its spectra. Long-term imaging and radial velocity monitoring of the central stars will be needed to ascertain the kinematic nature of the two stars, which is crucial to confirm the companionship of this candidate via a common proper motion analysis. With an apparent magnitude of 22.04 ± 0.13 mag in the H band and the age of the primary star, if it is confirmed to be a planetary-mass companion, it would be a planet with a mass of 3–5 $M_{\rm J}$ at a separation of 730 ± 10 au from the primary star. This would confirm it as a low-mass planet similar to 51 Eri b and AF Lep b and place it among known planets with the widest orbits imaged so far.

Chapter 5

A photometric and multiplicity study of young brown dwarfs and planetary-mass objects in the Taurus star-forming region

The work presented in this chapter is the result of a collaborative effort. Beth Biller led the initial study conceptualisation and proposal writing, and I led the data analysis. Specific components of the analysis were supported by several collaborators: Michele Scalco performed the KS2 reduction of the HST data, Beth Biller conducted the aperture photometry, and Loïc Albert led the membership analysis of the targets. The statistical framework was developed in consultation with Clémence Fontanive. I wrote the full chapter, incorporating feedback and comments from all collaborators.

5.1 Abstract

We present a photometric and multiplicity survey of 26 young objects with masses between $7\,M_{\rm J}$ and $28\,M_{\rm J}$ and spectral type later than M8 in the Taurus star-forming region with the Hubble Space Telescope. We search for companion candidates using two methods: a dedicated photometric technique based on the combination of colours from multi-band photometry and point spread function

fitting. No companion candidates are detected beyond 30 au. With an updated membership and age identification, we determine luminosity, temperature, and mass for these objects. We demonstrate that we are sensitive to companions with masses down to 1 M_J and even lower for some targets by artificial star injection tests. After survey completeness correction, we derive a binary frequency <6.5% for our sample in a 68% confidence interval for companions with mass ratios between 0.1 and 1 and separations between 30 and 7,000 au. We find no significant difference in binary frequency among planetary-mass objects in Taurus, Upper Scorpius, and the field. These findings support that the binary frequency of planetary-mass objects is settled at ages <1–10 Myr, suggesting that the formation of wide-orbit planetary-mass binaries is inefficient and the disruption of them likely occurs at a very early stage.

5.2 Introduction

The formation of brown dwarf binaries and planetary-mass binaries remains mysterious, although several formation channels have been proposed, including direct collapse and turbulent formation of dense cores resembling the formation of stellar binaries (Larson, 1972; Goodwin et al., 2004; André et al., 2019), gravitational instability in discs (Adams et al., 1989; Bonnell, 1994; Kratter & Lodato, 2016), and dynamical capture (Ostriker, 1994; Moeckel & Bally, 2007; Bate, 2012) and triple-system disruption (Reipurth & Mikkola, 2015). Each mechanism leaves imprints on the multiplicity fraction, separation distribution, mass-ratio distribution, and eccentricity of the resulting population. Thus, multiplicity is a key diagnostic of formation processes. The fraction of objects found in binary or multiple systems in the field decreases with the mass of the primary: about half of solar-type FGK stars are in binary systems (Raghavan et al., 2010), compared to 20–30% of M dwarfs (Janson et al., 2012; Ward-Duong et al., 2015), and less than 20% for brown dwarfs and planetary-mass objects (Bouy et al., 2003; Fontanive et al., 2018, 2023). Understanding how this decline arises is critical to distinguishing whether stars, brown dwarfs, and free-floating planetary-mass objects form through common or distinct mechanisms. Surveying brown dwarf binaries and planetary-mass binaries is therefore crucial to understanding their formation.

Although the first multiplicity surveys of very low-mass stars and brown dwarfs date back to the 1990s (Fischer & Marcy, 1992), the population of known binaries

in this regime has remained small. Nevertheless, observations reveal that very low-mass binaries differ from stellar binaries in both orbital separation and mass ratio distributions (Duchêne & Kraus, 2013; Offner et al., 2023). Burgasser et al. (2007) found that for systems with primary masses below 0.1 $M_\odot$, their mass ratios strongly peak near unity, even after correcting for observational biases. The orbital separation distribution of very low-mass binaries is narrower than higher mass systems: the separation of the majority of very low-mass binaries is found within 10 au via spectroscopic observations (spectroscopic binaries) and high angular resolution observations (visual binaries) (Reid et al., 2002; Basri & Reiners, 2006; Burgasser et al., 2012; Maxted & Jeffries, 2005; Allen et al., 2007). This indicates that brown dwarf and planetary-mass binaries are more likely to be found in equal-mass binaries at close separations, suggesting formation channels that favour similar-mass pairing with the greater dynamical stability of such configurations.

However, a handful of cases of wide binaries with separation larger than 10 au have been discovered by direct imaging, such as SDSS J1416+13AB (75 M_J, L7 + 30 M_J, T7.5, 45–135 au, >1 Gyr; Burningham et al., 2010), 2MASS J04414489+2301513 (20 M_J, M8.5 + 5–10 M_J, M9.5–L0, 15 au, ~1 Myr; Todorov et al., 2010), and Oph 98 ABs (15 M_J, M9–L1 + 8 M_J, L2–L6, 200 au, 1–7 Myr; Fontanive et al., 2020). These systems raise more questions about the formation of very low-mass binaries in extreme cases. Wide, very low-mass binaries have low binding energy and are subject to dynamical disruption after formation. Comparing very low-mass binary populations of different ages can provide clues on how dynamical evolution shapes the binary fraction. Fontanive et al. (2018, 2023) constrained the binary fraction of late-T and Y-type brown dwarfs in the field with age > 1 Gyr to be smaller than 4.9%. De Furio et al. (2022) found that the Orion Nebula Cluster (a mean age of ~2.2 Myr; Reggiani et al., 2011) has an excess of very low-mass binaries compared to the field, suggesting that dynamical scattering might disrupt very low-mass binaries after their formation.

The stellar environment, such as stellar density, may also have impacts on the observed multiplicity (e.g. Offner et al., 2023). Comparing multiplicity in various regions can examine the environment's impacts on binary formation and evolution. Simulations have found that high stellar density can disrupt binaries (Ivanova et al., 2005). Young, sparse regions therefore offer a window into primordial multiplicity before dynamical evolution erases the initial imprint of formation. As one of the youngest star-forming regions in the solar

neighbourhood, Taurus is a low-density environment with an age of 1–10 Myr (Kenyon et al., 2008; Luhman, 2023). A number of young planetary-mass objects have been discovered in Taurus in recent years (Esplin & Luhman, 2017; Luhman et al., 2017; Best et al., 2017b; Zhang et al., 2018), providing a unique opportunity to probe the multiplicity of planetary-mass objects in a young low-density environment.

In this chapter, we present a photometric and multiplicity survey of young brown dwarfs and planetary-mass objects in Taurus. We describe the sample selection and observations in Sect. 5.3. Then we detail our photometry analysis and mass estimation of the primary targets in Sect. 5.4. The multiplicity analysis including companion search, survey completeness and binary frequency is presented in Sect. 5.5. We discuss the results in Sect. 5.6 and conclude this work in Sect. 5.7.

5.3 Observations

5.3.1 Sample selection

This survey contains 26 young brown dwarfs and planetary-mass objects in the field of Taurus. 18 are from the W-band survey (Allers & Liu, 2020; Esplin & Luhman, 2019) and the rest is selected from the literature (Best et al., 2017a; Luhman et al., 2017; Esplin & Luhman, 2017; Zhang et al., 2018). They all have spectroscopic confirmation from NASA Infrared Telescope Facility (IRTF)/SpeX (Rayner et al., 2003) or Gemini Near-Infrared Spectrograph (GNIRS; Elias et al., 2006) with spectral types (SpT) ranging from M8 to L3. The field of Taurus is a complicated region including the Taurus star-forming region, young moving groups associated with Taurus molecular clouds and old moving groups (Liu et al., 2021; Kerr et al., 2021). We classified the sub-region membership of objects that are from the W-band survey using the Bayesian Analysis for Nearby Young AssociatioNs (BANYAN $\sum$) tool (Gagné et al., 2018b) as we have their positions, proper motion, and parallax measured by Canada France Hawaii Telescope (CFHT)/Wide-field InfraRed Camera (WIRCam) (Puget et al., 2004). We assigned the ages and distances of the parent associations to the 12 objects that have membership likelihood over 80%. They are from TAUMGLIU4 (2 Myr, 158 pc, Liu et al., 2021), TAUMGLIU9 (7–8 Myr, 176 pc, Liu et al., 2021), HSC1318 (5.5 Myr, 128 pc, Hunt & Reffert, 2023), L1551

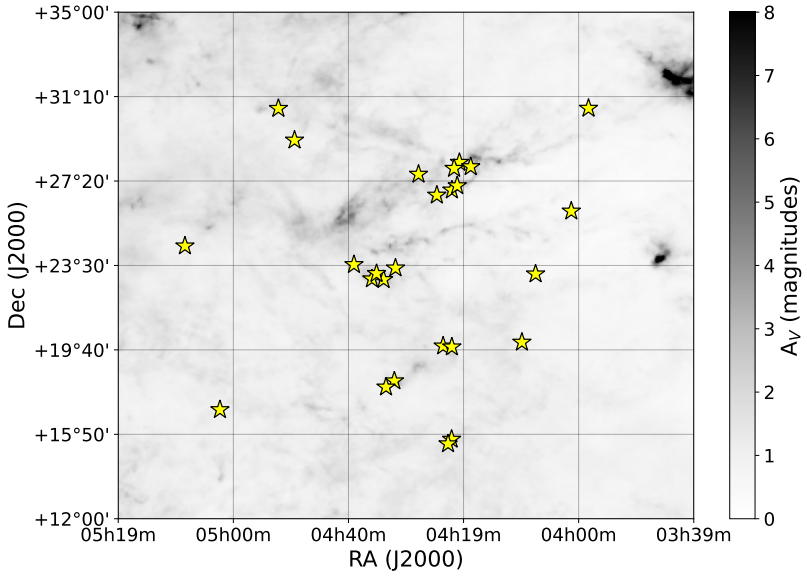


Figure 5.1: The extinction map of the Taurus field from Planck dust map (Planck Collaboration et al., 2014). Targets surveyed in this work are marked with the star symbol.

(7 Myr, 146 pc, Kerr et al., 2021), L1536 (3.3 Myr, 159 pc, Kerr et al., 2021), L1495 (3.8 Myr, 131 pc, Kerr et al., 2021), and L1529 (3.4 Myr, 129 pc Kerr et al., 2021). Four other targets have clear age characterisation from the literature: 2MASS J04011678+2557527 (1.5 ± 0.5 Myr, Best et al., 2017b), PSO J075.5825+16.9498 and PSO J059.5714+30.6327 (10–30 Myr, Zhang et al., 2018), and PSO J065.8871+19.8386 (<1 Myr, Zhang et al., 2018). We assigned the typical Taurus age of 1–10 Myr and distance 145±15 pc for the other 10 targets. General information for the targets is listed in Table 5.1, including simplified names of the targets used in this work. The sky map of the targets is presented in Fig. 5.1.

5.3.2 HST observations

The targets were observed with the Hubble Space Telescope (HST)/Wide Field Camera 3 (WFC3) in GO programme 15628 (PI Biller). They were observed in one optical filter on the UVIS detector F850LP (pivot wavelength = 0.92μm, width = 0.12 nm), and two filters on the IR detector: F127M (pivot wavelength = 1.27 μm, width = 0.69 μm) and F139M (pivot wavelength = 1.38 μm, width = 0.64 μm). The UVIS detector has a pixel scale of 0.″04 and a field of view (FoV) of 162 × 162 arcsec^2. The IR detector has a pixel scale of 0.″135 and FoV

Table 5.1: Target information.

Name	Short name	RA (J2000)	Dec (J2000)	SpT	Membership[a]	Age (Myr)	Distance (pc)	Ref.[b]
UGCS J043506.95+230750.6	J0435+2307	04:35:06.95	+23:07:50.69	M9-L1	TAUMGLIU4(92.3)	2.0±1.0	158.0±10.0	W, Esplin19
2MASS J04011678+2557527	J0401+2557	04:01:16.78	+25:57:52.73	L1	—	1.5±0.5	145±15	Best17
UGCS J042438.53+264118.5	J0424+2641	04:24:38.51	+26:41:18.95	M9.5	—	1–10	145±15	W, Esplin19
UGCS J042201.36+265512.1	J0422+2655	04:22:01.36	+26:55:12.10	M9-L3	—	1–10	145±15	W, Esplin17
2MASS J04220204+1947499	J0422+1947	04:22:02.05	+19:47:50.00	M9	—	1–10	145±15	W, Esplin19
UGCS J043555.45+225313.4	J0435+2253	04:35:55.45	+22:53:13.49	M9-L2	TAUMGLIU4(91.0)	2.0±1.0	158.0±10.0	W, Esplin19
2MASS J05082480+2422518	J0508+2422	05:08:24.80	+24:22:51.89	L2	TAUMGLIU9(82.1)	7.5±0.5	176.0±15.0	W, Best17
PSO J064.6887+27.9799	J064.68+27.97	04:18:45.30	+27:58:48.47	L0.7	HSC1318(98.3)	5.5±2.5	128.6±5.0	W, Zhang18
PSO J065.1792+28.1767	J065.17+28.17	04:20:43.01	+28:10:36.41	L1.6	HSC1318(99.4)	5.5±2.5	128.6±5.0	W, Esplin17, Zhang18
2MASS J04314964+2322524	J0431+2322	04:31:49.65	+23:22:52.42	M9-L2	TAUMGLIU4(90.9)	2.0±1.0	158.0±10.0	W, Esplin19
UGCS J043328.47+175833.0	J0433+1758	04:33:28.48	+17:58:33.05	M9-L1	L1551(93.0)	7.0±2.0	145.6±3.8	W, Esplin19
PSO J061.8714+23.1104	J061.87+23.11	04:07:29.12	+23:06:38.18	M9.9	—	1–10	145±15	Zhang18
2MASS J04095154+2000428	J0409+2000	04:09:51.55	+20:00:42.70	M9.1	—	1–10	145±15	Zhang18
PSO J075.5825+16.9498	J075.58+16.94	05:02:19.82	+16:56:59.32	M9.5	—	10–30	145±15	Zhang18
PSO J059.5714+30.6327	J059.57+30.63	03:58:17.16	+30:37:58.03	M9.7	—	10–30	145±15	Zhang18
2MASS J04274951+2738155	J0427+2738	04:27:49.52	+27:38:15.57	M9.5	—	1–10	145±15	Esplin17
2MASS J04320157+1815229	J0432+1815	04:32:01.57	+18:15:22.96	M9.5	—	1–10	145±15	W, Esplin17
UGCS J043354.07+225119.1	J0433+2251	04:33:54.07	+22:51:19.20	M9-L2	TAUMGLIU4(85.6)	2.0±1.0	158.0±10.0	W, Esplin17
UGCS J045210.35+303734.3	J0452+3037	04:52:10.35	+30:37:34.30	M9.5	L1536(90.2)	3.3±0.9	159.2±4.2	W, Esplin17
2MASS J04210636+2706545	J0421+2706	04:21:06.36	+27:06:54.57	M9.5	HSC1318(89.6)	5.5±2.5	128.6±5.0	W, Esplin19
2MASS J04213847+2754146	J0421+2754	04:21:38.48	+27:54:14.62	M9.5	L1495(97.2)	3.8±0.8	131.2±3.3	W, Esplin19
WBIS2241+1523	J0422+1523	04:22:41.75	+15:23:53.58	L0.0	—	1–10	145±15	W
2MASS J04390237+2332133	J0439+2332	04:39:02.37	+23:32:12.75	M9.0	L1529(96.4)	3.4±0.5	129.4±2.7	W
WBIS2204+1536	J0422+1536	04:22:04.49	+15:36:20.24	M8.0	—	1–10	145±15	W
PSO J065.8871+19.8386	J065.88+19.83	04:23:32.91	+19:50:19.26	L0	—	<1	145±15	Zhang18
2MASS J04492210+2911124	J0449+2911	04:49:22.11	+29:11:12.26	M8.5	—	1–10	145±15	Esplin17

Notes: (a).This work. Only targets with a membership probability > 80% (numbers in the parentheses) are assigned a membership. (b).References of sources: W: W-band survey, Best17: Best et al. (2017a), Esplin17: Esplin & Luhman (2017), Zhang18: Zhang et al. (2018), and Esplin19: Esplin & Luhman (2019).

of 135 × 135 arcsec^2. The instrument settings of most targets were the same. UGCS J043506.95+230750.6 is the only target that was observed in the full array with two dither positions because there was a candidate companion from previous Keck images. Its SAMP-SEQ and NSAMP parameters for IR observations were STEP50 × 13. All other targets were observed with the sub-array aperture UVIS2-2K2C-SUB (FoV = 81 × 81 arcsec^2) in F850LP and SQ512SUB (FoV = 68 × 68 arcsec^2) in F127M and F139M with three dither positions. Their SAMP-SEQ and NSAMP parameters were STEP25 × 14. There are a total of 31 observations after excluding three failed observations. Four targets were observed more than once. The valid observations of this sample are listed in Table 5.2.

The reason why we chose these three filters for observations is that we can build a reddening insensitive index ($Q_{\rm HST}$) with the fluxes in the three filters. This can be used to distinguish companion candidates from background stars in just one epoch. The technique is detailed in Dubber et al. (2021) and the expression for $Q_{\rm HST}$ is:

$$Q_{\rm HST} = -2.5 \log \left(\frac{F_{\rm F850LP}}{F_{\rm F127M}} \right) + e \times 2.5 \log \left(\frac{F_{\rm F127M}}{F_{\rm F139M}} \right), \tag{5.1}$$

where e is a constant of 5.81 calculated by the extinction ratio in the three bands: $e = (A_{F850LP} - A_{F127M})/(A_{F139M} - A_{F127M})$. The F139M filter can explore the water absorption band at 1.4 μm where late-type objects will have strong absorption while background stars earlier than M6 will not. Combining results from the three filters, a background star will have $Q_{\rm HST} \approx 0$, while an object with a spectral type of late-M, L or T will have $Q_{\rm HST} > 1$. Candidate companions around the targets should have $Q_{\rm HST}$ greater than that of the primary sources. Therefore, this technique can help to select bonafide companions and reject background stellar interlopers.

5.4 Photometric analysis

The raw data were calibrated with the automated calibration pipelines provided by the Space Telescope Science Institute (STScI). The *_flt* files are calibrated individual exposures after bias subtraction, dark current subtraction, and flat-field correction. For the F850LP filter, the flt files were further applied charge transfer efficiency (CTE) correction to mitigate the effects of charge transfer inefficiency in CCD detectors, resulting in *_flc* files. There are also *_drz* or

Table 5.2: HST observation summary.

Name	Date	F850LP Time (s)	F127M Time (s)	F139M Time (s)
J0435+2307	2019-12-03	478.0×3	349.2×3	349.2×3
J0435+2307	2019-12-17	478.0×3	349.2×3	349.2×3
J0401+2557	2019-07-30	270.0×3	197.2×3	197.2×3
J0424+2641	2019-09-02	270.0×3	197.2×3	197.2×3
J0422+2655	2019-12-14	270.0×3	197.2×3	197.2×3
J0422+1947	2019-07-26	267.0×3	197.2×3	197.2×3
J0435+2253	2019-12-04	267.0×3	197.2×3	197.2×3
J0508+2422	2019-09-08	267.0×3	197.2×3	197.2×3
J064.68+27.97	2019-12-15	270.0×3	197.2×3	197.2×3
J065.17+28.17	2019-08-01	270.0×3	197.2×3	197.2×3
J0431+2322	2019-12-13	267.0×3	197.2×3	197.2×3
J0433+1758	2019-08-31	267.0×3	197.2×3	197.2×3
J061.87+23.11	2019-08-01	267.0×3	197.2×3	197.2×3
J0409+2000	2019-11-25	233.0×3	197.2×3	197.2×3
J075.58+16.94	2019-08-29	267.0×3	197.2×3	197.2×3
J059.57+30.63	2019-08-23	275.0×3	197.2×3	197.2×3
J0427+2738	2019-12-24	270.0×3	197.2×3	197.2×3
J0432+1815	2019-09-02	267.0×3	197.2×3	197.2×3
J0433+2251	2019-12-14	267.0×3	197.2×3	197.2×3
J0452+3037	2019-08-26	275.0×3	197.2×3	197.2×3
J0421+2706	2019-12-23	270.0×3	197.2×3	197.2×3
J0421+2754	2019-09-02	270.0×3	197.2×3	197.2×3
J0422+1523	2019-08-29	267.0×3	197.2×3	197.2×3
J064.68+27.97	2019-12-23	270.0×3	197.2×3	197.2×3
J0439+2332	2019-08-31	267.0×3	197.2×3	197.2×3
J0452+3037	2019-08-26	275.0×3	197.2×3	197.2×3
J0422+1536	2019-07-24	267.0×3	197.2×3	197.2×3
J065.88+19.83	2019-07-25	267.0×3	197.2×3	197.2×3
J0449+2911	2019-08-28	270.0×3	197.2×3	197.2×3
J0421+2706	2020-03-01	270.0×3	197.2×3	197.2×3

_drc (applicable for F850LP) files available that are geometrically corrected and cosmic-ray-cleaned combined images from multiple exposures using the DrizzlePac software (Gonzaga et al., 2012).

5.4.1 Aperture photometry

We used PHOTUTILS (Bradley et al., 2024) to perform aperture photometry on *_drz* files for F127M and F139M and *_drc* files for F850LP. We adopted an aperture radius of 0.″4. The uncertainty is estimated by assuming the Poisson noise for the source flux and also includes the background noise by taking the three-sigma clipped standard deviation of 1000 random apertures on source-free positions, the same as the method used in Schneider et al. (2015); Fontanive et al. (2018). Then the fluxes of the sources were corrected to an infinite aperture using the encircled energy tables and calibrated to the zero point of the Vega magnitude system using the instructions provided by STScI[1]. We adopted the typical flux uncertainty of HST photometric calibration: 1.8% for WFC/UVIS and 2.0% for WFC/IR.

5.4.2 PSF fitting

We performed HST1PASS on individual *_flt* or *_flc* files to search for and detect sources by PSF fitting. HST1PASS is a package written in FORTRAN that uses empirical PSF libraries which contain spatially variable PSFs to run a single pass of source detection in individual exposures (Anderson, 2022). We adopted a template PSF size of 5 pixel × 5 pixel. The output products include source detection results and residuals after the subtraction of detected sources. We did not detect any companion candidates in the residual images.

To further combine multiple exposures and search for faint sources, we used KS2 to perform the second-pass photometry. KS2 is a package written in FORTRAN that can find and measure sources simultaneously in all exposures based on the results from the first-pass photometry of HST1PASS (Bellini et al., 2017; Nardiello et al., 2018). It creates a new coordinate system, maps detected sources to this system, and stacks all exposures into a single image. The data reduction process follows the procedures described in Scalco et al. (2021); Fontanive et al.

[1] https://www.stsci.edu/hst/instrumentation/wfc3/data-analysis/photometric-calibration

(2023). We supersampled the stacked images by a factor of 2. The output products also contain the stacked source-subtracted residuals. The current version of KS2 is only configured to fully reduce data in F127M and F139M filters. Therefore, we had second-pass photometry for sources in the two IR filters but only stacked images and source-subtracted residuals for F850LP. This is enough for our companion search because the candidates would be much brighter in F127M than F850LP as they are planetary-mass objects and emit most of their energy in the infrared, though angular resolution is worse than in F850LP. As a result, we have photometric measurements from KS2 only for the two IR filters. The instrumental magnitudes of sources were measured by PSF fitting in KS2. We followed the same method demonstrated in Scalco et al. (2021) to perform the photometric calibration, which includes corrections for the difference between PSF fitting and aperture photometry as well as the zero point (ZP) of the Vega magnitude system. The adopted ZP is 23.649 mag in F127M and 23.367 mag in F139M.

Table 5.3 lists the photometric measurements of aperture photometry and PSF fitting of the targets. The photometric measurements of the two methods agree with each other, although the uncertainty of aperture photometry is likely underestimated. We also computed the $Q_{\rm HST}$ using the photometric measurements of the two methods. We used the photometric flux measured by aperture photometry in F850LP for the $Q_{\rm HST}$ calculation of KS2 as it only has measurements in the two IR filters. All the targets have $Q_{\rm HST} > 1$ as expected, as shown in Fig. 5.2.

5.4.3 Primary masses

For targets without 2MASS J band measurements, we converted from the MKO photometric system to the 2MASS photometric system using the relation $J_{\rm 2MASS} = J_{\rm MKO} + 0.05$ which is for dwarfs with spectral types later than M6 (Zhang et al., 2018). Then we converted apparent $J_{\rm 2MASS}$ magnitudes to absolute magnitudes $M_{J\rm 2MASS}$ using the distance listed in Table 5.1 and extinction listed in Table 5.4. The A_V was converted to A_J by $A_J = 0.282 \times A_V$ (Cardelli et al., 1989). We estimated the bolometric correction BC_J by SpT (with SpT uncertainty of 1 subtype) using the polynomial relation provided in Filippazzo et al. (2015). The

Table 5.3: Photometric results of the targets.

Name	Aperture photometry				PSF fitting		
	F850LP (mag)	F127M (mag)	F139M (mag)	$Q_{\rm HST}$	F127M (mag)	F139M (mag)	$Q_{\rm HST}$
J0435+2307	19.13±0.02	17.14±0.02	17.45±0.02	4.86±0.20	17.13±0.09	17.40±0.06	4.66±0.71
J0401+2557	18.46±0.02	16.68±0.02	17.03±0.02	4.92±0.20	16.68±0.09	17.01±0.06	4.81±0.71
J0424+2641	19.49±0.03	17.36±0.02	17.58±0.02	4.53±0.20	17.36±0.09	17.56±0.06	4.37±0.71
J0422+2655	20.30±0.04	17.82±0.02	18.00±0.02	4.67±0.21	17.83±0.09	17.98±0.06	4.48±0.72
J0422+1947	18.02±0.02	16.34±0.02	16.65±0.02	4.58±0.20	16.37±0.09	16.63±0.06	4.25±0.70
J0435+2253	19.38±0.03	17.20±0.02	17.45±0.02	4.72±0.20	17.20±0.09	17.40±0.06	4.47±0.72
J0508+2422	18.57±0.02	16.86±0.02	17.18±0.02	4.73±0.20	16.86±0.09	17.16±0.07	4.56±0.71
J064.68+27.97	18.21±0.02	16.42±0.02	16.75±0.02	4.81±0.20	16.42±0.09	16.74±0.06	4.74±0.71
J065.17+28.17	18.33±0.02	16.52±0.02	16.89±0.02	5.05±0.20	16.53±0.09	16.78±0.06	4.38±0.71
J0431+2322	18.97±0.02	16.69±0.02	16.87±0.02	4.41±0.20	16.70±0.09	16.84±0.06	4.18±0.72
J0433+1758	19.59±0.03	17.53±0.02	17.81±0.02	4.78±0.20	17.53±0.09	17.73±0.06	4.32±0.72
J061.87+23.11	18.17±0.02	16.37±0.02	16.73±0.02	4.99±0.20	16.37±0.09	16.71±0.07	4.88±0.73
J0409+2000	16.78±0.02	15.43±0.02	15.66±0.02	3.81±0.20	15.39±0.09	15.58±0.06	3.58±0.74
J075.58+16.94	17.32±0.02	15.95±0.02	16.23±0.02	4.10±0.20	15.95±0.09	16.20±0.06	3.97±0.71
J059.57+30.63	17.32±0.02	15.87±0.02	16.07±0.02	3.70±0.20	15.86±0.09	16.03±0.07	3.56±0.72
J0427+2738	17.91±0.02	16.01±0.02	16.26±0.02	4.44±0.20	16.01±0.09	16.25±0.06	4.38±0.71
J0432+1815	18.95±0.02	16.82±0.02	17.06±0.02	4.63±0.20	16.82±0.09	17.07±0.06	4.73±0.72
J0433+2251	19.99±0.03	17.75±0.02	17.95±0.02	4.45±0.21	17.77±0.09	17.92±0.07	4.18±0.74
J0452+3037	18.83±0.02	16.89±0.02	17.27±0.02	5.27±0.20	16.88±0.09	17.25±0.06	5.19±0.71
J0421+2706	18.92±0.02	16.94±0.02	17.19±0.02	4.54±0.20	16.96±0.09	17.17±0.06	4.24±0.72
J0421+2754	18.54±0.02	16.47±0.02	16.80±0.02	5.06±0.20	16.48±0.09	16.79±0.06	4.97±0.71
J0422+1523	19.95±0.03	17.88±0.02	18.15±0.02	4.75±0.21	17.87±0.09	18.15±0.06	4.84±0.70
J0439+2332	18.98±0.02	17.03±0.02	17.29±0.02	4.57±0.20	17.03±0.09	17.27±0.06	4.42±0.70
J0422+1536	17.14±0.02	15.71±0.02	15.95±0.02	3.93±0.20	15.70±0.09	15.93±0.06	3.93±0.70
J065.88+19.83	14.84±0.02	13.45±0.02	13.77±0.02	4.34±0.20	13.44±0.09	13.60±0.06	3.46±0.72
J0449+2911	16.07±0.02	14.72±0.02	15.02±0.02	4.17±0.20	14.73±0.09	15.01±0.06	4.08±0.70

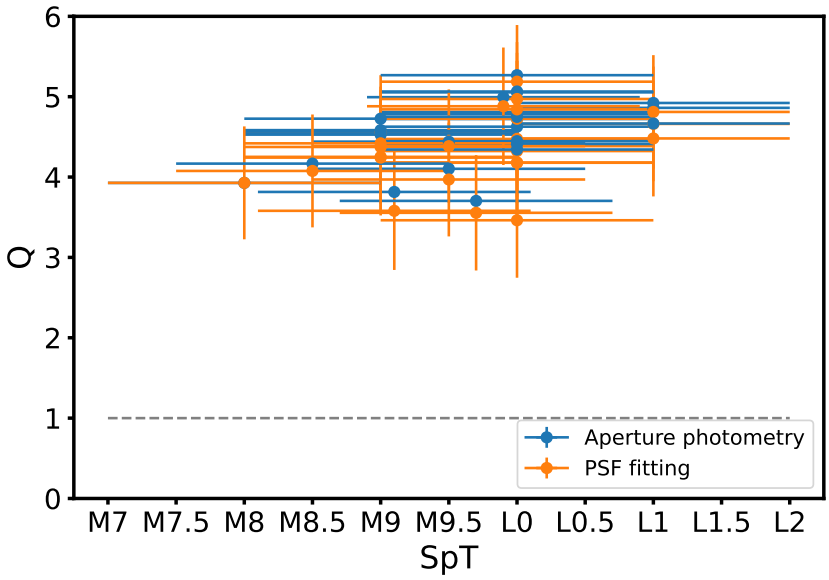


Figure 5.2: $Q_{\rm HST}$ of primary sources calculated by aperture photometry and PSF fitting. All the targets have $Q_{\rm HST} > 1$, verifying that they have SpT later than mid-M. Stars with earlier SpT should have $Q_{\rm HST} < 1$.

bolometric luminosity $Lbol$ is calculated by

$$Lbol = \log_{10}\left(\frac{L_{\rm bol}}{L_\odot}\right) = -\frac{M_{J2\rm MASS} + BC_J - M_{\rm bol,\odot}}{2.5}, \tag{5.2}$$

where $M_{\rm bol,\odot}$ is taken as 4.73 mag.

Then we chose the AMES-Dusty2000 evolutionary models (Chabrier et al., 2000) to derive the mass. We used the rejection sampling method (e.g., Dupuy & Liu, 2017) to evaluate the mass and $T_{\rm eff}$ by the derived bolometric luminosity. The results are listed in Table 5.4 together with the 2MASS and MKO magnitudes of the targets. Most of the targets have masses $< 20\,M_{\rm J}$ with five targets lower than $10\,M_{\rm J}$. J0401+2557 is the object of the lowest mass in this sample, which is $6.89^{+1.84}_{-1.76}\,M_{\rm J}$. There is one problematic target J065.88+19.83: it has an estimated mass of $\sim$34 $M_{\rm J}$. This mass is overestimated because its actual age should be younger than 1 Myr (Zhang et al., 2018). Because AMES-Dusty2000 evolutionary models only provide values for objects $\geq$ 1 Myr, it estimates a heavier mass when the age is older than the actual age given the same luminosity. Constraining the parameters of objects younger than 1 Myr is challenging as all the current evolutionary models have large uncertainties at this range. Hence, we assumed an age of 1 Myr to estimate its mass because this is the youngest age the AMES-Dusty2000 models provided. All the targets have $T_{\rm eff}$ over 1800 K, a typical $T_{\rm eff}$

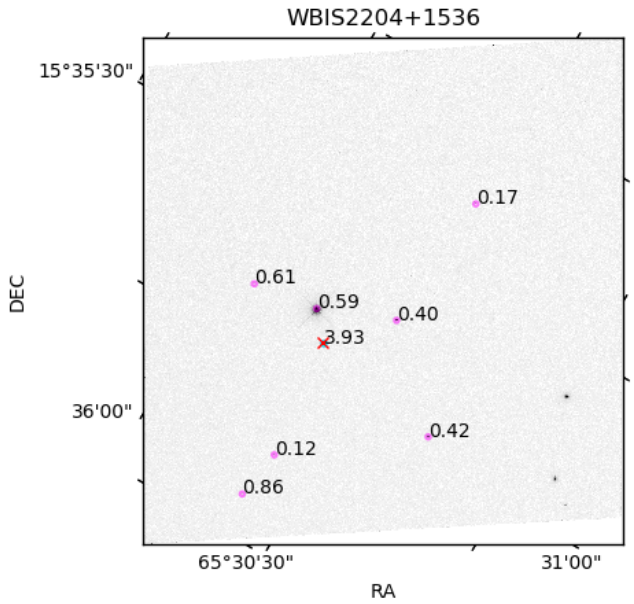


Figure 5.3: $Q_{\rm HST}$ of detected sources in the FoV of WBIS2204+1536. The primary target is marked by the red cross and other detected sources are marked by pink circles. Their $Q_{\rm HST}$ are labelled adjacent to them. Only the primary target has $Q_{\rm HST} > 1$.

for warm and dusty brown dwarfs.

5.5 Multiplicity analysis

5.5.1 Companion search

We used our $Q_{\rm HST}$ technique to search for wide-separated companion candidates with aperture photometry. The source detection was performed with DAOStarFinder (Stetson, 1987). We calculated the $Q_{\rm HST}$ of all the detected sources in the FoV of our targets. No candidates have $Q_{\rm HST} > 1$. Figure 5.3 shows the FoV of an example target (WBIS2204+1536) in F850LP with $Q_{\rm HST}$ of all detected sources. Only the primary target has $Q_{\rm HST}$ over 1, while the other sources have $Q_{\rm HST} < 1$, suggesting that they are background stars. We also performed a visual inspection of the residual images after subtraction of the primary target and two waves of finding with KS2. No close-in companion candidates were found.

5.5.2 Artificial star tests

To evaluate the sensitivity and reliability of our source detection method, we conducted artificial star injection and retrieval tests (ASTs) using the same method detailed in Fontanive et al. (2023). For each target, we injected 4×10^5 artificial sources using the PSFs modelled in Sect. 5.4.2 to all individual frames in F127M and F139M with one source injected and measured at a time. The artificial sources were uniformly injected across the FoV with a uniform distribution for instrumental magnitude between -7 and 4 mag in F127M and F139M filters, separately, which corresponds to an apparent magnitude of 16.5–27.5 in F127M and 16.4–27.4 in F139M.

KS2 outputs various parameters summarising the PSF fitting results. We explored these parameters and determined the criteria to identify if an artificial source is well recovered by comparing its injected and fitted values, following the procedures in Fontanive et al. (2023). The criteria can then be used to determine if a real source is well detected in a given filter. To start with, we applied an initial selection to filter out obvious dubious sources with sources that were retained following the criteria:

- sources are detected in all three images;
- the measured flux, photometric rms, and sky rms are valid numbers (>0 and not default outflow values (e.g. 9999));
- the measured flux is higher than local sky rms;
- the absolute difference between the injected and retrieved positions is within 1 pixel in X and Y, respectively;
- the absolute difference between the injected and retrieved magnitudes is within $-2.5 \times \log_{10}(2)$.

The remaining sources after the initial selection are well-detected sources. From here, we made a test of setting the threshold of three PSF fitting parameters to retain as many well-recovered sources as possible while excluding as many poorly-recovered sources as possible at the same time. The definitions of the three parameters are from Bedin et al. (2008); Scalco et al. (2021). The parameter o represents the initial ratio — before subtracting neighbouring sources — of the light from nearby neighbours within the fitting radius to the light from the target star. The parameter quality-of-fit (QFIT) indicates how well the PSF-fitting process performed when measuring a star's position and brightness with values

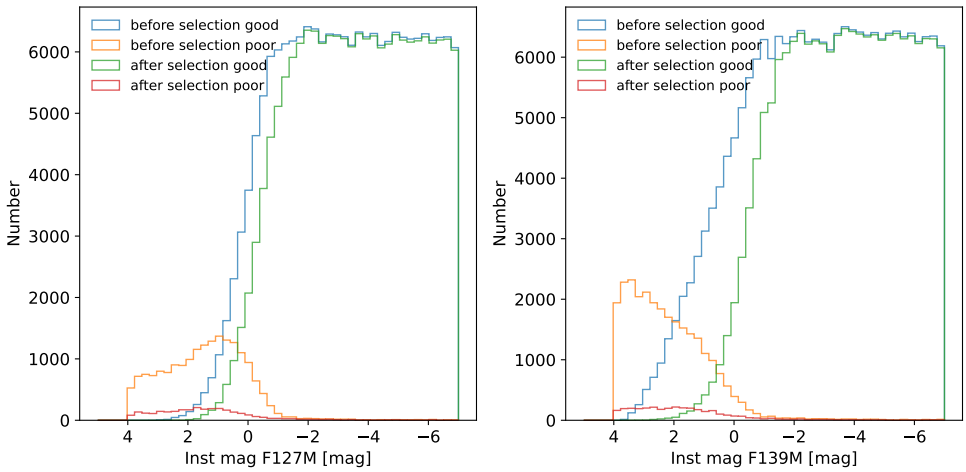


Figure 5.4: An example of well-recovered and poorly-recovered artificial stars before and after applying the selection threshold of o, QFIT, and RADXS. 'Good' and 'poor' refer to stars that pass the initial selection and not, separately.

closer to one suggesting that the source closely matches the assumed PSF model. The parameter RADXS quantifies deviations from the expected PSF shape by comparing the observed flux just outside the PSF core to that predicted by the PSF model. Extended sources like galaxies typically show large positive RADXS values, whereas unusually sharp sources, such as cosmic rays or hot pixels, yield large negative values.

We explored the values of o in the range of [2, 6], QFIT in the range of [0.7, 0.95], and the absolute value of RADXS in the range of [0.2, 0.5]. The optimised combination of them that meets our criterion is: $o < 4$, QFIT > 0.9, and $-0.35 <$ RADXS < 0.35. We applied the selection threshold independently in F127M and F139M. Figure 5.4 shows an example of the number of artificial sources before and after our selection. Poorly-measured sources are mainly sources with instrumental magnitudes fainter than -1 mag. Less than 15% of the poorly-measured sources passed the selection threshold. Over 80% of the sources that passed the initial criteria are retained after applying the selection threshold, and over 99% for sources brighter than -1 mag are retained.

5.5.3 Survey completeness

In order to reach a robust statistical result for binary fraction for any surveys, it is vital to estimate the completeness of the survey, which evaluates how likely

we can detect a companion at a given separation and contrast. A robust way to estimate completeness is to perform artificial star injections, as we did in the previous section. As we search for companions of the primary brown dwarfs, we injected 2×10^6 artificial sources as a function of the instrumental magnitude and separation to the primary targets with uniform distributions in instrumental magnitude, radial separation, and phase angle. As in Fontanive et al. (2023), we split the injection into four sets:

1. 4×10^5 sources of instrumental magnitude in the range of [-7, 4] mag injected between 1 and 20 pixels from the primary target;
2. 6×10^5 sources of instrumental magnitude in the range of [-3, 2] mag injected between 1 and 20 pixels from the primary target;
3. 4×10^5 sources of instrumental magnitude in the range of [-7, 4] mag injected beyond 20 pixels from the primary target to the edge of the image;
4. 6×10^5 sources of instrumental magnitude in the range of [-3, 2] mag injected beyond 20 pixels from the primary target to the edge of the image.

This division enabled us to fully explore the entire image while focusing on the parameter space where potential companions are likely located: slightly fainter than and at a small separation to the primary target. The injections were performed in both F127M and F139M filters. As the F127M filter has a smaller PSF size which results in better sensitivity at smaller separations, we took the ASTs in F127M to represent the completeness of our survey. We conducted the ASTs of the two million sources for each target and applied the initial selection and selection threshold to them. Then we determined the grid size of the completeness maps: an interval of 1 pixel for separation smaller than 20 pixels, an interval of 20 pixels for separation larger than 20 pixels, an interval of 0.5 mag for magnitude in the range of [-7, -3) and [2, 4], and an interval of 0.1 mag for magnitude in the range of [-3, 2). The detection probability of each grid is then calculated by the fraction of artificial stars that passed the initial selection and selection threshold among all the artificial stars injected in that grid. For separations where only a fraction of the area of the annuli centred on the primary target is located inside the image, we need to multiply the detection probability of these separations by that fraction. Otherwise, the detection probability at these wide separations would be overestimated because we can only detect companions that are located inside the image.

The observation setup and magnitude of most targets are the same, and therefore

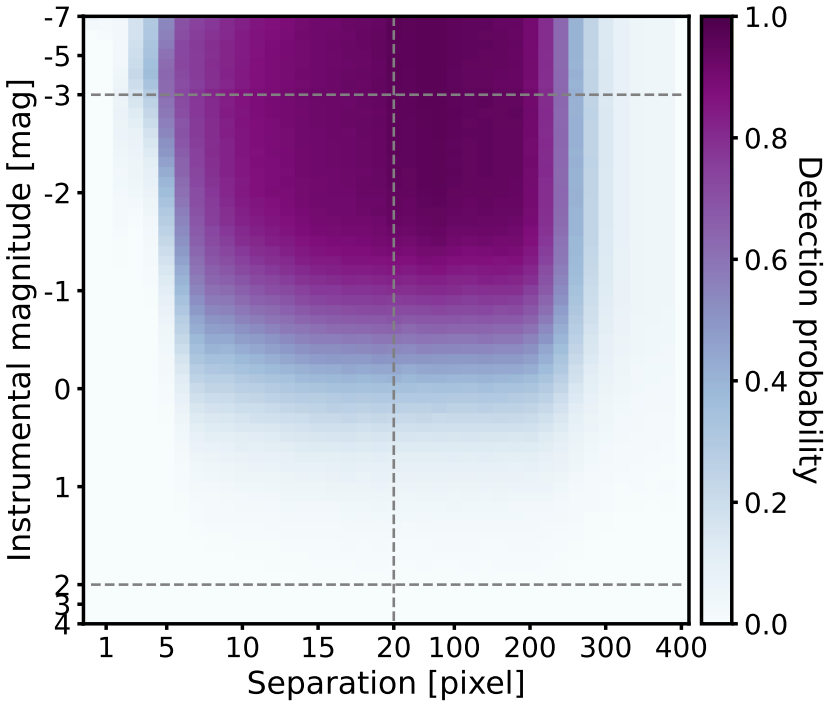


Figure 5.5: Average completeness map of this survey in F127M.

the completeness maps of most targets are similar, though some bright targets have shallower detection at smaller separations. For targets that have multiple observations, we chose the observation that has the best completeness maps. The average completeness map of the 26 targets in this survey is presented in Fig. 5.5. We can detect companions with instrumental magnitudes brighter than ~-1 mag at separations beyond ~5 pixels with a probability higher than 50%. At separations within three pixels, the detection probability is lower than 20%. The decrease in the detection probability at wide separations is due to the fact that only parts of the annuli are covered by our observations there and that the PSF fitting becomes less accurate when only a fraction of the source's PSF lies inside the image.

We used the pixel scale and photometric zero point to convert the completeness map as a function of pixel position and instrumental magnitude to a function of apparent magnitude and separation in au. While dusty models such as AMES-Dusty2000 are suitable for warm brown dwarfs with $T_{\rm eff}$ over ~2000 K, the potential companions probed by this survey are expected to have masses smaller than the masses of the primaries, e.g. <20 $M_{\rm J}$ and even <1 $M_{\rm J}$. For those low-mass objects, ATMO models are more suitable, and they are also one of the few models that provide estimation in the F127M filter. We therefore used

the ATMO evolutionary models of chemical equilibrium (Chabrier et al., 2023) to estimate mass by magnitude in the F127M filter. ATMO models are less accurate for warm brown dwarfs because they miss some opacity in the atmosphere when $T_{\rm eff}$ is higher than 2000 K (Phillips et al., 2020). We compared the mass of the primary target estimated by F127M with ATMO to the mass estimated by bolometric luminosity with AMES-Dusty2000. While ATMO produces smaller mass estimates than AMES-Dusty2000, the differences are within 1σ for most targets except for two targets: J075.58+16.94 (1.1σ) and J0439+2332 (1.4σ). Given that the differences are small, we adopted the primary mass estimated by F127M magnitude with ATMO models in the conversion of the completeness map for consistency. These masses are also presented in Table 5.4.

Because of the young ages of our targets, we reached the regime where some of the companion mass should be smaller than $1\,M_{\rm J}$ with the magnitude contrast we achieved in F127M. Currently, there are no suitable evolutionary models for objects smaller than $1\,M_{\rm J}$ at these ages. Therefore, we applied a cutoff at $1\,M_{\rm J}$ in the completeness map. We show the average completeness maps in different physical units in Fig. 5.6. For companions with masses higher than $1\,M_{\rm J}$ at angular separations between 0.3 and 40 arcsec, corresponding to 40 and 6000 au, our detection probability is higher than 10%. We reached a detection limit of 24 mag and magnitude contrast of 8 mag in F127M at this detection probability level in our surveys. Due to the cutoff at $1\,M_{\rm J}$, the mass ratio limit we achieved is 0.06 at a detection probability of 10%. The actual mass ratio limit we can reach should be smaller than this value.

5.5.4 Binary frequency

With the completeness map, we can estimate the binary frequency of the sample using Bayesian inference. Due to the lack of real companion detections, we could only place an upper limit on the binary frequency. We followed the statistical framework used in Fontanive et al. (2018, 2023) to calculate the binary frequency of this sample. It is common to use mass ratio instead of mass when dealing with the multiplicity of stars and sub-stellar objects, because mass ratio is a normalised parameter inherently related to their formation. Therefore, we use the mass ratio and projected physical separation in our calculation.

The statistical analysis is based on Bayesian inference. Bayesian inference derives the posterior distributions of model parameters given the data. It does not find

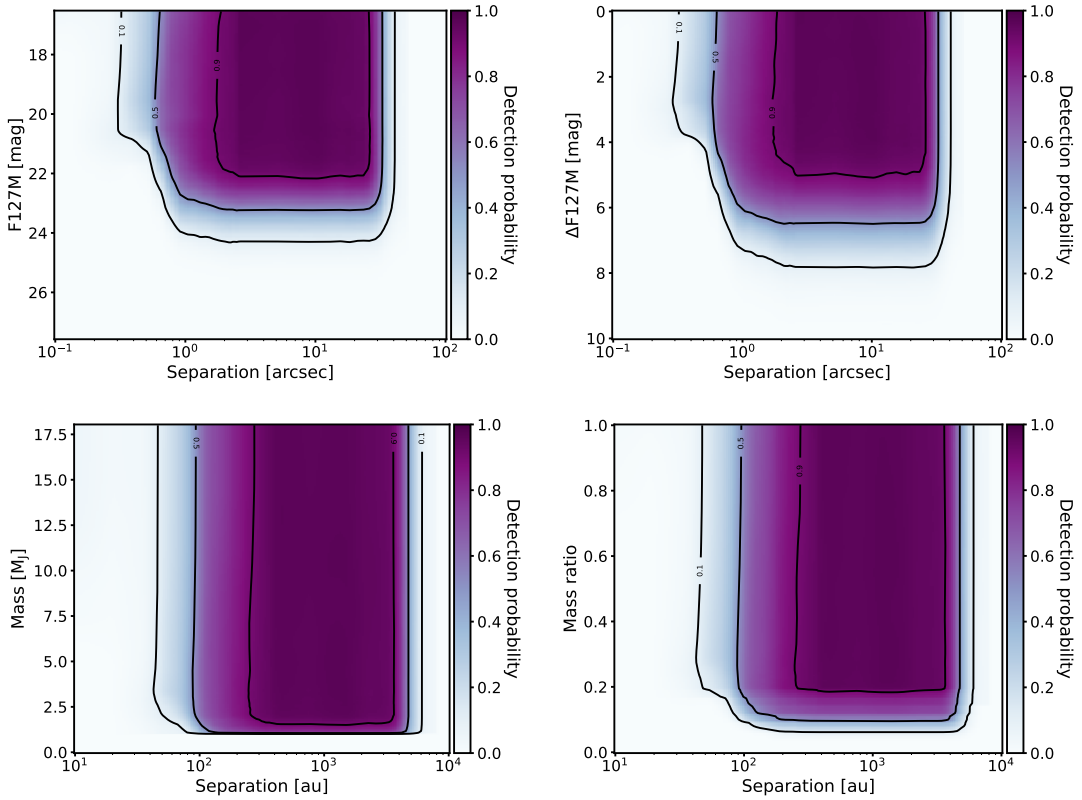


Figure 5.6: Average completeness maps in F127M. The black lines show the 90%, 50%, 10% contours of the detection probability. Top left panel: completeness map in units of apparent magnitude in F127M and angular separation; top right panel: completeness map in units of magnitude contrast and angular separation; lower left panel: completeness map in units of mass and physical projected separation; lower right panel: completeness map in units of mass ratio and physical projected separation.

the true underlying physical model, but derives the possible parameters of an assumed model. In our case, we assume distribution models for companion separation and mass ratio, and generate artificial companions drawn from the models. Then we apply the completeness correction for the number of predicted companions and compare them with the number of detected companions. The challenging part of the statistical analysis of this sample is what distributions we should assume for separation and mass ratio. Our targets are free-floating young planetary-mass objects whose formation mechanisms and multiplicity are not well constrained. Due to the distance of Taurus, we are only sensitive to companions at wide separations. We barely know anything about companions down to 1 $M_{\rm J}$ at wide separations of these objects. In turn, given the lack of detections from this survey, we would not be able to explore the distribution models well due to the lack of data.

The best way of solving this problem is to test prevalence distributions used in multiplicity studies of very-low-mass stars and compare the differences in derived binary frequency distributions between them. Here, we start with flat distributions. Our survey covers a wide range of separations beyond 30 au, so we adopted a loguniform distribution for separations between 30 and 7000 au. In reality, the mass ratio is not an independent parameter of separation and primary mass (Duchêne & Kraus, 2013). It has been found that low-mass objects, such as brown dwarfs, are more likely to have similar-mass companions at small separations (e.g. <10 au Burgasser et al., 2007; Bernat et al., 2010; Offner et al., 2023). But since we are sensitive only to companions beyond 30 au here, we probably probe the long flat tail of the mass ratio distribution. We adopted a uniform distribution for the prior of the mass ratio between 0.1 and 1.

We generate a large number of companions (n) and calculate the predicted number of companions to be detected in our survey (k) by this equation:

$$k = \sum_{i=1}^{n} (p_i) \times f \times \frac{N_*}{n}, \tag{5.3}$$

where p_i is the detection rate of the generated companion which is calculated in the completeness map, f is the binary frequency, and N_* is the sample size. The likelihood function is defined by a Poisson distribution:

$$\mathcal{L}(d \mid k) = \frac{k^d \, e^{-k}}{d!}, \tag{5.4}$$

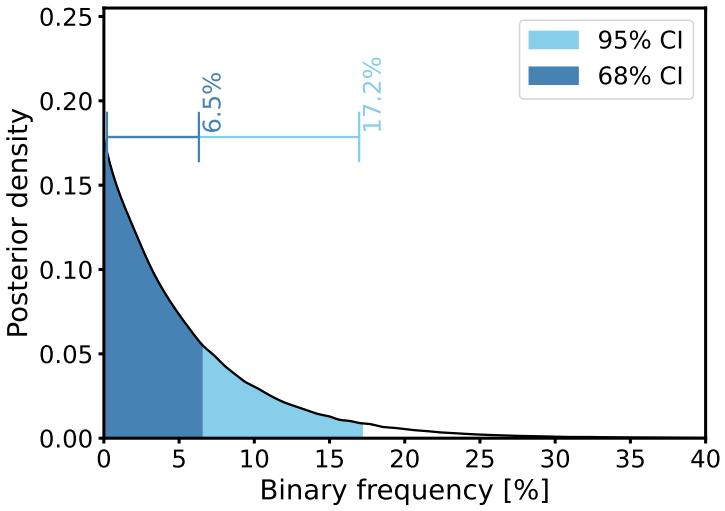


Figure 5.7: Posterior distribution of the binary frequency of the sample with null detection.

where d is the observed number of detections and k is the mean expected number of detections from the previous equation.

We sampled the likelihood function with the Markov Chain Monte Carlo (MCMC) method, using the PYTHON package EMCEE (Foreman-Mackey et al., 2013). We set n = 200,000 and a uniform prior for the binary frequency between 0 and 1. The posterior of the binary frequency is shown in Fig. 5.7. With null detection, the upper limit of the binary frequency is 6.5% in the 68% confidence interval and 17.1% in the 95% confidence interval.

5.6 Discussion

5.6.1 Binary frequency in Taurus and Upper Scorpius

Figure 5.8 presents the binary frequency measured in Taurus as a function of primary mass. The binary frequency reported in Kraus et al. (2011) is the fraction of solar-type stars that have at least one companion beyond 3 au measured with ground-based AO observations. The binary frequency reported in Todorov et al. (2014) and Bouy et al. (2025) is beyond 10 and 7 au surveyed with HST imaging, respectively. While the binary frequency reported in our work is corrected for incompleteness and is calculated for the parameter range of mass ratio in the

range of [0.1, 1] and separation between 30 and 7000 au, the binary frequency from the literature (Kraus et al., 2011; Todorov et al., 2014; Bouy et al., 2025) is not corrected for incompleteness and does not have clearly defined mass ratio and separation range. These binary frequencies are calculated as the number of detections divided by the total number of targets, which could be slightly higher after being corrected for completeness. Nevertheless, the binary frequency in Taurus shows a descent when the primary mass decreases from solar mass to planetary mass ($>5\,M_{\rm J}$), agreeing with the observed trend for field objects (e.g. Offner et al., 2023). As Taurus is a sparse star-forming region of only 1–10 Myr, this suggests that the decreasing binary frequency with primary mass is settled at a very early star-forming stage. The low binary frequency of brown dwarfs and planetary-mass objects is therefore determined by their formation mechanisms.

Both our work and Bouy et al. (2025) measured the binary frequency of young planetary-mass objects of similar mass and spectral types in Taurus with HST/WFC3 for the first time. Bouy et al. (2025) surveyed 33 objects with masses between 5 and 33 $M_{\rm J}$ in UVIS filters of F814W and F850LP. They detected one companion candidate with a mass of 3–6 $M_{\rm J}$ at a separation of 18 au and calculated the binary frequency of $3.8^{+5.2}_{-2.8}$% including this candidate. While there are no overlaps between the two surveys, the binary frequency agrees with each other. The binary frequency of planetary-mass objects is extremely low at wide separations as no companions are detected over 30 au for the total of 59 targets surveyed in the two surveys. This indicates that it is intrinsically rare to form planetary-mass binaries, for instance, the direct molecular collapse or filament or disc fragmentation is not efficient and the binary systems are extremely vulnerable to dynamical disruptions.

Upper Scorpius (Upper Sco) is another star-forming region in the solar neighbourhood with an age of ~11 Myr (Pecaut et al., 2012), and is frequently studied for multiplicity. We present the binary frequency measured for objects with SpT later than M4 in Upper Sco from Kraus et al. (2005); Biller et al. (2011); Todorov et al. (2014); Bouy et al. (2025) in the right panel of Fig. 5.8. Similar to Taurus, Upper Sco also shows a descending trend as the primary mass goes down. There is no significant difference in the binary frequency of brown dwarfs and planetary-mass objects between Taurus and Upper Sco. Taurus is a low-density star-forming region, and therefore, dynamical interactions between objects are not frequent after their formation. Wide-separated low-mass binaries are of low-binding energies and were thought to be likely to be disrupted after 10 Myr (e.g.

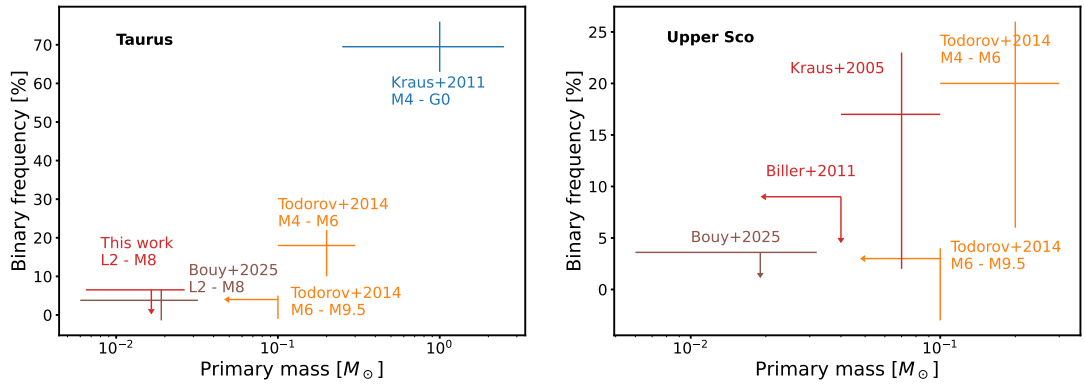


Figure 5.8: Left panel: binary frequency as a function of primary mass in Taurus; right panel: binary frequency as a function of primary mass in Upper Scorpius. The binary frequency from the listed literature is not corrected for incompleteness, and their separation resolution limit is between 3 and 10 au: Kraus et al. (2005, 2011); Todorov et al. (2014); Bouy et al. (2025); Biller et al. (2011).

Todorov et al., 2014). Parker et al. (2025) found that a large fraction of planetary-mass binaries would be destroyed within a few Myrs in dense star-forming regions such as the Orion Nebula Cluster. Since Upper Sco is a denser and older region than Taurus, this suggests that the low binary frequency of these objects might have been settled at an earlier stage, e.g. <1–10 Myr.

5.6.2 Binary frequency as a function of age

According to evolutionary models, the young planetary-mass objects in our survey will cool to objects with SpT of T8 to Y2+ when they are older than 1 Gyr. Comparing the binary frequency of young objects and objects in the field of the same mass can probe the dynamical stability of planetary-mass objects. We present the binary frequency of field objects as a function of primary mass together with the binary frequency measured in this work in Fig. 5.9. We applied the same data reduction and statistical analysis to our sample as Fontanive et al. (2018, 2023) did to a similar sample of field objects. The binary frequency of young planetary-mass objects in Taurus does not exhibit a discernible difference compared to the late-T and Y dwarfs in the field surveyed by them. Biller et al. (2011) also found that the binary fraction of brown dwarfs in Upper Sco is of no significant difference from that of field T dwarfs. Therefore, with the current small sample statistics and large uncertainty of the binary frequency, we cannot draw a conclusive summary of the trend of binary frequency as a function of age,

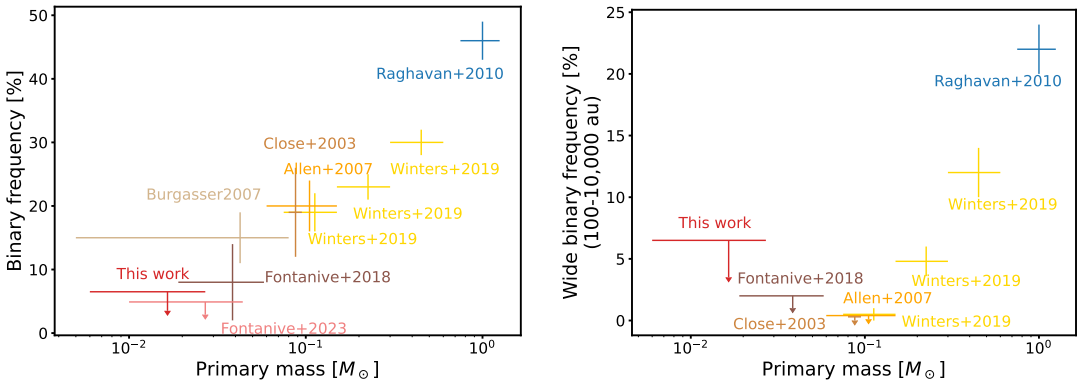


Figure 5.9: Left panel: overall binary frequency as a function of primary mass for field objects; right panel: wide binary frequency as a function of primary mass for field objects. We also include our results for young planetary-mass objects for the purpose of comparing with field planetary-mass objects. The data come from Offner et al. (2023) which are corrected for incompleteness. The original surveys are reported in Close et al. (2003); Allen et al. (2007); Burgasser et al. (2007); Raghavan et al. (2010); Winters et al. (2019); Fontanive et al. (2018, 2023).

although both the field and young planetary-mass objects clearly have low binary frequencies.

Since our survey is sensitive to wide separations, we also compared the wide binary fraction at separations between 100 and 10000 au in the right panel of Fig. 5.9. The fraction also drops with the decrease in the masses of field objects. The same as the overall binary frequency, the difference between young and field brown dwarfs is not evident as only the upper limit of wide binary frequency is constrained. Actually the separation of the majority of the discovered sub-stellar binaries is within 15 au, such as WISE J033605.5-014350.4 (a close Y+Y binary Calissendorff et al., 2023) and WISE J014656.66+423410.0 (a spectroscopic binary at T/Y transition Bardalez Gagliuffi et al., 2025a), indicating that the peak of the separation distribution is at tight separations and it is rare to have wide planetary-mass binaries.

The multiplicity surveys of planetary-mass objects are mainly direct-imaging surveys which are only sensitive to separations larger than ~10 au. Given that planetary-mass binaries are more likely to form at small separations, spectroscopy and interferometry surveys are necessary to probe tight binaries (e.g.<1 au). However, these kinds of surveys are subject to the faintness of these objects. As they are bright in the mid-infrared, JWST and the Extremely Large Telescope

(ELT) instruments such as METIS will be capable of detecting more tight planetary-mass objects by spectroscopy. The demography of planetary-mass binaries, to be completed in the future, will reveal the detailed separation and mass ratio distributions of these binaries, as well as the binary frequency as a function of age, which is crucial for understanding the formation of stars and substellar worlds.

5.7 Conclusion

We conducted an HST/WFC3 direct imaging survey of 26 young brown dwarfs and planetary-mass objects with SpT later than M8 and masses between 7 and 28 $M_{\rm J}$ in the Taurus star-forming region. We performed photometry analysis of the targets in the F850LP, F127M, and F139M filters and estimated their masses using updated membership analysis. We constructed the $Q_{\rm HST}$ value by combining flux measured in the three filters: objects with SpT later than late-M will have $Q_{\rm HST} > 1$, while background stars should have $Q_{\rm HST} < 1$. Together with PSF fitting conducted with KS2, no companion candidate is detected at separations over 30 au. Artificial star injection tests were performed to build the completeness maps of our survey. Using Bayesian statistics, we constrained the upper limit of the binary frequency to 6.5% in a 68% confidence interval after completeness correction for mass ratio between 0.1 and 1 and separation between 30 and 7000 au. We confirm that binary frequency decreases smoothly from solar-type stars to the planetary-mass regime in Taurus. Similar to planetary-mass objects in the field, it is rare to find these low-mass binaries at wide separations. No significant difference in binary frequency is detected between planetary-mass objects in Taurus and the field. A larger sample combined with future surveys of different star-forming regions will tell if the binary frequency varies with ages and stellar density, which is essential for understanding their formation.

Table 5.4: Photometry and mass of the targets.

Name	J_{2MASS} (mag)	H_{2MASS} (mag)	K_{2MASS} (mag)	J_{MKO} (mag)	A_V (mag)	Lbol (dex)	Teff (K)	Mass[a] (M_J) (Dusty)	Mass[b] (M_J) (ATMO)
J0435+2307	—	—	—	17.27±0.04	2.33	-3.04±0.13	2121^{+88}_{-118}	$9.67^{+2.72}_{-2.54}$	7.46
J0401+2557	16.81±0.17	15.73±0.14	15.36±0.17	—	0.00	-3.17±0.16	1985^{+112}_{-169}	$6.89^{+1.84}_{-1.76}$	5.92
J0424+2641	—	—	—	17.34±0.09	3.04	-3.18±0.13	2077^{+103}_{-139}	$12.41^{+2.54}_{-3.68}$	11.03
J0422+2655	—	—	—	17.94±0.11	5.21	-3.06±0.15	2159^{+114}_{-182}	$13.57^{+2.93}_{-4.30}$	11.73
J0422+1947	16.63±0.13	15.88±0.17	15.12±0.16	16.44±0.03	0.95	-3.12±0.13	2128^{+103}_{-149}	$13.15^{+2.60}_{-3.92}$	13.07
J0435+2253	—	—	—	17.45±0.07	4.25	-2.97±0.12	2168^{+88}_{-104}	$10.61^{+2.90}_{-2.71}$	9.38
J0508+2422	16.93±0.14	16.47±0.24	15.82±0.22	16.99±0.03	0.75	-3.09±0.12	2180^{+88}_{-138}	$15.22^{+1.48}_{-2.02}$	13.65
J064.68+27.97	16.69±0.12	15.85±0.12	15.25±0.12	16.64±0.03	1.08	-3.18±0.11	2091^{+91}_{-121}	$12.70^{+2.17}_{-3.11}$	11.67
J065.17+28.17	16.77±0.12	15.98±0.15	15.23±0.11	16.67±0.02	0.79	-3.25±0.11	2037^{+93}_{-120}	$11.91^{+2.20}_{-2.88}$	10.78
J0431+2322	16.62±0.16	15.78±0.18	14.71±0.11	16.97±0.06	0.13	-3.08±0.13	2091^{+90}_{-136}	$9.16^{+2.64}_{-2.45}$	6.86
J0433+1758	—	—	—	17.59±0.07	0.84	-3.48±0.10	1876^{+84}_{-112}	$10.64^{+1.60}_{-1.91}$	9.03
J061.87+23.11	16.41±0.12	15.70±0.15	15.19±0.13	—	1.68	-2.90±0.17	2252^{+134}_{-222}	$15.24^{+3.32}_{-5.21}$	14.17
J0409+2000	15.57±0.06	14.93±0.07	14.38±0.05	—	0.21	-2.77±0.16	2359^{+139}_{-182}	$17.58^{+3.29}_{-5.27}$	17.06
J075.58+16.94	16.14±0.08	15.37±0.08	14.74±0.09	—	0.00	-3.01±0.16	2359^{+161}_{-186}	$25.20^{+9.79}_{-8.01}$	16.38
J059.57+30.63	16.02±0.08	15.37±0.09	14.72±0.09	—	0.00	-2.95±0.16	2417^{+158}_{-216}	$27.61^{+10.50}_{-9.47}$	19.54
J0427+2738	16.10±0.09	15.44±0.11	14.64±0.09	—	1.03	-2.87±0.13	2294^{+106}_{-136}	$16.23^{+2.66}_{-4.47}$	15.11
J0432+1815	—	16.02±0.24	15.02±0.12	17.02±0.06	3.91	-2.91±0.14	2268^{+106}_{-141}	$15.68^{+2.70}_{-4.49}$	15.10
J0433+2251	—	—	—	17.71±0.11	2.08	-3.32±0.12	1917^{+89}_{-129}	$6.99^{+1.91}_{-1.80}$	5.50
J0452+3037	—	—	13.84±0.04	17.08±0.05	0.88	-3.19±0.10	2054^{+76}_{-101}	$10.21^{+1.83}_{-1.89}$	8.94
J0421+2706	—	16.12±0.15	15.32±0.14	17.15±0.06	2.67	-3.25±0.09	2043^{+74}_{-94}	$12.02^{+1.99}_{-2.74}$	11.21
J0421+2754	16.73±0.12	15.40±0.08	14.84±0.09	16.57±0.03	2.16	-3.06±0.11	2166^{+78}_{-106}	$12.63^{+2.04}_{-2.20}$	11.18
J0422+1523	—	—	—	18.05±0.08	3.26	-3.39±0.14	1913^{+111}_{-168}	$10.22^{+2.53}_{-3.24}$	9.13
J0439+2332	16.94±0.15	16.30±0.20	15.62±0.19	17.15±0.05	0.00	-3.44±0.10	1855^{+80}_{-102}	$7.84^{+1.05}_{-1.07}$	6.31
J0422+1536	—	—	—	15.69±0.01	0.71	-2.79±0.12	2361^{+101}_{-125}	$17.70^{+2.45}_{-4.38}$	16.24
J065.88+19.83	13.78±0.02	13.03±0.03	12.59±0.03	—	0.00	-2.03±0.16	2730^{+63}_{-133}	$34.46^{+7.47}_{-10.30}$ [c]	29.11
J0449+2911	—	—	—	14.87±0.01	0.00	-2.54±0.12	2555^{+95}_{-120}	$23.07^{+5.64}_{-4.29}$	20.82

Notes: 2MASS photometric magnitudes were queried from Simbad. J_{MKO} were measured in the W-band survey and queries from UKIDSS. a).this mass is estimated with bolometric luminosity and dusty models; b).this mass is estimated with magnitude in F127M and ATMO models; c).the mass is overestimated because there are no reliable models for objects younger than 1 Myr.

Chapter 6

Conclusions

6.1 Summary

This thesis has explored the detection and characterisation of brown dwarfs and planetary-mass objects with direct imaging. It focuses on the population investigation and statistical analysis. It includes results from four surveys: a variability survey of young planetary-mass objects, a direct imaging survey searching for wide-orbit exoplanets in the Fornax-Horologium association, a planetary-mass candidate discovered from the Young Suns Exoplanet Survey, and a photometric and multiplicity survey of young brown dwarfs and planetary-mass objects in the Taurus star-forming region. It has advanced our understanding of the atmospheric structures of young planetary-mass objects and contributed to the constraints on formation models of wide-orbit substellar companions and planetary-mass binaries, particularly in relation to the stellar environments.

6.1.1 Chapter 2

In Chapter 2, I present a near-infrared variability survey of young planetary-mass objects. I conducted photometric variability monitoring of 18 planetary-mass objects with spectral types between L5 and T8 belonging to nearby young moving groups, using the near-infrared imager SOFI on NTT. The four new variables detected are 2M1119-1137AB (L7), W1147-2040 (L7), J0819-0335 (T4), and J2323-0152 (T6), all presenting peak-to-peak variability amplitude over 1.5%.

The rotation periods detected from the variability of the four new variables are longer than field brown dwarfs, agreeing with the expected conservation of momentum, as objects age, contract and spin up. This is the first near-infrared variability survey of young T dwarfs. I combined this survey with previous variability survey of young L dwarfs (Vos et al., 2019), field brown dwarfs (Radigan et al., 2014), and L/T transition dwarfs (Eriksson et al., 2019). This results in the largest sample of brown dwarf variability in the near-infrared. Using a statistical framework based on Bayesian analysis, I find that young planetary-mass objects tend to be more variable than field brown dwarfs across the entire L and T spectral types within peak-to-peak variability amplitude ranges of 0.5–10% and period ranges of 1.5–20 hr. For the first time, I constrain the variability rate of young T dwarfs to be 56^{+20}_{-18}% compared to 25^{+8}_{-7}% of field T dwarfs. Regardless of surface gravity, both young and field brown dwarfs are more likely to present strong variability at the L/T transition with a higher variability rate and amplitude.

This work expands the critical role of surface gravity on atmospheric structures from L dwarfs to T dwarfs. Lower surface gravity on young brown dwarfs leads to more complicated atmospheric structures, resulting in a higher variability rate compared to field brown dwarfs. As directly imaged exoplanets are similar to these young free-floating planetary-mass objects, we can infer that they are likely to have similar atmospheric structures and thus present variability. This work can serve as a guideline to select imaged exoplanets for variability observations: younger objects with a SpT at or close to the L/T transition are the most likely to present strong variability. The two variable young T dwarfs detected in this survey verify that mid-late T dwarfs can have inhomogeneous atmospheric structures, possibly due to sulfide clouds or chemical instability. Moreover, with a census of all the known variable brown dwarfs, several low surface gravity young objects present extremely strong variability between L6 and L7.5, raising questions about the sources of this variability.

6.1.2 Chapter 3

Chapter 3 is a direct imaging survey of wide-orbit planets in a nearby young association Fornax-Horologium. I present the first results of this survey, focusing on the detection of a companion at the hydrogen-burning limit orbiting HD 24121 at a separation of 206 au, HD 24121B. I estimated a photometric mass of 74.9 ±

7.5 M_J for it. With the unique age of 30–40 Myr of this association, this companion can serve as a benchmark object at the hydrogen-burning limit for evolutionary models. The high eccentricity derived from orbit fitting for this companion suggests dynamic scattering during its formation. I report another low-mass stellar companion at an eccentric orbit, together with four other planetary-mass companion candidates.

This is an ongoing survey. The high eccentricity of the two confirmed companions is a sign of frequent dynamic scattering in this association in the past. With a dissolving open cluster in the centre at the moment, Fornax-Horologium association was a more compact stellar region when the stars were formed. The two massive wide-orbit companions are likely formed by gravitational collapse or disc fragmentation, followed by gravitational interactions between another fragment or stars. The statistical analysis of the wide-orbit planet occurrence rate will be conducted once the survey is completed.

6.1.3 Chapter 4

In Chapter 4, I present a planetary-mass candidate at a separation of 730 au imaged in the Young Suns Exoplanet Survey. Though the central star was resolved to be a binary of a sun-like star and an M-dwarf, I found tensions in explaining the central system as a binary system and inferred that there must be at least another hidden companion. Due to the unknown barycentre of the system, it is impossible to confirm the candidate as a comoving planet of the central stars by common proper motion analysis, though it shows a comparable proper motion to the primary star. The faintness of the candidate resulted in detection only in the H band with a magnitude of 22.04 ± 0.13 mag, making it challenging to confirm it as a planetary-mass object by colour as well. I estimated the probability ratio of the candidate being a background star and a bound companion as a function of the mass ratio of the central two stars.

This work reveals the challenges of confirming extremely faint candidate companions at large separations, especially when the central star is not a single star. With two wide-orbit planets over 100 au have already been detected in YSES (YSES 1bc, Bohn et al., 2020b,c), if this candidate is confirmed to be a planet of the central stellar system, it would be a third wide-orbit planet discovered in YSES. Together with HD 106906b (Bailey et al., 2014), HIP 65426b, b Centaurib, 1RXS 1609b (Lafrenière et al., 2008), and GSC 6214-210b (Ireland et al., 2011),

Sco-Cen has a remarkably larger number of imaged planets over 100 au, suggesting a possible link between stellar regions and wide-orbit planet formation. Though these wide-orbit planets are likely to be formed by disc fragmentation, it is still difficult to form this candidate, which is of 3–5 $M_{\rm J}$ at a separation over 700 au, challenging current planet formation mechanisms. Formation by capture is a likely scenario for planets found over 500 au from their host stars (Daffern-Powell et al., 2022).

6.1.4 Chapter 5

Chapter 5 reports the preliminary results of a photometry and multiplicity survey of young brown dwarfs and planetary-mass objects in Taurus. This survey contains 26 free-floating young planetary-mass objects with SpT later than M8 observed in F850LP, F127M, and F139M filters by HST/WFC3. The companion search was conducted by Q_{HST} value, which was calculated by the combination of flux in the three filters with $Q_{HST} < 1$ for background stars and $Q_{HST} > 1$ for objects with SpT later than late-M, and PSF fitting based on KS2. No companion candidate is detected at separations over 30 au. I updated the sub-membership of the targets in Taurus and estimated the primary masses with the updated ages. I performed artificial star injection to derive the completeness maps of this survey and demonstrated that we can detect companions as low as 1 $M_{\rm J}$. After correcting the incompleteness of this survey with a Bayesian framework, I constrain the upper limit of the binary frequency to 6.5% in the 1σ confidence interval for mass ratio between 0.1 and 1 and separation between 30 and 7000 au.

This binary frequency is of no significant difference compared to field T dwarfs of similar masses by Fontanive et al. (2019, 2023). As Taurus is a sparse star-forming region, this low binary rate of wide separations is likely primordial and suggests this is the natural result of binary formation at low masses or the disruption of wide-separated planetary-mass binaries occurs at a very early stage. It also indicates that young planetary-mass binaries should have separations peaking at small separations, following the trend found for low-mass stars and brown dwarfs. This is one of the pioneer works to explore the separation and mass ratio distributions of young planetary-mass binaries, which will constrain binary formation models, which remain largely unexplored for planetary-mass binaries.

6.2 Outlook

6.2.1 Atmospheric structures

The current variability rate statistical analysis in Chapter 2 only divides and compares the sample to field and young objects, which is based on the conventional criterion that objects older than 1 Gyr are field objects with high surface gravity. The reason why I did not divide them into small sample bins by age is that the limited sample size would result in large uncertainty, which would make the comparison neither meaningful nor informative. With more young planetary-mass objects detected in the future, it will be possible to analyse the variability rate as a function of age in small intervals, which will benefit the detailed analysis of how surface gravity impacts the atmospheric structures.

JWST opens a new era for characterising the atmospheres of planetary-mass objects. It enables multi-wavelength variability monitoring across 1 μm to 14 μm. The current spectroscopic variability data of several planetary-mass objects present complicated patterns that are beyond simulation models. Observations are now leading simulations in this area. As it probes both horizontal and vertical structures, 3D models such as general circulation models (GCMs) are necessary to simulate the atmosphere (e.g. Tan & Showman, 2019, 2021). Moreover, JWST/NIRcam can obtain dual-band coronagraph imaging with very high sensitivity, e.g.<1% variability. It will probe the atmospheric structures of several directly imaged exoplanets, for instance, 2M1207b (Programme ID: GO 3181), β Pic b (Programme ID: GO 4758), and HR 8799 bcde (Programme ID: GO 6139), making it possible to compare their variability with free-floating planetary-mass objects in the near future. While it is extremely difficult to detect the variability of ultracool and faint objects from the ground, such as Y dwarfs, JWST can also probe the clouds and other heterogeneous atmospheric structures on them.

Variability monitoring is an indirect way to resolve the surface of brown dwarfs. Assuming a radius of 1 $R_{\rm J}$ for brown dwarfs, to resolve the surface of the nearest brown dwarfs, WISE1049AB, which are at a distance of about 2 pc, we need to reach an angular resolution power of 0.4 mas. Very Large Telescope Interferometer (VLTI) has a resolution power of ~1.6 mas at 2 μm, according to interferometry resolution equation $\theta \approx \frac{\lambda}{2B}$, where B is the maximum baseline length. Therefore, it is well below the current resolution limit. Future 30–40 metre telescopes such

as the Extremely Large Telescope (ELT) will not be able to resolve it either. However, heterodyne interferometry between VLT and ELT with a baseline longer than 1000 metres can resolve the surface of WISE1049AB at 4 μm in the far future. The heterodyne interferometry technology in the mid-infrared is currently being developed in the laboratory (Bourdarot, 2022).

6.2.2 The relation between stellar environment and giant planet formation

Chapter 3 is a dedicated survey of all stars in the Fornax-Horologium association (FH) that are suitable for observations with SPHERE. While this is still an ongoing survey, its aim is to derive wide-orbit planet occurrence rates for FH once the survey is completed. As there are large archival high contrast imaging data of nearby young moving groups and associations from other surveys, such as SHINE and GPIES, it is possible to calculate the planet occurrence rate of different stellar regions such as β Pictoris moving group and Sco-Cen, and then investigate the correlation between stellar environment and giant planet occurrence rate, such as the impacts of the stellar density and age on planet formation. With a dissolving open cluster at the centre, FH was a more compact stellar region when stars and planets were formed, though the density was still low compared to regions such as ONC. Nevertheless, studying the planet occurrence rate as a function of stellar density, especially for wide-orbit planets, is crucial to understanding if a high stellar density environment favours more wide-orbit planets and the resulting eccentricity and separation distribution. N-body simulations have found that planet orbits can be altered and planets can be ejected, exchanged and captured due to dynamical interactions in a cluster (Parker & Quanz, 2012; Daffern-Powell et al., 2022). High stellar density promotes the formation of free-floating planets due to the ejection of planets (Daffern-Powell et al., 2022), while it can also trigger more gravitational instabilities during planet formation. The outcome is a battle between them and other factors, including the initial state of spatial and kinematic substructure in a star-forming region (Daffern-Powell et al., 2022). Statistical results of various stellar regions will put constraints on this question.

While there are no companions detected around planetary-mass objects in Taurus over 30 au in Chapter 5, we are applying a double PSF fitting technique to detect companion candidates at closer separations, which can probe companions at separations even below the diffraction limit of HST/WFC3 (De Furio et al., 2022).

This would present parameter ranges more similar to those of the field planetary-mass objects studied by Fontanive et al. (2018, 2021). There is also a similar multiplicity survey of another young star-forming region, Ophiuchus (Fontanive et al., 2020). Combining these surveys with archival multiplicity surveys, we can compare the binary rate of planetary-mass objects in Taurus, Upper-Sco, Ophiuchus, and the field, investigating any differences in binary rates between different environments.

6.2.3 Sub-Jupiter planets, small separations, and cold systems

Direct imaging of exoplanets is a promising and rapidly developing field. With current and future instruments, smaller planets such as sub-Jupiter planets and jovian planets at small separations (e.g.<10 au) or old systems are being imaged. Though JWST/NIRCam coronagraph has a large inner working angle (~0.6 mas at 4μm), it has demonstrated that JWST can image planets even within the inner working angle (Franson et al., 2024). The unparalleled sensitivity of NIRCam at 4–5 μm makes it possible to image cold planets, such as 14 Her c imaged around a 4.6 Gyr old solar-mass star (Bardalez Gagliuffi et al., 2025b). More sub-Jupiter planets or even Saturn-mass planets are likely to be detected by NIRCam.

Gaia DR4 is scheduled to be released after the middle of 2026, publishing epoch astrometry and a catalogue of planets detected by astrometry. It covers 5.5 years of astrometric monitoring. Therefore, it is most sensitive to planets with orbits that are smaller or similar to this length. As demonstrated in Fig. 6.1, Gaia DR4 can detect planets with masses down to 1 $M_{\rm J}$ and orbital periods between ~100 days and ~3000 days. Figure 6.2 presents companion's minimum mass ratio to the host star that can be detected by Gaia DR4 at a distance of 100 pc similar to Sco-Cen and at a distance of 20 pc similar to β Pictoris moving group. While this parameter range is where radial velocity is sensitive, it would observe only <50% of these planets, as the technique is subject to the planets' orbital inclinations and the ages of the host stars. The planets with long orbital periods can be probed by direct imaging and also interferometry with VLTI/GRAVITY, which can obtain their spectra and thus characterise their atmospheres. Moreover, some of these planets at separations ≥~1 au, can be imaged by future instruments such as the Mid-infrared ELT Imager and Spectrograph (METIS) on ELT (Brandl et al., 2021).

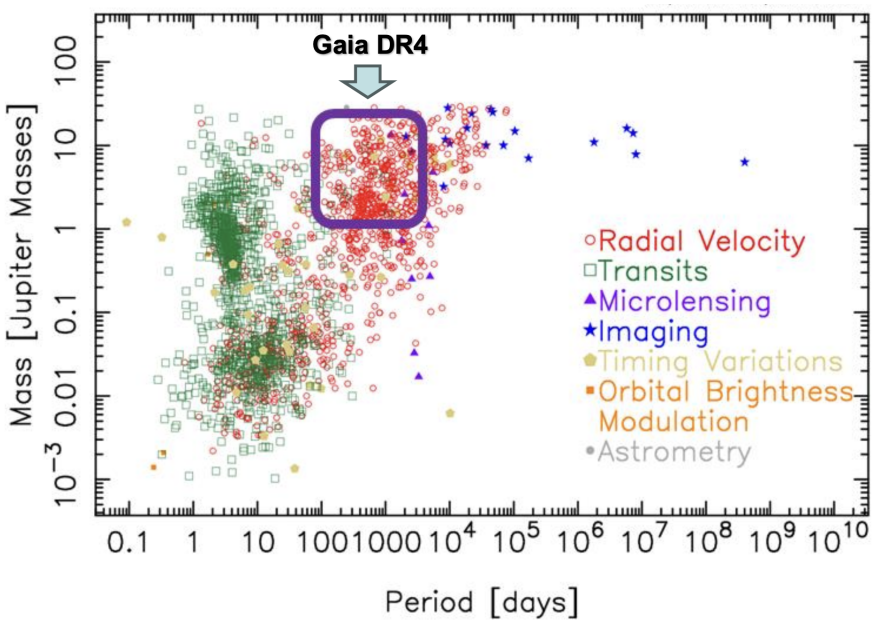


Figure 6.1: Mass versus period of discovered planets by 10 Jan 2024. The purple square shows the region where Gaia DR4 is sensitive to. Gaia DR4 can detect planets down to 1 M_J with periods between ~100 days and ~3000 days. Figure credit: A. Sozzetti at ExoPAG 31.

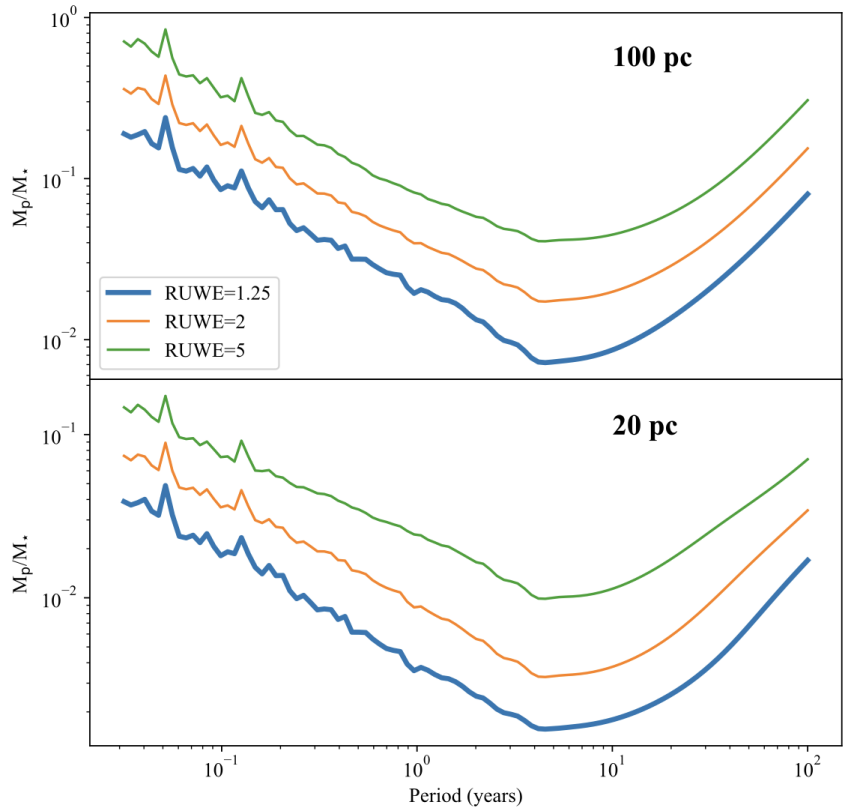


Figure 6.2: Minimum mass ratio versus period of companions that can be detected by Gaia DR4 at a distance of 100 pc (top) and 20 pc (bottom). The figure comes from Wallace et al. (2025).

As scheduled to be launched by 2027, the Nancy Grace Roman Space Telescope Coronagraph Instrument will perform the first test to image exoplanets in reflected light. It is designed to achieve a contrast of 10^{-7} and even lower in visible light (Bailey et al., 2023). In 100 hr integration time, it is possible to detect Jupiter-like planets at 10 pc in cold and old systems (Bailey et al., 2023). Roman will demonstrate the techniques required to image planets in visible light, paving the way for the Habitable Worlds Observatory (HWO). In the far future, HWO will search for Earth twins around nearby stars, requiring a detection limit of 10^{-10}. Ultimately, we will detect bio-signatures in exoplanets, answering the question 'Are we alone in the universe?'.

Appendix A

Appendix of Chapter 2

A.1 Reference stars and MAD-magnitude plots

We show the target and selected reference stars of all observations, including the MAD and instrumental magnitude relationship plots. If not specified, observations are in the J_S band.

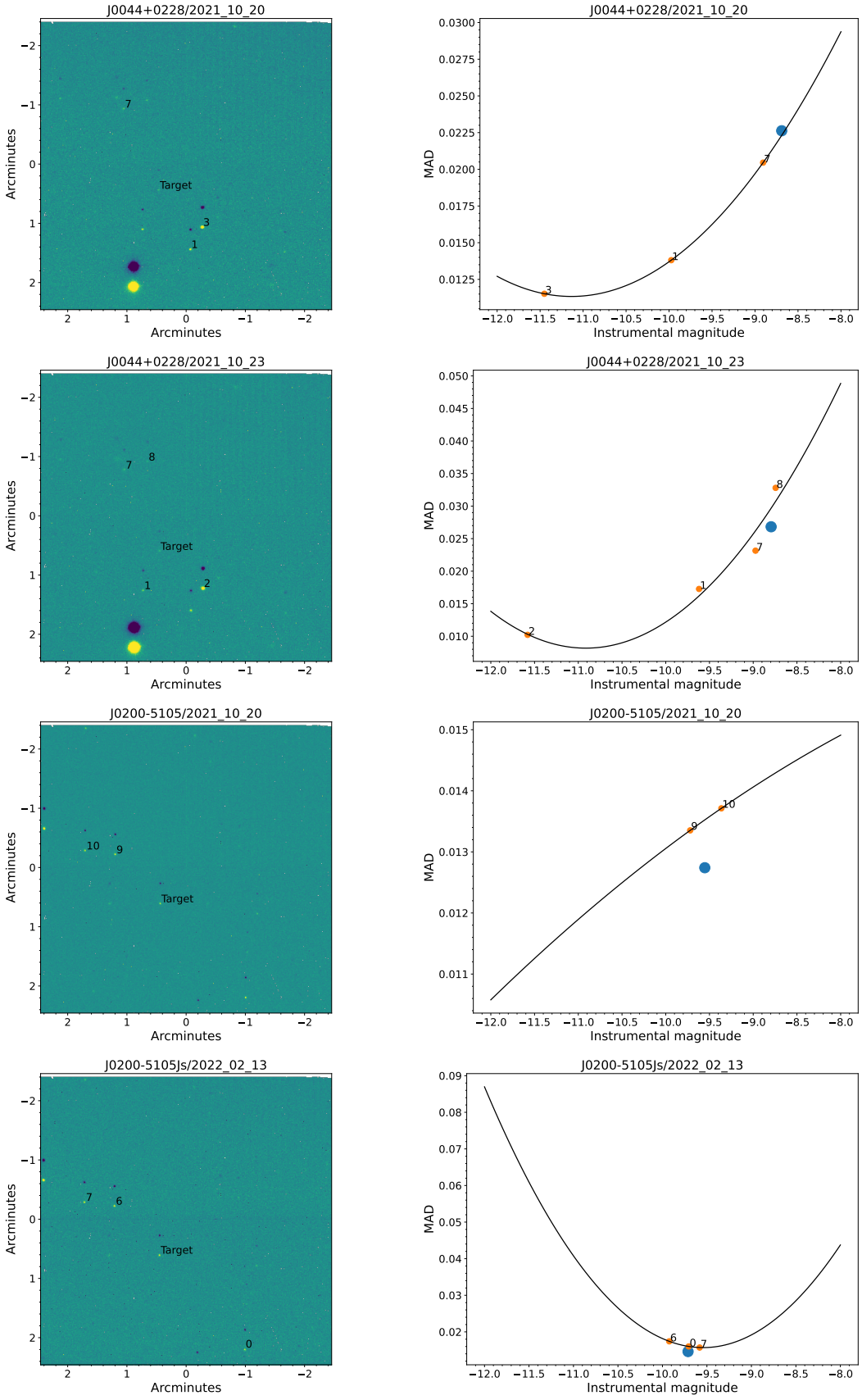


Figure A.1: Targets and their selected reference stars. North is left and east is down.

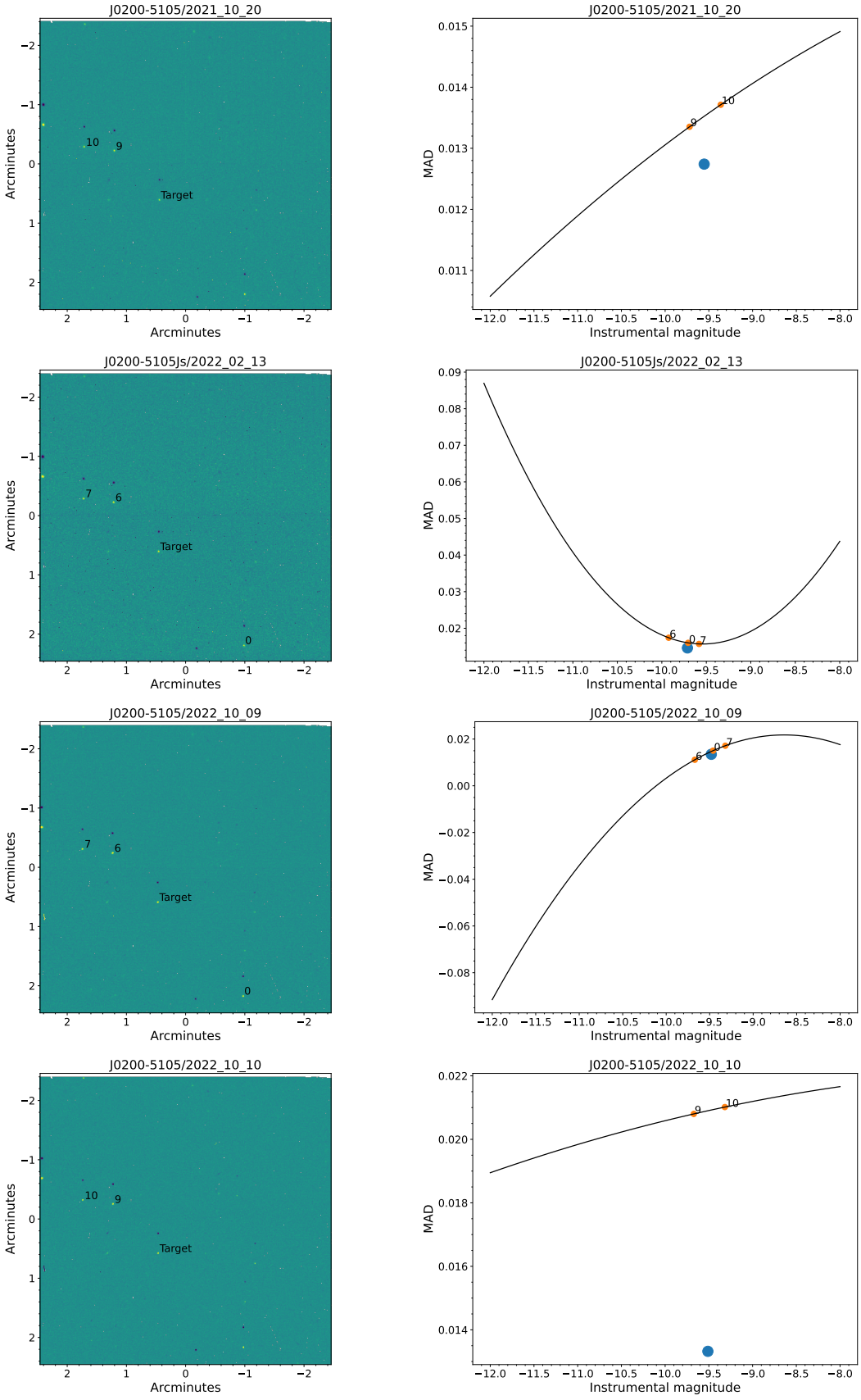


Figure A.1: (Continued.)

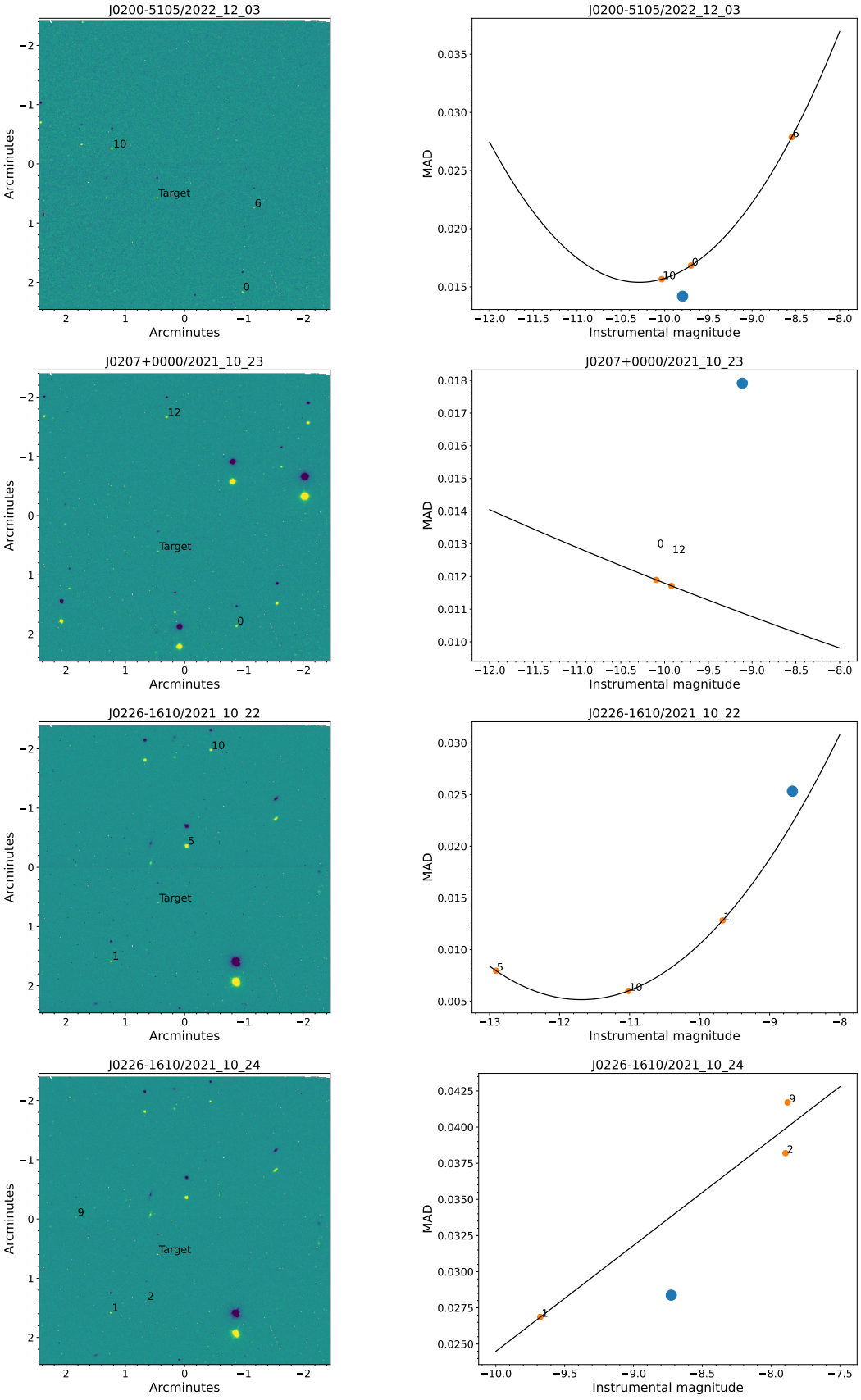


Figure A.1: (Continued.)

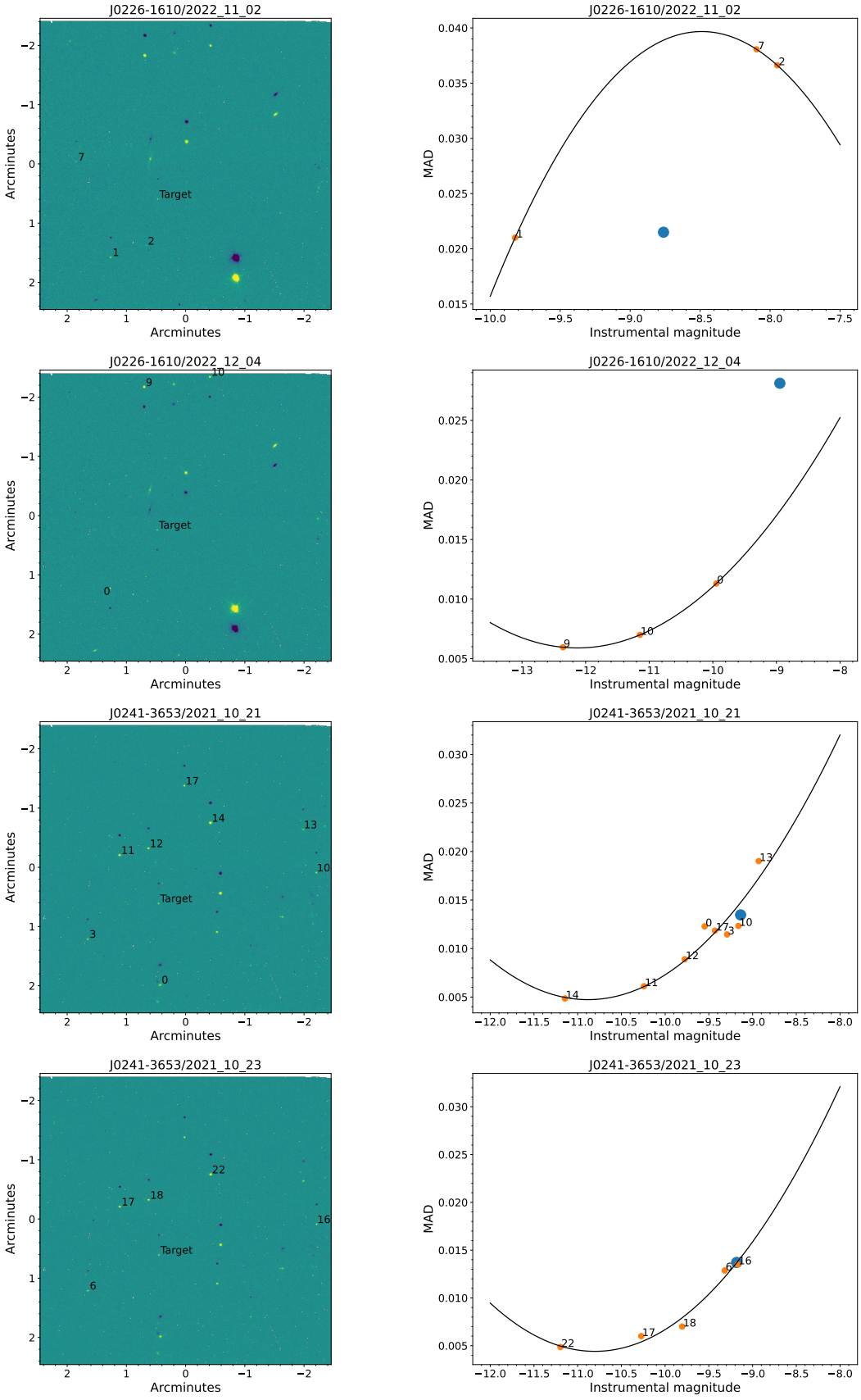


Figure A.1: (Continued.)

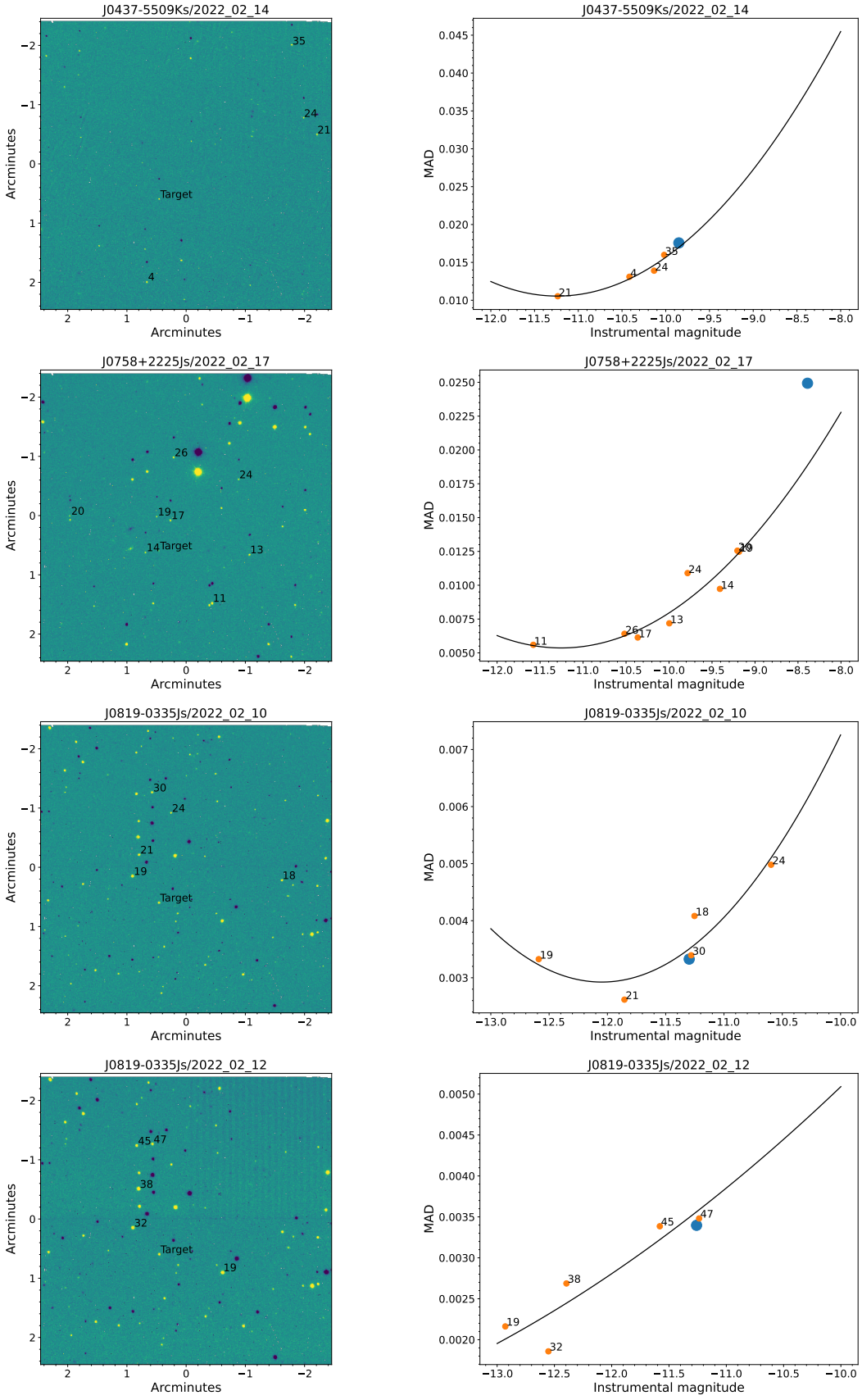


Figure A.1: (Continued.)

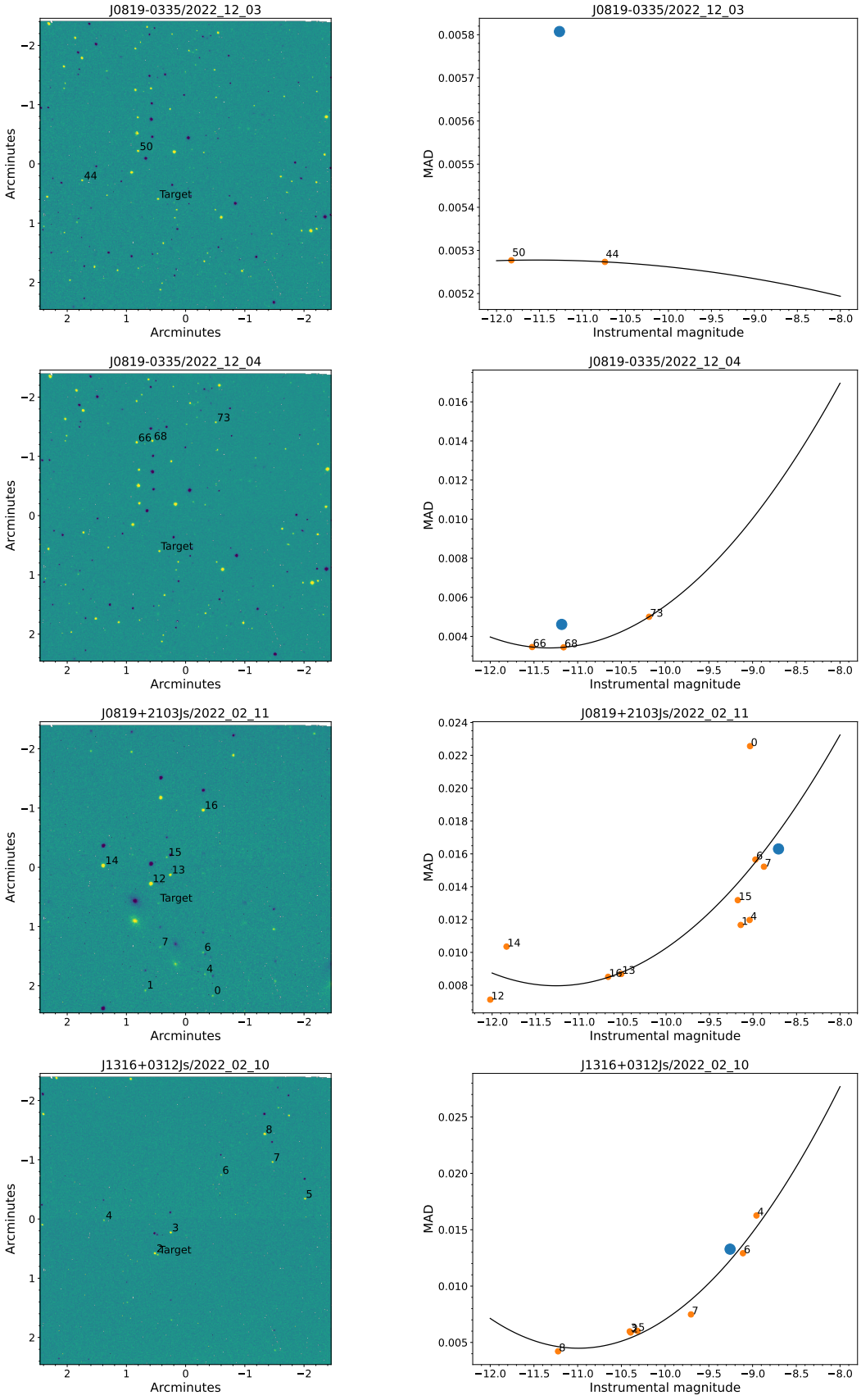


Figure A.1: (Continued.)

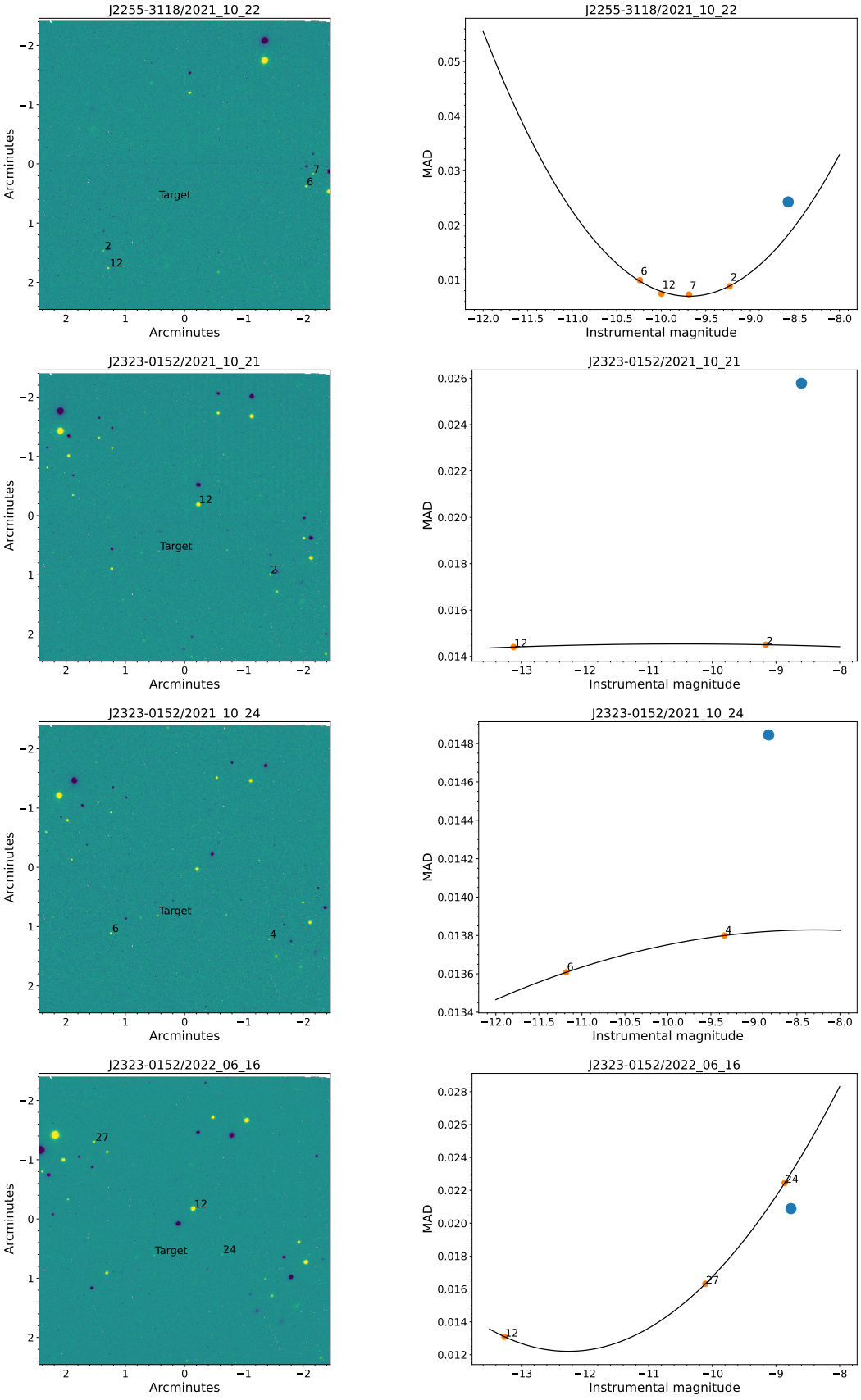


Figure A.1: (Continued.)

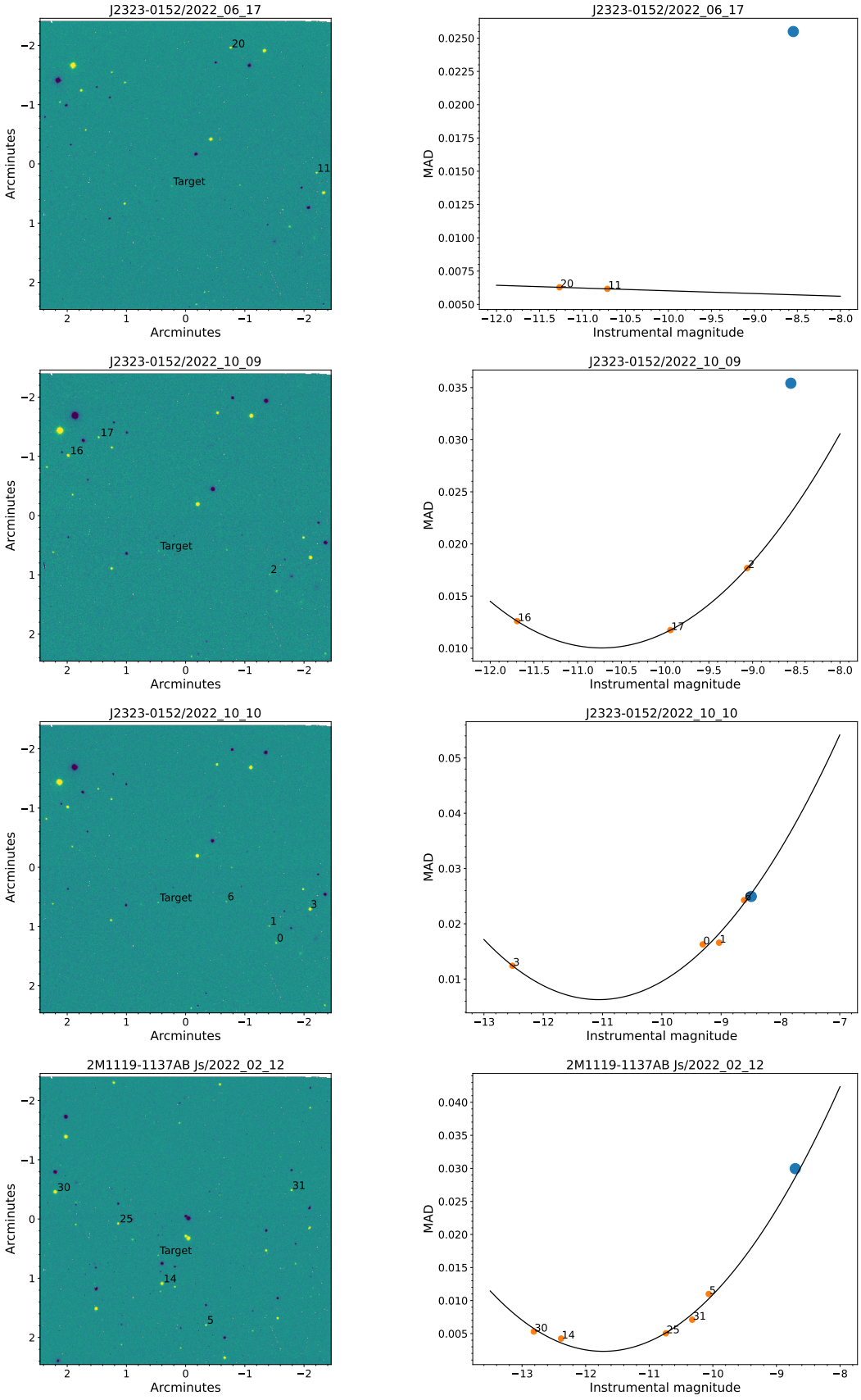


Figure A.1: (Continued.)

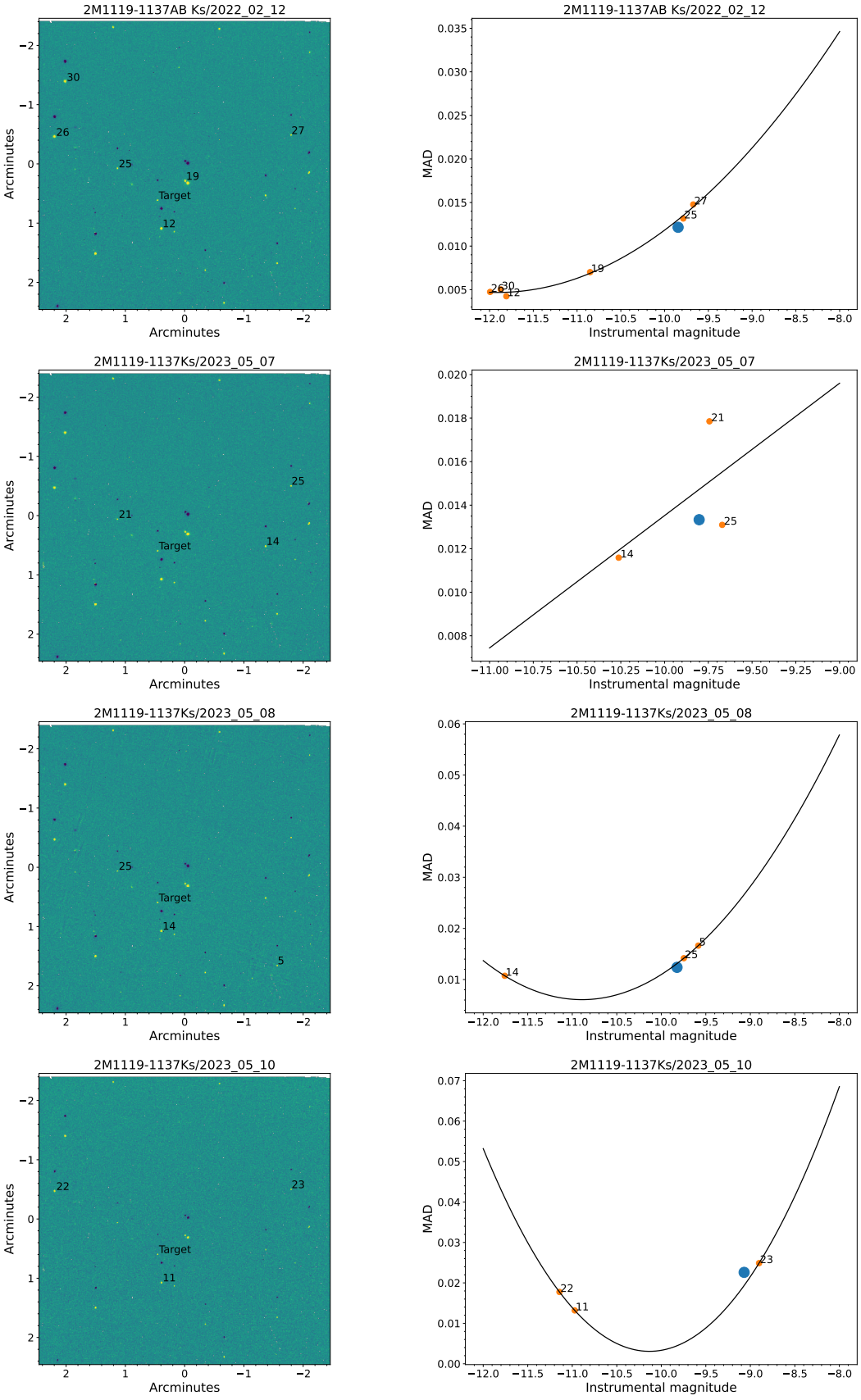


Figure A.1: (Continued.)

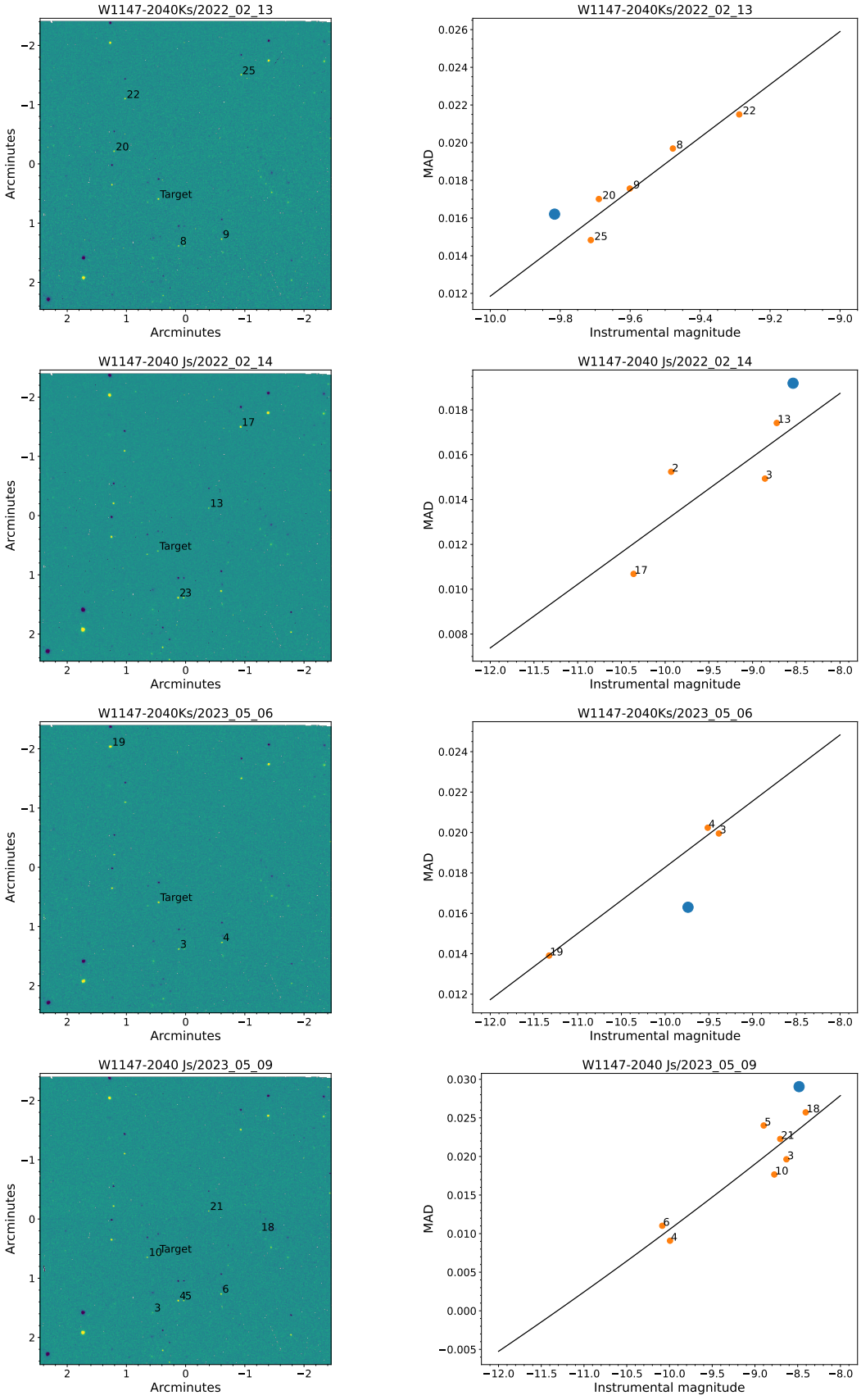


Figure A.1: (Continued.)

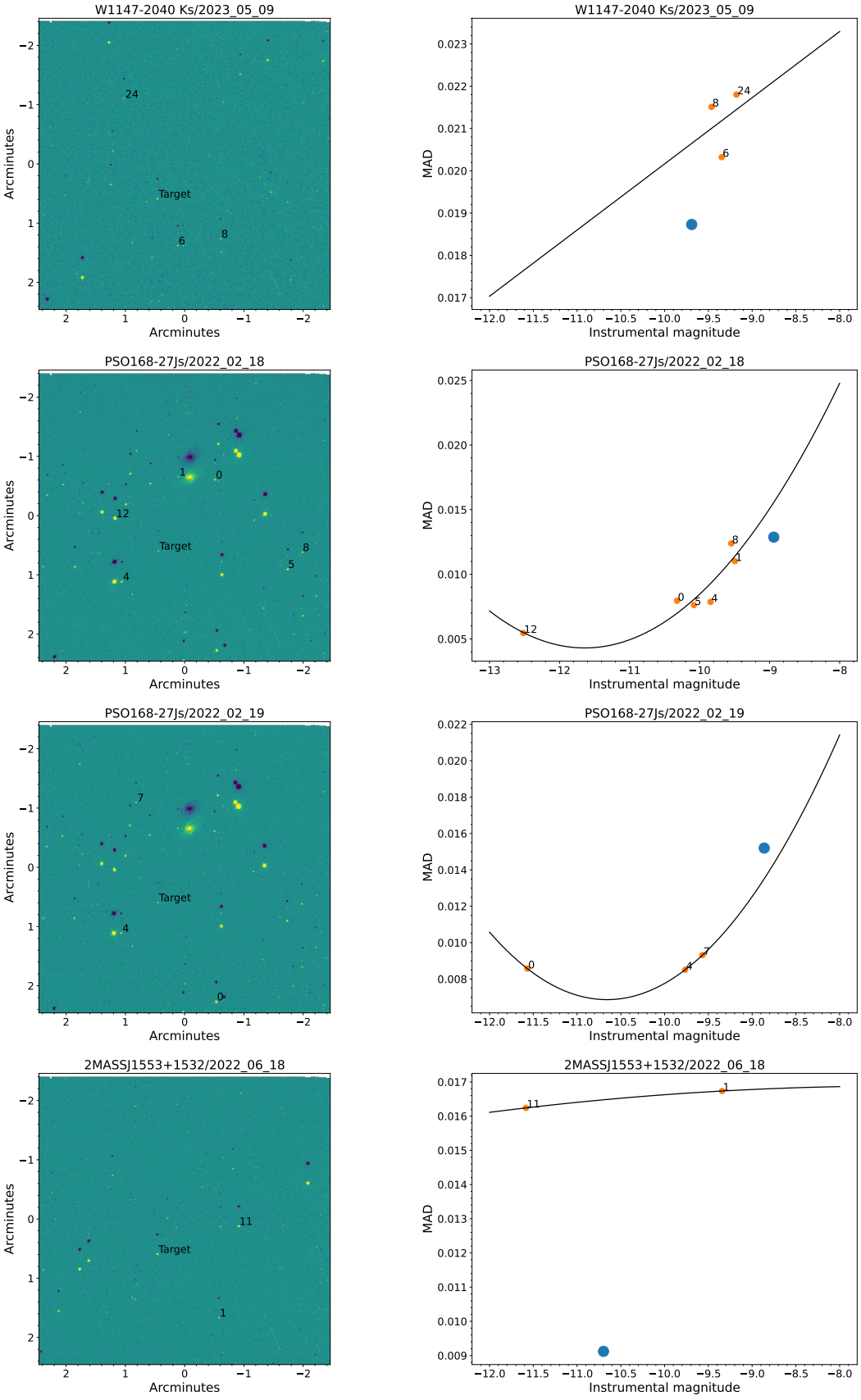


Figure A.1: (Continued.)

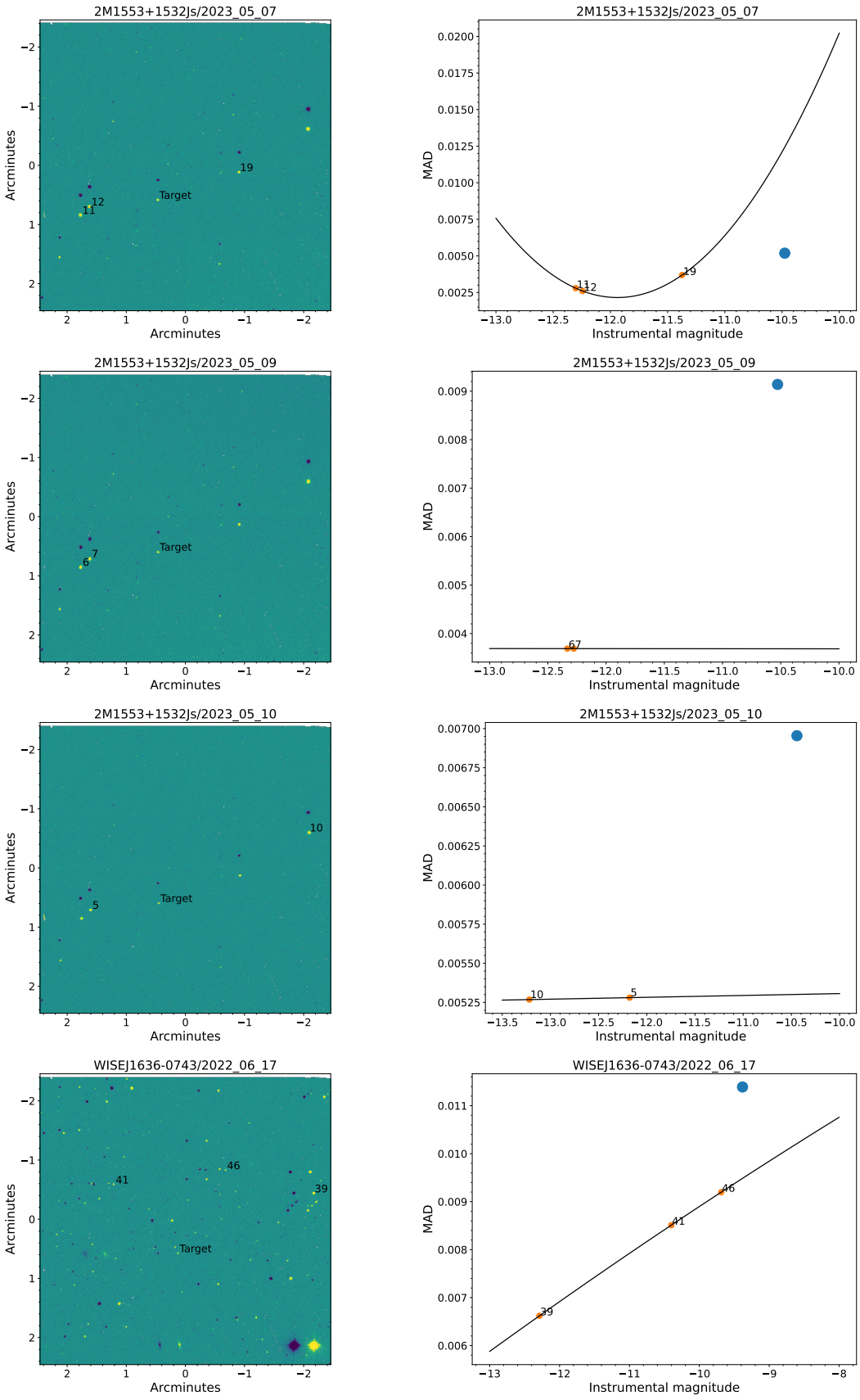


Figure A.1: (Continued.)

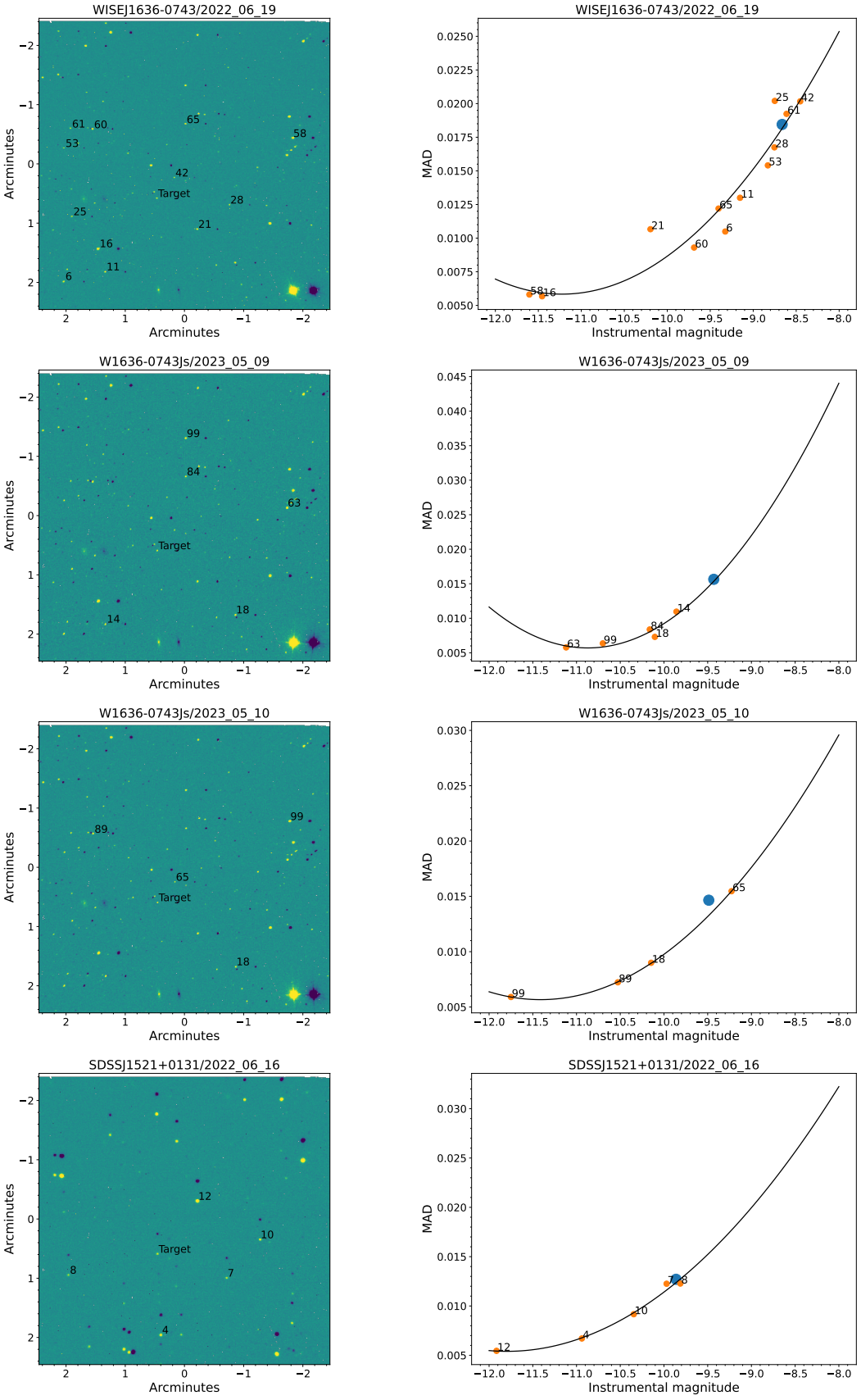


Figure A.1: (Continued.)

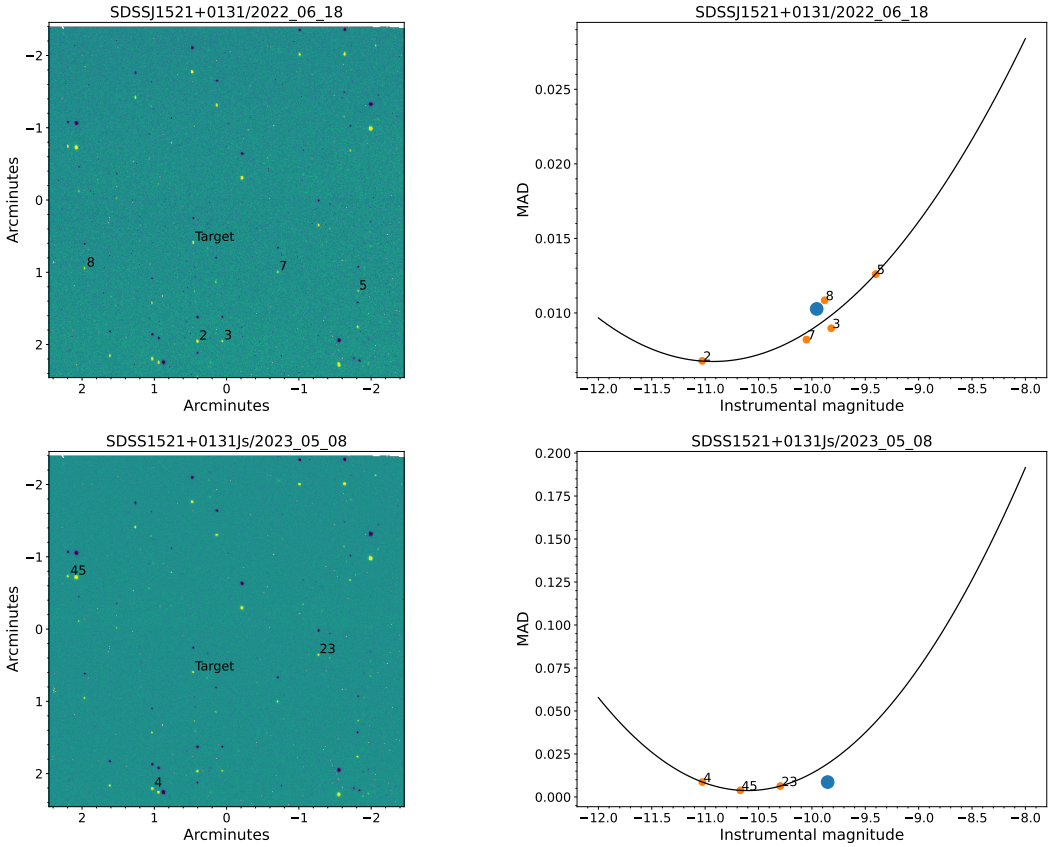


Figure A.1: (Continued.)

A.2 Potentially variable light curves

Potentially variable light curves, periodograms, and sensitivity plots.

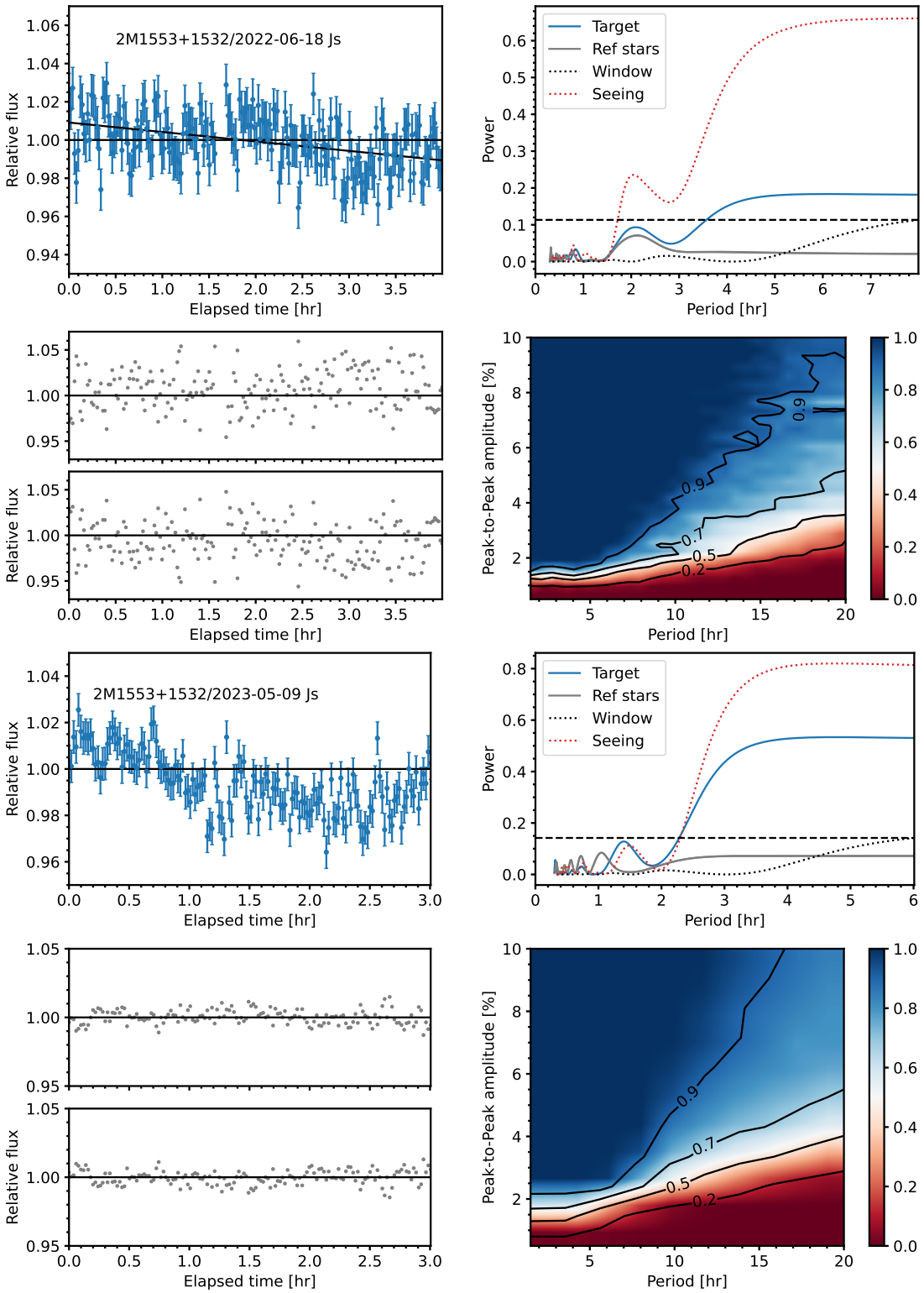


Figure A.2: Potentially variable light curves, periodograms, and sensitivity plots of 2M1553+1532, including the detrended light curves and periodograms of the reference stars. While 2M1553+1532 clearly shows a variability above the 1% FAP level in the periodogram of both nights, it overlaps with the periodogram of the seeing curve, making it a suspicious variable.

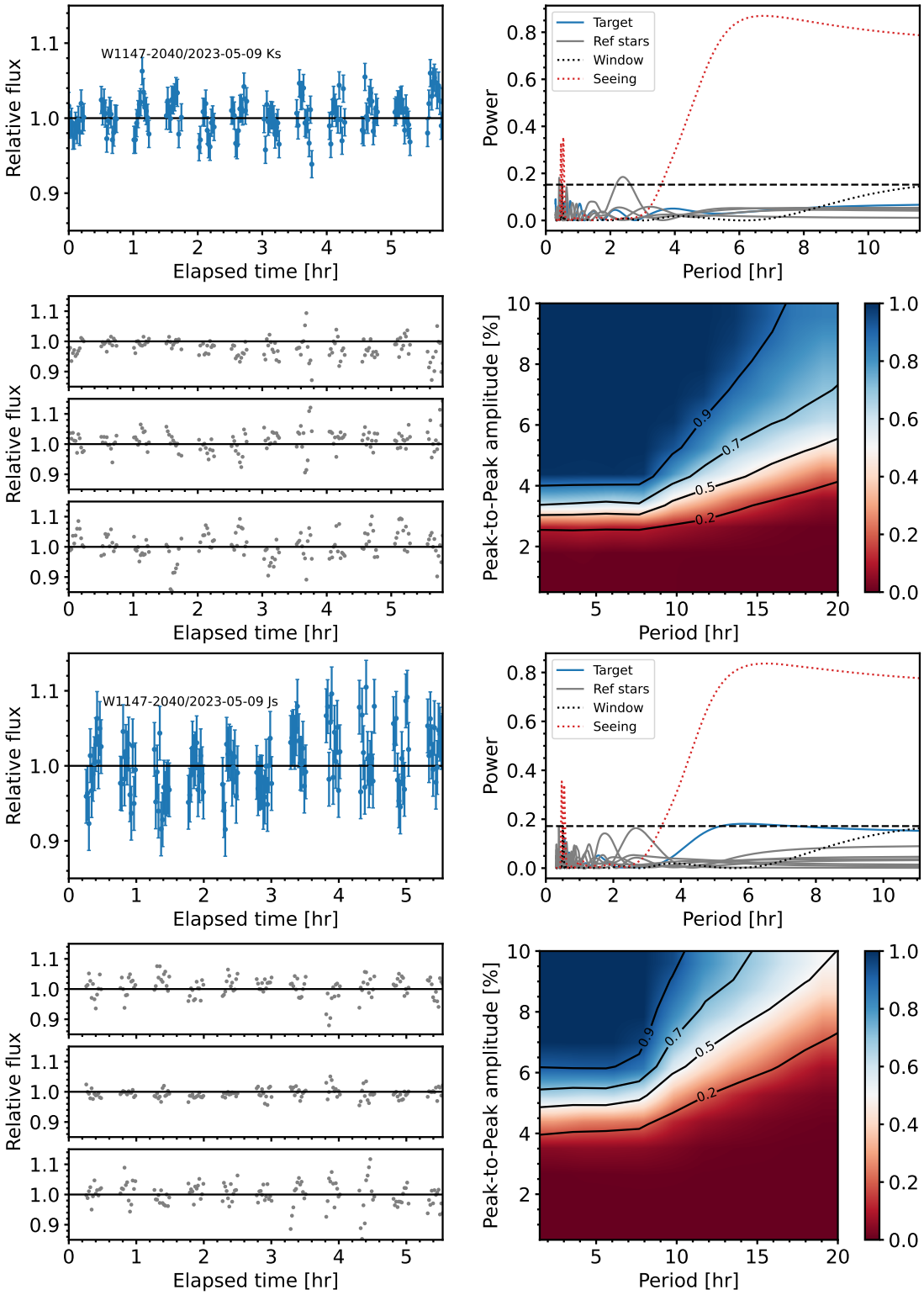


Figure A.3: Interleaved K_S- and J_S-band light curves, periodograms, and sensitivity plots of W1147-2040 on 2023-05-09, including detrended light curves and periodograms of their reference stars. W1147-2040 shows potential variation in the J_S band which is probably correlated with the seeing.

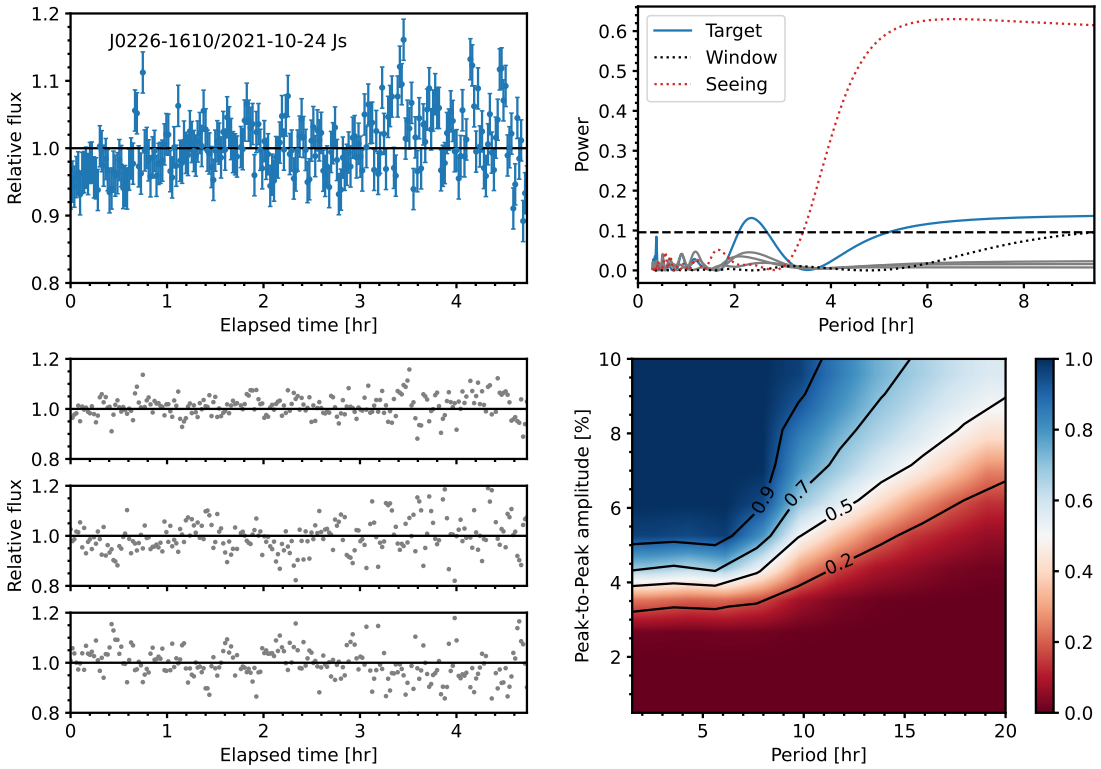


Figure A.4: Potentially variable light curve, periodogram, and sensitivity plot of J0226-1610, including detrended light curves and periodograms of its reference stars. While it shows variability slightly above the 1% FAP level in the periodogram, we are cautious about the variability due to large scatter in the detrended light curves of the reference stars.

A.3 Non-variable light curves

Non-variable light curves, periodograms and sensitivity plots.

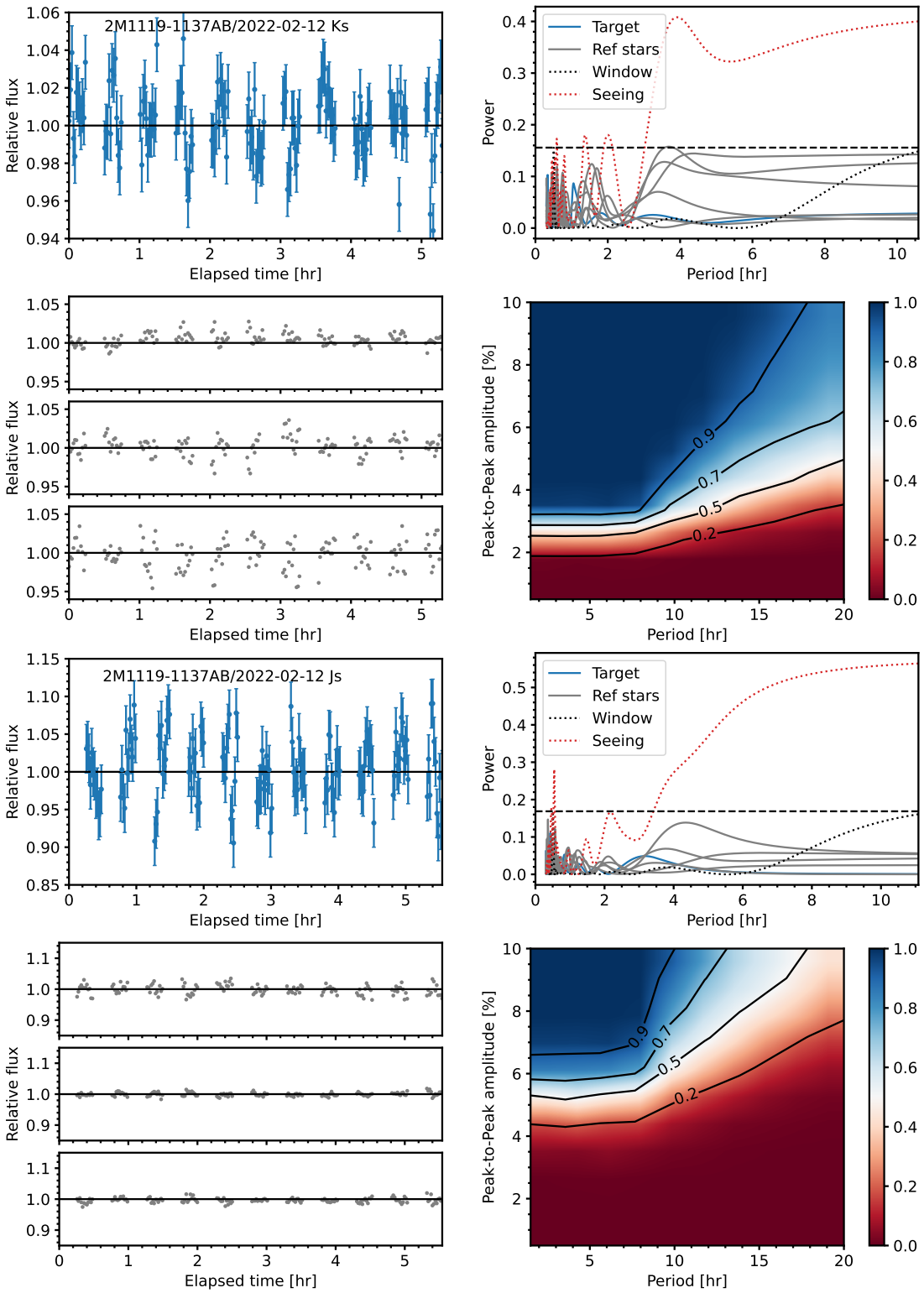


Figure A.5: Interleaved J_S- and K_S-band non-variable light curves, periodograms, and sensitivity plots of a variable object 2M1119-1137AB, including detrended light curves and periodograms of its reference stars.

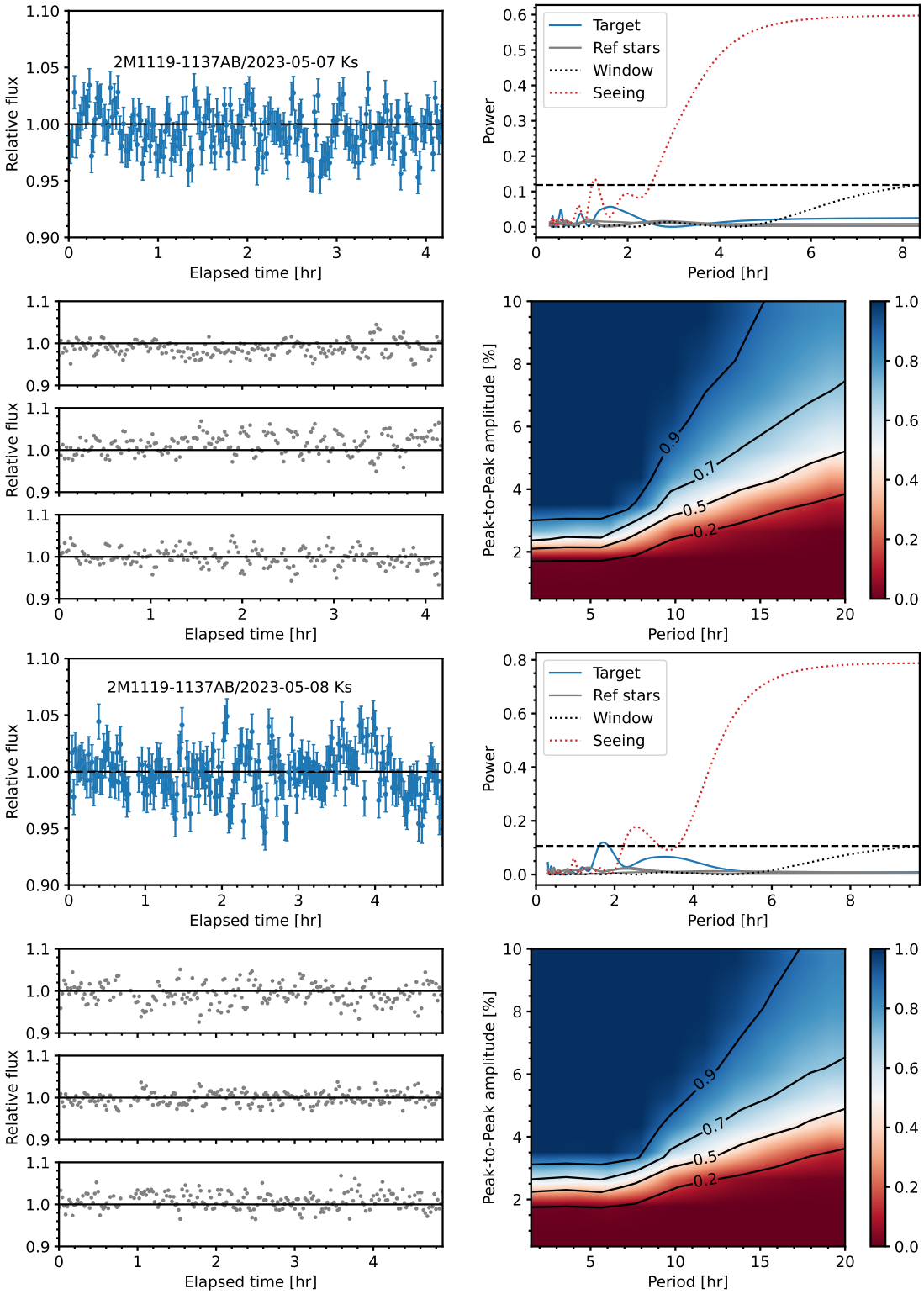


Figure A.6: K_S-band non-variable light curves, periodograms, and sensitivity plots of a variable object 2M1119-1137AB, including detrended light curves and periodograms of its reference stars.

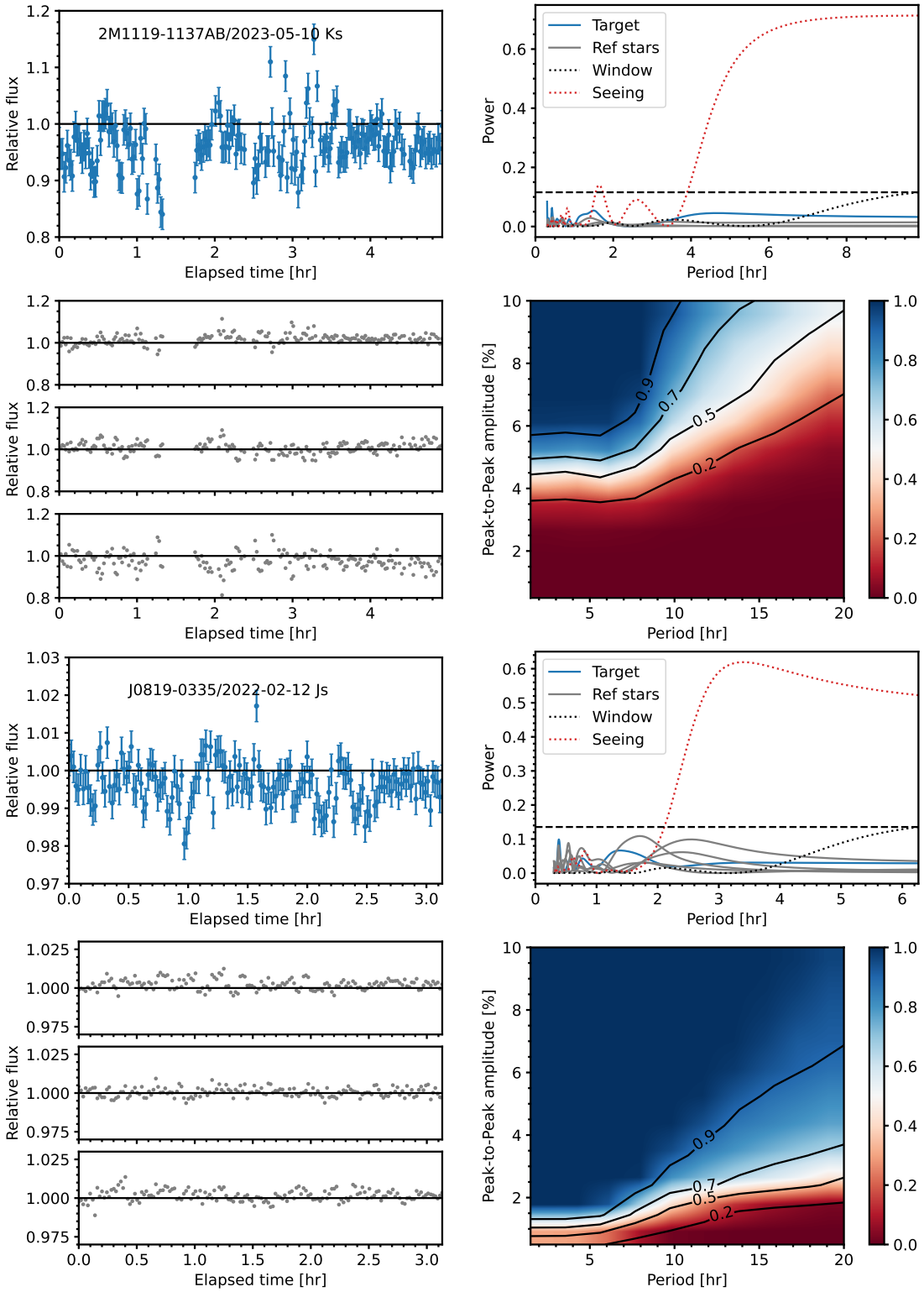


Figure A.7: Non-variable light curves, periodograms, and sensitivity plots of two variable objects 2M1119-1137AB and J0819-0335, including detrended light curves and periodograms of their reference stars

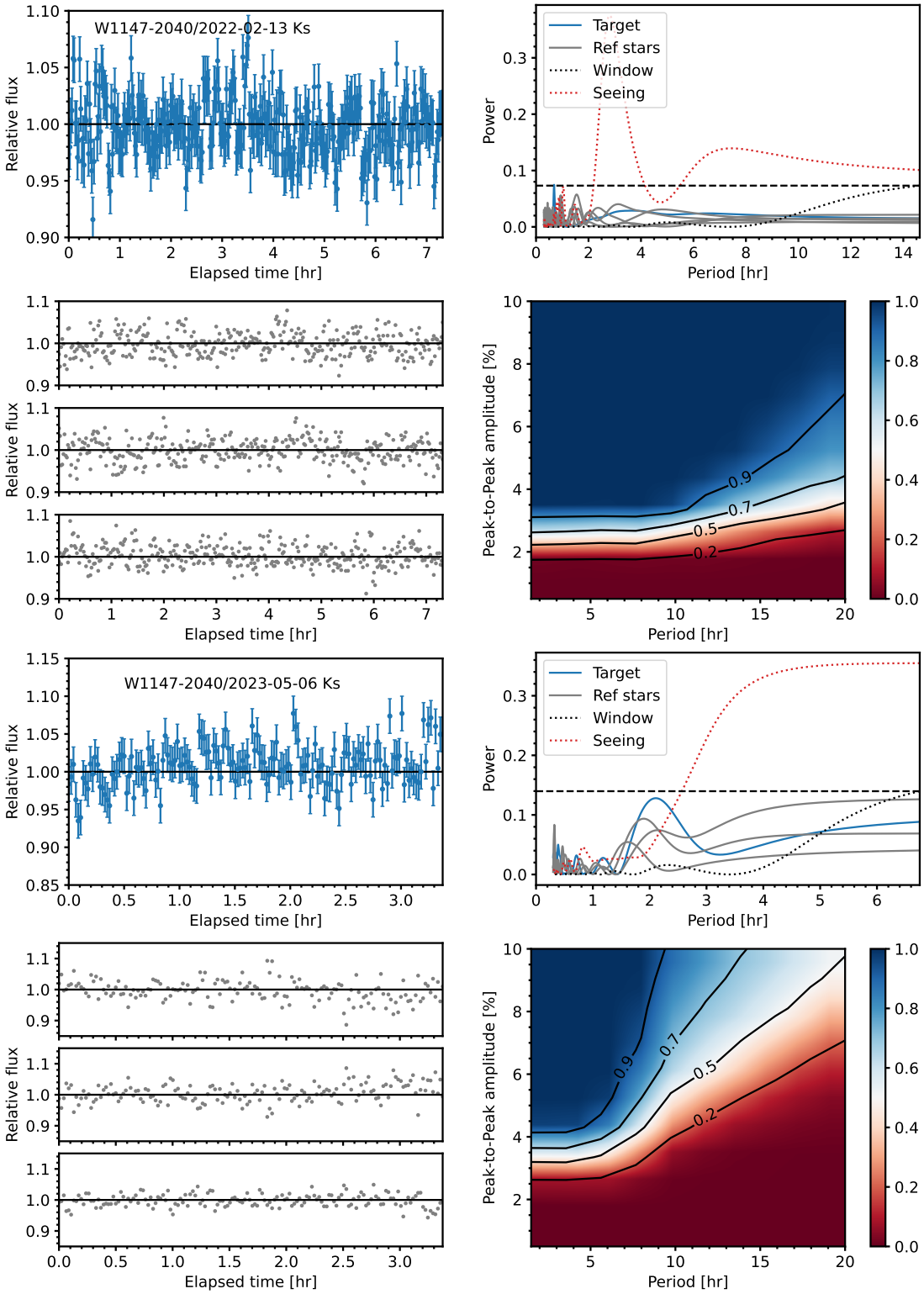


Figure A.8: Non-variable light curves, periodograms, and sensitivity plots of a variable object W1147-2040, including detrended light curves and periodograms of its reference stars

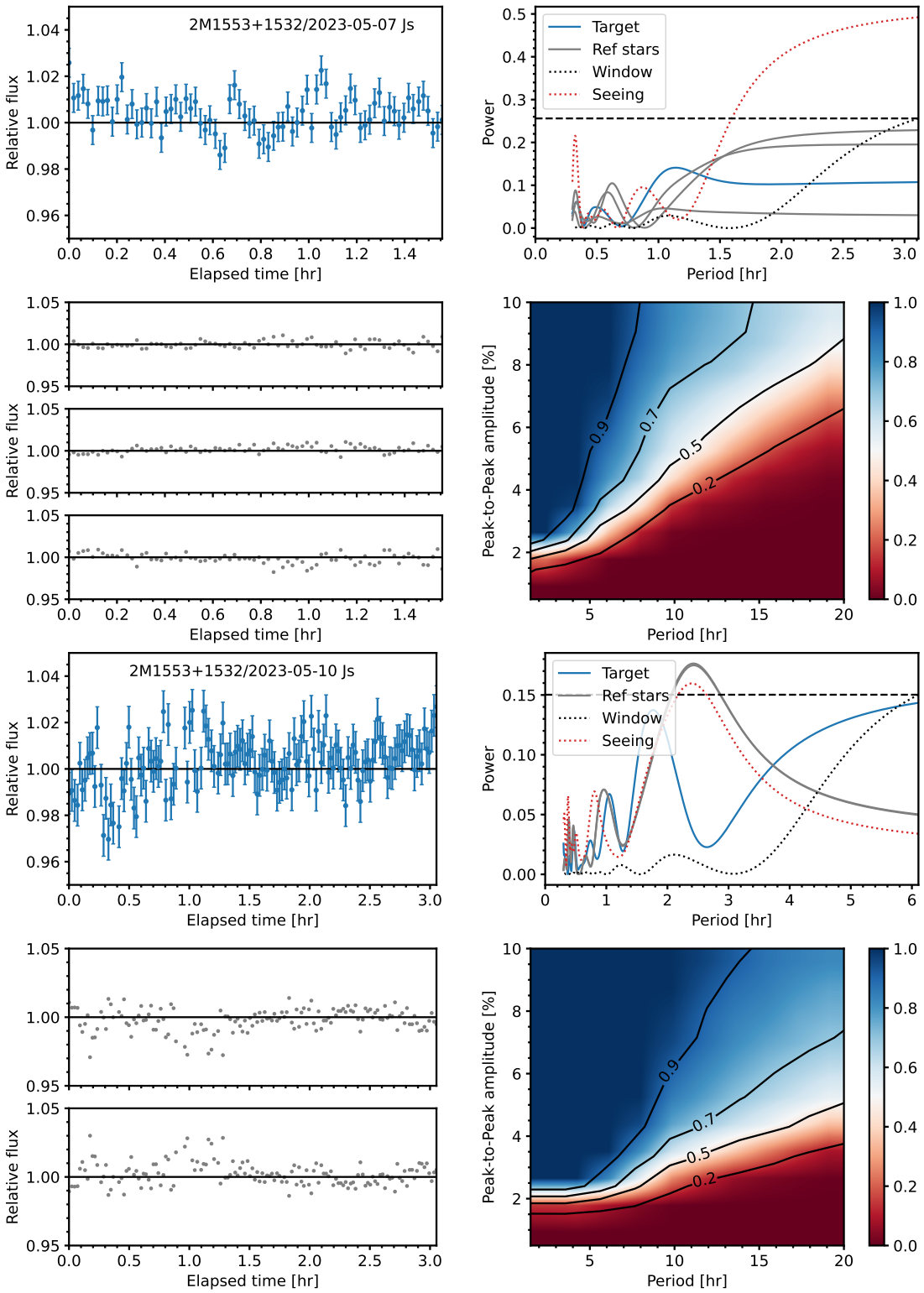


Figure A.9: Non-variable light curves, periodograms, and sensitivity plots of a variable object 2M1552+1532, including detrended light curves and periodograms of its reference stars

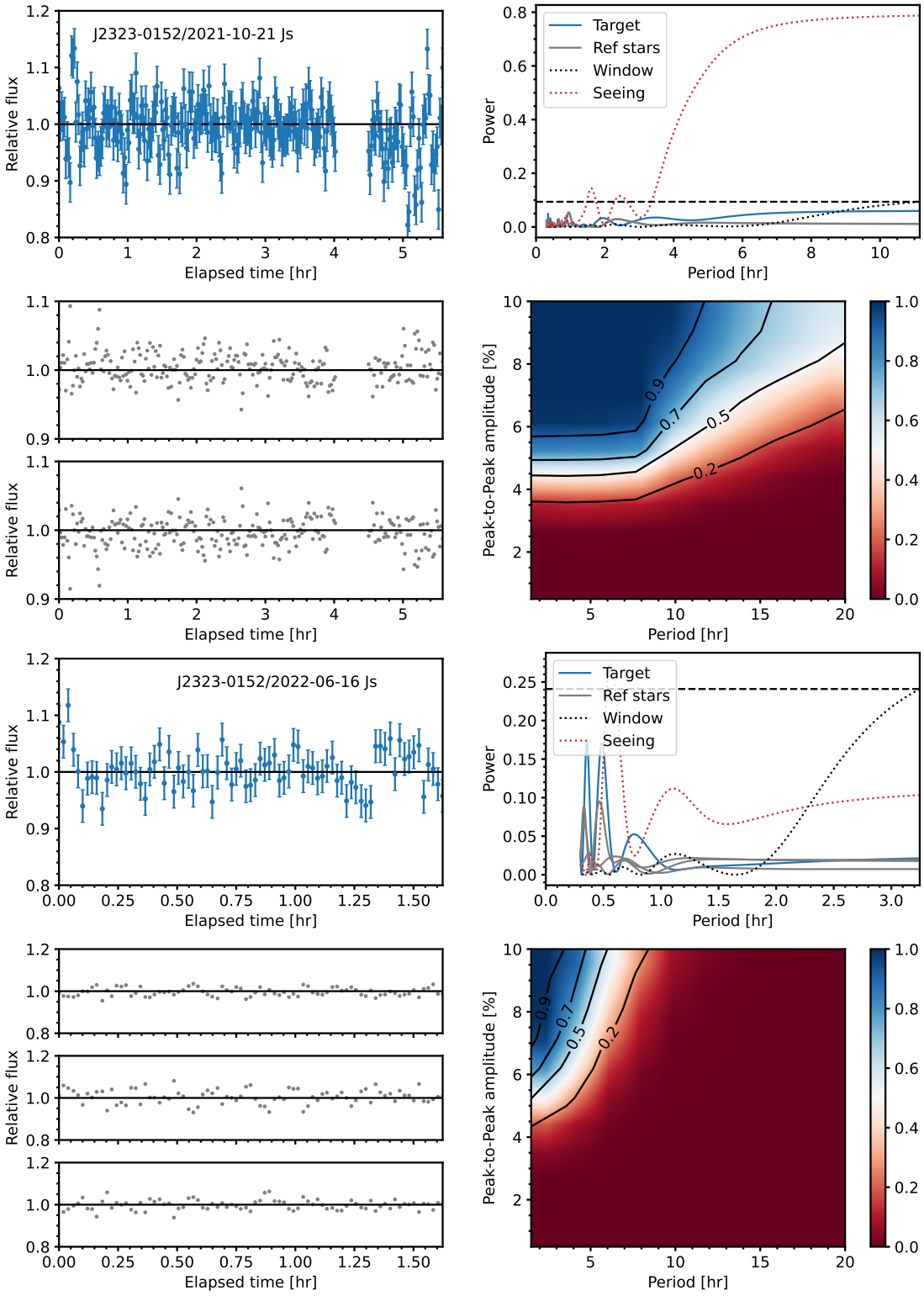


Figure A.10: Non-variable light curves, periodograms, and sensitivity plots of a variable object J2323-0152, including detrended light curves and periodograms of its reference stars.

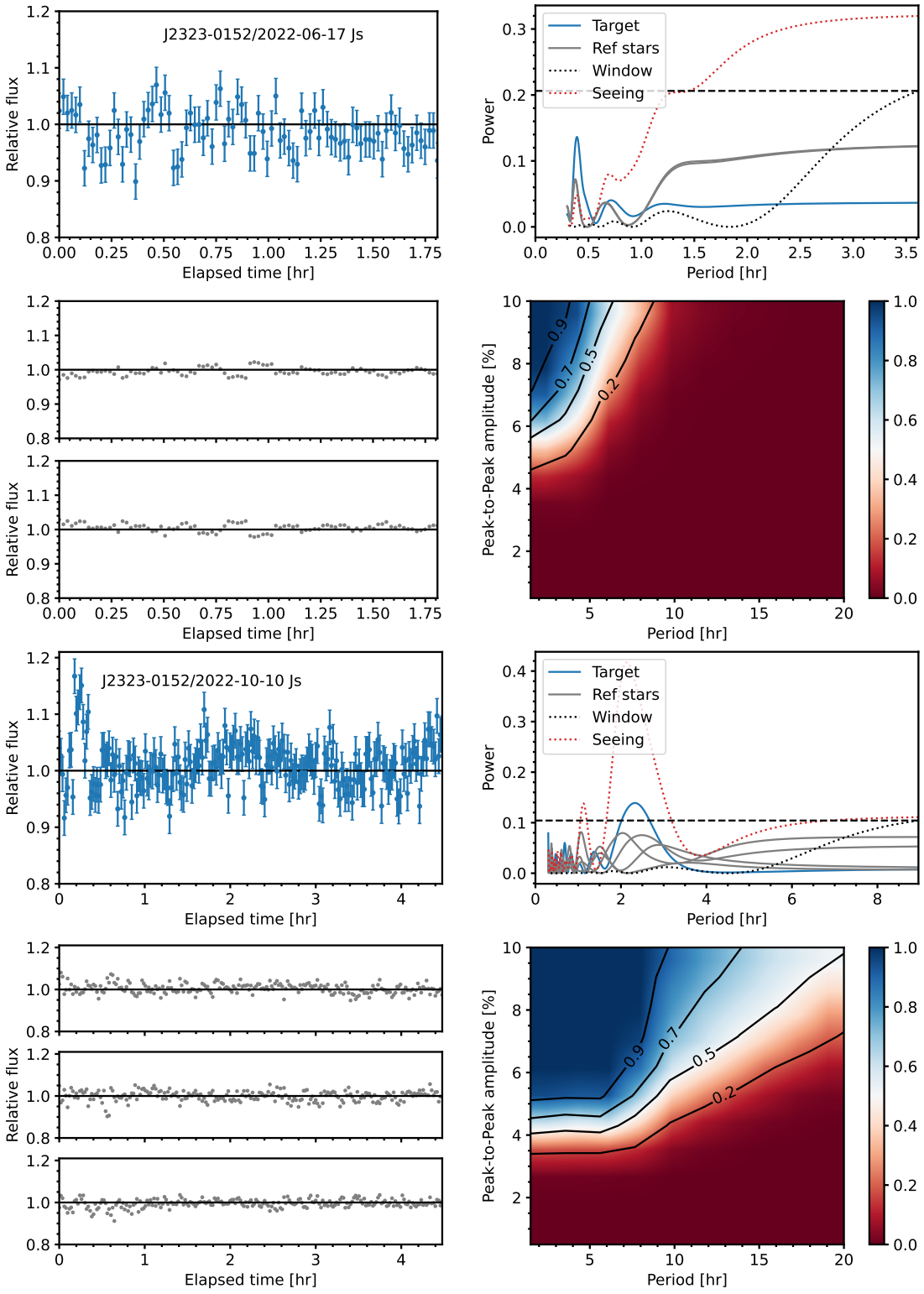


Figure A.10: (Continued.)

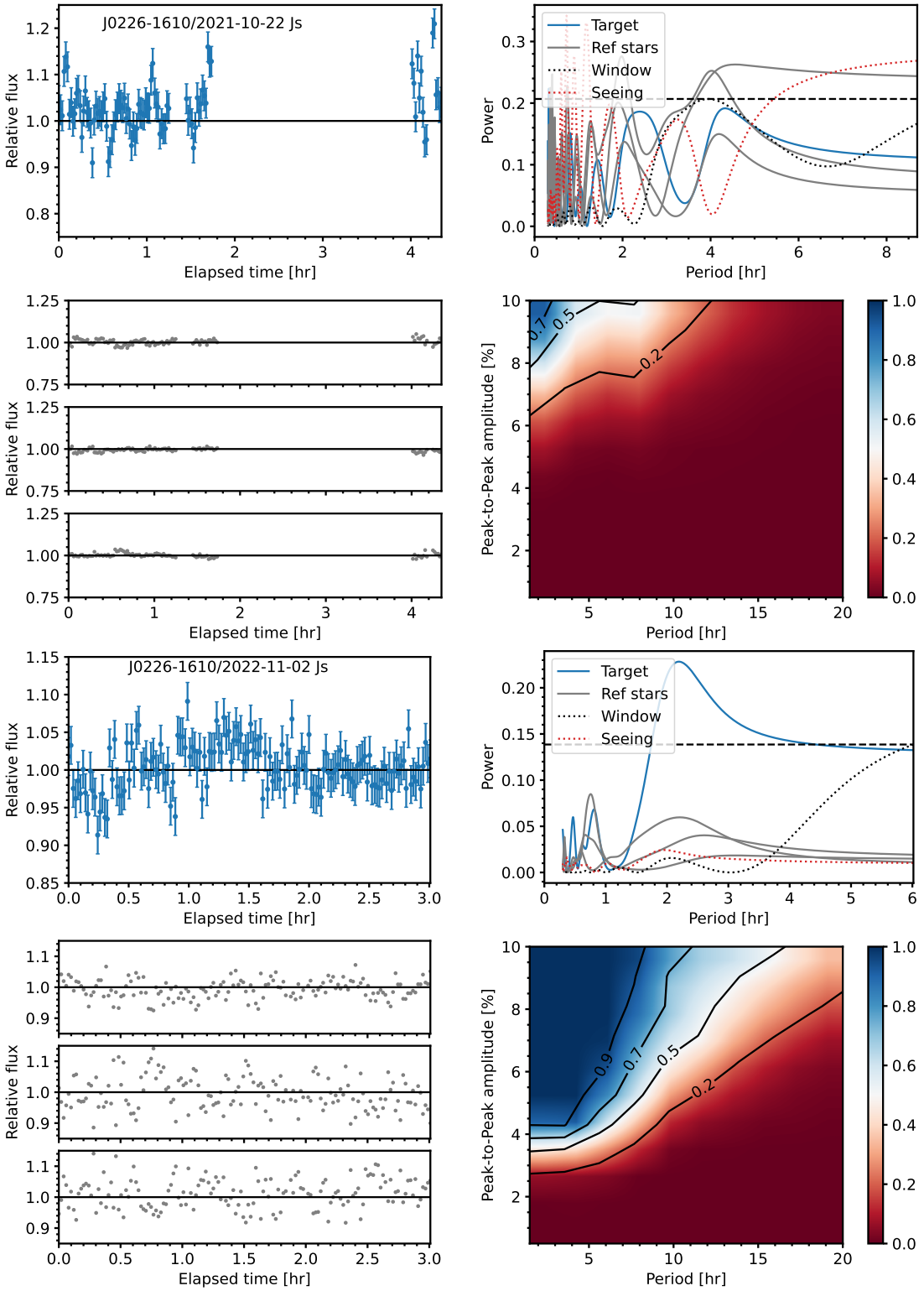


Figure A.11: Non-variable light curves, periodograms, and sensitivity plots of a variable candidate J0226-1610, including detrended light curves and periodograms of its reference stars.

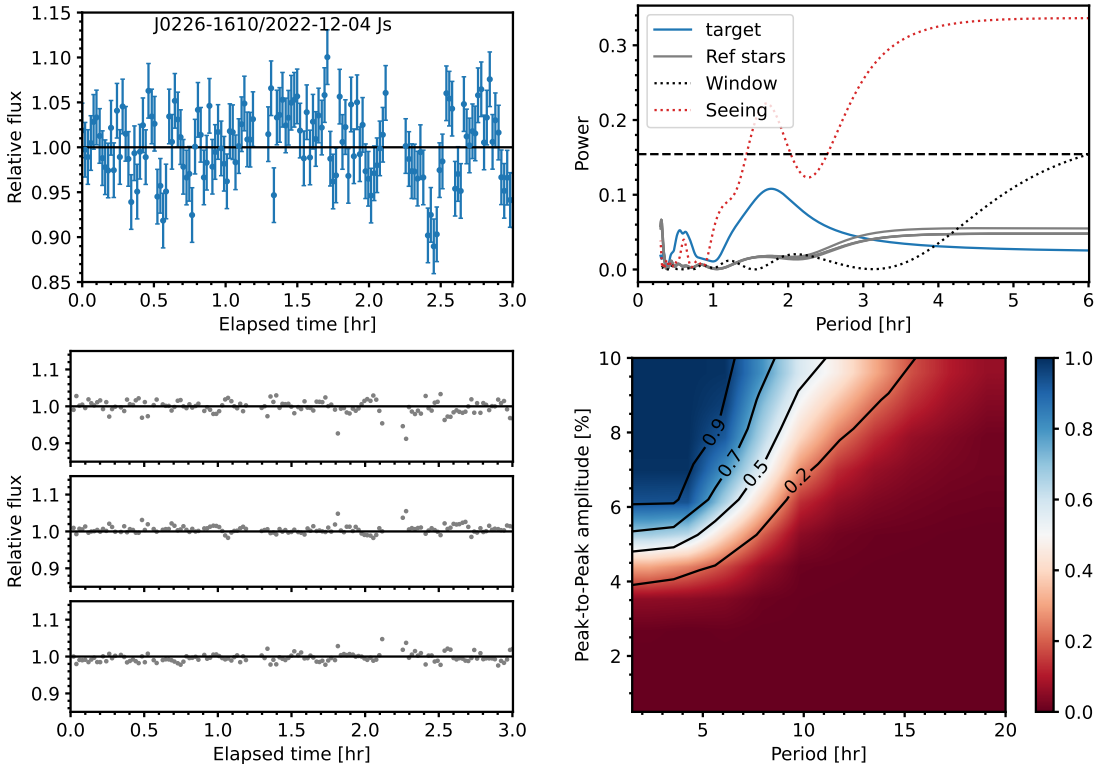


Figure A.11: (Continued.)

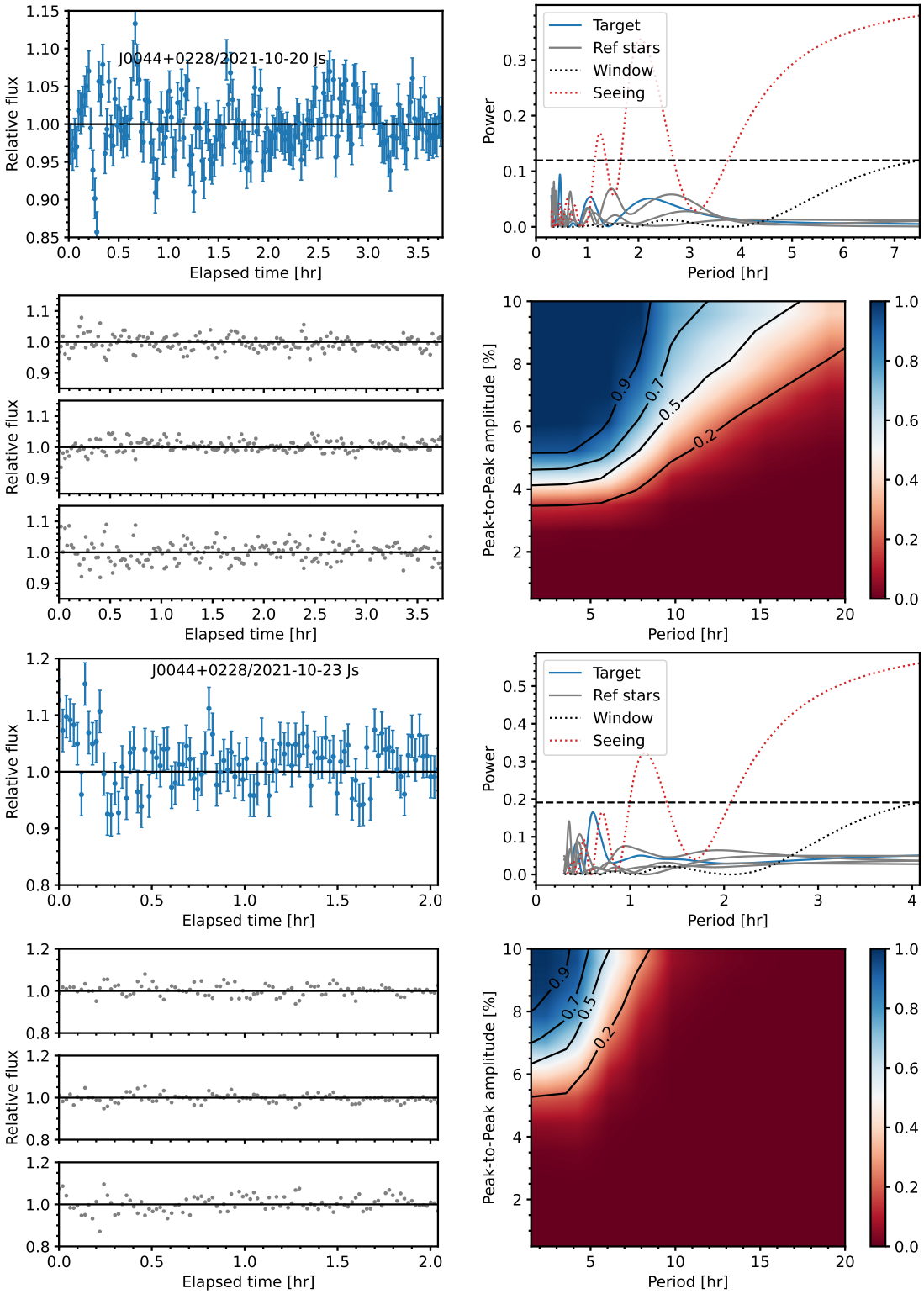


Figure A.12: Light curves, periodograms, and sensitivity plots of a non-variable object J0044+0228, including detrended light curves and periodograms of its reference stars.

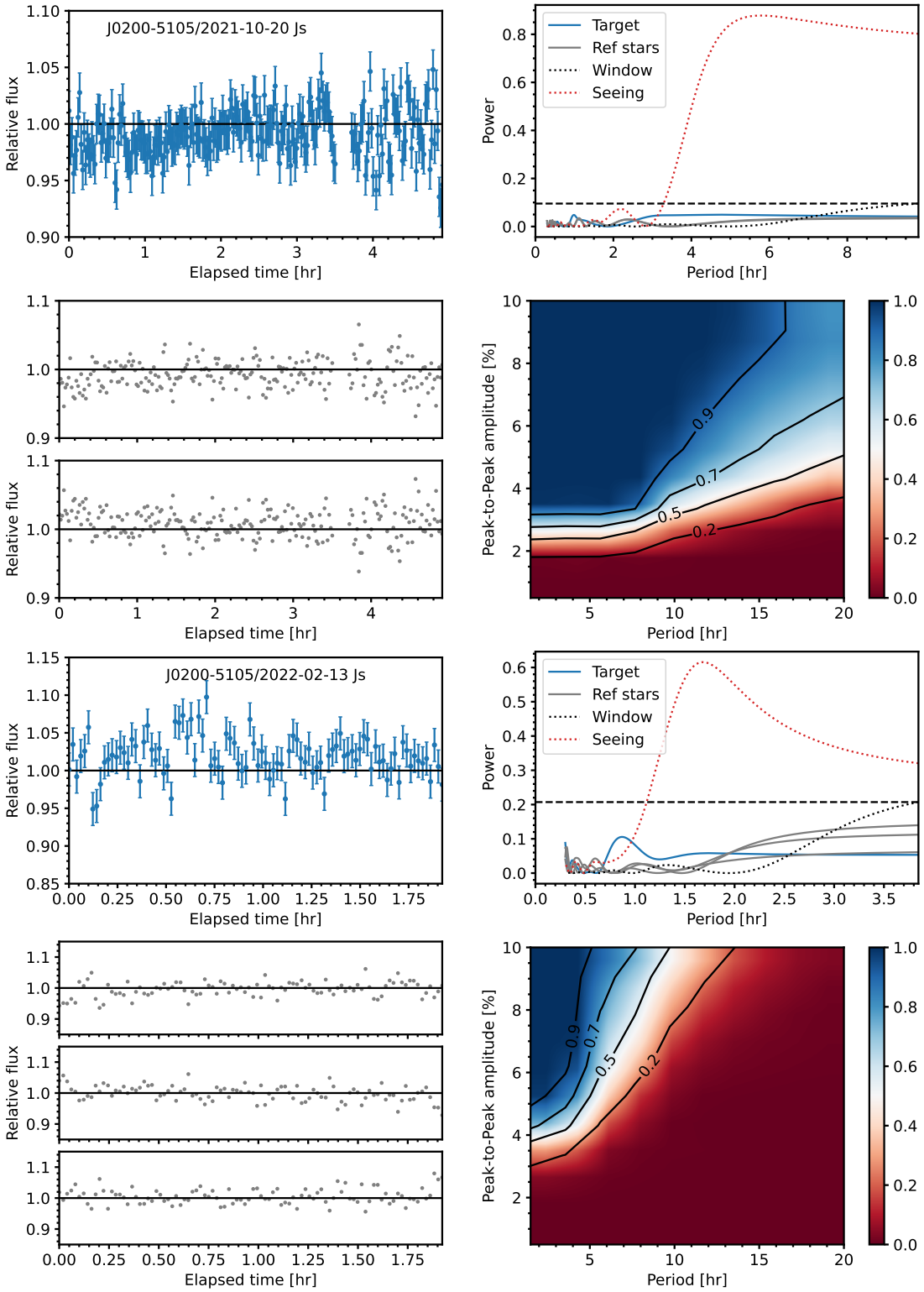


Figure A.13: Light curves, periodograms, and sensitivity plots of a non-variable object J0200-5105, including detrended light curves and periodograms of its reference stars.

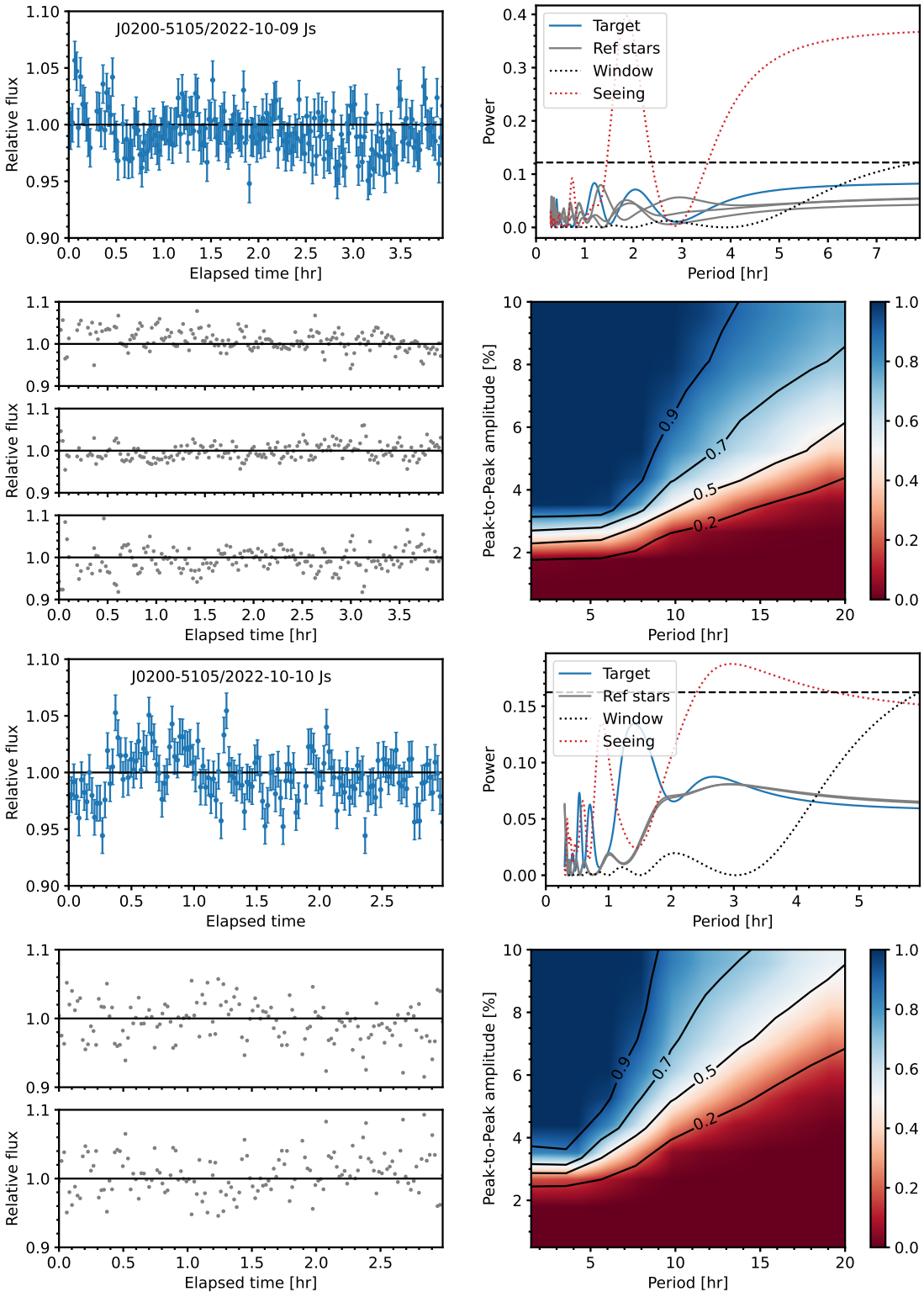


Figure A.13: (Continued.)

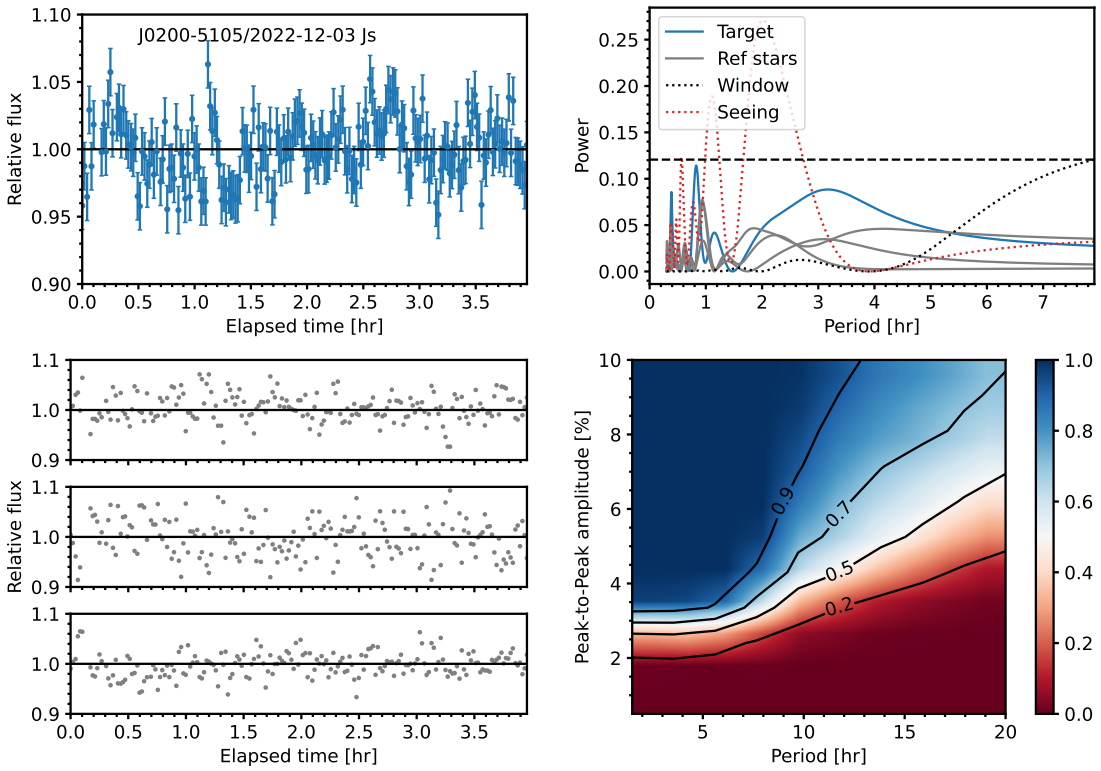


Figure A.13: (Continued.)

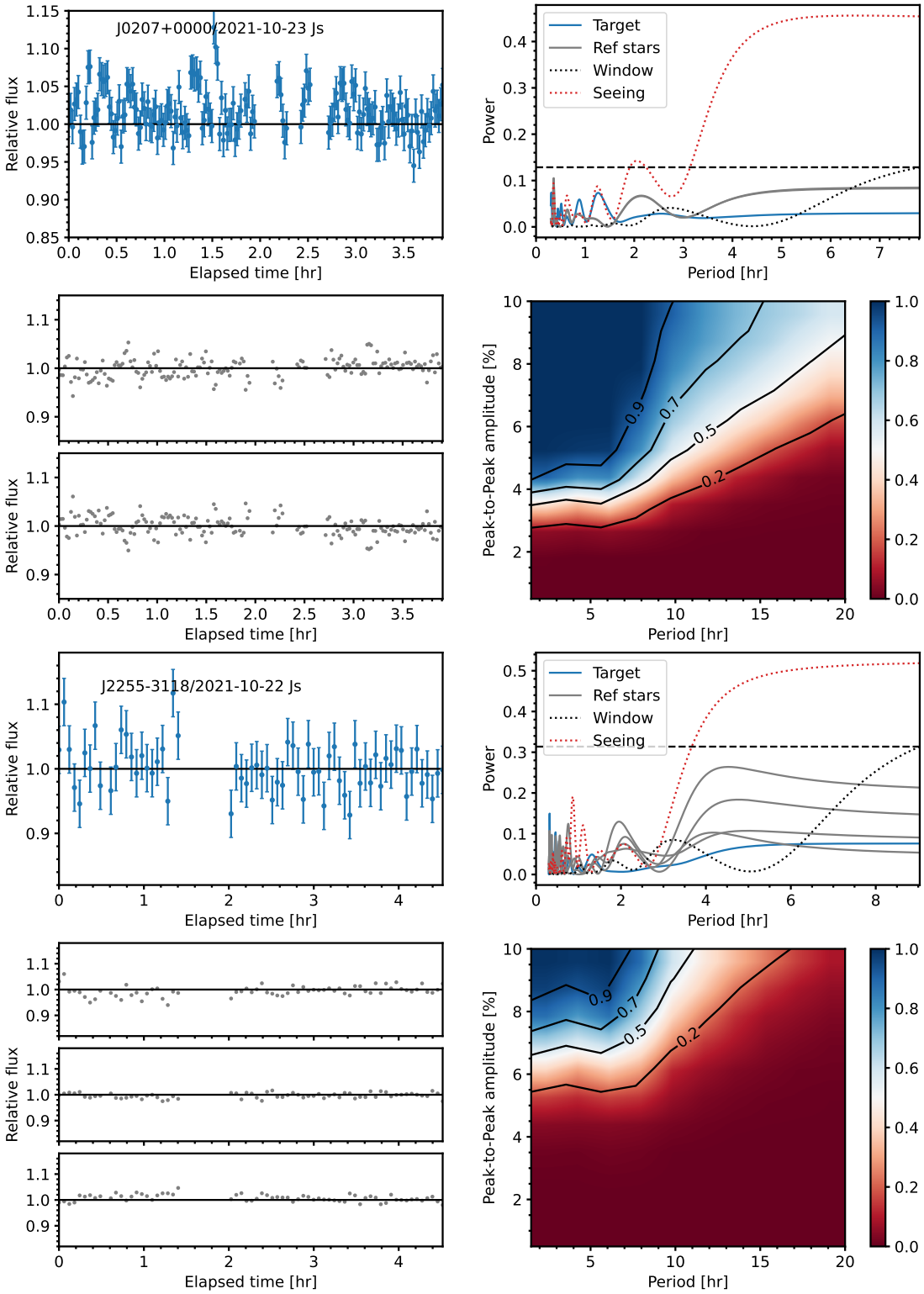


Figure A.14: Light curves, periodograms, and sensitivity plots of non-variable objects J0207+0000 and J2255-3118, including detrended light curves and periodograms of their reference stars.

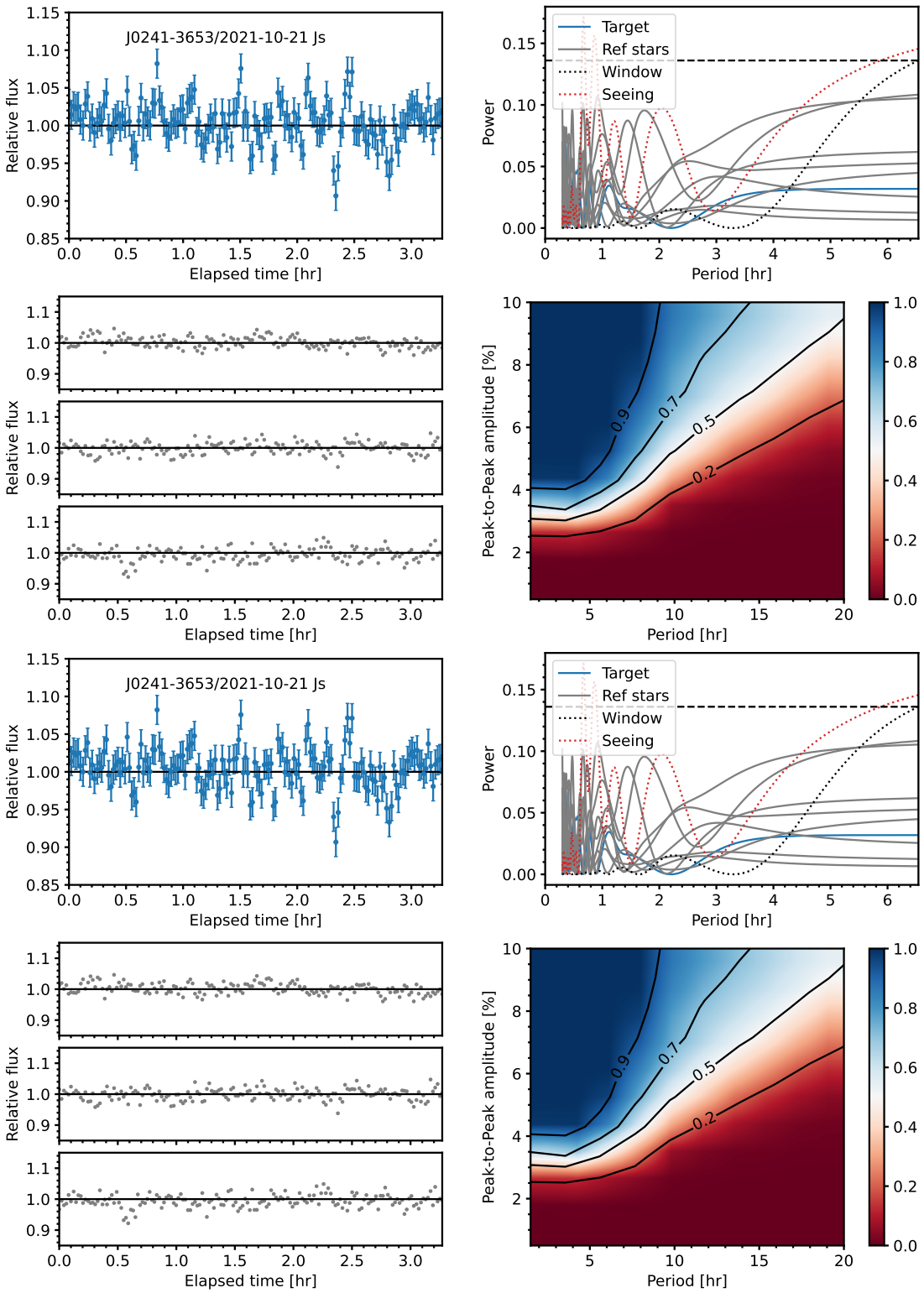


Figure A.15: Light curves, periodograms, and sensitivity plots of a non-variable object J0241-3653, including detrended light curves and periodograms of its reference stars.

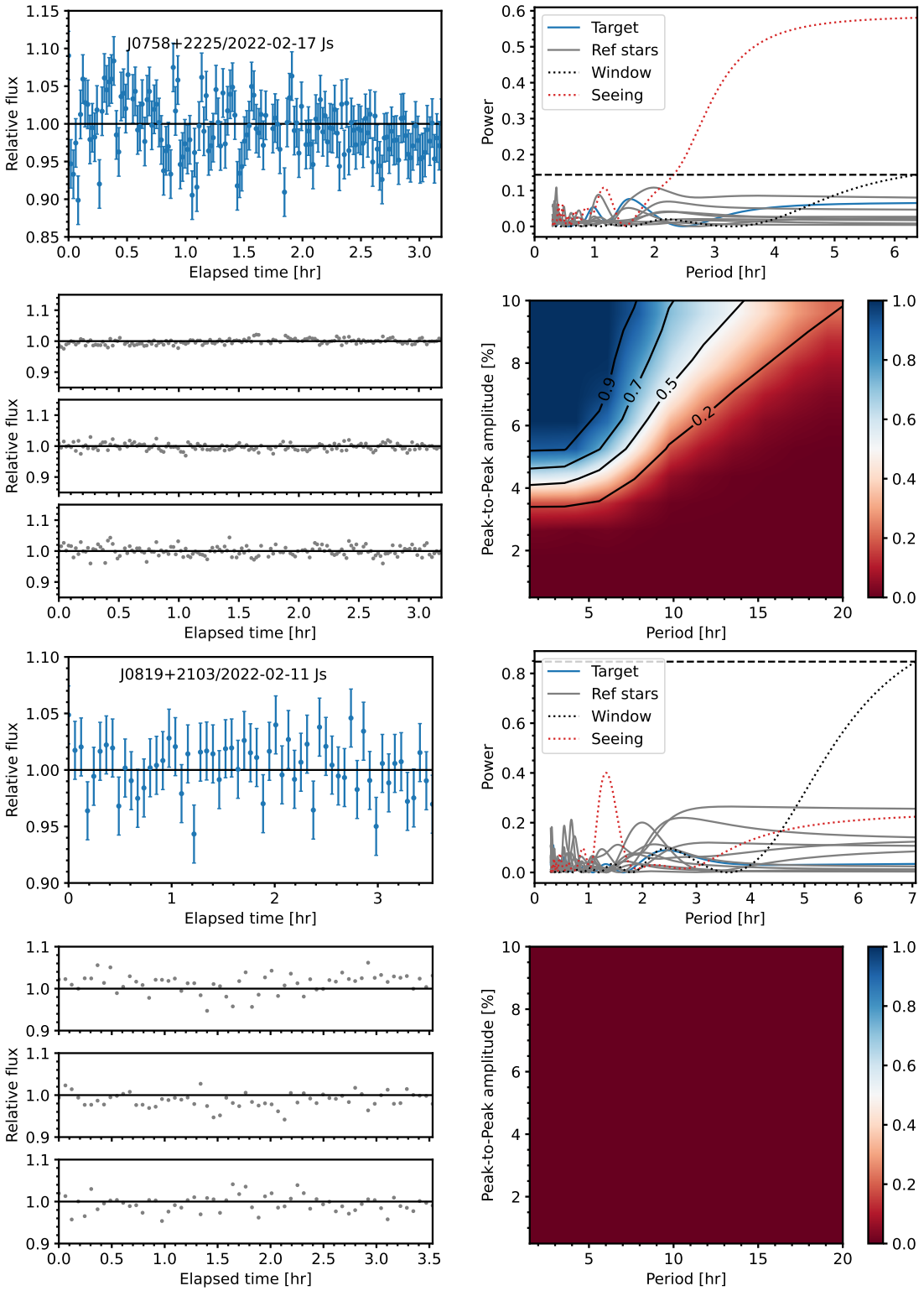


Figure A.16: Light curves, periodograms, and sensitivity plots of non-variable objects J0758+2225 and J0819+2103, including detrended light curves and periodograms of their reference stars.

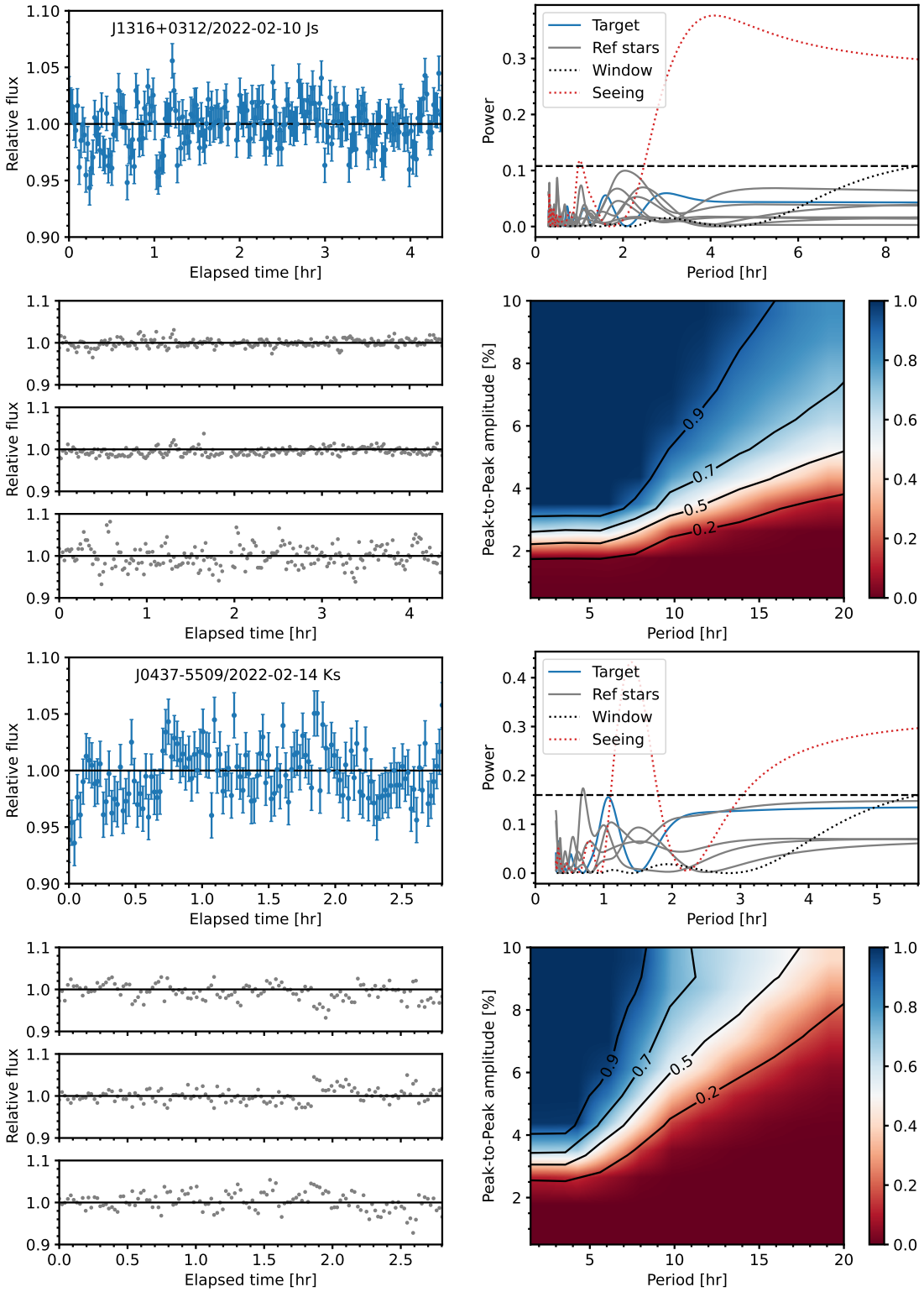


Figure A.17: Light curves, periodograms, and sensitivity plots of non-variable objects J1316+0312 and J0437-5509, including detrended light curves and periodograms of their reference stars.

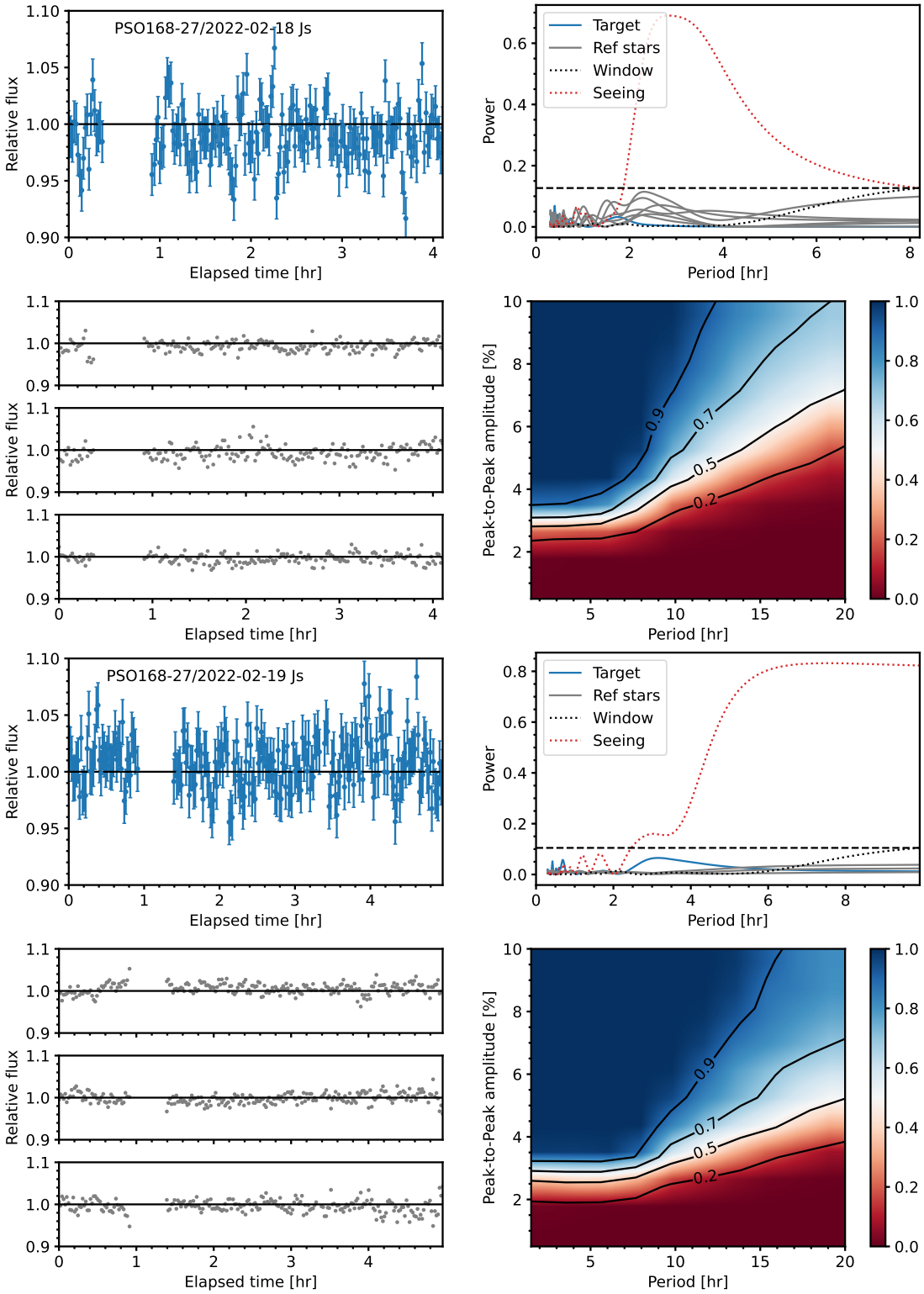


Figure A.18: Light curves, periodograms, and sensitivity plots of a non-variable object PSO168-27, including detrended light curves and periodograms of its reference stars.

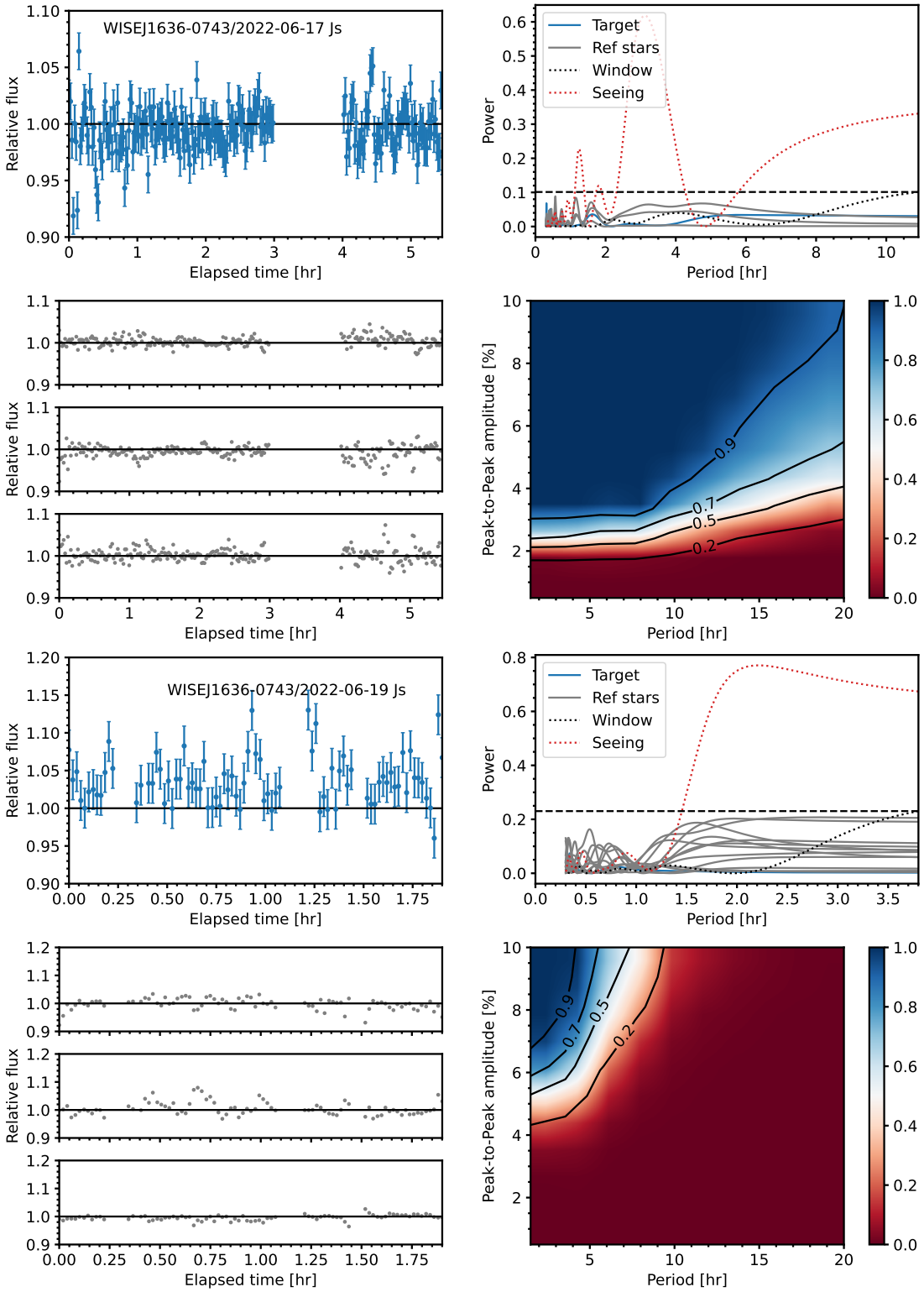


Figure A.19: Light curves, periodograms, and sensitivity plots of a non-variable object WISEJ1636-0743, including detrended light curves and periodograms of its reference stars.

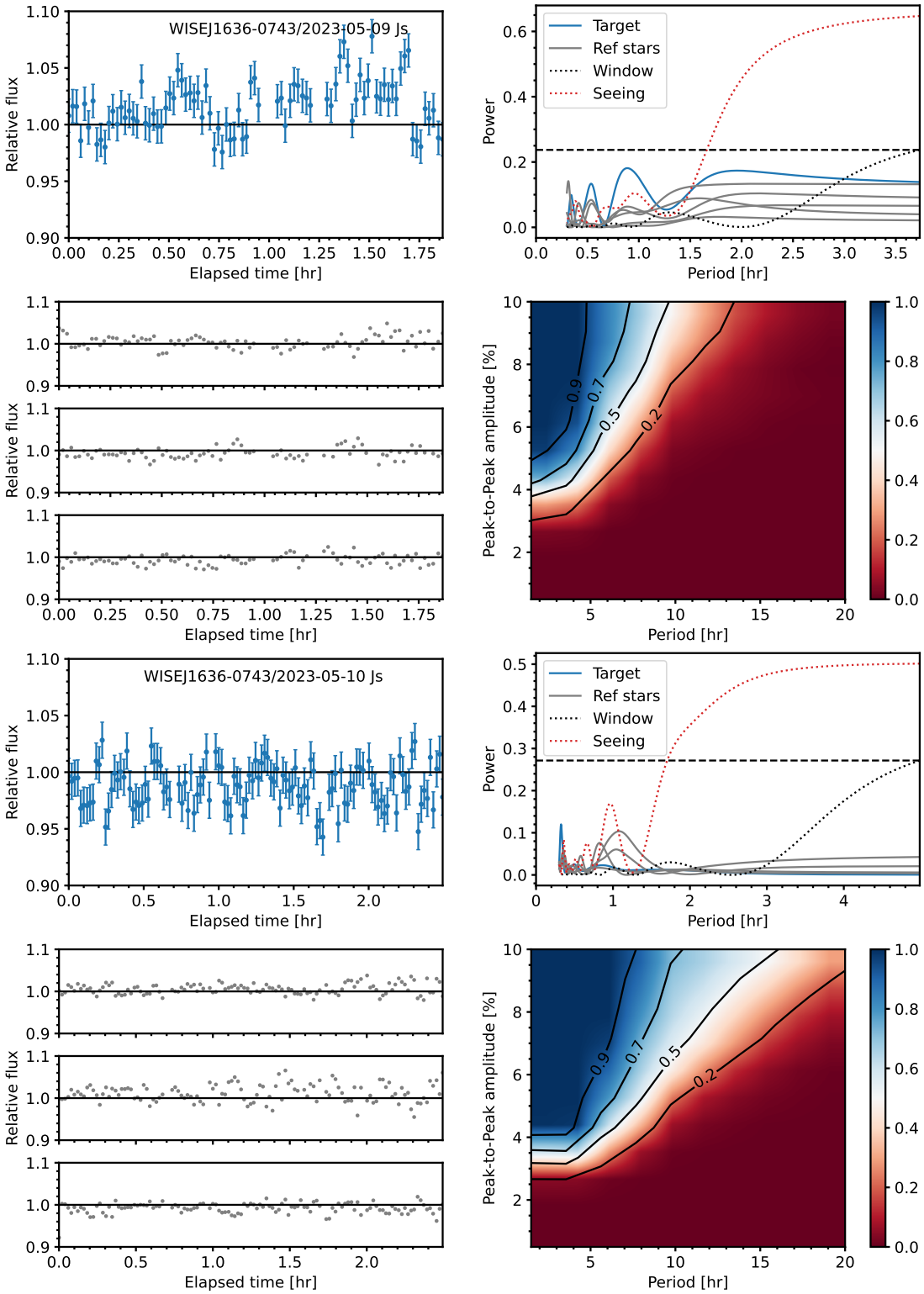


Figure A.19: (Continued.)

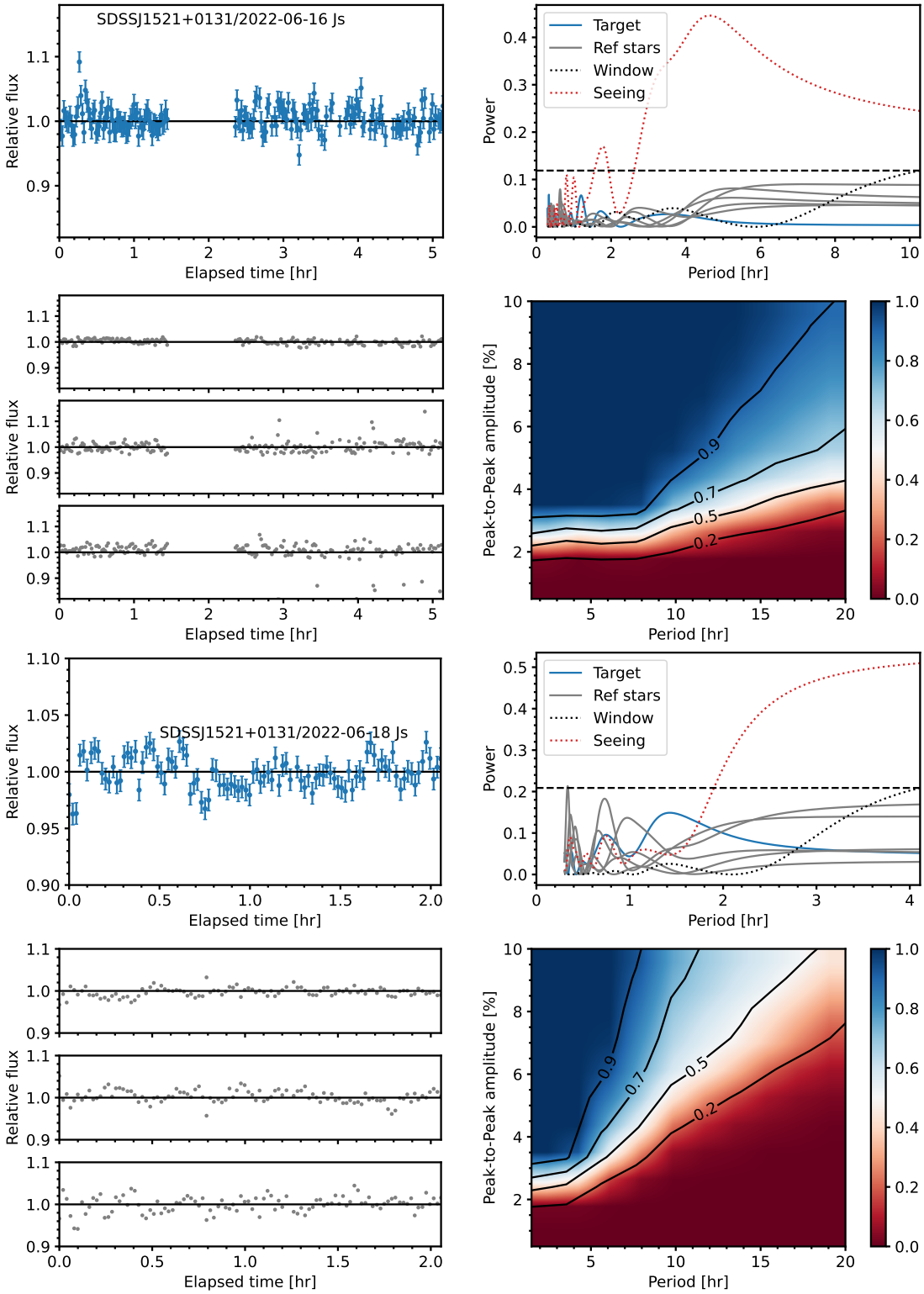


Figure A.20: Light curves, periodograms, and sensitivity plots of a non-variable object SDSS1521+0131, including detrended light curves and periodograms of its reference stars.

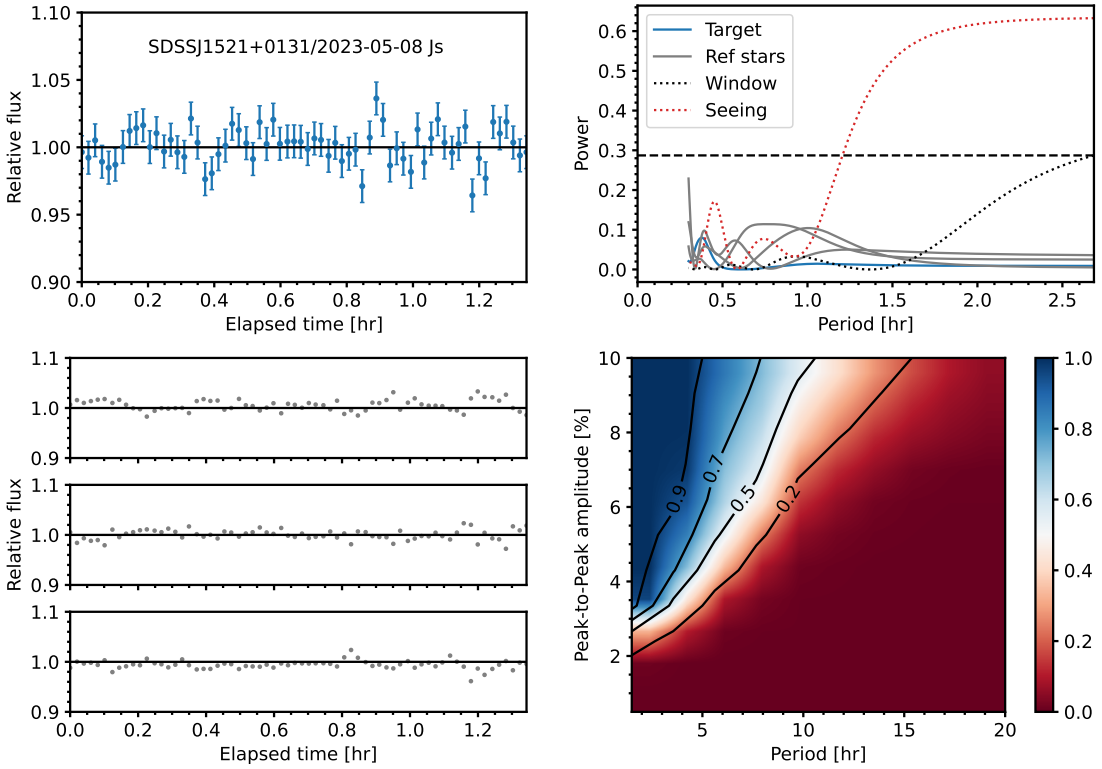


Figure A.20: (Continued.)

Appendix B

Appendix of Chapter 4

B.1 Central star images

The images of the central stars from 2018-11-15 to 2024-03-23 in the H and z' bands are presented in Fig. B.1, including residuals after model fitting and subtraction.

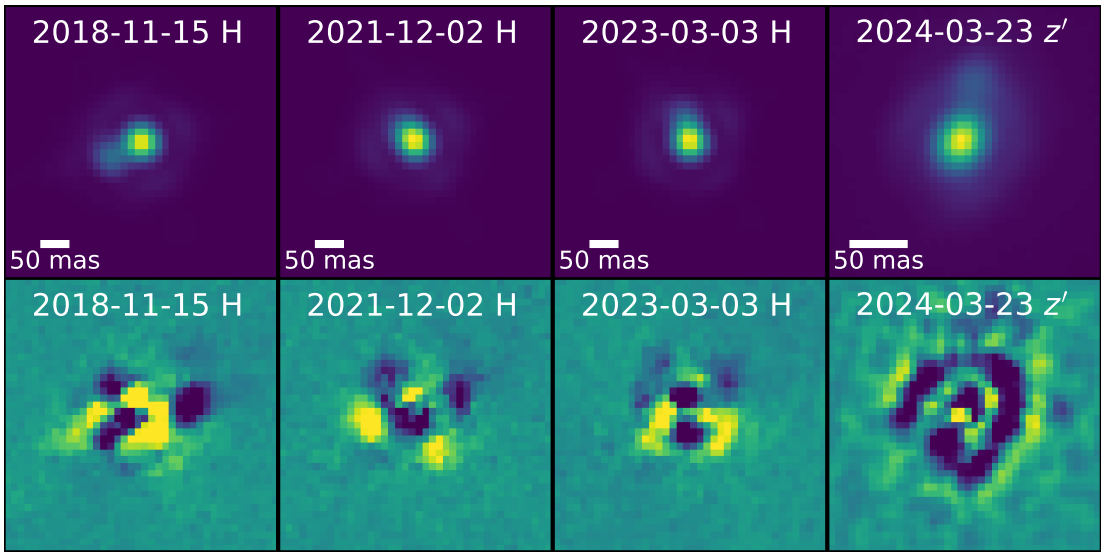


Figure B.1: Images of the central stars from 2018-11-15 to 2024-03-23. All images are rotated to the direction where north is up and east is left. Upper panel: Star images before subtraction. Bottom panel: Residuals after model fitting and subtraction.

B.2 Posterior distribution of SED fitting for the central two stars

The posterior distributions of SED parameter fitting of the central two stars are presented in Fig. B.2.

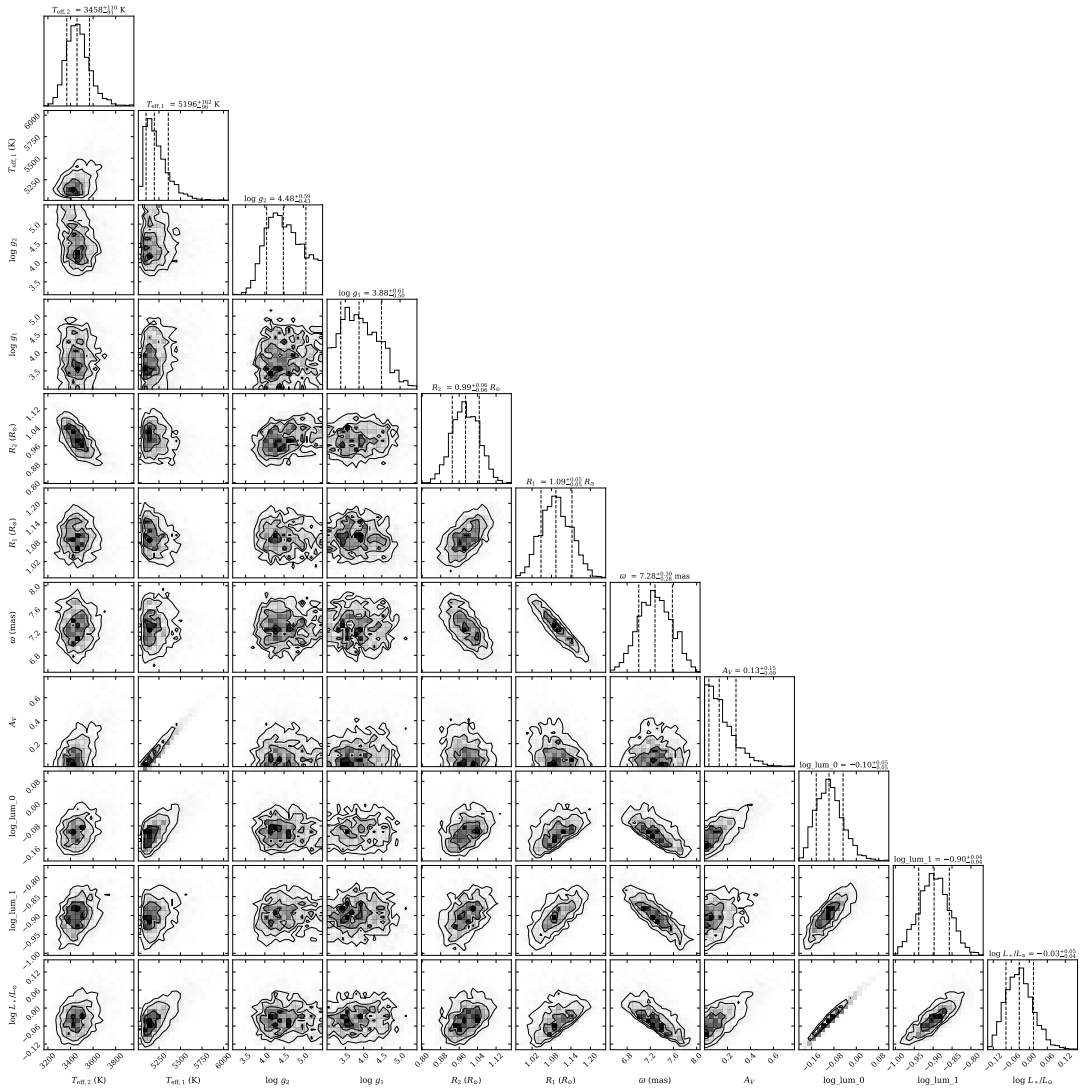


Figure B.2: Posterior distributions of the SED fitting parameters for the central stars.

B.3 Radial velocity injection test

We injected artificial signals in the VIS-X IFU data to verify the PCA method we developed in Sect. 4.4.4. We fit a 2D Gaussian model to the primary star and used the fitted model as the PSF template. Then we created a 1D Gaussian signal with an amplitude of 0.2 as the injected spectrum which is of similar brightness to the fainter star. We scaled the PSF template with the 1D Gaussian signal and injected it at the same separation and blue shift as the fainter star but in the opposite direction. We retrieved the signal successfully using the same PCA method we developed for the fainter star as demonstrated in Fig. B.3.

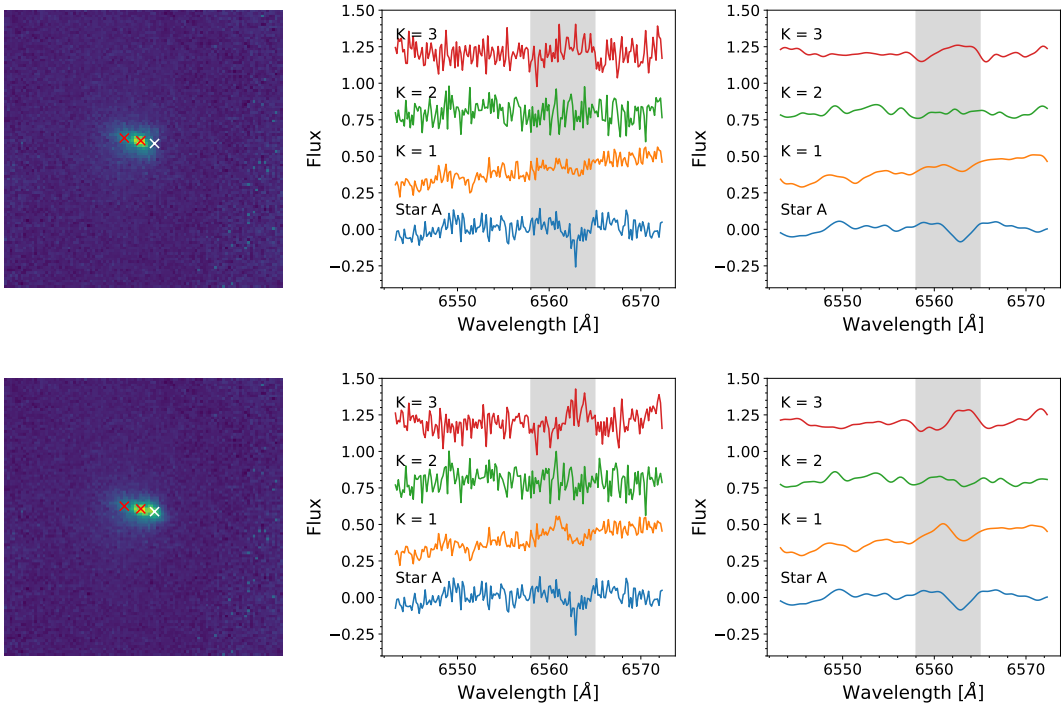


Figure B.3: Injection test for radial velocity measurements in VIS-X IFU data. Upper panel: original data. Bottom panel: fake Gaussian signal of the same contrast and same blue shift as the fainter star injected at the same separation but in the opposite direction, shown by the cross marker in white. Before the injection, there is no signal in the first component (K=1) in the upper panel. After the injection, we detected the emission at the supposed blue shift and amplitude in the first component (K=1) in the lower panel.

B.4 Relative astrometry of all sources

Figure. B.4 shows the relative astrometry of all sources in FoV when the mass ratio = 0 and 1. Regardless of the mass ratio of the central stars, the candidate has the most significant motion compared to other sources except for the central stars and it deviates from the proper motion cluster of other sources.

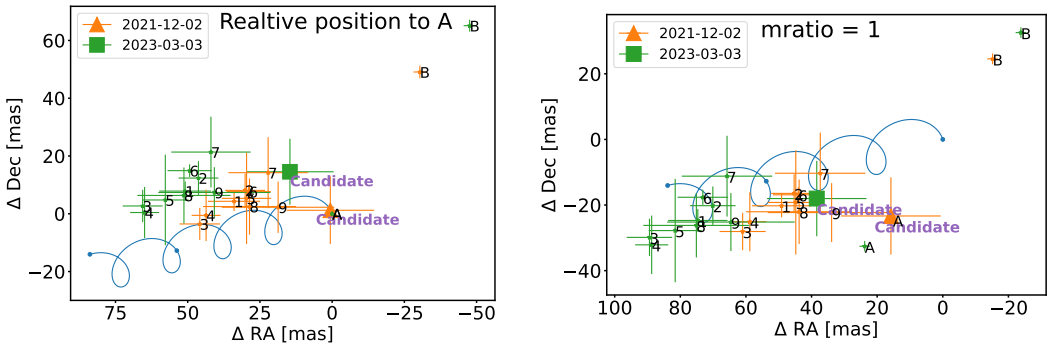


Figure B.4: Relative astrometry all sources in RA and Dec offsets. Left panel: relative astrometry of all sources to the primary star (mass ratio = 0). Right panel: relative astrometry of all the sources to the barycentre when the mass ratio = 1. The positions of all sources of the first epoch are calibrated to the origin, so the positions of the later epochs are subtracted by the positions of the first epoch. The candidate is shown by the triangle and square markers with the epoch 2021-12-02 in orange and the epoch 2023-03-03 in green. The sources are labelled with the same number in Fig. 4.1, using the same colour convention for epochs. The blue line is the trajectory of a static background star evolving from 2018-11-15 and the two points on the track are the positions on 2021-12-02 and 2023-03-03 calculated by the proper motion and parallax reported in Gaia.

Bibliography

ALMA Partnership et al., 2015, ApJ, 808, L3

Ackerman A. S., Marley M. S., 2001, ApJ, 556, 872

Adams F. C., Ruden S. P., Shu F. H., 1989, ApJ, 347, 959

Albert L., Artigau É., Delorme P., Reylé C., Forveille T., Delfosse X., Willott C. J., 2011, AJ, 141, 203

Allard F., Hauschildt P. H., Alexander D. R., Tamanai A., Schweitzer A., 2001, ApJ, 556, 357

Allard F., Guillot T., Ludwig H.-G., Hauschildt P. H., Schweitzer A., Alexander D. R., Ferguson J. W., 2003, in Martín E., ed., IAU Symposium Vol. 211, Brown Dwarfs. p. 325

Allard F., Homeier D., Freytag B., 2012, Philosophical Transactions of the Royal Society of London Series A, 370, 2765

Allard F., Homeier D., Freytag B., Schaffenberger W., Rajpurohit A. S., 2013, Memorie della Societa Astronomica Italiana Supplementi, 24, 128

Allen P. R., Koerner D. W., McElwain M. W., Cruz K. L., Reid I. N., 2007, AJ, 133, 971

Allers K. N., Liu M. C., 2013, ApJ, 772, 79

Allers K. N., Liu M. C., 2020, PASP, 132, 104401

Allers K. N., Gallimore J. F., Liu M. C., Dupuy T. J., 2016, ApJ, 819, 133

Amara A., Quanz S. P., 2012, MNRAS, 427, 948

Anderson J., 2022, One-Pass HST Photometry with hst1pass, Instrument Science Report ACS 2022-02

André P., Arzoumanian D., Könyves V., Shimajiri Y., Palmeirim P., 2019, A&A, 629, L4

Andrews S. M., Wilner D. J., Hughes A. M., Qi C., Dullemond C. P., 2009, ApJ, 700, 1502

Apai D., Radigan J., Buenzli E., Burrows A., Reid I. N., Jayawardhana R., 2013, ApJ, 768, 121

Apai D., et al., 2016, ApJ, 820, 40

Apai D., et al., 2017, Science, 357, 683

Artigau É., Doyon R., Lafrenière D., Nadeau D., Robert J., Albert L., 2006, ApJ, 651, L57

Artigau É., Bouchard S., Doyon R., Lafrenière D., 2009, ApJ, 701, 1534

Astropy Collaboration et al., 2013, A&A, 558, A33

Astropy Collaboration et al., 2018, AJ, 156, 123

Avenhaus H., Quanz S. P., Meyer M. R., Brittain S. D., Carr J. S., Najita J. R., 2014, ApJ, 790, 56

Babcock H. W., 1953, PASP, 65, 229

Bae J., et al., 2019, ApJ, 884, L41

Baig S., Smart R. L., Jones H. R. A., Gagné J., Pinfield D. J., Cheng G., Moranta L., 2024, MNRAS, 533, 3784

Bailer-Jones C. A. L., Mundt R., 1999, A&A, 348, 800

Bailer-Jones C. A. L., Mundt R., 2001, A&A, 367, 218

Bailer-Jones C. A. L., Rybizki J., Fouesneau M., Demleitner M., Andrae R., 2021, AJ, 161, 147

Bailey V., et al., 2014, ApJ, 780, L4

Bailey V. P., et al., 2023, in Society of Photo-Optical Instrumentation Engineers (SPIE) Conference Series. p. 126800T (arXiv:2309.08672), doi:10.1117/12.2679036

Bally J., Langer W. D., 1982, ApJ, 255, 143

Balmer W. O., et al., 2025, AJ, 169, 30

Baraffe I., Chabrier G., Allard F., Hauschildt P. H., 2002, A&A, 382, 563

Baraffe I., Chabrier G., Barman T. S., Allard F., Hauschildt P. H., 2003, A&A, 402, 701

Baraffe I., Homeier D., Allard F., Chabrier G., 2015, A&A, 577, A42

Bardalez Gagliuffi D. C., et al., 2019, ApJ, 883, 205

Bardalez Gagliuffi D. C., et al., 2025a, ApJ, 984, 74

Bardalez Gagliuffi D. C., et al., 2025b, ApJ, 988, L18

Barman T. S., Macintosh B., Konopacky Q. M., Marois C., 2011a, ApJ, 733, 65

Barman T. S., Macintosh B., Konopacky Q. M., Marois C., 2011b, ApJ, 735, L39

Barman T. S., Konopacky Q. M., Macintosh B., Marois C., 2015, ApJ, 804, 61

Basri G., Reiners A., 2006, AJ, 132, 663

Bate M. R., 2012, MNRAS, 419, 3115

Becklin E. E., Zuckerman B., 1988, Nature, 336, 656

Bedin L. R., King I. R., Anderson J., Piotto G., Salaris M., Cassisi S., Serenelli A., 2008, ApJ, 678, 1279

Beichman C., Gelino C. R., Kirkpatrick J. D., Barman T. S., Marsh K. A., Cushing M. C., Wright E. L., 2013, ApJ, 764, 101

Beiler S. A., Allers K. N., Cushing M., Faherty J., Marley M., Skemer A., 2023, MNRAS, 518, 4870

Bell C. P. M., Mamajek E. E., Naylor T., 2015, MNRAS, 454, 593

Bellini A., Anderson J., Bedin L. R., King I. R., van der Marel R. P., Piotto G., Cool A., 2017, ApJ, 842, 6

Belokurov V., et al., 2020, MNRAS, 496, 1922

Benisty M., et al., 2023, in Inutsuka S., Aikawa Y., Muto T., Tomida K., Tamura M., eds, Astronomical Society of the Pacific Conference Series Vol. 534, Protostars and Planets VII. p. 605 (arXiv:2203.09991), doi:10.48550/arXiv.2203.09991

Bergfors C., et al., 2010, A&A, 520, A54

Bernat D., et al., 2010, ApJ, 715, 724

Best W. M. J., et al., 2015, ApJ, 814, 118

Best W. M. J., et al., 2017a, ApJ, 837, 95

Best W. M. J., Liu M. C., Dupuy T. J., Magnier E. A., 2017b, ApJ, 843, L4

Best W. M. J., Liu M. C., Magnier E. A., Dupuy T. J., 2020, AJ, 159, 257

Beuzit J. L., et al., 2019, A&A, 631, A155

Biller B. A., et al., 2007, ApJS, 173, 143

Biller B. A., et al., 2010, ApJ, 720, L82

Biller B., Allers K., Liu M., Close L. M., Dupuy T., 2011, ApJ, 730, 39

Biller B. A., et al., 2013a, ApJ, 777, 160

Biller B. A., et al., 2013b, ApJ, 778, L10

Biller B. A., et al., 2015, ApJ, 813, L23

Biller B. A., et al., 2018, AJ, 155, 95

Biller B. A., et al., 2021, MNRAS, 503, 743

Biller B. A., et al., 2022, A&A, 658, A145

Biller B. A., et al., 2024, MNRAS, 532, 2207

Blum J., Wurm G., 2008, ARA&A, 46, 21

Blunt S., et al., 2020, AJ, 159, 89

Boffin H. M. J., Watkins S. J., Bhattal A. S., Francis N., Whitworth A. P., 1998, MNRAS, 300, 1189

Bohn A. J., et al., 2019, A&A, 624, A87

Bohn A. J., et al., 2020a, MNRAS, 492, 431

Bohn A. J., et al., 2020b, MNRAS, 492, 431

Bohn A. J., et al., 2020c, ApJ, 898, L16

Bohn A. J., et al., 2021, A&A, 648, A73

Bohn A. J., et al., 2022, A&A, 657, A53

Bonavita M., de Mooij E. J. W., Jayawardhana R., 2013, PASP, 125, 849

Bonavita M., et al., 2022, A&A, 663, A144

Bond I. A., et al., 2004, ApJ, 606, L155

Bonnefoy M., et al., 2016, A&A, 587, A58

Bonnell I. A., 1994, MNRAS, 269, 837

Bonnell I. A., Clark P., Bate M. R., 2008, MNRAS, 389, 1556

Borucki W. J., et al., 2010, Science, 327, 977

Bosman A. D., et al., 2021, ApJS, 257, 7

Boss A. P., 1997, Science, 276, 1836

Boss A. P., 2011, ApJ, 731, 74

Bourdarot G., 2022, in Mérand A., Sallum S., Sanchez-Bermudez J., eds, Society of Photo-Optical Instrumentation Engineers (SPIE) Conference Series Vol. 12183, Optical and Infrared Interferometry and Imaging VIII. p. 1218312, doi:10.1117/12.2635601

Bouvier J., Matt S. P., Mohanty S., Scholz A., Stassun K. G., Zanni C., 2014, in Beuther H., Klessen R. S., Dullemond C. P., Henning T., eds, Protostars and Planets VI. p. 433 (arXiv:1309.7851), doi:10.2458/azu_uapress_9780816531240-ch019

Bouy H., Brandner W., Martín E. L., Delfosse X., Allard F., Basri G., 2003, AJ, 126, 1526

Bouy H., et al., 2022, A&A, 664, A111

Bouy H., et al., 2025, arXiv e-prints, p. arXiv:2506.14380

Bowler B. P., 2016a, PASP, 128, 102001

Bowler B. P., 2016b, PASP, 128, 102001

Bowler B. P., Liu M. C., Dupuy T. J., Cushing M. C., 2010, ApJ, 723, 850

Bowler B. P., Liu M. C., Shkolnik E. L., Dupuy T. J., 2013, ApJ, 774, 55

Bowler B. P., et al., 2017, AJ, 153, 18

Bowler B. P., Blunt S. C., Nielsen E. L., 2020a, AJ, 159, 63

Bowler B. P., Zhou Y., Morley C. V., Kataria T., Bryan M. L., Benneke B., Batygin K., 2020b, ApJ, 893, L30

Bradley L., et al., 2024, astropy/photutils: 2.0.2, doi:10.5281/zenodo.13989456, https://doi.org/10.5281/zenodo.13989456

Brandl B., et al., 2021, The Messenger, 182, 22

Brandner W., et al., 2000, AJ, 120, 950

Brandt T. D., 2021, ApJS, 254, 42

Brandt T. D., Dupuy T. J., Li Y., Brandt G. M., Zeng Y., Michalik D., Bardalez Gagliuffi D. C., Raposo-Pulido V., 2021a, AJ, 162, 186

Brandt G. M., Brandt T. D., Dupuy T. J., Michalik D., Marleau G.-D., 2021b, ApJ, 915, L16

Buenzli E., et al., 2012, ApJ, 760, L31

Buenzli E., Apai D., Radigan J., Reid I. N., Flateau D., 2014, ApJ, 782, 77

Buenzli E., Saumon D., Marley M. S., Apai D., Radigan J., Bedin L. R., Reid I. N., Morley C. V., 2015a, ApJ, 798, 127

Buenzli E., Marley M. S., Apai D., Saumon D., Biller B. A., Crossfield I. J. M., Radigan J., 2015b, ApJ, 812, 163

Burgasser A. J., Kirkpatrick J. D., Brown M. E., 2002, in American Astronomical Society Meeting Abstracts #200. p. 11.05

Burgasser A. J., Kirkpatrick J. D., Reid I. N., Brown M. E., Miskey C. L., Gizis J. E., 2003, ApJ, 586, 512

Burgasser A. J., Kirkpatrick J. D., Cruz K. L., Reid I. N., Leggett S. K., Liebert J., Burrows A., Brown M. E., 2006, ApJS, 166, 585

Burgasser A. J., Reid I. N., Siegler N., Close L., Allen P., Lowrance P., Gizis J., 2007, in Reipurth B., Jewitt D., Keil K., eds, Protostars and Planets V. p. 427 (arXiv:astro-ph/0602122), doi:10.48550/arXiv.astro-ph/0602122

Burgasser A. J., et al., 2010, ApJ, 725, 1405

Burgasser A. J., Gelino C. R., Cushing M. C., Kirkpatrick J. D., 2012, ApJ, 745, 26

Burgasser A. J., Sheppard S. S., Luhman K. L., 2013, ApJ, 772, 129

Burgasser A. J., et al., 2014, ApJ, 785, 48

Burningham B., et al., 2010, MNRAS, 404, 1952

Burningham B., et al., 2013, MNRAS, 433, 457

Burrows A., et al., 1997, ApJ, 491, 856

Burrows A., Hubbard W. B., Lunine J. I., Liebert J., 2001, Reviews of Modern Physics, 73, 719

Burrows A., Sudarsky D., Hubeny I., 2006, ApJ, 640, 1063

Calissendorff P., et al., 2023, ApJ, 947, L30

Cantalloube F., et al., 2015, A&A, 582, A89

Cardelli J. A., Clayton G. C., Mathis J. S., 1989, ApJ, 345, 245

Carter E. J., Stamatellos D., 2023, MNRAS, 525, 1912

Castro-Ginard A., et al., 2024, arXiv e-prints, p. arXiv:2404.14127

Chabrier G., 2001, ApJ, 554, 1274

Chabrier G., Baraffe I., 1997, A&A, 327, 1039

Chabrier G., Baraffe I., 2000, ARA&A, 38, 337

Chabrier G., Baraffe I., Allard F., Hauschildt P., 2000, ApJ, 542, 464

Chabrier G., Johansen A., Janson M., Rafikov R., 2014, in Beuther H., Klessen R. S., Dullemond C. P., Henning T., eds, Protostars and Planets VI. pp 619–642 (arXiv:1401.7559), doi:10.2458/azu_uapress_9780816531240-ch027

Chabrier G., Baraffe I., Phillips M., Debras F., 2023, A&A, 671, A119

Chambers J., 2021, ApJ, 914, 102

Chambers K. C., et al., 2016, arXiv e-prints, p. arXiv:1612.05560

Chauvin G., 2018, in Close L. M., Schreiber L., Schmidt D., eds, Society of Photo-Optical Instrumentation Engineers (SPIE) Conference Series Vol. 10703, Adaptive Optics Systems VI. p. 1070305 (arXiv:1808.02454), doi:10.1117/12.2314273

Chauvin G., et al., 2005, A&A, 438, L29

Chauvin G., et al., 2017, A&A, 605, L9

Chen X., et al., 2025, MNRAS, 539, 3758

Chomez A., et al., 2025, A&A, 697, A99

Clarke F. J., Hodgkin S. T., Oppenheimer B. R., Robertson J., Haubois X., 2008, MNRAS, 386, 2009

Close L. M., Siegler N., Freed M., Biller B., 2003, ApJ, 587, 407

Close L. M., et al., 2013, ApJ, 774, 94

Close L. M., et al., 2018, in Adaptive Optics Systems VI. pp 1227–1236

Codona J. L., Kenworthy M. A., Hinz P. M., Angel J. R. P., Woolf N. J., 2006, in McLean I. S., Iye M., eds, Society of Photo-Optical Instrumentation Engineers (SPIE) Conference Series Vol. 6269, Society of Photo-Optical Instrumentation Engineers (SPIE) Conference Series. p. 62691N, doi:10.1117/12.672727

Cosentino R., et al., 2014, in Ramsay S. K., McLean I. S., Takami H., eds, Society of Photo-Optical Instrumentation Engineers (SPIE) Conference Series Vol. 9147, Ground-based and Airborne Instrumentation for Astronomy V. p. 91478C, doi:10.1117/12.2055813

Cowley S. W. H., Bunce E. J., 2001, Planet. Space Sci., 49, 1067

Crepp J. R., et al., 2012, ApJ, 751, 97

Crepp J. R., Gonzales E. J., Bechter E. B., Montet B. T., Johnson J. A., Piskorz D., Howard A. W., Isaacson H., 2016, ApJ, 831, 136

Croll B., Muirhead P. S., Lichtman J., Han E., Dalba P. A., Radigan J., 2016, arXiv e-prints, p. arXiv:1609.03587

Cumming A., Butler R. P., Marcy G. W., Vogt S. S., Wright J. T., Fischer D. A., 2008, PASP, 120, 531

Currie T., et al., 2014, ApJ, 795, 133

Currie T., et al., 2020, in Schreiber L., Schmidt D., Vernet E., eds, Society of Photo-Optical Instrumentation Engineers (SPIE) Conference Series Vol. 11448, Adaptive Optics Systems VII. p. 114487H (arXiv:2012.05241), doi:10.1117/12.2576349

Currie T., et al., 2023, Science, 380, 198

Cushing M. C., Rayner J. T., Vacca W. D., 2005, ApJ, 623, 1115

Cushing M. C., et al., 2008, ApJ, 678, 1372

Cushing M. C., et al., 2011, ApJ, 743, 50

Cushing M. C., et al., 2016, ApJ, 823, 152

Czekaj M. A., Robin A. C., Figueras F., Luri X., Haywood M., 2014, A&A, 564, A102

Daffern-Powell E. C., Parker R. J., Quanz S. P., 2022, MNRAS, 514, 920

Davies R., et al., 2023, A&A, 674, A207

De Furio M., Meyer M. R., Reiter M., Monnier J., Kraus A., Dupuy T., 2022, ApJ, 925, 112

De Rosa R. J., Nielsen E. L., Wahhaj Z., Ruffio J.-B., Kalas P. G., Peck A. E., Hirsch L. A., Roberson W., 2023, A&A, 672, A94

Desidera S., et al., 2021, A&A, 651, A70

Dias W. S., Alessi B. S., Moitinho A., Lépine J. R. D., 2002, A&A, 389, 871

Dickson-Vandervelde D. A., Wilson E. C., Kastner J. H., 2020, Research Notes of the American Astronomical Society, 4, 25

Dipierro G., Price D., Laibe G., Hirsh K., Cerioli A., Lodato G., 2015, MNRAS, 453, L73

Dodson-Robinson S. E., Veras D., Ford E. B., Beichman C. A., 2009, ApJ, 707, 79

Dohlen K., et al., 2008, in McLean I. S., Casali M. M., eds, Society of Photo-Optical Instrumentation Engineers (SPIE) Conference Series Vol. 7014, Ground-based and Airborne Instrumentation for Astronomy II. p. 70143L, doi:10.1117/12.789786

Dong R., Zhu Z., Whitney B., 2015, ApJ, 809, 93

Drążkowska J., et al., 2023, in Inutsuka S., Aikawa Y., Muto T., Tomida K., Tamura M., eds, Astronomical Society of the Pacific Conference Series Vol. 534, Protostars and Planets VII. p. 717 (arXiv:2203.09759), doi:10.48550/arXiv.2203.09759

Dubber S., et al., 2021, MNRAS, 505, 4215

Duchêne G., Kraus A., 2013, ARA&A, 51, 269

Dupuy T. J., Liu M. C., 2012, ApJS, 201, 19

Dupuy T. J., Liu M. C., 2017, ApJS, 231, 15

Dupuy T. J., Liu M. C., Ireland M. J., 2009, ApJ, 699, 168

Dupuy T. J., Liu M. C., Evans E. L., Best W. M. J., Pearce L. A., Sanghi A., Phillips M. W., Bardalez Gagliuffi D. C., 2023, MNRAS, 519, 1688

Duquennoy A., Mayor M., 1991, A&A, 248, 485

Durisen R. H., Boss A. P., Mayer L., Nelson A. F., Quinn T., Rice W. K. M., 2007, in Reipurth B., Jewitt D., Keil K., eds, Protostars and Planets V. p. 607 (arXiv:astro-ph/0603179), doi:10.48550/arXiv.astro-ph/0603179

Dye S., et al., 2018, MNRAS, 473, 5113

Elias J. H., Joyce R. R., Liang M., Muller G. P., Hileman E. A., George J. R., 2006, in McLean I. S., Iye M., eds, Society of Photo-Optical Instrumentation Engineers (SPIE) Conference Series Vol. 6269, Ground-based and Airborne Instrumentation for Astronomy. p. 62694C, doi:10.1117/12.671817

Epchtein N., et al., 1999, A&A, 349, 236

Eriksson S. C., Janson M., Calissendorff P., 2019, A&A, 629, A145

Esplin T. L., Luhman K. L., 2017, AJ, 154, 134

Esplin T. L., Luhman K. L., 2019, AJ, 158, 54

Esplin T. L., Luhman K. L., Cushing M. C., Hardegree-Ullman K. K., Trucks J. L., Burgasser A. J., Schneider A. C., 2016, ApJ, 832, 58

Esposito S., et al., 2010, in Ellerbroek B. L., Hart M., Hubin N., Wizinowich P. L., eds, Society of Photo-Optical Instrumentation Engineers (SPIE) Conference Series Vol. 7736, Adaptive Optics Systems II. p. 773609, doi:10.1117/12.858194

Faherty J. K., et al., 2016, ApJS, 225, 10

Faherty J. K., et al., 2024, Nature, 628, 511

Fedele D., van den Ancker M. E., Henning T., Jayawardhana R., Oliveira J. M., 2010, A&A, 510, A72

Feroz F., Hobson M. P., Bridges M., 2009, MNRAS, 398, 1601

Fetherolf T., et al., 2023, ApJS, 268, 4

Filippazzo J. C., Rice E. L., Faherty J., Cruz K. L., Van Gordon M. M., Looper D. L., 2015, ApJ, 810, 158

Fischer D. A., Marcy G. W., 1992, ApJ, 396, 178

Fischer D. A., et al., 2016, PASP, 128, 066001

Flasseur O., Denis L., Thiébaut É., Langlois M., 2018, A&A, 618, A138

Follette K. B., 2023, PASP, 135, 093001

Fontanive C., Biller B., Bonavita M., Allers K., 2018, MNRAS, 479, 2702

Fontanive C., Mužić K., Bonavita M., Biller B., 2019, MNRAS, 490, 1120

Fontanive C., et al., 2020, ApJ, 905, L14

Fontanive C., Bedin L. R., Bardalez Gagliuffi D. C., 2021, MNRAS, 501, 911

Fontanive C., Bedin L. R., De Furio M., Biller B., Anderson J., Bonavita M., Allers K., Pantoja B., 2023, MNRAS, 526, 1783

Foreman-Mackey D., Hogg D. W., Lang D., Goodman J., 2013, PASP, 125, 306

Forgan D., Parker R. J., Rice K., 2015, MNRAS, 447, 836

Forgan D. H., Hall C., Meru F., Rice W. K. M., 2018, MNRAS, 474, 5036

Franson K., et al., 2023, ApJ, 950, L19

Franson K., et al., 2024, ApJ, 974, L11

Fried D. L., 1966, Journal of the Optical Society of America (1917-1983), 56, 1372

Fujii M. S., Hori Y., 2019, A&A, 624, A110

Fusco T., et al., 2006, Optics Express, 14, 7515

Gagné J., 2024, PASP, 136, 063001

Gagné J., et al., 2015, ApJS, 219, 33

Gagné J., et al., 2017a, ApJS, 228, 18

Gagné J., et al., 2017b, ApJ, 841, L1

Gagné J., Allers K. N., Theissen C. A., Faherty J. K., Bardalez Gagliuffi D., Artigau É., 2018a, ApJ, 854, L27

Gagné J., et al., 2018b, ApJ, 856, 23

Gaia Collaboration et al., 2016, A&A, 595, A1

Gaia Collaboration et al., 2018, A&A, 616, A1

Gaia Collaboration et al., 2021a, A&A, 649, A1

Gaia Collaboration et al., 2021b, A&A, 649, A1

Galicher R., et al., 2016, A&A, 594, A63

Galli P. A. B., Bouy H., Olivares J., Miret-Roig N., Sarro L. M., Barrado D., Berihuete A., 2021, A&A, 654, A122

Gauza B., Béjar V. J. S., Pérez-Garrido A., Zapatero Osorio M. R., Lodieu N., Rebolo R., Pallé E., Nowak G., 2015, ApJ, 804, 96

Gelino C. R., Marley M. S., Holtzman J. A., Ackerman A. S., Lodders K., 2002, ApJ, 577, 433

Gillon M., Triaud A. H. M. J., Jehin E., Delrez L., Opitom C., Magain P., Lendl M., Queloz D., 2013, A&A, 555, L5

Gillon M., et al., 2017, Nature, 542, 456

Girardin F., Artigau É., Doyon R., 2013, ApJ, 767, 61

Goldreich P., Lithwick Y., Sari R., 2004, ARA&A, 42, 549

Golimowski D. A., et al., 2004, AJ, 127, 3516

Gonzaga S., Hack W., Fruchter A., Mack J., 2012, The DrizzlePac Handbook

González Picos D., et al., 2024, A&A, 689, A212

González Picos D., Snellen I. A. G., de Regt S., Landman R., Zhang Y., Gandhi S., Sánchez-López A., 2025, A&A, 693, A298

Goodwin S. P., Whitworth A. P., Ward-Thompson D., 2004, A&A, 414, 633

Gould A., et al., 2006, ApJ, 644, L37

Gratton R., et al., 2024, A&A, 685, A119

Gratton R., et al., 2025, A&A, 694, A175

Gravity Collaboration et al., 2017, A&A, 602, A94

Gravity Collaboration et al., 2019, A&A, 623, L11

Gray R. O., Kaye A. B., 1999, AJ, 118, 2993

Guyon O., 2018, ARA&A, 56, 315

Guyon O., Pluzhnik E. A., Kuchner M. J., Collins B., Ridgway S. T., 2006, ApJS, 167, 81

Haffert S. Y., Bohn A. J., de Boer J., Snellen I. A. G., Brinchmann J., Girard J. H., Keller C. U., Bacon R., 2019, Nature Astronomy, 3, 749

Haffert S. Y., et al., 2022, arXiv preprint arXiv:2208.02720

Haisch Jr. K. E., Lada E. A., Lada C. J., 2001, ApJ, 553, L153

Hall C., Forgan D., Rice K., 2017, MNRAS, 470, 2517

Hallinan G., et al., 2015, Nature, 523, 568

Hardy J. W., 1998, Adaptive Optics for Astronomical Telescopes

Hayashi C., Nakano T., 1963, Progress of Theoretical Physics, 30, 460

Heinze A. N., Metchev S., Kellogg K., 2015, ApJ, 801, 104

Helling C., et al., 2008, MNRAS, 391, 1854

Helling C., Jardine M., Mokler F., 2011, ApJ, 737, 38

Hennebelle P., Teyssier R., 2008, A&A, 477, 25

Henry G. W., Marcy G. W., Butler R. P., Vogt S. S., 2000, ApJ, 529, L41

Hillenbrand L. A., 1997, AJ, 113, 1733

Hoch K. K. W., et al., 2025, Nature, 643, 938

Høg E., et al., 2000, A&A, 355, L27

Hunt E. L., Reffert S., 2023, A&A, 673, A114

Hunt E. L., Reffert S., 2024, A&A, 686, A42

Hunziker S., et al., 2020, A&A, 634, A69

Hurley J. R., Shara M. M., 2002, ApJ, 565, 1251

Hwang H.-C., Ting Y.-S., Zakamska N. L., 2022, MNRAS, 512, 3383

Ireland M. J., Kraus A., Martinache F., Law N., Hillenbrand L. A., 2011, ApJ, 726, 113

Ivanova N., Belczynski K., Fregeau J. M., Rasio F. A., 2005, MNRAS, 358, 572

Janson M., et al., 2012, ApJ, 754, 44

Janson M., et al., 2021a, Nature, 600, 231

Janson M., et al., 2021b, A&A, 646, A164

Jiang H., Ormel C. W., 2023, MNRAS, 518, 3877

Jin S., Li S., Isella A., Li H., Ji J., 2016, ApJ, 818, 76

Johnson B. M., Gammie C. F., 2003, ApJ, 597, 131

Johnson J. A., Aller K. M., Howard A. W., Crepp J. R., 2010, PASP, 122, 905

Jovanovic N., et al., 2015, PASP, 127, 890

Karalidi T., Marley M., Fortney J. J., Morley C., Saumon D., Lupu R., Visscher C., Freedman R., 2021, ApJ, 923, 269

Kasper M., Apai D., Janson M., Brandner W., 2007, A&A, 472, 321

Kellogg K., Metchev S., Geißler K., Hicks S., Kirkpatrick J. D., Kurtev R., 2015, AJ, 150, 182

Kellogg K., Metchev S., Gagné J., Faherty J., 2016, ApJ, 821, L15

Kenworthy M. A., Codona J. L., Hinz P. M., Angel J. R. P., Heinze A., Sivanandam S., 2007, ApJ, 660, 762

Kenyon S. J., Gómez M., Whitney B. A., 2008, in Reipurth B., ed., , Vol. 4, Handbook of Star Forming Regions, Volume I. p. 405, doi:10.48550/arXiv.0810.1298

Keppler M., et al., 2018, A&A, 617, A44

Kerr R. M. P., Rizzuto A. C., Kraus A. L., Offner S. S. R., 2021, ApJ, 917, 23

Kerr R., Kraus A. L., Murphy S. J., Krolikowski D. M., Bedding T. R., Rizzuto A. C., 2022, ApJ, 941, 143

Kervella P., Arenou F., Mignard F., Thévenin F., 2019, A&A, 623, A72

Kiraga M., 2012, Acta Astron., 62, 67

Kirkpatrick J. D., 2005, ARA&A, 43, 195

Kirkpatrick J. D., Henry T. J., McCarthy Jr. D. W., 1991, ApJS, 77, 417

Kirkpatrick J. D., et al., 1999, ApJ, 519, 802

Kirkpatrick J. D., Barman T. S., Burgasser A. J., McGovern M. R., McLean I. S., Tinney C. G., Lowrance P. J., 2006, ApJ, 639, 1120

Kirkpatrick J. D., et al., 2011, ApJS, 197, 19

Kley W., Nelson R. P., 2012, ARA&A, 50, 211

Knapp G. R., et al., 2004, AJ, 127, 3553

Koen C., Matsunaga N., Menzies J., 2004, MNRAS, 354, 466

Koen C., Tanabé T., Tamura M., Kusakabe N., 2005, MNRAS, 362, 727

Konopacky Q. M., Barman T. S., Macintosh B. A., Marois C., 2013, Science, 339, 1398

Konopacky Q. M., Marois C., Macintosh B. A., Galicher R., Barman T. S., Metchev S. A., Zuckerman B., 2016a, AJ, 152, 28

Konopacky Q. M., et al., 2016b, ApJ, 829, L4

Kraft R. P., Burrows D. N., Nousek J. A., 1991, ApJ, 374, 344

Kratter K., Lodato G., 2016, ARA&A, 54, 271

Kratter K. M., Perets H. B., 2012, ApJ, 753, 91

Kraus A. L., White R. J., Hillenbrand L. A., 2005, ApJ, 633, 452

Kraus A. L., Ireland M. J., Martinache F., Hillenbrand L. A., 2011, ApJ, 731, 8

Kroupa P., 2001, MNRAS, 322, 231

Krumholz M. R., Klein R. I., McKee C. F., 2012, ApJ, 754, 71

Kühnle H., et al., 2025, A&A, 695, A224

Kumar S. S., 1963, ApJ, 137, 1121

Lacour S., et al., 2021, A&A, 654, L2

Lafrenière D., Marois C., Doyon R., Nadeau D., Artigau É., 2007a, ApJ, 660, 770

Lafrenière D., et al., 2007b, ApJ, 670, 1367

Lafrenière D., Jayawardhana R., van Kerkwijk M. H., 2008, ApJ, 689, L153

Lagrange A. M., et al., 2010, Science, 329, 57

Lagrange A. M., et al., 2025, Nature, 642, 905

Lambrechts M., Johansen A., 2012, A&A, 544, A32

Lambrechts M., Johansen A., 2014, A&A, 572, A107

Lange J. U., 2023, MNRAS, 525, 3181

Langer W. D., Graedel T. E., Frerking M. A., Armentrout P. B., 1984, ApJ, 277, 581

Langlois M., et al., 2014, in Ramsay S. K., McLean I. S., Takami H., eds, Society of Photo-Optical Instrumentation Engineers (SPIE) Conference Series Vol. 9147, Ground-based and Airborne Instrumentation for Astronomy V. p. 91479P, doi:10.1117/12.2055535

Langlois M., et al., 2021, A&A, 651, A71

Larson R. B., 1972, MNRAS, 156, 437

Lavie B., et al., 2017, AJ, 154, 91

Lawrence A., et al., 2007, MNRAS, 379, 1599

Lee M. H., Peale S. J., 2002, ApJ, 567, 596

Leggett S. K., et al., 2016, ApJ, 830, 141

Lew B. W. P., et al., 2016, ApJ, 829, L32

Limbach M. A., Vos J. M., Winn J. N., Heller R., Mason J. C., Schneider A. C., Dai F., 2021, ApJ, 918, L25

Liu M. C., et al., 2013, ApJ, 777, L20

Liu M. C., Dupuy T. J., Allers K. N., 2016, ApJ, 833, 96

Liu J., Fang M., Tian H., Liu C., Yang C., Xue X., 2021, ApJS, 254, 20

Liu P., et al., 2024, MNRAS, 527, 6624

Liu P., Biller B. A., Kenworthy M. A., Fontanive C., Kerr R. M. P., Stolker T., Ginski C., 2025a, A&A, 696, L10

Liu P., et al., 2025b, A&A, 699, A78

Lo Curto G., et al., 2015, The Messenger, 162, 9

Lomb N. R., 1976, Ap&SS, 39, 447

Long J. D., et al., 2025, AJ, 169, 36

Lucas P. W., Roche P. F., 2000, MNRAS, 314, 858

Lucas P. W., Roche P. F., Allard F., Hauschildt P. H., 2001, MNRAS, 326, 695

Luhman K. L., 2012, ARA&A, 50, 65

Luhman K. L., 2013, ApJ, 767, L1

Luhman K. L., 2014, ApJ, 786, L18

Luhman K. L., 2022, AJ, 163, 24

Luhman K. L., 2023, AJ, 165, 37

Luhman K. L., 2024, AJ, 168, 230

Luhman K. L., 2025, MNRAS, 542, L126

Luhman K. L., Esplin T. L., Loutrel N. P., 2016, ApJ, 827, 52

Luhman K. L., Mamajek E. E., Shukla S. J., Loutrel N. P., 2017, AJ, 153, 46

Luhman K. L., Alves de Oliveira C., Baraffe I., Chabrier G., Geballe T. R., Parker R. J., Pendleton Y. J., Tremblin P., 2024, AJ, 167, 19

Lyot B., 1939, MNRAS, 99, 580

Lyra W., Johansen A., Klahr H., Piskunov N., 2009, A&A, 493, 1125

Macintosh B., et al., 2014, Proceedings of the National Academy of Science, 111, 12661

Macintosh B., et al., 2015, Science, 350, 64

Madhusudhan N., 2019, ARA&A, 57, 617

Mainzer A., et al., 2014, ApJ, 792, 30

Maire A. L., et al., 2020, A&A, 633, L2

Maire A.-L., et al., 2021, Journal of Astronomical Telescopes, Instruments, and Systems, 7, 035004

Males J. R., et al., 2016, in Marchetti E., Close L. M., Véran J.-P., eds, Society of Photo-Optical Instrumentation Engineers (SPIE) Conference Series Vol. 9909, Adaptive Optics Systems V. p. 990952, doi:10.1117/12.2234105

Males J. R., et al., 2022, in Adaptive Optics Systems VIII. pp 61–70

Mamajek E. E., 2016, in Kastner J. H., Stelzer B., Metchev S. A., eds, IAU Symposium Vol. 314, Young Stars & Planets Near the Sun. pp 21–26 (arXiv:1507.06697), doi:10.1017/S1743921315006250

Manjavacas E., et al., 2014, A&A, 564, A55

Manjavacas E., et al., 2018, AJ, 155, 11

Manjavacas E., et al., 2019a, AJ, 157, 101

Manjavacas E., et al., 2019b, ApJ, 875, L15

Marley M. S., Robinson T. D., 2015, ARA&A, 53, 279

Marley M. S., Saumon D., Goldblatt C., 2010, ApJ, 723, L117

Marley M. S., Saumon D., Cushing M., Ackerman A. S., Fortney J. J., Freedman R., 2012, ApJ, 754, 135

Marley M. S., et al., 2021, ApJ, 920, 85

Marocco F., et al., 2021, ApJS, 253, 8

Marois C., Lafrenière D., Doyon R., Macintosh B., Nadeau D., 2006, ApJ, 641, 556

Marois C., Macintosh B., Barman T., Zuckerman B., Song I., Patience J., Lafrenière D., Doyon R., 2008, Science, 322, 1348

Marois C., Zuckerman B., Konopacky Q. M., Macintosh B., Barman T., 2010, Nature, 468, 1080

Martín E. L., Zapatero Osorio M. R., Lehto H. J., 2001, ApJ, 557, 822

Matthews E. C., et al., 2024, Nature, 633, 789

Mawet D., Pueyo L., Moody D., Krist J., Serabyn E., 2010, in Atad-Ettedgui E., Lemke D., eds, Society of Photo-Optical Instrumentation Engineers (SPIE) Conference Series Vol. 7739, Modern Technologies in Space- and Ground-based Telescopes and Instrumentation. p. 773914, doi:10.1117/12.858240

Mawet D., et al., 2012, in Clampin M. C., Fazio G. G., MacEwen H. A., Oschmann Jacobus M. J., eds, Society of Photo-Optical Instrumentation Engineers (SPIE) Conference Series Vol. 8442, Space Telescopes and Instrumentation 2012: Optical, Infrared, and Millimeter Wave. p. 844204 (arXiv:1207.5481), doi:10.1117/12.927245

Maxted P. F. L., Jeffries R. D., 2005, MNRAS, 362, L45

Mayor M., Queloz D., 1995, Nature, 378, 355

McCarthy A. M., et al., 2025, ApJ, 981, L22

Meisner A. M., et al., 2020, ApJ, 889, 74

Mesa D., et al., 2023, A&A, 672, A93

Metchev S. A., Hillenbrand L. A., 2006, ApJ, 651, 1166

Metchev S. A., et al., 2015, ApJ, 799, 154

Miles-Páez P. A., Metchev S., Luhman K. L., Marengo M., Hulsebus A., 2017, AJ, 154, 262

Miles-Páez P. A., et al., 2019, ApJ, 883, 181

Miles B. E., et al., 2023, ApJ, 946, L6

Miret-Roig N., et al., 2022, Nature Astronomy, 6, 89

Moeckel N., Bally J., 2007, ApJ, 656, 275

Mollière P., Snellen I. A. G., 2019, A&A, 622, A139

Mollière P., et al., 2020, A&A, 640, A131

Moore K., Scholz A., Jayawardhana R., 2019, ApJ, 872, 159

Moorwood A., Cuby J. G., Lidman C., 1998, The Messenger, 91, 9

Morales-Calderón M., et al., 2006, ApJ, 653, 1454

Morley C. V., Fortney J. J., Marley M. S., Visscher C., Saumon D., Leggett S. K., 2012, ApJ, 756, 172

Morley C. V., Marley M. S., Fortney J. J., Lupu R., 2014, ApJ, 789, L14

Morley C. V., Skemer A. J., Miles B. E., Line M. R., Lopez E. D., Brogi M., Freedman R. S., Marley M. S., 2019, ApJ, 882, L29

Morley C. V., et al., 2024, ApJ, 975, 59

Mortier A., Faria J. P., Correia C. M., Santerne A., Santos N. C., 2015, BGLS: A Bayesian formalism for the generalised Lomb-Scargle periodogram (ascl:1504.020)

Motte F., Andre P., Neri R., 1998, A&A, 336, 150

Mróz P., et al., 2017, Nature, 548, 183

Mukherjee S., et al., 2024, ApJ, 963, 73

Müller A., et al., 2018, A&A, 617, L2

Muterspaugh M. W., et al., 2010, AJ, 140, 1657

Nakajima T., Oppenheimer B. R., Kulkarni S. R., Golimowski D. A., Matthews K., Durrance S. T., 1995, Nature, 378, 463

Nardiello D., et al., 2018, MNRAS, 481, 3382

Naud M.-E., et al., 2014, ApJ, 787, 5

Naud M.-E., Artigau É., Rowe J. F., Doyon R., Malo L., Albert L., Gagné J., Bouchard S., 2017, AJ, 154, 138

Nielsen E. L., et al., 2012, ApJ, 750, 53

Nielsen E. L., et al., 2013, ApJ, 776, 4

Nielsen E. L., et al., 2017, AJ, 154, 218

Nielsen E. L., et al., 2019, AJ, 158, 13

Noll K. S., Geballe T. R., Leggett S. K., Marley M. S., 2000, ApJ, 541, L75

Oasa Y., Tamura M., Sugitani K., 1999, ApJ, 526, 336

Öberg K. I., Bergin E. A., 2021, Phys. Rep., 893, 1

Öberg K. I., Murray-Clay R., Bergin E. A., 2011, ApJ, 743, L16

Offner S. S. R., Moe M., Kratter K. M., Sadavoy S. I., Jensen E. L. N., Tobin J. J., 2023, in Inutsuka S., Aikawa Y., Muto T., Tomida K., Tamura M., eds, Astronomical Society of the Pacific Conference Series Vol. 534, Protostars and Planets VII. p. 275 (arXiv:2203.10066), doi:10.48550/arXiv.2203.10066

Ostriker E. C., 1994, ApJ, 424, 292

Padoan P., Nordlund Å., 2004, ApJ, 617, 559

Papaloizou J. C., Savonije G. J., 1991, MNRAS, 248, 353

Parker R. J., Quanz S. P., 2012, MNRAS, 419, 2448

Parker R. J., Goodwin S. P., Diamond J. L., 2025, MNRAS, 540, L104

Peña Ramírez K., Béjar V. J. S., Zapatero Osorio M. R., Petr-Gotzens M. G., Martín E. L., 2012, ApJ, 754, 30

Pearson S. G., McCaughrean M. J., 2023, arXiv e-prints, p. arXiv:2310.01231

Pecaut M. J., Mamajek E. E., 2013, ApJS, 208, 9

Pecaut M. J., Mamajek E. E., 2016, MNRAS, 461, 794

Pecaut M. J., Mamajek E. E., Bubar E. J., 2012, ApJ, 746, 154

Pepe F., et al., 2004, A&A, 423, 385

Pepe F., et al., 2021, A&A, 645, A96

Perets H. B., Kouwenhoven M. B. N., 2012, ApJ, 750, 83

Peretti S., et al., 2019, A&A, 631, A107

Perrin M. D., et al., 2015, ApJ, 799, 182

Perryman M. A. C., et al., 1997, A&A, 323, L49

Phillips M. W., et al., 2020, A&A, 637, A38

Pinilla P., Benisty M., Birnstiel T., 2012, A&A, 545, A81

Pinte C., et al., 2019, Nature Astronomy, 3, 1109

Piscarreta L., Mužić K., Almendros-Abad V., Scholz A., 2024, A&A, 686, A37

Planck Collaboration et al., 2014, A&A, 571, A11

Pollack J. B., Hubickyj O., Bodenheimer P., Lissauer J. J., Podolak M., Greenzweig Y., 1996, Icarus, 124, 62

Preibisch T., Mamajek E., 2008, in Reipurth B., ed., , Vol. 5, Handbook of Star Forming Regions, Volume II. p. 235

Pueyo L., et al., 2012, ApJS, 199, 6

Puget P., et al., 2004, in Moorwood A. F. M., Iye M., eds, Society of Photo-Optical Instrumentation Engineers (SPIE) Conference Series Vol. 5492, Ground-based Instrumentation for Astronomy. pp 978–987, doi:10.1117/12.551097

Racine R., Walker G. A. H., Nadeau D., Doyon R., Marois C., 1999, PASP, 111, 587

Radigan J., 2014, ApJ, 797, 120

Radigan J., Jayawardhana R., Lafrenière D., Artigau É., Marley M., Saumon D., 2012, ApJ, 750, 105

Radigan J., Lafrenière D., Jayawardhana R., Artigau E., 2014, ApJ, 793, 75

Rafikov R. R., 2005, ApJ, 621, L69

Raghavan D., et al., 2010, ApJS, 190, 1

Ratzenböck S., et al., 2023, A&A, 678, A71

Rayner J. T., Toomey D. W., Onaka P. M., Denault A. J., Stahlberger W. E., Vacca W. D., Cushing M. C., Wang S., 2003, PASP, 115, 362

Reggiani M., Robberto M., Da Rio N., Meyer M. R., Soderblom D. R., Ricci L., 2011, A&A, 534, A83

Reid I. N., Gizis J. E., Hawley S. L., 2002, AJ, 124, 2721

Reipurth B., Clarke C., 2001, AJ, 122, 432

Reipurth B., Mikkola S., 2015, AJ, 149, 145

Rich E. A., Currie T., Wisniewski J. P., Hashimoto J., Brandt T. D., Carson J. C., Kuzuhara M., Uyama T., 2016, ApJ, 830, 114

Ricker G. R., et al., 2014, in Oschmann Jr. J. M., Clampin M., Fazio G. G., MacEwen H. A., eds, Society of Photo-Optical Instrumentation Engineers (SPIE) Conference Series Vol. 9143, Space Telescopes and Instrumentation 2014: Optical, Infrared, and Millimeter Wave. p. 914320 (arXiv:1406.0151), doi:10.1117/12.2063489

Riello M., et al., 2021, A&A, 649, A3

Robinson T. D., Marley M. S., 2014, ApJ, 785, 158

Roellig T. L., et al., 2004, ApJS, 154, 418

Rouan D., Riaud P., Boccaletti A., Clénet Y., Labeyrie A., 2000, PASP, 112, 1479

Ruane G., et al., 2018, in Lystrup M., MacEwen H. A., Fazio G. G., Batalha N., Siegler N., Tong E. C., eds, Society of Photo-Optical Instrumentation Engineers (SPIE) Conference Series Vol. 10698, Space Telescopes and Instrumentation 2018: Optical, Infrared, and Millimeter Wave. p. 106982S (arXiv:1807.07042), doi:10.1117/12.2312948

Ruane G., et al., 2019, AJ, 157, 118

Samland M., et al., 2017, A&A, 603, A57

Samland M., Bouwman J., Hogg D. W., Brandner W., Henning T., Janson M., 2021, A&A, 646, A24

Savvidou S., Bitsch B., 2023, A&A, 679, A42

Scalco M., et al., 2021, MNRAS, 505, 3549

Scargle J. D., 1982, ApJ, 263, 835

Schmid H. M., et al., 2018, A&A, 619, A9

Schneider A. C., et al., 2015, ApJ, 804, 92

Schneider A. C., Windsor J., Cushing M. C., Kirkpatrick J. D., Wright E. L., 2016, ApJ, 822, L1

Schneider A. C., Windsor J., Cushing M. C., Kirkpatrick J. D., Shkolnik E. L., 2017, AJ, 153, 196

Schneider A. C., Hardegree-Ullman K. K., Cushing M. C., Kirkpatrick J. D., Shkolnik E. L., 2018, AJ, 155, 238

Scholz A., Jayawardhana R., Muzic K., Geers V., Tamura M., Tanaka I., 2012, ApJ, 756, 24

Scholz A., Moore K., Jayawardhana R., Aigrain S., Peterson D., Stelzer B., 2018, ApJ, 859, 153

Schwarz H., Ginski C., de Kok R. J., Snellen I. A. G., Brogi M., Birkby J. L., 2016, A&A, 593, A74

Seager S., Deming D., 2010, ARA&A, 48, 631

Shkolnik E. L., Allers K. N., Kraus A. L., Liu M. C., Flagg L., 2017, AJ, 154, 69

Silvotti R., et al., 2007, Nature, 449, 189

Sivaramakrishnan A., et al., 2023, PASP, 135, 015003

Skemer A. J., et al., 2014, ApJ, 792, 17

Skrutskie M. F., et al., 2006, AJ, 131, 1163

Skrzypek N., Warren S. J., Faherty J. K., 2016, A&A, 589, A49

Smith B. A., Terrile R. J., 1984, Science, 226, 1421

Smith R. L., Pontoppidan K. M., Young E. D., Morris M. R., 2015, ApJ, 813, 120

Snellen I., et al., 2015, A&A, 576, A59

Soummer R., Pueyo L., Larkin J., 2012, ApJ, 755, L28

Sozzetti A., et al., 2023, A&A, 677, L15

Sparks W. B., Ford H. C., 2002, ApJ, 578, 543

Spiegel D. S., Burrows A., Milsom J. A., 2011, ApJ, 727, 57

Stam D. M., 2003, in Fridlund M., Henning T., Lacoste H., eds, ESA Special Publication Vol. 539, Earths: DARWIN/TPF and the Search for Extrasolar Terrestrial Planets. pp 615–619

Stamatellos D., Whitworth A. P., 2009, MNRAS, 392, 413

Stanford-Moore S. A., Nielsen E. L., De Rosa R. J., Macintosh B., Czekala I., 2020, ApJ, 898, 27

Stefánsson G., et al., 2025, AJ, 169, 107

Stetson P. B., 1987, PASP, 99, 191

Stolker T., et al., 2020, A&A, 635, A182

Stone J. M., et al., 2016, ApJ, 818, L12

Su K. Y. L., et al., 2009, ApJ, 705, 314

Suárez G., Metchev S., 2022, MNRAS, 513, 5701

Suarez G., Vos J. M., Metchev S., Faherty J. K., Cruz K., 2023, arXiv e-prints, p. arXiv:2308.02093

Sumi T., et al., 2011, Nature, 473, 349

Tan X., Showman A. P., 2019, ApJ, 874, 111

Tan X., Showman A. P., 2021, MNRAS, 502, 678

Tannock M. E., et al., 2021, AJ, 161, 224

Tinney C. G., Tolley A. J., 1999, MNRAS, 304, 119

Todorov K., Luhman K. L., McLeod K. K., 2010, ApJ, 714, L84

Todorov K. O., Luhman K. L., Konopacky Q. M., McLeod K. K., Apai D., Ghez A. M., Pascucci I., Robberto M., 2014, ApJ, 788, 40

Toomre A., 1964, ApJ, 139, 1217

Torres C. A. O., Quast G. R., da Silva L., de La Reza R., Melo C. H. F., Sterzik M., 2006, A&A, 460, 695

Tremblin P., Amundsen D. S., Mourier P., Baraffe I., Chabrier G., Drummond B., Homeier D., Venot O., 2015, ApJ, 804, L17

Tremblin P., Amundsen D. S., Chabrier G., Baraffe I., Drummond B., Hinkley S., Mourier P., Venot O., 2016, ApJ, 817, L19

Tsuji T., Nakajima T., 2003, ApJ, 585, L151

Tsuji T., Ohnaka K., Aoki W., Nakajima T., 1996, A&A, 308, L29

Tuthill P. G., Monnier J. D., Danchi W. C., 2000, in Léna P., Quirrenbach A., eds, Society of Photo-Optical Instrumentation Engineers (SPIE) Conference Series Vol. 4006, Interferometry in Optical Astronomy. pp 491–498, doi:10.1117/12.390244

VanderPlas J. T., 2018, ApJS, 236, 16

Veras D., Raymond S. N., 2012, MNRAS, 421, L117

Vigan A., 2020, vlt-sphere: Automatic VLT/SPHERE data reduction and analysis (ascl:2009.002), doi:10.5281/zenodo.6563998

Vigan A., Moutou C., Langlois M., Allard F., Boccaletti A., Carbillet M., Mouillet D., Smith I., 2010, MNRAS, 407, 71

Vigan A., et al., 2012, A&A, 544, A9

Vigan A., et al., 2021, A&A, 651, A72

Vos J. M., Allers K. N., Biller B. A., 2017, ApJ, 842, 78

Vos J. M., Allers K. N., Biller B. A., Liu M. C., Dupuy T. J., Gallimore J. F., Adenuga I. J., Best W. M. J., 2018, MNRAS, 474, 1041

Vos J. M., et al., 2019, MNRAS, 483, 480

Vos J. M., et al., 2020, AJ, 160, 38

Vos J. M., Faherty J. K., Gagné J., Marley M., Metchev S., Gizis J., Rice E. L., Cruz K., 2022, ApJ, 924, 68

Vos J. M., et al., 2023, ApJ, 944, 138

Wagner K., et al., 2018, ApJ, 863, L8

Wahhaj Z., et al., 2011, ApJ, 729, 139

Wahhaj Z., et al., 2013, ApJ, 779, 80

Wallace A. L., Casey A. R., Brown A. G. A., Castro-Ginard A., 2025, MNRAS, 536, 2485

Wang J. J., et al., 2018, AJ, 156, 192

Wang J., et al., 2020, AJ, 160, 150

Ward-Duong K., et al., 2015, MNRAS, 449, 2618

Whitworth A. P., Zinnecker H., 2004, A&A, 427, 299

Wilson P. A., Rajan A., Patience J., 2014, A&A, 566, A111

Winters J. G., et al., 2019, AJ, 157, 216

Wizinowich P., et al., 2000, PASP, 112, 315

Wolszczan A., Frail D. A., 1992, Nature, 355, 145

Wright J. T., Gaudi B. S., 2013, in Oswalt T. D., French L. M., Kalas P., eds, , Planets, Stars and Stellar Systems. Volume 3: Solar and Stellar Planetary Systems. p. 489, doi:10.1007/978-94-007-5606-9_10

Wright E. L., et al., 2010, AJ, 140, 1868

Xuan J. W., et al., 2024, Nature, 634, 1070

Yang H., et al., 2015, ApJ, 798, L13

Yang H., et al., 2016, ApJ, 826, 8

York D. G., et al., 2000, AJ, 120, 1579

Youdin A. N., Goodman J., 2005, ApJ, 620, 459

Zacharias N., Finch C., Frouard J., 2017, AJ, 153, 166

Zapatero Osorio M. R., Béjar V. J. S., Martín E. L., Rebolo R., Barrado y Navascués D., Bailer-Jones C. A. L., Mundt R., 2000, Science, 290, 103

Zapatero Osorio M. R., Caballero J., Martín E. L., Béjar V. J. S., Rebolo R., 2004, Ap&SS, 292, 673

Zapatero Osorio M. R., Martín E. L., Bouy H., Tata R., Deshpande R., Wainscoat R. J., 2006, ApJ, 647, 1405

Zhang Z., et al., 2018, ApJ, 858, 41

Zhang Z., et al., 2020, ApJ, 891, 171

Zhang Y., et al., 2021a, Nature, 595, 370

Zhang Y., Snellen I. A. G., Mollière P., 2021b, A&A, 656, A76

Zhang Z., Liu M. C., Best W. M. J., Dupuy T. J., Siverd R. J., 2021c, ApJ, 911, 7

Zhang Z., Liu M. C., Claytor Z. R., Best W. M. J., Dupuy T. J., Siverd R. J., 2021d, ApJ, 916, L11

Zhang Z., et al., 2025, AJ, 169, 9

Zheng X., Kouwenhoven M. B. N., Wang L., 2015, MNRAS, 453, 2759

Zhou Y., Apai D., Schneider G. H., Marley M. S., Showman A. P., 2016, ApJ, 818, 176

Zhou Y., Bowler B. P., Morley C. V., Apai D., Kataria T., Bryan M. L., Benneke B., 2020, AJ, 160, 77

Zhou Y., Bowler B. P., Apai D., Kataria T., Morley C. V., Bryan M. L., Skemer A. J., Benneke B., 2022, AJ, 164, 239

Zhu Z., Stone J. M., Rafikov R. R., 2012, ApJ, 758, L42

Zuckerman B., 2019a, ApJ, 870, 27

Zuckerman B., 2019b, ApJ, 870, 27

Zuckerman B., Bessell M. S., Song I., Kim S., 2006, ApJ, 649, L115

de Boer J., et al., 2016, A&A, 595, A114

de Regt S., et al., 2024, A&A, 688, A116

de Zeeuw P. T., Hoogerwerf R., de Bruijne J. H. J., Brown A. G. A., Blaauw A., 1999, AJ, 117, 354

Žerjal M., Ireland M. J., Crundall T. D., Krumholz M. R., Rains A. D., 2023, MNRAS, 519, 3992

van Elteren A., Portegies Zwart S., Pelupessy I., Cai M. X., McMillan S. L. W., 2019, A&A, 624, A120

van Leeuwen F., 2007, A&A, 474, 653